2019

NANOHARVESTING AND DELIVERY OF BIOACTIVE MATERIALS USING ENGINEERED SILICA NANOPARTICLES

Md Arif Khan
University of Kentucky, makh226@g.uky.edu
Author ORCID Identifier:
https://orcid.org/0000-0001-8471-4200
Digital Object Identifier: https://doi.org/10.13023/etd.2019.419

STUDENT AGREEMENT:

I represent that my thesis or dissertation and abstract are my original work. Proper attribution has been given to all outside sources. I understand that I am solely responsible for obtaining any needed copyright permissions. I have obtained needed written permission statement(s) from the owner(s) of each third-party copyrighted matter to be included in my work, allowing electronic distribution (if such use is not permitted by the fair use doctrine) which will be submitted to UKnowledge as Additional File.

I hereby grant to The University of Kentucky and its agents the irrevocable, non-exclusive, and royalty-free license to archive and make accessible my work in whole or in part in all forms of media, now or hereafter known. I agree that the document mentioned above may be made available immediately for worldwide access unless an embargo applies.

I retain all other ownership rights to the copyright of my work. I also retain the right to use in future works (such as articles or books) all or part of my work. I understand that I am free to register the copyright to my work.

REVIEW, APPROVAL AND ACCEPTANCE

The document mentioned above has been reviewed and accepted by the student's advisor, on behalf of the advisory committee, and by the Director of Graduate Studies (DGS), on behalf of the program; we verify that this is the final, approved version of the student's thesis including all changes required by the advisory committee. The undersigned agree to abide by the statements above.

Md Arif Khan, Student

Dr. Barbara L. Knutson, Major Professor

Dr. Stephen E. Rankin, Director of Graduate Studies

NANOHARVESTING AND DELIVERY OF BIOACTIVE MATERIALS USING ENGINEERED SILICA NANOPARTICLES

DISSERTATION

A dissertation submitted in partial fulfillment of the
requirements for the degree of Doctor of Philosophy in the
College of Engineering
at the University of Kentucky

By

Md Arif Khan

Lexington, Kentucky

Co- Directors: Dr. Barbara L. Knutson, Professor of Chemical Engineering

and Dr. Stephen E. Rankin, Professor of Chemical Engineering

Lexington, Kentucky

2019

https://orcid.org/0000-0001-8471-4200

ABSTRACT OF DISSERTATION

NANOHARVESTING AND DELIVERY OF BIOACTIVE MATERIALS USING ENGINEERED SILICA NANOPARTICLES

Mesoporous silica nanoparticles (MSNPs) possess large surface areas and ample pore space that can be readily modified with specific functional groups for targeted binding of bioactive materials to be transported through cellular barriers. Engineered silica nanoparticles (ESNP) have been used extensively to deliver bio-active materials to target intracellular sites, including as non-viral vectors for nucleic acid (DNA/RNA) delivery such as for siRNA induced interference. The reverse process guided by the same principles is called "nanoharvesting", where valuable biomolecules are carried out and separated from living and functioning organisms using nano-carriers. This dissertation focuses on ESNP design principles for both applications.

To investigate the bioactive materials loading, the adsorption of antioxidant flavonoids was investigated on titania (TiO_2) functionalized MSNPs (mean particle diameter ~170 nm). The amount of flavonoid adsorbed onto particle surface was a strong function of active group (TiO_2) grafting and a 100-fold increase in the adsorption capacity was observed relative to nonporous particles with similar TiO_2 coverage. Active flavonoid was released from the particle surface using citric acid-mediated ligand displacement. Afterwards, nanoharvesting of flavonoids from plant hairy roots is demonstrated using ESNP in which TiO_2 and amine functional groups are used as specific binding sites and positive surface charge source, respectively. Isolation of therapeutics was confirmed by increased pharmacological activity of the particles. After nanoharvesting, roots are found to be viable and capable of therapeutic re-synthesis. In order to identify the underlying nanoparticle uptake mechanism, TiO_2 content of the plant roots was quantified with exposure to nanoparticles. Temperature (4 or 23 °C) dependent particle recovery, in which time dependent release of ESNP from plant cells showed a similar trend, indicated an energy independent process (passive transport).

To achieve the selective separation and nanoharvesting of higher value therapeutics, amine functionalized MSNPs were conjugated with specific functional oligopeptides using a hetero-bifunctional linker. Fluorescence spectroscopy was used to confirm and determine binding efficiency using fluorescently attached peptides. Binding of targeted compounds was confirmed by solution depletion using liquid chromatography–mass spectrometry. The conjugation strategy is generalizable and applicable to harvest the pharmaceuticals produced in plants by selecting a specific oligopeptide that mimic the appropriate binding sites.

For related gene delivery applications, the thermodynamic interaction of amine functionalized MSNPs with double-stranded (ds) RNA was investigated by isothermal titration calorimetry (ITC). The heat of interaction was significantly different for particles with larger pore size (3.2 and 7.6 nm) compared to that of small pore particles (1.6 nm) and nonporous particles. Interaction of dsRNA also depended on molecular length, as longer RNA (282 base pair) was unable to load into 1.6 nm particles, consistent with previous confocal microscopy observations. Calculated thermodynamic parameters (enthalpy, entropy and free energy of interaction) are essential to design pore size dependent dsRNA loading, protection and delivery using MSNP carriers. While seemingly diverse, the highly tunable nature of ESNP and their interactions with cells are broadly applicable, and enable facile nano-harvesting and delivery based on a continuous uptake-expulsion mechanism.

KEYWORDS: Engineered silica nanoparticle, Nanoharvesting, Nucleic acid delivery, Cellular interactions, Functional oligopeptide, Conjugation

Md Arif Khan

October 29, 2019

Date

NANOHARVESTING AND DELIVERY OF BIOACTIVE MATERIALS USING ENGINEERED SILICA NANOPARTICLES

By
Md Arif Khan

Barbara L. Knutson, Ph.D.
Co-Director of Dissertation

Stephen E. Rankin, Ph.D.
Co-Director of Dissertation

Stephen E. Rankin, Ph.D.
Director of Graduate Studies

October 29, 2019
Date

DEDICATION

Dedicated to two persons who motivated, guided and encouraged me very early on my life, without them even thinking about graduate study would never have been possible.

My late grandfather and eternal inspiration
Hussain Ahmad Khan

&

My uncle
Mozammel Haque Bhuiya

ACKNOWLEDGMENTS

This dissertation would never be possible to come into fruition without my doctoral advisors Prof. Barbara Knutson and Prof. Stephen Rankin. The first and foremost, their extreme care, guidance and patience for me was invaluable throughout my doctoral study. In a word, they taught me how to perform scientific research with the completion of little steps that culminates into bigger success, while always keeping the feet grounded by critical thinking rather than diving headlong. Their perseverance in reviewing and correcting my drafts (abstracts, manuscripts, reports) and thorough practice presentations helped me a lot in preparing myself as better writer and speaker. I always wished to have mentors same as their capacity and caliber in my present and future life.

My gratitude are infinite toward my other doctoral committee members Prof. Bruce Webb and Prof. J. Zach Hilt for their comments during my proposal defense and yearly committee meetings. Their advices were very helpful in setting up the research projects and concluding them with experiments and analysis. They have also guided me to think outside of the box and expand my vision towards much broader perspectives. I also thank Prof. Luke Bradley for spending his valuable time being my external examiner for this dissertation and providing valuable advice to finish up this dissertation.

I am expressing my sincere and deep gratefulness toward our collaborating laboratories at the University of Kentucky, whose contribution is immeasurable for the completion of this work. Prof. Bruce Webb's lab at the Department of Entomology has collaborated in the RNA delivery project and I very much appreciate Dr. Webb, Emily Nadeau and Emrah Ozel for performing the hard work of synthesizing and concentrating insect RNA for isothermal titration calorimetry work. I also thank our collaborators Prof.

Luke Bradley of Neuroscience Department and Prof. Bert Lynn of Chemistry Department to provide different kinds of oligopeptides timely for nanoparticle attachment and running the β-estradiol binding assay, respectively, which were essential for the completion of functional oligopeptide attachment project. I also share immense gratitude toward our industrial collaborating company Naprogenix Inc. for being greatly supportive during all the projects related to nanoharvesting. Dr. John Littleton, CEO of Naprogenix was extremely helpful, kind and generous in letting me using the laboratories, taking ample amount of plant roots for the projects to be completed. The biweekly meetings with Nanprogenix peoples were extremely thoughtful, informative and encouraging to the future research. I especially appreciate the effort put up by Mr. Jatinder Sambi for sustaining root cultures and providing me with short notice, and Dr. Trent Rogers for performing the biological activity assays and estrogen binding experiments. I also enjoyed many lively discussion with Dr. Rogers on science topics.

I am also grateful to Dr. Dali Qian and Dr. Nicholas Briot of Electron Microscopy Center for their help in performing TEM and SEM imaging and characterization; and Mr. Jason Backus of Kentucky Geological Survey for XRD analysis. Peoples from other research laboratory at the Chemical Engineering Department, especially Dr. Rupam Sharma, Saiful Islam and Dr. Andrew Colburn from Bhattacharyya Lab; and Dr. Jacob Lilly and Dr. Calvin Cahall from Berron Lab has provided tremendous help in dynamic light scattering and fluorescence microscopy, respectively. Also, many appreciation to Dr. Hilt for letting me using 96-well plate reader for UV-vis and fluorescent spectroscopy. I also thank and appreciate Dr. Joseph Strzalka of Advanced Photon Source at Argonne

National Laboratory for his help during synchrotron x-ray scattering experiment and later data analysis and reviewing manuscripts.

Help and support provided by my fellow lab members from past and present, my dearest colleagues, is indispensable during my graduate study. I have never felt an iota of boredom or being left alone for a slightest of minutes in the lab or when we were out together or in a conference or symposium. In a word, I have spent some of the most wonderful time in my entire life with them. Most notably, my work was heavily engaged with that of Mahsa Moradipour, Dr. Shanshan Zhou, Dr. Syed Islam, Dr. Suraj Nagpure and Yuxing He. Namal Wanninayake of Dr. Doo-Young Kim's laboratory of Chemistry Department was fun to work with. Dr. Daniel Schlipf, Dr. Saikat Das and Dr. Ravinder Garlapalli has provided valuable advice and help during the initiation of my graduate research. I always enjoyed the presence of Dr. Kwabena Darkwah, Joshua Garay, Aniruddha Shirodhkar and Andrew Drake. I can never forget what these people has brought in my life, I am lucky to interact with them in this tortuous journey called life.

This work would never have been completed without the hard work put up by the undergraduate students working on various projects under my guidance. Efforts put by Maelyn Kiser, Ramy Ghanim, William Wallace and Elliot Rushing on different projects were essential for the projects to come into fruition. I also had the joy of working with NSF REU undergraduate students Justin Zhong of University of Texas and Madeleine Fugate of Montana State University in the summer of 2017 and 2018, respectively and with several high school students throughout my graduate study.

My special thanks also goes to Prof. Thomas Dziubla (then Director of Graduate Studies and now the Department Chair of Chemical and Materials Engineering) for his

advice and guidance during the five years long stay at the department. I am delighted and excited to have him as my future mentor for postdoctoral research, as I am planning to work with him after completing my Ph.D. degree. All other department professors were amiable whenever I met them and their joyful and caring presence has always inspired me toward my success. I also acknowledge the help and support received from departmental staff Ms. Marlene Spurlock, Ms. Melissia Witt, Ms. Paula McGee, Ms. Amy Terry, Ms. Nancy Miller, Ms. Chelsea Hansing, Mr. Bruce Cole, Mr. Nick Cprek and Mr. Joshua Duruttya. They were extremely helpful and proficient whenever I ran into any difficulties and problems. I thank all the graduate students at MACE for organizing various activities, which kept me engaged to the department and made the whole graduate study life much more pleasurable. There are numerous other persons at the University of Kentucky that I failed to mention here, but helped me along the way in the doctoral study.

I surely acknowledge and appreciate the funding and financial supports received from United States Government agencies and industrial collaborators, Commonwealth of Kentucky agencies, University of Kentucky College of Engineering and the Department of Chemical and Materials Engineering. This work was supported and funded by United States National Institutes of Health (NIH Grant nos.R41AT008312 and 2R44AT008312-02), National Science Foundation sponsored Center for Arthropod Management Technologies (CAMTech) (NSF Industry-University Cooperative Research Center award no. 1238087), National Science Foundation Experimental Program to Stimulate Competitive Research (EPSCoR) grant (award no, 1355438), Department of Energy (DOE Grant No. DE-FG02-07-ER46375) and Kentucky Science and Engineering Foundation (KSEF-2929-RDE-016). X-ray scattering experiments at the Advanced Photon Source of

Argonne National Laboratory were conducted by using resources supported by United States Department of Energy (DOE) Office of Science User Facility operated under Contract No. DE-AC02-06CH11357. I also acknowledge the Block Funding received from the University of Kentucky College of Engineering and Department of Chemical and Materials Engineering for multiple travel to Argonne National Laboratory, IL and Graduate School and Department of Chemical and Materials Engineering travel awards for going to national conferences to present my works.

In retrospect, I remember and cherish the contribution of my Master's and Bachelor's professors toward inspiring and polishing me to pursue doctoral study. My Master's supervisor Prof. Yusuf Adewuyi, then Graduate Director and mentor Prof. Shamsuddin Ilias, the late Prof. Franklin King and Prof. Lijun Wang of North Carolina A&T State University were instrumental in supporting me. I am immensely grateful to my undergraduate professor and mentor Dr. A. K. M. Abdul Quader and professor and friend Dr. Iftheker A. Khan for guiding me through some rough and tumultuous undergraduate years and encouraging me to pursue graduate study early on.

Foremost, my wife Fatema Sikder's contributions to this dissertation and my doctoral study is illimitable throughout. I am enormously fortunate to have such a caring and loving partner in my life, who put my success and well-being above all her needs and desires. Her care and sacrifice during experimentation and writing long time by depriving her continuously (even during her pregnancy now) is what I most feel for and my gratitude to her is unfathomable for that reason.

Finally, I also want to stress the inspiration and encouragements I have received from my other family members: my parents, my sister, brothers, uncles and aunts, cousins

and my in-laws. Their sacrifices have elevated me here, their eternal love and affections is what I am the luckiest to have and driving me forward through the toughest of the times in graduate study. I also thank my friends at Bangladesh Student Association of the University of Kentucky for the support and activities together.

TABLE OF CONTENTS

LIST OF TABLES

LIST OF FIGURES

CHAPTER 1. GENERAL INTRODUCTION AND SCOPE

1.1 General Introduction

The use of plant-derived natural compounds for therapeutic and medicinal application is well known throughout the history of mankind and recorded as early as 2600 B.C. [1-3]. Plants primarily synthesize two types of metabolites: primary metabolites that are essential to normal plant growth, development and reproduction through biosynthesis and breakdown of proteins, fats, carbohydrates and nucleic acids; and secondary metabolites, which are not directly involved in plant vitality but are produced to respond to a plant's particular environment and as a defense mechanism against predators [1, 4]. Secondary metabolites are subdivided into many groups, of which alkaloids, terpenoids and flavonoids are the most prevalent and have tremendous therapeutic and medicinal applications [5-7]. Flavonoids are polyphenolic compounds, normally found in different organelles of plant cells and perform functions including the inhibitory activity against disease-inflicting organisms and herbivores [5]. Because these secondary metabolites often bind to human receptors to induce favorable responses to diseases and pathogens, they provide a vast reservoir for new drug development and therapeutic applications [8].

Despite their rich history and future potential, new drug development based on plant-derived natural products is in decline recently due to challenges including the identification, analysis and large scale production of targeted compounds [8, 9]. Secondary metabolite production in plant cells is strictly regulated by controlled transcription of biosynthetic genes and overproduction of targeted compounds depending largely on the internal and/or external signals that leads to controlled transcription [10]. Recently, techniques for environmental and genetic modification of plant systems have been

developed (especially in hairy root cultures) by external manipulation of biosynthetic pathways in order to enrich targeted metabolites [11-13]. Hairy root plant cell cultures have swift and spontaneous regrowth potential, and increased yields of bioactive compounds in hairy roots has been achieved by genetic transformation [14]. Genetic alterations of biosynthetic pathways in plants are traditionally observed by cloning desired genes by protein sequencing and verifying the gene expression through recombinant protein in an appropriate host, a very slow and tedious method that requires random testing of many genes [2]. As a result, traditional therapeutics extraction methods that involve maceration of the whole tissue pose a significant obstacle for the long term economic viability of plant-derived biomolecule isolation project. To overcome this limitation, nanoparticulate carriers can be utilized to transport metabolites out of living plants (termed as nanoharvesting [15, 16]), where particles can be engineered to penetrate inside the cells, bind desired metabolites and exit without killing the plants.

Although nanoharvesting was preliminary demonstrated for flavonoids in *Arabidopsis* plants by nonporous titania nanoparticles (average diameter < 3 nm) [15], nonporous particles provide low surface area and tenability, and separation of particles after exposure to plants is particularly difficult. As a result, designing a viable and industrially profitable nanoharvesting process using nonporous particles is unlikely. On the other hand, a porous nano-carrier with high surface area such as mesoporous silica nanoparticles (MSNPs), with their surface modified to include biomolecule affinity and cell membrane penetration property, will be feasible to isolate large amount of metabolites during nanoharvesting. Silica surface is particularly amenable to modify with varieties of inorganic and organic active groups on its surface [17, 18], thus engineering of MSNPs for

the purpose of nanoharvesting is conceivable. Moreover, MSNP surface can also be modified with functional groups that selectively binds with a single or specific classes of biomolecules with high value pharmaceutical and medicinal compounds, which can provide extremely high selectivity during biomolecule separation from organic mixtures or nanoharvesting from transgenic plants, rendering the later-separation step completely redundant.

Regarding genetic modification in plants, a significant portion of hereditary alteration and gene expression growth were achieved by delivering nucleic acids and recent technologies have utilized gene delivery and RNA interference (RNAi) extensively. As an example, this technique was successfully implemented to cause poppy plants, *Papaver somniferum*, to produce benzylisoquinoline alkaloid instead of the natural product morphine [19]. On the other hand, DNA delivery is one of the most useful methods for non-viral gene therapy [20]. Nucleic acids (DNA fragments and small interfering (si) RNA) delivery to targeted intracellular locations of eukaryotic cell by an extracellular carrier is necessary to obtain desired genetic modification and RNAi, respectively [21-23]. External carriers are principally required for nucleic acids delivery to intracellular sites since DNA/RNAs are extremely susceptible to enzymatic degradation (by nucleases) as soon as they enter through the cell membranes. Ideal carriers for nucleic acid delivery provide protection against enzymatic degradation in addition to high loading capacity and controlled release at the targeted sites [24]. Highly tunable properties of MSNPs to create mesopores with different sizes can be utilized efficiently for pore size dependent protection, where large enzyme molecules can be excluded from entering optimally determined pore sizes with loaded nucleic acids. Foreign DNA delivery to plants using

functionalized MSNPs were demonstrated in tobacco leaves and *Arabidopsis* roots [25, 26]. However, siRNA delivery to plants are less explored to date but it promises huge opportunity in terms of genetic transformation. Another rapidly developing related field regarding nucleic acid delivery to living organisms is RNAi mediated pest control, where double-stranded (ds) RNA related to specific insects' mortality can be utilized for bio-based control of their population in contrast to chemical insecticides [27, 28]. The application of MSNPs for these purposes remains relatively unexplored.

In light of these and related applications, this dissertation will be centered on the design of mesoporous silica nanoparticles (MSNPs) for controlled interactions with whole cells, and the controlled binding and release of target bioactive compounds. Silica nanomaterials can be synthesized in a variety of morphological forms with precise size and surface properties control, and are a versatile platform for biomolecule separation and transport purposes [29, 30]. MSNPs with high surface area and tunable surface properties suitable for biomaterial accommodation have been deployed for drug delivery and biomedical applications [31]. In addition, silica nanocomposites with a variety of other active materials (polymer, metal oxides *etc.*) have been prepared with improved thermal, physical and chemical properties, but the main challenge is maintaining surface properties of pure silica nanomaterials after nanocomposite formation [32, 33]. Another way to incorporate active groups onto silica nanomaterials while retaining favorable properties of silica is to functionalize the silica surface with them [34]. Surface functionalization of silica nanoparticles with amine ($-NH_2$) group provides colloidal stability, enhances their biocompatibility and facilitates their internalization by living cells [35, 36]. Also, amine functionalization provides silica nanomaterials with much needed positive charge to

covalently bind negatively charged nucleic acids for nucleic acid loading [37]. By loading nucleic acids onto amine functionalized MSNPs, an effective carrier for gene and RNA delivery can be designed, where MSNP-based efficient nucleic acid carrying systems combine three capabilities: loading, protection from nucleases and controlled release at the target sites.

1.2 Scope of the Work and Dissertation Outline

The dissertation is focused on designing engineered silica nanoparticles (ESNP) for transporting biomolecules across the cell membrane of living organisms in nanoharvesting and nanodelivery applications. Tuning and modification of silica surface properties start with the synthesis of nanoparticles (providing desired particle size, shape and pore size) and culminates in several post-synthesis modification stepwise to provide various active and functional groups on the surface, predominantly inside the mesopores. The specific mesoporous silica nanoparticles (MSNPs) used in this work were synthesized with varying pore size (2.2, 4.1 and 7.9 average pore diameter) and particle size 140-170 nm (suitable for cell membrane penetration), along with nonporous particles with 190 nm diameter as controls. Particles were functionalized/conjugated with active groups (titania, amine and oligopeptides) to facilitate biomolecule adsorption and loading on silica surface. Titania functionalization was used to provide an active group for the complexation of plant-derived therapeutic polyphenolic compounds, amine functionalization to provide positive charge for membrane penetration and binding to nucleic acids for delivery, and functional oligopeptides were conjugated for selective separation and nanoharvesting. Finally thermodynamic interactions of amine functionalized MSNPs with various pore sizes with double stranded (ds) RNA (two different lengths: 84 and 282 base pair long) were studied to design facile engineered silica nanoparticle-based nucleic acid delivery systems. Research projects investigated in this dissertation and their potential contributions are presented schematically in **Figure 1.1** to provide a clear visual guide to the readers. A detail chapter-by-chapter outline is provided below.

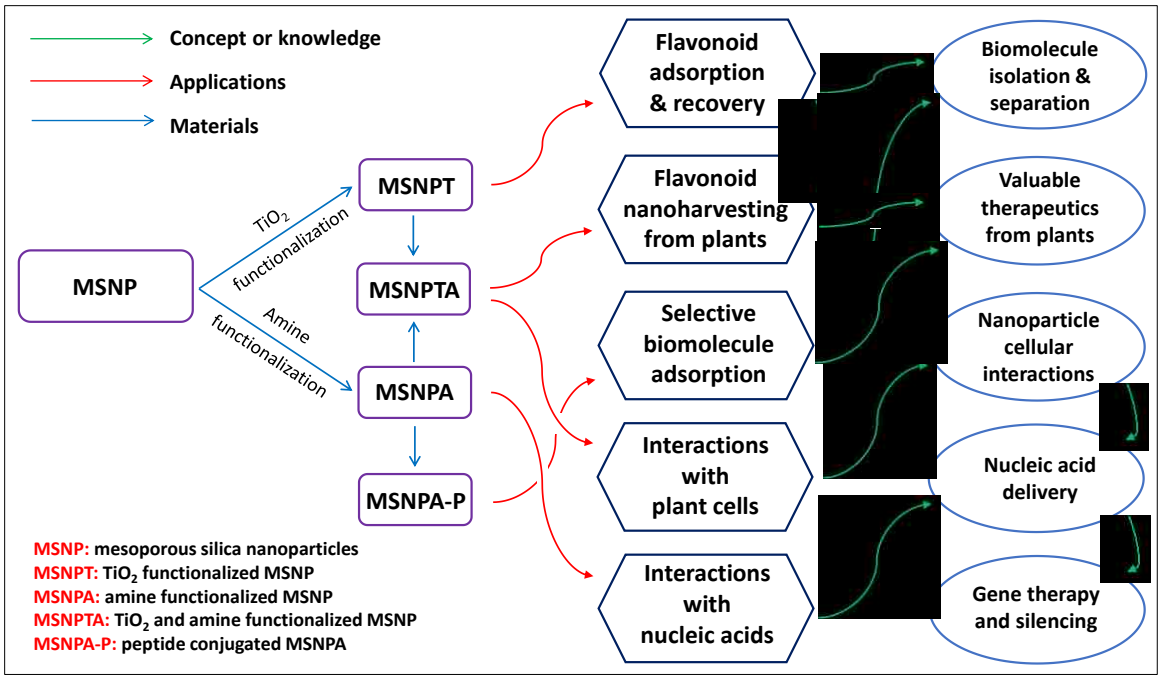

Figure 1.1 A schematic diagram of the outline of research projects carried out in this dissertation and the respective contributing research sectors.

The dissertation is divided into **8 chapters** including this **Chapter 1,** where a brief introduction of the study is provided along with defining the scope of the investigation and the outline of the dissertation. In **Chapter 2**, a detailed background and literature review for the dissertation topics is provided, including different types of silica nanoparticulate materials, silica surface functionalization techniques for various applications, interactions of biomolecules with engineered silica surfaces, aspects of nanoparticle interaction with living cells and tissues, and finally designing nanoparticulate carriers for biomolecule delivery to cells. In the first section of **Chapter 2**, MSNP synthesis strategies for particles with controlled particles size and shape, and introduction of pores with well-defined geometry and shape is reviewed. Both nanoparticles suitable for interaction with cells and microparticles for visualization are discussed. Relevant procedures for surface functionalization of MSNPs, and surface interactions with MSNP surfaces are discussed.

The next section of **Chapter 2** reviews interactions of MSNPs with cells, especially plants, including internalization, intracellular transport and export mechanism. Finally, carrier design is discussed to allow biomolecule (chiefly RNA and DNA) delivery to cells with loading, transport, protection from biological defense mechanism, and controlled release at target sites.

The remaining chapters detail the specific projects conducted towards fulfilling the main aim of the dissertation, design of engineered mesoporous silica for nanoharvesting and delivery. One requirement for nanoharvesting is to create selective sites for binding of target compounds, and **Chapter 3** describes the development of a method for functionalizing MSNPs with titania (TiO_2) for chelation with and isolation of flavonoids. Based on measurements of flavonoid adsorption by solution depletion, an optimized TiO_2 grafting density on MSNPs is determined. For recovery of flavonoids from the particles without damaging the TiO_2 sites, a method based on citric acid mediated ligand displacement is developed. Antiradical activity of surface bound and recovered flavonoid is confirmed. University of Kentucky undergraduate student William Wallace made significant contribution in particle synthesis and functionalization during this project. This work is published in *ACS Applied Materials and Interfaces* (Khan et al., ACS appl. Mater. Interfaces, 2017, 9, 32114-32125 [38]) and reproduced here with permission from the American Chemical Society.

Based on the optimized engineered silica nanoparticle design in **Chapter 3**, titania and amine functionalized MSNPs are deployed in **Chapter 4** to isolate flavonoids from living *Solidago nemoralis* (goldenrod) hairy root cultures (nanoharvesting), where roots were genetically modified to overproduce quercetin-derived flavonoids. The chapter

provides experimental evidence that the four criteria for an ideal nanoharvesting process are met by these particles: efficient uptake of nanoparticles, excellent metabolite binding, rapid nanoparticles recovery to maintain minimal exposure time, and cell viability after exposure to the nanoparticles. MSNPs with sizes suitable for plant cell uptake (< 200 nm) are synthesized and functionalized with both TiO_2 and positively charged amine group to provide the binding site for flavonoids and facilitate their uptake inside root cells, respectively. Nanoparticle internalization inside hairy roots is confirmed by fluorescent microscopy after tagging the particles with fluorophore rhodamine B isothiocyanate (RITC). Presence of metabolites on particle surface after exposure to hairy roots were confirmed by increased radical scavenging activity and flavonoid-specific nicotinic receptor ligand displacement activity. Finally, viability of roots and ability of roots to continue to synthesize active flavonoids were demonstrated to ensure continuous production and harvesting. This project was carried out in collaboration with Naprogenix Inc. Mr. Jatinder Sambi of Nanoprogenix provided the roots from continuous cultures, and periodically checked and re-cultured flavonoid overproducing roots. He also performed measurement of flavonoid biosynthesis of roots after nanoharvesting. Dr. Trent Rogers of Naprogenix measured ligand displacement activity of root extracts and nanoparticles exposed to roots. A manuscript on this project is published in *Materials Science and Engineering C* (Khan et al., Mater. Sci. Eng. C, 2020, 106, 110190 [39]), which is reproduced with permission from Elsevier.

As a continuation of nanoharvesting by engineered silica nanoparticles, the detailed mechanisms of particle internalization, intracellular transport and expulsion during nanoharvesting are studied in **Chapter 5**. Nanoparticles uptake is quantified by the

chemical analysis of the Ti-content of roots after exposure to nanoparticles, and expulsion by fluorescent spectroscopy of particles (fluorophore RITC labeled) in solution. Fluorescence micoroscopy is used to establish time and concentration dependent nanoparticle uptake inside hairy roots. Temperature (4 and 23 ºC) dependent uptake and recovery experiments are used to distinguish between activated (energy mediated) or surface charge dependent direct penetration (by passive diffusion) through cell membranes. Finally, recovery of fluorescent nanoparticle is performed in the solution of non-fluorescent particles (exchange) to demonstrate dynamic and spontaneous nature of nanoparticle uptake and expulsion. The findings are valuable for further optimizing design parameters (types and extent of functionalization) of nanoparticles for nanoharvesting applications. This project was also conducted in collaboration with Naprogenix Inc., and Mr. Jatinder Sambi cultured and provided *S. nemoralis* hairy roots.

While Ti-complexation is a route for binding compounds with catechol-like groups such as flavonoids, selective separation of biomolecules from a biological mixture can be more generally achieved by using a peptide or protein that has specific host-guest interaction with a target molecule. This approach has been used in stationary phases such as chromatography columns, but the technique can be extended to nanoharvesting. In this case, selective isolation of therapeutics from living transgenic plant cultures can be achieved by conjugating the particles with oligopeptides that mimic biomolecules' binding sites. In **Chapter 6**, a highly controllable strategy is developed for conjugation of oligopeptide Gly-Gly-Gly-Gly (GGGG or 4G), Arg-Ser-Ser-Val (RSSV) and its derivative 4RSSV (RSSVRSSVRSSVRSSV) to amine-functionalized MSNPs (with 8 nm pore diameter) by using a heterobifunctional linker Sulfo-NHS-LC-diazirine. The linker has an

amine reactive NHS ester group at one end and long-wavelength (350-370 nm) UV-activable diazirine group at the other end, which remain dormant until exposure to UV light. This combination provides great control over binding efficiency and allows the design of processes that compensate for slow diffusion of reactants into mesopores. Preservation of peptide functionality upon surface binding is demonstrated from increased binding of β-estradiol, which indicates their mimicry of human estrogen binding sites. This project was accomplished in collaboration with Naprogenix, Prof. Luke Bradley's lab in the Department of Neuroscience and Prof. Bert Lynn's lab in the Department of Chemistry. Prof. Bradley provided purified oligopeptides and Prof. Lynn performed β-estradiol analysis for quantitation of binding using LC-MS.

The delivery of nucleic acids into eukaryotic cells using amine functionalized MSNPs can be effectively carried out by pore size selective loading, protection from enzymatic hydrolysis and controlled release. Thermodynamic interactions of nucleic acids with surface bound amine functional groups is an important factor to be considered during nanoparticle design for nanodelivery purpose. In **Chapter 7**, thermodynamics of double stranded RNA binding with amine-functionalized MSNPs is measured by isothermal titration calorimetry as a function of RNA length (84 and 282 base pairs) and pore size (nonporous, 1.6, 3.2 and 7.6 nm). The thermodynamic parameters (enthalpy, entropy, stoichiometry and free energy of binding) are evaluated by fitting single or double distinct binding site model to the isotherms derived from raw heat curves during injection. The results are interpreted in terms of the nature of binding (enthalpy or entropy dominated), heat release and reorientation of molecules, and equilibrium stoichiometric binding ratio. This study is an essential part of a larger project regarding siRNA delivery to insects using

engineered silica nanoparticles in collaboration with Dr. Bruce Webb's laboratory in Entomology Department of University of Kentucky. Emily Nadaeu and Emrah Ozel performed the synthesis of 84 and 282 base pair dsRNA for this work.

The dissertation concludes in **Chapter 8** with concluding remarks and suggestions for extensions of this work in new directions. Future directions involve using more highly dispersed titania as a functional group for flavonoid adsorption and loading; developing magnetic core-mesoporous silica shell nanoparticles in nanoharvesting for external magnetic field enhanced control during cellular transport; targeting other high value biomolecules for the selective separation and nanoharvesting using specific peptide/protein functionality; and delivering nucleic acids to cells using amine functionalized MSNPs. The supporting information for **Chapter 3 to 7** is provided in **Appendices A to E**, respectively.

CHAPTER 2. BACKGROUNDS

2.1 Silica Particles

Silicon is the second most abundant element in earth's crust and its oxide silica (SiO_2) is plentiful in Earth's surface. Silica has been used from ancient time to manufacture glass and ceramic materials. In silica materials, each Si-atom is tetrahedrally coordinated with four O atoms and a network of Si-O-Si exist throughout the materials that provides for mechanical and thermal stability. Recent innovations made it possible to synthesize varieties of silica materials (particles, films, membranes *etc.*) from Si-alkoxide based precursors using sol-gel synthesis techniques [40, 41]. The mild conditions used for sol-gel processing (near-ambient temperature and pressure, mild pH) also allows the incorporation of pores within silica particles using various surfactant templates. The ability of the silica framework to withstand harsh condition also allows organic templates to be removed while keeping silica framework intact (giving rise to mesoporous silica nanoparticles, MSNPs), thus providing extremely high porosity with the preservation of bulk silica properties in the particles [42, 43].

Mesoporous silica has a high surface area terminated with hydroxyls, which can be functionalized with a wide variety of active groups. Different kinds of mesoporous silica materials are used as supports for different inorganic and organic active groups such as transition metal oxides and enzymes for catalytic and biocatalytic applications, and artificial lipid membranes and embedded proteins for biomimetic analyte detection and transport [44-47]. Because of their tunable surface chemistry, MSNPs are used in biosensing, separations, biomolecule transport and catalytic applications, as they provide optical transparency to allow sensing of biomaterials and a surface which can be tailored

with other functional groups [18]. The ability of silica materials to be functionalized with numerous active groups extend the versatility of their applications. Throughout the 20th and 21st centuries, a vast number of silica particles have been developed for innumerable applications and some major classes are outlined below.

2.1.1 Nonporous Silica Nanoparticles (SNPs)

SNPs are the simplest types of silica particulate materials widely used as fillers, abrasives, and rheological modifiers [48], but here they provide a standard case where internal mass transport limitations associated with mesopores are avoided. During biomolecule loading and adsorption, nonporous silica nanoparticles provide information about physicochemical processes on outer surface of the particles, contrasting with the loading inside mesopores [49]. Synthesis of nonporous silica nanoparticles (SNPs) from alkoxysilane precursors (subsequently named the sol-gel synthesis procedure) was first reported by Stöber et al. using ammonia as catalyst, tetraalkyl orthosilicates (*a.k.a.* tetraalkoxysilanes) as precursors, and ethanol/water mixed solvents [50]. A schematic diagram of the formation of SNPs is presented in **Figure 2.1a**, where silica precursor condensed into a Si-O-Si networks after hydrolysis to yield SNPs which follow a nucleation-growth kinetic mechanism. Since Stöber's initial report, detailed instigations of several process parameters (temperature, ammonia, water and Si-alkoxide concentrations) on particle size were performed by different researchers showing that particle sizes from 20-800 nm can be obtained [32, 51]. Although Stöber particle preparation mechanism is already well-established, its thorough understanding is still important for the synthesis of mesoporous silica nanoparticles with various morphology. Particle growth was found to

occur by a surface reaction controlled condensation of Si-alkoxide monomer or small oligomers and aggregation of smaller sub-particulates after concentration-dependent nucleation [52-55]. In this dissertation, SNPs are utilized as a control case for titania functionalization and flavonoid adsorption in **Chapter 3** and for thermodynamic interaction with RNA after amine functionalization (**Chapter 7**).

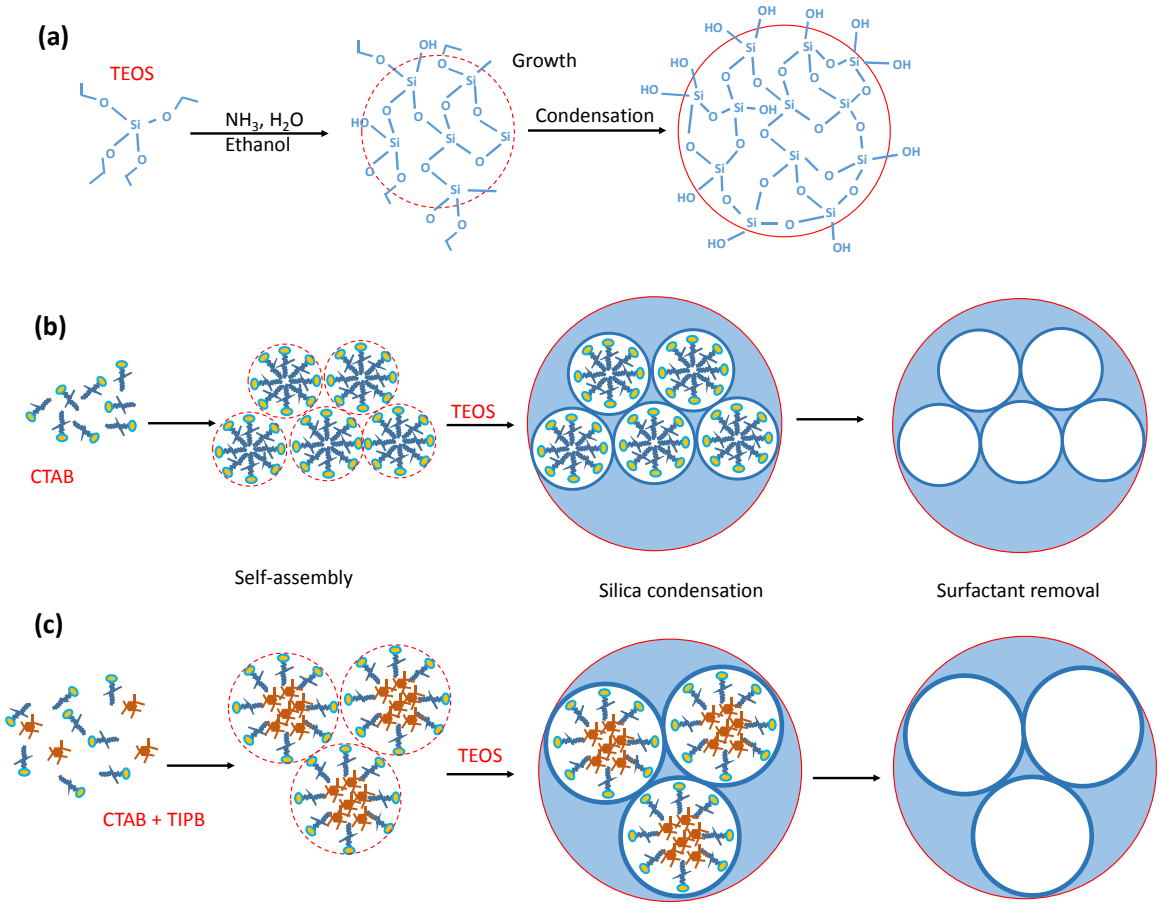

Figure 2.1 General synthesis strategy of the silica nanoparticles used in this dissertation: (a) nonporous silica nanoparticles, (b) mesoporous silica nanopartilces (pore size < 4 nm) and (c) mesoporous silica nanopartilces (pore size > 4 nm). TEOS: silica source, CTAB: surfactant, TIPB: pore swelling agent.

2.1.2 Nonporous Silica Microspheres

Nonporous silica microspheres are the expanded versions of SNPs that are of interest here as a base case nonporous control for studies of mesoporous silica microspheres by microscopy methods. During the Stöber process, it is generally agreed that nucleation begins from partially hydrolyzed TEOS monomers to form primary particles, generate larger particles through a combination of aggregation and slow growth at the surface [53, 56]. The size of particles formed by aggregation is tuned and limited by colloidal forces, as described by DLVO theory [57]. Since DLVO forces favor submicron particles, and since the rate of surface reaction is very slow compared to nucleation and aggregation (below a certain size) it is very difficult to obtain nonporous silica particles larger than 1 μm by the batch Stöber method [58]. However, larger (> 5 μm) nonporous silica particles (silica microspheres) are useful to contrast biomolecules at external surfaces with internal diffusion and transport, such as in florescence recovery after photobleaching (FRAP) measurements [46, 59]. Nakabayashi et al. [60] reported a semi-batch method for the synthesis of nonporous silica microspheres up to 6.6 μm in diameter by an electrolyte (KCl) mediated modified Stöber process. In their process, TEOS in dilute ethanol solution was fed very slowly to another ethanol solution of ammonia and KCl, which prevented new nucleation and promoted surface condensation [60]. We have successfully used this method before to synthesize nonporous silica microspheres > 6 μm to measure biomolecule external surface diffusivity using FRAP [46]. The particles were also used to measure the surface diffusivity of dsRNA as control case for their mobility inside the pore [61], which is the basis of obtaining RNA delivery and leading to the much more

fundamental investigations of thermodynamic interactions between silica nanoparticles and RNAs (as presented in **Chapter 7**).

2.1.3 Mesoporous Silica Nanoparticles (MSNPs)

MSNPs have tunable shape, size and high surface area, and their native hydroxyl terminated surfaces can be easily functionalized with other active groups for biomolecule loading and transport, making them useful for applications ranging from controlled drug delivery to theranostics [29, 62-64]. Because of their high surface area and pore volume, MSNPs are ideal for loading a high quantity of sensing elements for biomolecules, which indeed makes it possible to amplify signals for detection at very small concentration. MSNPs are suitable for loading a large dose of drugs based on porosity and facile functionalization of their surface with other active groups for biomolecule loading [65].

The general synthesis strategy of MSNPs involves surfactant self-assembly or co-assembly with inorganic precursors followed by silica condensation (**Figure 2.1b-c**). This process gives rise to particles with different shapes and sizes (dependent on synthesis conditions), and highly ordered pore structures (lamellar, hexagonal or cubic) with high surface area and pore volume. Before self-assembly, silicate poly-anions interact with surfactant head-groups through electrostatic and hydrogen bonding interactions and the final mesophase assembles itself into the lowest free energy state to provide the final micellar mesostructure [66]. Pore orientation in MSNPs is an important factor for the accessibility to biomolecule during loading and release. Different particle morphology, pore structures and orientations are obtained based on the types of surfactant used, the solution compositions and conditions such as pH and ionic strength of the solution [67, 68]. For example, by changing alkoxide molar ratio and concentration, varieties of pore

orientation (cubic, 2D hexagonal, disordered or mixed) have been obtained [69]. The final particle size (important for cellular internalization and expulsion) can be controlled by manipulating hydrolysis and condensation of silica precursor [70] (much like SNPs) by changing pH or temperature of the solution, or adding other chemicals.

The final MSNPs with void pores are obtained following surfactant template removal by high temperature calcination or solvent extraction (usually by an organic solvent at low pH and elevated temperature). High temperature calcination generally reduces the number of hydroxyl groups on silica surface, thus reduce their potential for later functionalization by other active groups. Hence, we use solvent extraction of the template (by acidic ethanol washing) in this dissertation. Surfactant removal is usually ensured by spectroscopic characterization techniques like infrared spectroscopy, where disappearance of infrared absorption peaks corresponding to surfactant functional groups indicated complete surfactant removal. It is very important to ensure complete surfactant removal from the particles before applications in cells because residual surfactant can have large influence on cellular interactions, which are mostly detrimental on cell viability [62]. We have ensured the removal of surfactants and other organics after synthesis using Fourier transform infrared (FTIR) spectroscopy for all MSNPs.

The synthesis, engineering and cellular application of MSNPs for biomolecule harvesting/delivery is the essence of this dissertation. The opportunities for different applications arise from the tremendous multifunctional properties of MSNPs, and relevant features for this dissertation are depicted in **Figure 2.2** in light of their interactions with living cells. Surface functionalization with transition metal oxides (as active group), functional organic moieties (oligopeptides), and amine groups were all accommodated by

the versatile properties of MSNPs. The amine groups serve multiple purposes for biomolecule loading, MSNP delivery/harvesting in cells, and fluorescent molecule attachment for intracellular detection.

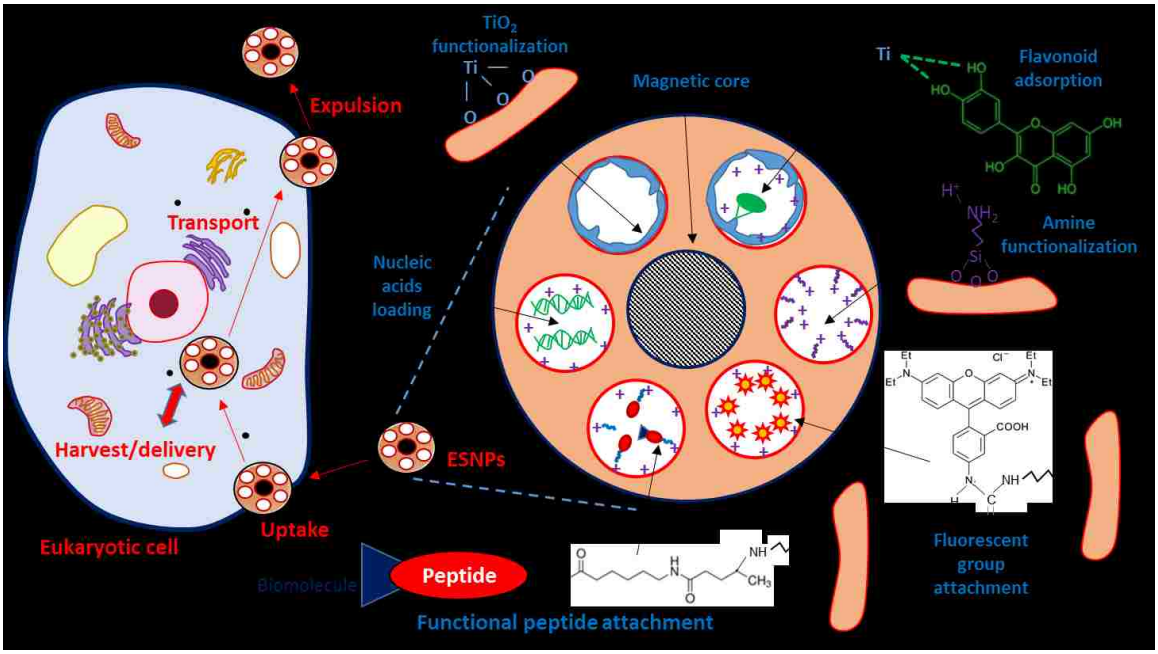

Figure 2.2 Multi-functionality of mesoporous silica nanoparticles (MSNPs) allowing their use for nanoharvesting and delivery. Relevant features include functional groups for small drug molecule loading *via* adsorption or chelation, peptide conjugation, nucleic acids loading, adding amines to promote cellular uptake for nanoharvesting and delivery, and possible magnetic core incorporation for controlled movement.

2.1.3.1 Small Pore (< 4 nm) MSNPs

Small pore MSNPs are a general class of MSNPs produced by the surfactant templated sol-gel processes when small molecules, generally ionic surfactants, are used. The pore size in MSNPs depends on the size of the surfactant, especially the length of the hydrocarbon tail. The most common surfactant used for "Mobile Crystalline Material" (MCM-41 and MCM-48) type MSNPs is cetyltrimethylammonium bromide (CTAB), which provides cylindrical pores in MCM-41 (hexagonal columnar pore symmetry) of 2.5-

3 nm diameter [69, 71]. The general synthesis strategy for surfactant templated sol-gel synthesis of small pore MSNPs are presented in **Figure 2.1b**, with CTAB as an example. Adjusting the surfactant tail length from 8 to 18 carbon has been shown to allow for tuning of pore diameter from 1.5 to 3.8 nm [72, 73]. The pores are generally highly oriented in hexagonal, cubic or radially oriented symmetry based on the surfactant, alkoxide, water, ethanol concentration and molar ratio. Engineered CTAB templated MSNPs (< 3 nm pore size) are utilized extensively in this dissertation for small molecule therapeutics (flavonoids) loading and isolation in **Chapter 3**. The particles are also used for nanoharvesting of small biomolecules from living plant cultures (**Chapter 4**) and to study their interactions with plant cells during nanoharvesting (**Chapter 5**). They are also used to study the pore size dependent thermodynamic interaction with RNA by isothermal titration calorimetry (ITC) in **Chapter 7**.

2.1.3.2 Large Pore (> 4 nm) MSNPs

Because biomolecules such as polynucleic acids, lipid bilayers and proteins have characteristics sizes larger than the default pore diameter obtained by cationic surfactant templating, many strategies have been developed to produce larger pores. One approach is to use larger block copolymer pore templates such as Pluronic surfactants [74], but this tends to not give good control over particle morphology and pore orientation. An alternative strategy for increasing the pore size of CTAB-templated MSNPs is to use an auxiliary nonpolar organic molecule during the sol-gel process to swell the hydrocarbon cores of the micelle templates, and thus to create large pores after template removal [75]. Blin and Su have reported expanding pore diameter of CTAB templated mesoporous silica

(not particles) up to 4.9 nm using decane and trimethylbenzene (TMB) as pore expanders [76]. Corma et al. reported another pore expansion strategy by using tetramethyl ammonium ions (TMA^+) and hydrothermal treatment (150 ºC) with CTAB templated silica, where the TMA^+ was thought to partition to the surfactant/silica interface, thereby expanding pore size up to 6.6 nm [77]. Initial studies of these organic pore expanders used to synthesize either bulk mesoporous silica or uncontrolled MCM-41 powders rather than morphology-controlled MSNPs. It was only recently that large pore MSNPs have been developed using micelle swelling agents. Han and Ying reported MSNPs with pore sizes of 5-20 nm based on fluorocarbon surfactant templating and TMB micelle swelling, but the resultant particle diameter was relatively large (400-500 nm) [78]. Subsequently, many researchers reported the synthesis of large pore MSNPs, but the resultant particles were either still too large for cellular internalization [79, 80] or had irregular non-spherical shapes [81, 82].

Only recently, Gu et al. reported the synthesis of MSNPs with <150 nm particle diameter and up to 4.5 nm pore diameter by using octyltrimethylammonium bromide (OTAB) as surfactant and N,N-dimethylhexadecylamine (DMHA) as pore expanding agent [83]. Continued efforts to simultaneously control micelle structure, swelling and particle morphology led to a report of ~170 nm MSNPs with average pore diameter up to 8.2 nm using CTAB template expanded by triisopropylbenzene (TIPB) [84]. Very recently in 2016, ultra-large pores of > 20 nm were reported for CTAB-templated MSNPs with TMB as pore swelling agent after a long hydrothermal treatment at 140 ºC [85]. Schematic representation of the synthesis of large pore MSNPs by pore swelling technique is presented in **Figure 2.1c**, for CTAB and TIPB as an example. 8 nm porous particles are

used for functional oligopeptide attachment in **Chapter 6** in this dissertation. We have also utilize this technique for synthesizing large pore MSNPs (with ~ 4 and 8 nm pore size) by the method of Gu et al. [83] and Yamada et al. [84], respectively, for studying pore size dependent interaction with RNA in **Chapter 7**.

2.1.4 Mesoporous Silica Microspheres

To expand the range of applications of the pore space of silica materials, it is possible to synthesize mesoporous silica microspheres with diameter greater than several micrometers and tunable pore size from 2-12 nm [59]. These (along with nonporous silica microspheres) have large enough size for direct visualization of functional groups and biomolecule distribution in a confocal microscope, thus provide opportunities to directly visualize pore accessibility and to measure transport properties (diffusivity) of biomolecules confined inside pores [46].

Spherical silica microspheres (SBA-15) of diameter > 5 μm can be synthesized from acid catalyzed reaction of TEOS templated by Pluronic P123 [59]. Nonionic triblock copolymer P123 provides larger pore diameter compared to ionic surfactants, and the pore size can be tuned by hydrothermal treatment from 3-15 nm [86]. Tunable pore sizes of hexagonal cylindrical pores were obtained based on different degrees of solvation of the ethylene oxide block of P123 molecule depending on the reaction temperature [43]. To obtain microspheres, CTAB has been used as secondary surfactant to control particle size and spherical morphology. Although we have not directly used mesoporous silica microspheres in this dissertation, they have relevancy here as a large amount of information

regarding biomolecular interaction inside silica mesopores can be obtained from microscopic techniques only suitable for silica microsphere.

2.1.5 Core-Shell and Magnetic Silica Nanoparticles

In addition to being able to control pore structure and particle morphology, additional functionality has been created in magnetic core-shell type silica nanoparticles for applications in diagnostics and therapeutics (*e.g.* as magnetic resonance imaging (MRI) contrast agent), and *in vivo* delivery vehicle for therapeutics [87]. Magnetic Fe_3O_4 core-mesoporous silica shell nanoparticles are particularly important in designing magnetic field-induced drug release system. The general synthesis strategy of these of particles is to synthesize the magnetic nanocrystal or nanosphere first and creating a mesoporous shell by sol-gel synthesis with ionic surfactant (for example: CTAB) template after stabilization. These particles have numerous theranostic (therapeutic and diagnostic) applications mainly in MRI and drug delivery as well as controlled separation of biomolecules. Although magnetic MSNPs were not directly applied to any of the applications in this dissertation, their implication as future directions stemming from this work is significant as incorporation of magnetic core to the engineered MSNPs developed here will provide extra dimension in biomolecule isolation and transport. Incorporation of magnetic core in MSNPs is proposed as a future direction in **Chapter 8**.

2.2 Silica Surface Functionalization and Engineering

The pure silica surface remains negatively charged at physiological conditions, but this can present challenges for biological applications [62]. Proper surface modification with a positively charged group (such as amine) is important for cellular uptake, expulsion and intermediate trafficking of nanoparticles. Surface modification is also important for enhanced internalization and endosomal escape as well as less collision with unwanted intracellular organelles during their pathways between entry and exit [62]. Surface functionalization helps nanoparticles in camouflaging themselves (stealth entry) and reducing unwanted binding. It also dictates the ultimate fate of nanoparticles inside the cells and whether the nanoparticles will exit the cell (*via* mechanisms such as exocytosis) or not. Surface functionalization is also the only alternative for protein loading, when protein do not adsorb by electrostatic interactions alone.

Surface functionalization of silica nanoparticles offers the opportunity to tune chemical properties at the interface, which enables facile loading of hydrophilic or hydrophobic drugs, enhanced binding with specific cellular targets and controlled uptake and release of target compounds. Two kind of surface functionalization strategies are generally followed: post-synthesis grafting, and co-condensation or co-precipitation (one pot) depending on application requirements [62]. During post-synthesis functionalization, active groups are attached to the silica surface after silica particle synthesis, generally through alkoxy- or chloro- silane condensation with hydroxyl groups. The main advantages of post-synthesis functionalization is the retention of mesopososity and mesostructure, and easy grafting of organic groups. The main drawbacks are the potential for a nonselective inhomogeneous distribution of functional groups and partial blocking of pore openings. The effectiveness of post-synthesis functionalization also depends on the preparation route

(especially template removal method) of parent MSNPs. Calcination (heating in the presence of air or oxygen) usually leads to complete template removal, but tends to reduce surface silanol density. On the other hand, solvent (acid) extraction preserves surface silanol density but may be less effective for template removal [88].

In co-condensation, functional groups are directly incorporated into the material by mixing an organosilane with the silica precursor (such as TEOS) and surfactant template. To avoid loss of the organic function group, the template should be removed by solvent extraction in this method [89]. This method increases the likelihood of achieving a homogeneous distribution of functional groups, but some of the functional groups may be buried in the silica matrix (and not usable). The range of conditions giving an ordered, well-defined pore structure may also be limited in the co-condensation approach [90].

Another highly desirable functionalization technique is to selectively attach functional groups only on the outer surface of MSNPs while leaving the internal pore surface intact for biomolecule loading [17, 91]. During co-condensation synthesis, if the organofunctional silane is added at the end of particle synthesis, it may be possible to attach the functional groups only in the external surface of MSNPs [89]. For post-synthesis grafting, leaving the template in place during functionalization and limiting the time of reaction of the organoalkoxysilane are strategies to give external functionalization. Alternatively, bulky molecules such as polyethylene glycol (PEG) can be used to block the pores prior to functionalization, which was successfully used for carboxylic acid, amine and hydrocarbon functional groups for MSNPs with pore diameter up to 5.5 nm [92-94]. The functionalization and surface modification of MSNPs carried out in the projects

presented in **Chapter 3 to 7** are described below along with a few competing approaches, and their relative advantages and disadvantages.

2.2.1 Amine Functionalization

Polycationic surface functionalization of MSNPs has been shown to enhance nanoparticle uptake as well as their endosomal escape capability [95, 96]. Silica surface functionalization with amines is used to create interactions of biomolecules with silica, to provide structural/conformational stability of proteins, to facilitate adsorption of negatively charged nucleic acids (DNA/RNA), and also to provide a site for conjugation, such as with fluorescent tags [97-99]. In addition, for other applications, amine functionalized MSNPs have been used for loading and release of drug molecule that possess carboxylic/carbonyl groups [100, 101].

The most common amine functionalization method is post-synthesis grafting by amino-alkyl-alkoxysilane condensation on MSNP surface, *e.g.* with aminopropyl-triethoxysilane (APTES). Amine grafting densities, degree of coverage (monolayer/ multilayer) and polymerization depend on the aminosilane type and concentration, solvent type (polar/non-polar), and the presence and concentration of water [94, 102, 103]. Polar solvents like ethanol tend to provide more uniform layer-type coverage whereas nonpolar solvents like toluene are used for more isolated tridentate grafting. In the presence of excess trace water, highly heterogeneous, branched or ladder-like polymerized aminosilane grafting is obtained (**Figure 2.3**) [102]. In actual grafting scenarios a mixture of isolated, uniform and ladder like grafting occurs as it is very difficult to remove water from a hydrophilic surface like silica. Hence, it should be carefully considered whether to provide

a large amount of amine groups to provide maximum surface coverage or to use bare minimum to prevent any unwanted condensed structures. The degree of reduction in both surface area and pore size indicates whether uniform grafting is obtained or any resulting pore blockage occurs [104]. Post-synthesis amine functionalization of MSNPs is used heavily in this dissertation. In **Chapter 4 and 5** (during nanoharvesting), amine functionalization is used to promote cell membrane penetration and as binding site for fluorescent molecules. **Chapter 6** involves using amine groups as conjugation sites for functional peptide attachment and positively charged amine groups are used for the interaction with negatively charged RNA in **Chapter 7.** Amine coverage on silica surface is quantified to interpret the state of grafted amine on different MSNPs.

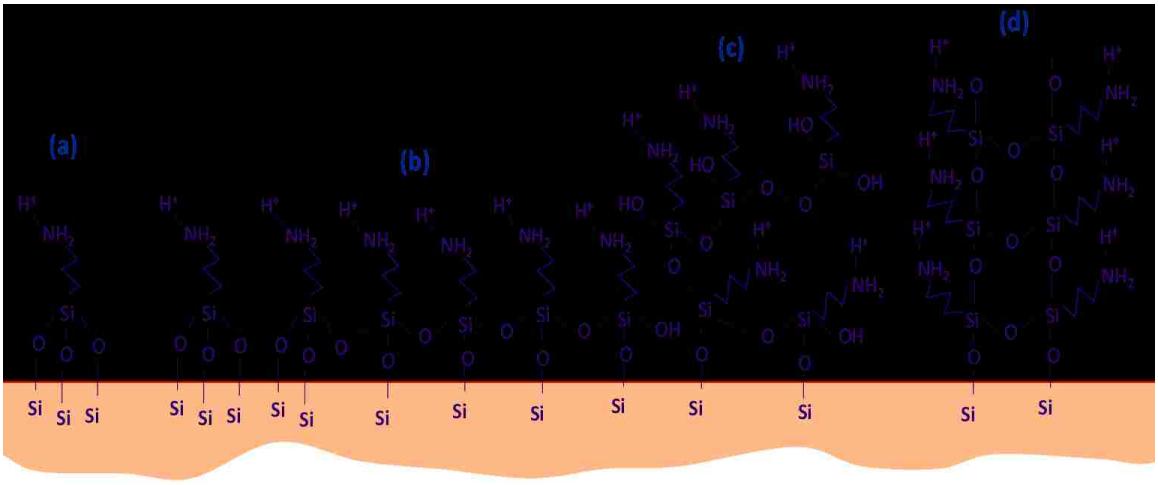

Figure 2.3 Different modes of post-synthesis grafting of aminosilane on silica surface: (a) isolated tridentate, (b) uniform cross-linked monolayer, (c) multilayer and (d) ladder-like oligomeric structures. Adapted from Bauer et al. [102] and Liu et al. [105].

2.2.2 Titania (TiO_2) Functionalization

MSNPs also serve as ideal support and host materials for the incorporation of various transition metal oxides (Ti, Cr, V) due to their high surface area, tunable surface properties, and thermal stability for application in catalysis, separations, optics and

electronics [106]. Titania (TiO_2) loaded silica is probably the most widely used mixed oxide system starting from the synthesis of titanosilicate-1 and 2 (TS-1 and TS-2) zeolites in the 1980's and 90's as oxidation catalysts for small molecules [107, 108]. Later, Ti-atom was incorporated in mesoporous silica to utilize the large pore size for higher diffusion of large reactants and products [109, 110]. Although titania functionalization of MSNPs has mainly been used for catalytic and photocatalytic applications, titania coordinates with several classes of biomolecules including phosphates and catechol-containing molecules, which provide wonderful opportunities for using titania functionalized MSNPs as high surface area adsorbents [111]. Besides this, titania on the silica surface has been shown to interact with biomolecules through outer sphere binding mechanisms including charge transfer and electrostatic interactions [112]. Titania also binds various amino acids and polypeptides, which provides tremendous opportunity for peptide functionalization and protein delivery applications [113].

Strategies to incorporate Ti into silica frameworks can be divided into two broad categories similar to other functionalizations: one pot and post synthesis. A one pot co-condensation route is often used incorporate Ti-atoms in silica frameworks mainly to obtain oxidation/epoxidation catalysts or photocatalysts [33, 114, 115]. This method is not suitable for adsorption applications because well-dispersed surface-associated sites are required in contrast to crystallites formed during high temperature calcination. Also, due to higher reactivity of Ti-alkoxides in the presence of water, proper stabilization techniques are needed such as sub-stoichiometric water addition to prehydrolyze the silica precursor, ligand addition, or non-hydrolytic route in one pot synthesis [116]. A large quantity of isolated and uniform tetra-coordinated Ti-sites were incorporated in the silica matrix of

cetyltrimethylammonium bromide (CTAB)-templated mesoporous silica thin films in our group using a post-synthesis grafting approach with complexation to a carbohydrate surfactant to stabilize the Ti-precursor [117]. Post synthesis processes generally involves a non-polar solvent, which provides a low-water stabilized environment for the alkoxides. Still, obtaining isolated tetra-coordinated Ti-sites in silica mesostructures is elusive as seen in **Figure 2.4,** where the effect of Ti-precursor concentration is shown schematically. Increasing the precursor concentration (in order to increase Ti-coverage) usually form thick TiO_2 clusters and crystals, which are not suitable for adsorption applications.

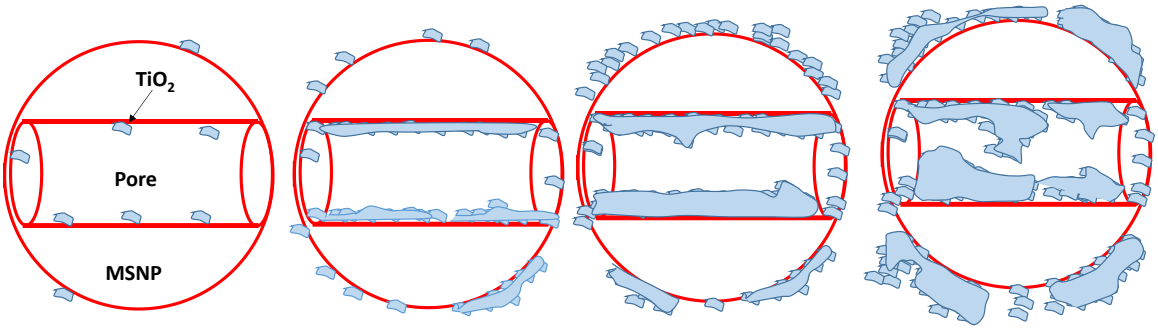

Figure 2.4 Schematic diagram of the post synthesis titania functionalization with increasing titania-precursor concentration starting from little titania coverage with most of the surface empty (left) to ideal monolayer coverage to thick titania deposition rendering the pores almost inaccessible and blocked. Adapted from Beyers et al. [114].

Titania functionalization is used in this dissertation for designing high capacity materials for biomolecule adsorption (**Chapter 3**) and for the nanoharvesting of polyphenolic compounds in **Chapter 4**. We have used a post synthesis TiO_2 functionalization technique involving hydrolysis of Ti-precursor in ethanol, which is not supposed to provide isolated titania grafting. On the other hand, ligand assisted functionalization (one-pot or post-synthesis) of silica particles can provide isolated tetra-coordinated Ti-sites, which is proposed as a future direction in **Chapter 8**.

2.2.3 Functional Protein and Peptide Attachment

Protein and oligopeptide attachment and interaction with silica nanoparticles provides a platform for biosensing, bioseparation, biocatalysis and biochemical synthesis applications. MSNPs with immobilized enzymes, proteins and oligopeptides have been used for highly diverse applications including highly specific biosensing applications, in detection and separation of antibodies, and also promoting cellular internalization during biomolecule delivery [118-120]. In this dissertation (**Chapter 6**), we are using oligopeptide conjugation to high surface area of MSNPs to design high capacity and selective biomolecule isolation carriers. The most general conjugation strategy of peptides with the MSNP surface will use so-called zero length linkers, which covalently attaches an amine group to a carboxylic group to form an ester bond [121]. One of the highly utilized conjugation agents is 1-ethyl-3-(3-dimethylaminopropyl) carbodiimide (EDC) with N-hydroxysuccinimide (NHS) esters, which was used for the conjugation of the N-terminus of peptide/proteins to carboxylic acid-functionalized silica nanoparticles [122-125]. However, functionalization with carboxylic groups render the particles neutral or negatively charged and an application where the particles will be applied for cellular internalization (nanoharvesting or delivery) may encounter difficulty in utilizing weakly charged particles. Hence, a peptide conjugation strategy based on a group that is positive at physiological pH (amine) is necessary where the N-terminus of the peptide will be attached to the amine moieties of MSNPAs with the preservation of particle positive charge. Various linkers are available for this purpose, which are discussed below with relative *pros and cons*, and selection criteria.

2.2.3.1 Linkers for Conjugation

Linkers are used to covalently attach functional biomolecules such as peptides to surfaces, and to provide spacers between the surface and the bio-functional group to minimize the alteration of functionality due to surface interactions. Some of the linkers have bonds cleavable by redox reaction, pH change or UV light, which can be used to analyze and confirm attachment efficiency, and for targeted release [24, 126, 127]. However, the most important factor to consider during conjugation of functional groups is the type of spacer to use in order to provide distance between proteins/peptides and the surface. The spacers are generally inert molecular units (such as aliphatic hydrocarbon chains) or other functionalities. Bifunctional linkers with or without spacers are available for peptide conjugation, which can be mainly divided into two types: homo-bifunctional and hetero-bifunctional. Homo-bifunctional linkers such as bis(sulfosuccinimidyl)suberate (BS^3) have two amine-reactive NHS ester groups at the either end, which can react with amine functionalized particles at one end and with the amine terminal group of a peptide at the other. The challenge of using this type of linker is that rapid hydrolysis of one end can occur, while the other end is being used for binding [128]. Controlling the rate of reaction with both the peptide and the surface can also be challenging.

On the other hand, hetero-bifunctional linkers such as N-sulfosuccinimidyl-6-(40-azido-20-nitrophenylamino)hexanoate (sulfo-SANPAH) provide amine reactive groups at one end and UV active groups at the other end. This and other hetero-bifunctional linkers provide greater control over binding because the UV-active group remain dormant during conjugation of the other end. The only problem with UV-active nitrophenilo-azide groups is that they are activated by short wavelength UV radiation (~280 nm), which can cause

deactivation of protein molecules through free radical creation. Recently, hetero-bifunctional linkers with diazirine groups (such as sulfo-succinimidyl-6-(4,4'-azipentanamido)hexanoate (sulfo-NHS-LC-diazirine or SNLD)) have been developed that are activated to react with amine groups at much higher UV wavelength (~365 nm).

A schematic diagram for peptide attachment using BS^3 and SNLD is presented in Figure **2.5**, which shows the relative advantages of using a hetero-bifunctional linker like SNLD to provide adequate binding control and efficiency. We have used SNLD to conjugate functional peptides to amine functionalized MSNP surface in **Chapter 6** in this dissertation.

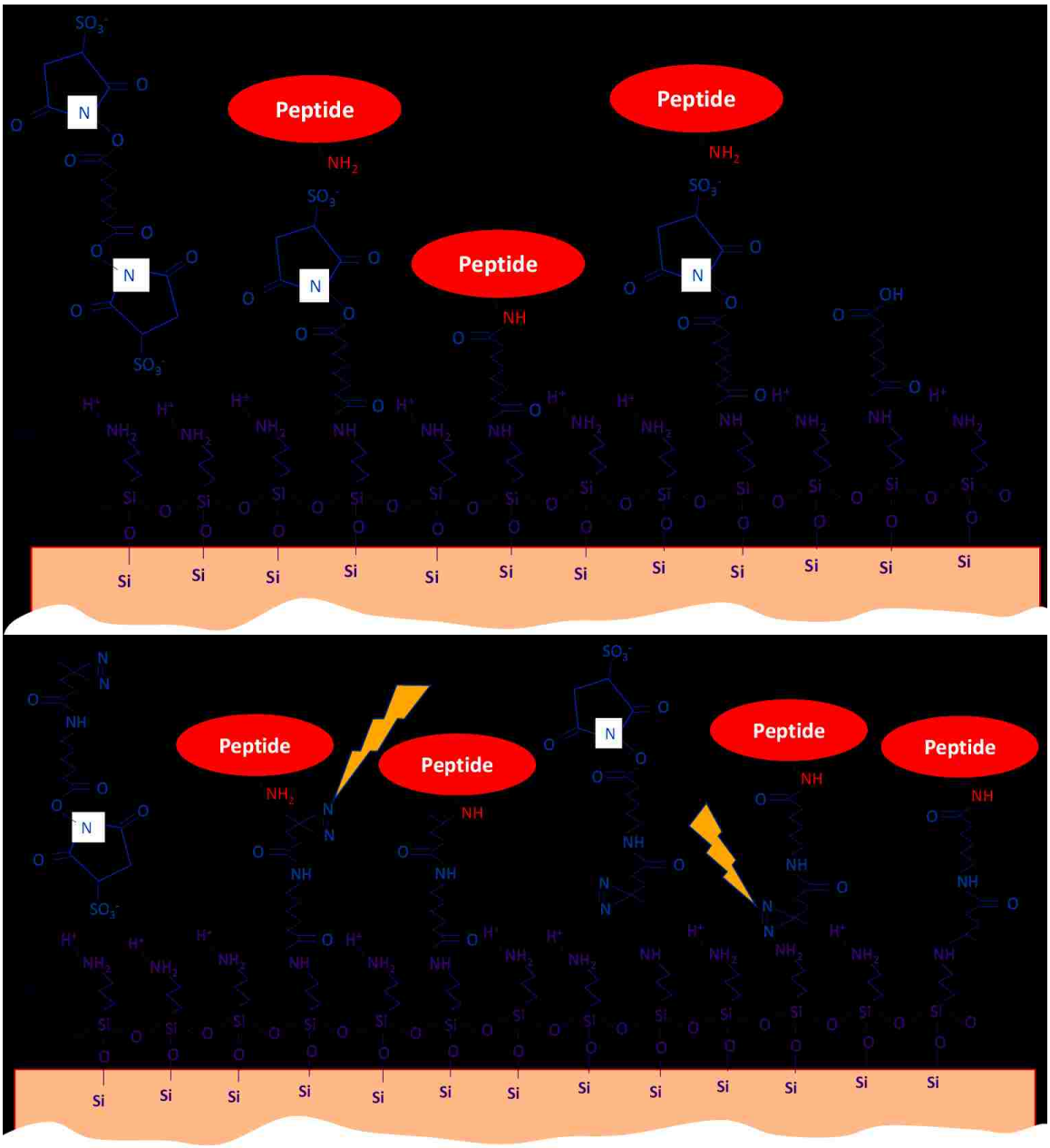

Figure 2.5 Schematic representation of the peptide conjugation on amine functionalized MSNPs using (a) homo-bifunctional amine reactive linker BS^3 that undergoes rapid and competitive hydrolysis yielding very low attachment, and (b) hetero-bifunctional amine reactive and UV-activable linker SNLD providing highly controllable conjugation (without any competing hydrolysis reaction).

2.2.4 Competing Approaches for Surface Engineering

Besides the surface engineering techniques discussed above and used in this dissertation, there are some other techniques for surface functionalization. For context, a brief outline of the other approaches for related applications is presented here, along with a summary of some of their advantages and shortfalls. Numerous functional groups like vinyl groups, carboxylic acids, fluorescent dyes, hydrophobic and hydrophilic biomolecules, and aromatic groups were grafted on to silica surface in a self-assembled monolayer fashion using alkoxysilane or chlorosilane condensation [129]. Other positively charged groups can be incorporated on MSNP surface, but most of them are polymers (such as chitosan) that do not provide the control and ease of functionalization by aminosilanes. Functionalizing MSNP surface with phosphate group by alkoxymethylsilane phosphonate is another technique, which provide the particles with highly negative charge required for strong metal ion binding and breaking up cytotoxic intracellular aggregation [130].

Thiol (-HS) functionalization is another technique to attach biomolecules to silica surface, which provide negative charge at physiological pH. Post-synthesis thiol functionalization is normally carried out by the condensation reaction of mercapto-alkoxysilane. Hetero-bifunctional conjugation agent with maleimide groups are thiol-reactive (much like NHS esters for amine), which can be used to load biomolecules on thiol functionalized silica [131]. They also can be used to conjugate cysteine terminated proteins and peptides. It should be noted that maleimide functionality remains after conjugation (unlike NHS esters, which detaches from the molecules) and sometimes provides protection against non-specific binding due to their hydrophilic nature [132]. Another advantage of thiol functionalization is the ability of thiol groups to undergo thiol-ene click

chemistry, which allows binding with broad classes of biomolecules that is vinyl terminated [133, 134]. However, negatively charged functionalization is not appropriate for an application like nanoharvesting or nanodelivery (where positive charge is required for cellular internalization). Also, thiol functionalization cannot be used for negatively charged nucleic acid loading.

Molecular imprinting is the techniques of creating specific molecular recognition sites in an inorganic/organic matrix through using same molecule as a template. Molecularly imprinted silica nanomaterials (especially particles) has vast number of applications in selective adsorption, separation, sensing and catalysis [135, 136]. The technique provides selective isolation of molecules of interests and can be a competing technique for functional polypeptide attachment. Several articles have reported Stöber particles with molecularly imprinted polymer shells for selective separation of different organic molecules [137-139]. However, it is not easy to create molecular imprinted sites in mesoporous materials with preservation of high surface area. Besides, there are several disadvantages and difficulties associated with molecular imprinting techniques including requirement of large amount of high quality imprinting molecules, inability to macromolecule imprinting, low binding and mass transfer, leakage of templates, and difficulty avoiding heterogeneous binding sites [140, 141]. It is also extremely difficult to imprint water soluble biological macromolecules (proteins, nucleic acids) in their natural environment to ensure conformational stability [142].

2.3 Biomolecule Interactions with Nanoparticles

Understanding the interaction of different classes of biomolecules with inorganic surfaces is of absolute necessity in order to design proper nanoparticulate vehicles for bioactive material transport across cell barriers. Useful information required to obtain from experimental and modeling investigations are: the region of the biomolecule responsible for surface interaction, nature of the contact, preferential orientation and selection of surfaces, and conformational changes upon binding [65]. Owing to their properties, MSNPs can serve as hosts and delivery vehicle for different kinds of therapeutics and bioactive materials [62]. Interaction of biomolecules with solid surfaces is not only dependent on solid-liquid interface properties but also solution pH, concentration, and ionic strength [113]. The role of water in biomolecule interaction is prominent as water acts as co/competitive adsorbent with the molecule, which modulates the chemical behavior of the surface greatly [113, 143]. At room temperature and pressure, silica is hydroxyl terminated and surface silanol density is close to 5 -OH groups/nm^2 [65], which renders the surface amenable to varieties of surface modification as described in **Section 2.2**. High density of surface hydroxyl groups also modulate surface interactions with biomolecules along with controlling hydrophilicity [144, 145]. Besides, biomolecule interaction and recognition on a specific surface involves the complex interplay between electrostatic interactions, H-bonding, and dispersive hydrophobic interactions. It is not a trivial task to isolate effects of each interaction.

Hence, a general understanding of biomolecule-biomolecule and biomolecule-silica surface interactions is important for designing functional nanoparticles in nanoharvesting and delivery application. Selective biomolecule recognition and separation, loading in pores, and delivering them in a time dependent and controlled manner require

complete understanding of complexation/decomplexation interactions. Understanding the interaction of nucleic acid derivatives (nucleotides, base-pairs and DNA/RNA sequences) with solid surfaces is also highly important in gene therapy, DNA/RNA devices, purification, and hybridization techniques [65]. The solid-solvent interaction strongly influence the degree and energy of biomolecule adsorption. Understanding the protein-surface interaction with engineered MSNPs also allows us to understand their behavior in protein rich surroundings such as biological media and inside cells, which is tremendously important in designing nanoparticles for biomolecule transport. Although covalent bonding is utilized to conjugate peptides, to attach fluorescent groups, and to stabilize the protein conformation [146], we are focusing on the physical interactions of biomolecules with functional silica surfaces here.

2.3.1 Binding Mechanisms of Biomolecules

The complexation between a biomolecule (*A*) and a surface (*B*) can be expressed using **Equation 2.1**, representing the two-step thermodynamic processes of noncovalent bond formation and solvent (water) reorganization [147].

$$A \bullet xH_2O + B \bullet yH_2O \leftrightarrow A \bullet B \bullet (x + y - z)H_2O + zH_2O \quad (2.1)$$

Hence, binding or adsorption mechanism can be divided into two broad categories based on water shell retention after biomolecule binding: inner-sphere and outer-sphere binding [148]. Outer-sphere adsorption typically happens through electrostatic interaction and a layer of water remains between the surface and biomolecule. On the other hand, inner-sphere bonding happens through covalent or coordination binding and no water layer remain between the surface and the biomolecule. In **Figure 2.6**, inner and outer sphere

complexation is shown for relevant systems here (TiO_2 and amine functionalized surface for flavonoid and nucleic acid, respectively). Several other non-covalent interactions such as π-π, cation/anion-π, dispersive forces and hydrophobic forces are important in identifying and describing surface-ligand binding. Another important factor in surface binding is cooperativity, which can be positive or negative, where occupation of one binding site with a molecule strengthen or weaken neighboring binding sites [149]. It is worth noting that weak forces like van der Waals forces, dipole-dipole, ion-dipole and induced dipole can have combined effects in soft matter, colloid and surface science, and are sometimes as prominent as covalent or ionic bonding [150]. They are the inherent attractive forces (except when very close to each other) between particles and represent forces to overcome to maintain colloidal stability. In absence of other repulsive forces (electrostatic repulsion), van der Waals forces are primarily responsible for particle aggregation is solution [151]. Biomolecule adsorption on charged particle surface sometimes neutralizes some of the surface charge and can cause aggregation during nanoharvesting and delivery applications, which as a result, should be carefully considered when designing particles. These are often very weak interactions and masked by associated stronger interactions (such as H-bonding), but can produce surprising results if not carefully considered. Here we are focused on the most relevant interactions for this dissertation: coordination, electrostatic interactions, hydrogen bonding and hydrophobic interactions between biomolecule and functionalized silica surface and how they primarily affects the design of ESNP.

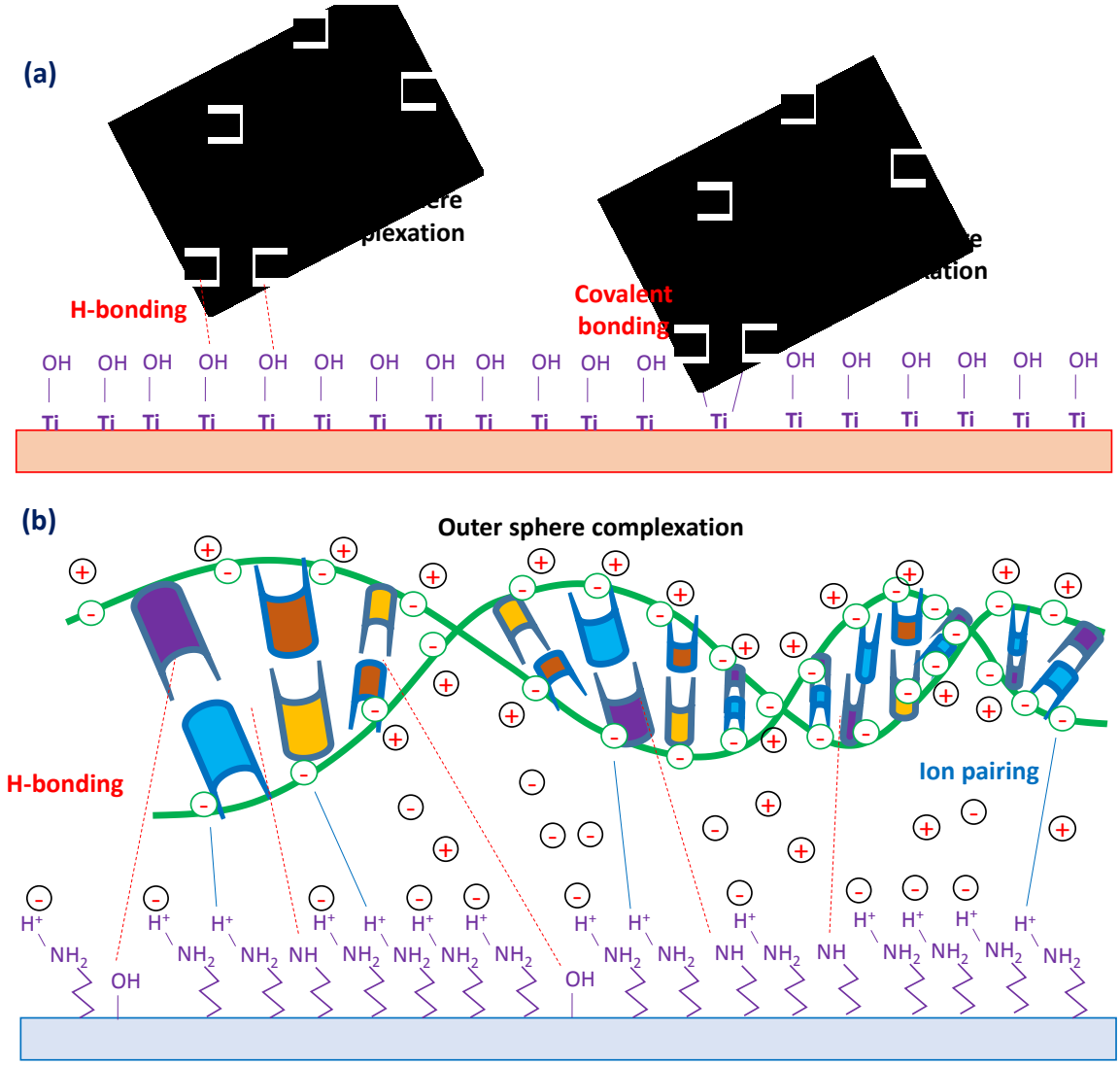

Figure 2.6 Examples of biomolecules' interaction with surfaces used in this dissertation showing inner and outer sphere complexation: (a) TiO_2 surface produces both inner- (covalent) and outer- (H-bonding) sphere complex whereas (b) positively charged amine produces outer sphere complex (H-bonding, ion pairing/electrostatic interactions) with nucleic acids.

2.3.1.1 Coordination

Some biomolecule tend to form strong coordination complexes with transition metal oxide surface especially TiO_2. It was reported that peptide and other biomolecule (especially polyphenolics) adsorption on TiO_2 surface happens through coordination of

carbonyl group with surface Ti atoms [113]. As a transition metal, Ti create complexes with vast classes of biomolecules containing hydroxyaromatic (phenoxy) and hydroxyl groups, and thus show strong binding affinity to produce inner sphere complexes (**Figure 2.7**). This strong binding capabilities can be utilized to bind and separate biomolecules from their host environment as well as from solution, which will be investigated in **Chapter 3** for polyphenolic flavonoids. TiO_2 also shows strong coordination binding capability towards poly-carboxylic acids (citric acid), which is used to displace polyphenolic flavonoids in **Chapter 3** after adsorption on TiO_2 functionalized silica, thus enable to recycle or reuse the particles. There are also some unexpected or unwanted coordination binding should be considered especially when polar solvent like dimethyl sulfoxide (DMSO) is used with water to solubilize hydrophobic compounds. DMSO strongly chelates cations [152], which can interfere when estimating the primary binding processes. Similar unwanted coordination can happen for phosphate ions (*esp.* when using a phosphate buffer), which also should be considered.

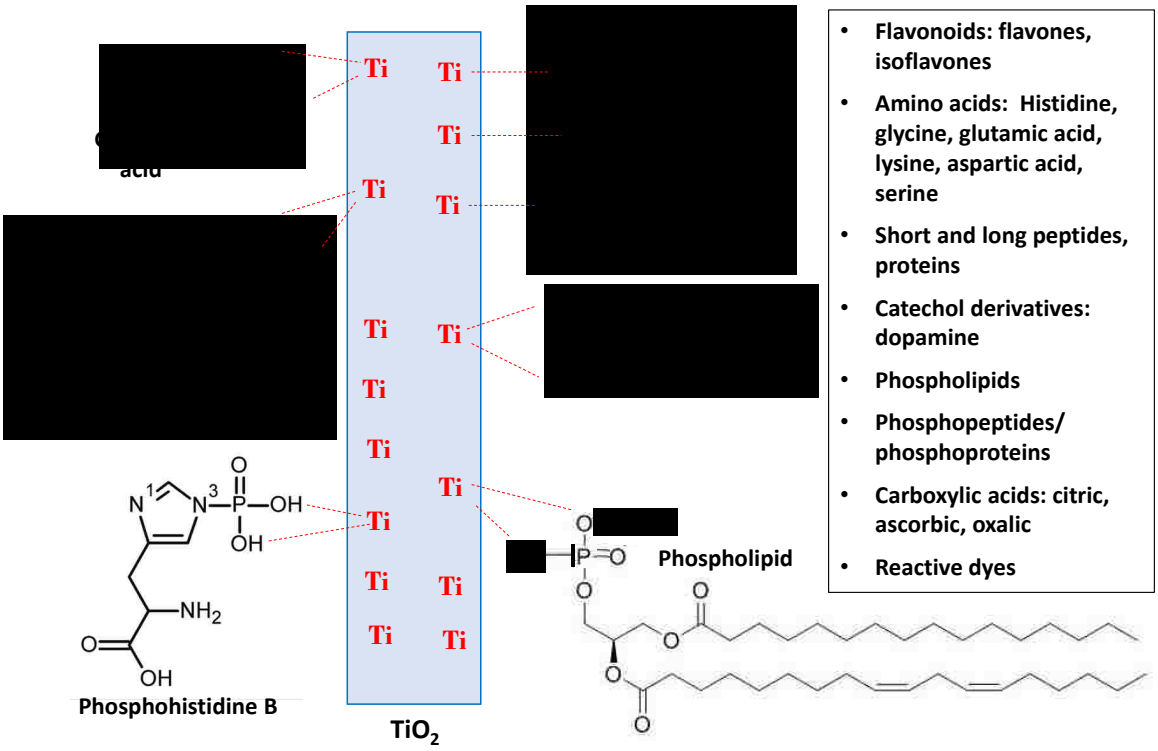

Figure 2.7 Schematic representation and list of vast classes of compounds that produces coordination complexes with Ti.

2.3.1.2 Electrostatic Interactions, Ionic Bonding/Pairing

Ionic bonding is the non-covalent interaction between cationic and anionic sites of different molecules, driven by electrostatic interactions, which generally form outer sphere complexes [153]. In aqueous medium, it is generally entropy driven and endothermic for polyelectrolytes arising from the large amount of counterion released as water. The electrostatic interaction between cationic and anionic moieties of one molecule or surface toward the aromatic rings of another molecule may also be very important. Many π-π stacking interactions are also electrostatic in nature due to interaction of aromatic ring with opposite partial charge [154].

Many biomolecules' adsorption onto silica surfaces happens through mixed electrostatic interactions and outer-sphere complex ($Si{-}O^{-}\cdots(HX)^{+}$) formation, where $(HX)^{+}$ represents protonated biomolecule [155]. Cell membrane interaction with amine functionalized silica surfaces is primarily happens through electrostatic interactions, where positively charged particles bind with negatively charged cell membrane lipid molecules moieties [156]. The mode of many amino acids and peptides adsorption onto hydrophilic surface is also strongly influenced by electrostatic attraction, and hence is pH dependent [113]. Electrostatic attractive interaction of proteins are sometimes also pH dependent, as some of the proteins and enzymes show positive charge at physiological pH and thus are attracted towards negatively charged silica surface. During nucleic acid binding to positively charged surface (amine groups), the majority of contributions come from the electrostatic interaction (ion pairing) between surface positive charge and nucleic acids' negative charge (**Figure 2.6**).

Hence, a major emphasis should be given to surface charge (zeta potential) and solution pH and ionic strength, all of which modulate electrostatic interactions between the ESNP surface and biomolecules. Since surface charge is modulable by changing pH of the solution, the nature of interactions can be changed (for example: electrostatic to H-bonding) as desirable during electrostatic interaction. Here, besides electrostatic interactions for cell-membrane penetration (in **Chapter 4** and **5**), this work also deals with the electrostatic interaction between positively charged amine group and negatively charged nucleic acid for DNA/RNA loading, protection and release. It is particularly important to understand the nature of electrostatic interactions in relation to other non-

covalent forces when estimating the thermodynamic nature and parameters of DNA binding by isothermal titration calorimetry (**Chapter 7**).

2.3.1.3 Hydrogen Bonding

Hydrogen bonding (H-bonding) is probably the most important type of non-covalent binding. It is often considered as a strong dipole-dipole interaction, which exists between lone pair electron of electronegative atoms and a hydrogen atom. Contributions from H-bonding should always be considered during any interactions between biomolecule and surfaces. Direct measurement of interaction energies associated with H-bonding are difficult, can possibly be determined only in gas phase analysis [157]. Host-guest complexes in biological macromolecules often form *via* several simultaneous H-bonds, creating significant difficulties to isolate and analyzing the binding. H-bonding of molecular interactions in water (H_2O to H_2O) is probably very similar to that of between Si-OH and H_2O, which makes detection and analysis of only H-bonding interactions difficult in systems involving silica. Silica, owing to its high surface silanol density, forms both strong and weak H-bonding with adsorbed water and H-bonding primarily regulates the water layer and interaction with other biomolecules [143]. Due to the presence of H-bonding, the silica surface is strongly hydrophilic and during biomolecular interaction on silica surfaces the presence of an adsorbed water layer should be considered.

H-bonding happens during nucleic acid interactions with polyamines, when amine groups are fully deprotonated [158]. Thus H-bonding is also modulable like electrostatic interactions by changing solvent pH. It should be noted that in confined silica surfaces (*i.e.* MSNPs), Si–OH groups show less propensity for H-bonding compared to unconstrained

silica surfaces, which has to be considered for mesopores of the particles. Here, the presence of H-bonding along with other interactions is analyzed by isothermal titration calorimetry (ITC) measurements between nucleic acids and MSNPAs (**Chapter 7**).

2.3.1.4 Hydrophobic Interactions

Hydrophobic interactions are mostly solvent (water) driven, as the solvation shell around one cavity of two lipophilic molecules in close proximity is favored compared to two cavities of separated lipophilic molecules [159]. The formation of micelles, aggregates, and protein folding are often described as the reduction of water accessible surface area through hydrophobic interactions [160]. Peptides also adsorb on hydrophobic surfaces through hydrophobic interactions [113]. There are some innovative strategies to adsorb nonionic surfactant molecules to silica surface by using hydrophobic interaction with another ionic surfactants (co-adsorption). Cationic surfactants generally have higher adsorption affinity toward silica surface, which non-ionic surfactants do not show. However, once an ionic surfactant is adsorbed onto silica surface, non-ionic surfactants also adsorb through hydrophobic interaction with ionic surfactant tails [117]. Hydrophobicity is generally measured by its octanol-water partition coefficient. It is worth noting that large biomolecules like proteins and nucleic acids have water molecules in their cavities and thus it is not straightforward to explain their adsorption on a surface solely based on lipophilicity. Hydrophobic molecules are preferentially attractive to a surface from aqueous solution and as a result produces very high non-specific binding solely due to hydrophobic interaction, which create a tremendous challenge in quantifying other specific interactions. We expect the analyte in **Chapter 6** (β-estradiol) to show high degree

of non-specific binding to the particles due to its hydrophobic nature. Hydrophobic interactions should also contribute during nanoharvesting and delivery of lipophilic molecules like flavonoids in **Chapter 4**.

2.3.2 Thermodynamic Nature of Equilibrium Binding Process

Physicochemical binding processes must satisfy the laws of thermodynamics and as a result, a process only occur when the Gibbs free energy change (ΔG) is favorable (negative). Since, there are two components of Gibbs free energy change, which are enthalpy change (ΔH) and entropy change (ΔS) as shown in **Equation 2.2** (Gibbs-Helmholtz equation), minimization of Gibbs free energy can be achieved either from large enough favorability from enthalpy change or the process has to have entropic favorability.

$$\Delta G = \Delta H - T\Delta S \tag{2.2}$$

where T is the isothermal temperature of the experiments.

Thus, two inherent equilibrium binding processes arise from thermodynamic points of view: enthalpy dominant process and entropy driven process. Careful determination and analysis of the thermodynamic nature and associated parameters (free energy, entropy and enthalpy change) is important in designing engineered nanoparticles and selecting proper functional groups in order to isolate a particular biomolecule. A phenomena that usually exists in most cases of non-covalent binding is the so-called "enthalpy-entropy compensation". This arises from the fact that strong enthalpic binding usually restricts the mobility of bound molecules and thus exhibits an unfavorable entropic contribution, and *vice versa* [161, 162]. Enthalpy-entropy compensation exists whenever a plot of $T\Delta S$ versus ΔH produces a straight line [147, 163]. The linear correlation can be expressed as:

$$T\Delta S = \alpha\Delta H + T\Delta S_o \quad (2.3)$$

where, α is the slope of the curve and $T\Delta S_o$ is the y-intercept. $T\Delta S_o$ represent the stability of formed complex in absence of any enthalpic stabilization (ΔH = 0). The physical meaning of the slope, α, is found by differentiating Gibbs-Helmholtz equation and using **Equation 2.3**, which yields the following **Equation 2.4** [147].

$$d(\Delta G) = d(\Delta H) - d(T\Delta S) = (1 - \alpha)\, d(\Delta H) \quad (2.4)$$

Hence, the slope α represents the contribution of enthalpic gain to the free energy change, as some of the enthalpy is nullified by accompanying entropy loss and *vice versa*, which in combination with intercept $T\Delta S_o$ are used as a quantitative, empirical measure of conformational changes and desolvation (water release) upon binding, respectively [147].

A Gibbs free energy change is also associated with the kinetics of binding (formation of an activated complex) by the following **Equation 2.5**.

$$\Delta G = - RT*ln(K_a) \quad (2.5)$$

where, K_a is the equilibrium coefficient for forming the activated state and R is the gas constant. Analyzing both enthalpy and entropy changes and their relative contributions in addition to the free energy change are important as these two contributions can be different for same free energy change. As an example, even though some host molecules seemed to produce the same free energy change when binding to two ions, calorimetric investigation revealed two very fundamentally different processes [164]. Usually, dehydration/water release, structural rearrangement and electrostatic repulsion are endothermic, and chemical reaction, electrostatic attraction and H-bonding formation are exothermic [165]. For example, during large peptide or protein binding, ion pairs formed by deprotonation of amine and carboxylic acid moieties are entropy driven but due to extensive H-bonding,

enthalpic contribution can become significant and provide partial electrostatic contributions to free energy [166]. Non-covalent interactions (electrostatic, H-bonding, π-π interactions *etc.*) are exothermic, and desolvation and conformational changes are endothermic and associated with large positive entropy change [167, 168]. Multiple interactions within a single complexation process and the associated occurrence of conformational change is not easy to isolate and analyze.

For a process to be enthalpy driven, the enthalpy change should be highly favorable (exothermic) to compensate for unfavorable entropy change. Positive cooperativity between binding sites produces greater binding strength and as a result associated with greater enthalpic energy release and entropic penalties, and *vice versa* for negative cooperativity [169]. On the other hand, several binding processes are entropy driven even though association of molecules inherently does not have entropic favorability. As mentioned earlier for polyelectrolytes, ion pairing in the aqueous solution is completely dominated by entropy driven processes, associated with large positive ΔH due to desolvation of interacting ion upon association [166, 170]. The dominant physical interactions of nucleic acids with other cations are entropy driven, as associated with large amount of counterion release as water, and their associated enthalpic penalties. Entropic contribution is usually harder to quantify, as they are often confused with several non-covalent interactions.

In this dissertation, the thermodynamic nature of binding between several classes of biomolecules and different ESNP are important to understand for nanoharvesting and delivery applications. Although thermodynamic parameters are not directly measured for the interactions in **Chapter 3 to 6**, general understanding from a thermodynamic point of

view is necessary. Interaction of polyphenolic flavonoids to TiO_2-functionalized particles (**Chapter 3 and 4**) are due to coordination complex formation, which is expected to be highly enthalpy driven. Interaction of nucleic acids with MSNPAs is measured directly in **Chapter 7**, in order to find the underlying thermodynamic parameters. We expect the interaction to be complex based on the literature studies on nucleic acid interaction with polycations in solution, characterized by concentration-dependent heats of interaction (changing exo-/endothermic heat signals) and multifaceted due to involvement of several interactions [171-174].

2.3.3 Energy of Interactions

Energy of interaction is the total energy contributed during the interaction of two systems being considered arising from all the process combined. It needs to be determined when designing appropriate systems based on biological systems for drug design, and selecting host materials for their delivery [166]. Interaction energy for non-covalent binding is difficult to determine because of its small magnitude. Weak interactions are sometimes estimated by a competitive binding assay with another strongly interacting ligand for the same site, and estimating the binding energy from the difference. Non-covalent forces act less freely on a surface due to constraints in free energy as compared to in solution and thus require higher care during experimental design for estimation.

Methods used for estimating energies and thermodynamics of interaction are traditional spectroscopic techniques and NMR [175]. On the other hand, surface plasmon resonance can measure the kinetics of binding processes in addition to binding energies [176]. Chemical force microscopy (such as atomic force microscopy or AFM) can directly

measure associated non-covalent forces [177]. However, recent developments in isothermal titration calorimetry (ITC) allow it to provide reliable thermodynamics of the binding process in the form of entropy, enthalpy and free energy changes [161, 166]. Cooperative binding between two sites also poses a high degree of difficulty in estimating binding energy corresponding to one of them, but ITC data can be fitted with different models (cooperative, multiple sites) to isolate these processes. The technique is very important in estimating and quantifying molecule-molecule and surface-molecule interactions and discussed in more detail below.

2.3.3.1 Isothermal titration calorimetry (ITC)

Isothermal titration calorimetry (ITC) directly measures measures heat of interaction (ΔH), and through modeling the corresponding free energy change (ΔG) in a physicochemical process at constant temperature. ITC utilizes a power compensation technique to maintain constant temperature in a cell (where physical or chemical process take place) compared to a reference cell of equal volume kept at same temperature, by a heater/cooler assembly (see **Figure 2.8**) [178]. The detector can sense infinitesimal temperature change in the sample cell with respect to reference cell and an opposite power is applied as compensation using the heater/cooler assembly. Heat generation/consumption during the process is calculated based on this supplied power and the raw signal generated by ITC equipment is the power needed to continuously keep the system isothermal during the process. During a typical experimental run, a syringe is used to inject a solution to the sample cell in a stepwise or continuous manner. The whole assembly is situated in an adiabatic jacket to absolutely minimize any heat transfer with the surroundings. Raw data

with every injection (called “thermograms”) can be processed and integrated heat per mole of chemical versus mol ratio of ligand and receptor (called “isotherms”) can be fitted with various binding models in order to decouple thermodynamic processes and to estimate the underlying thermodynamic parameters. As mentioned before, ITC will be used to study thermodynamic interactions between dsRNA and MSNPA in **Chapter 7**. Next, a brief description of equilibrium binding models and data fitting is provided.

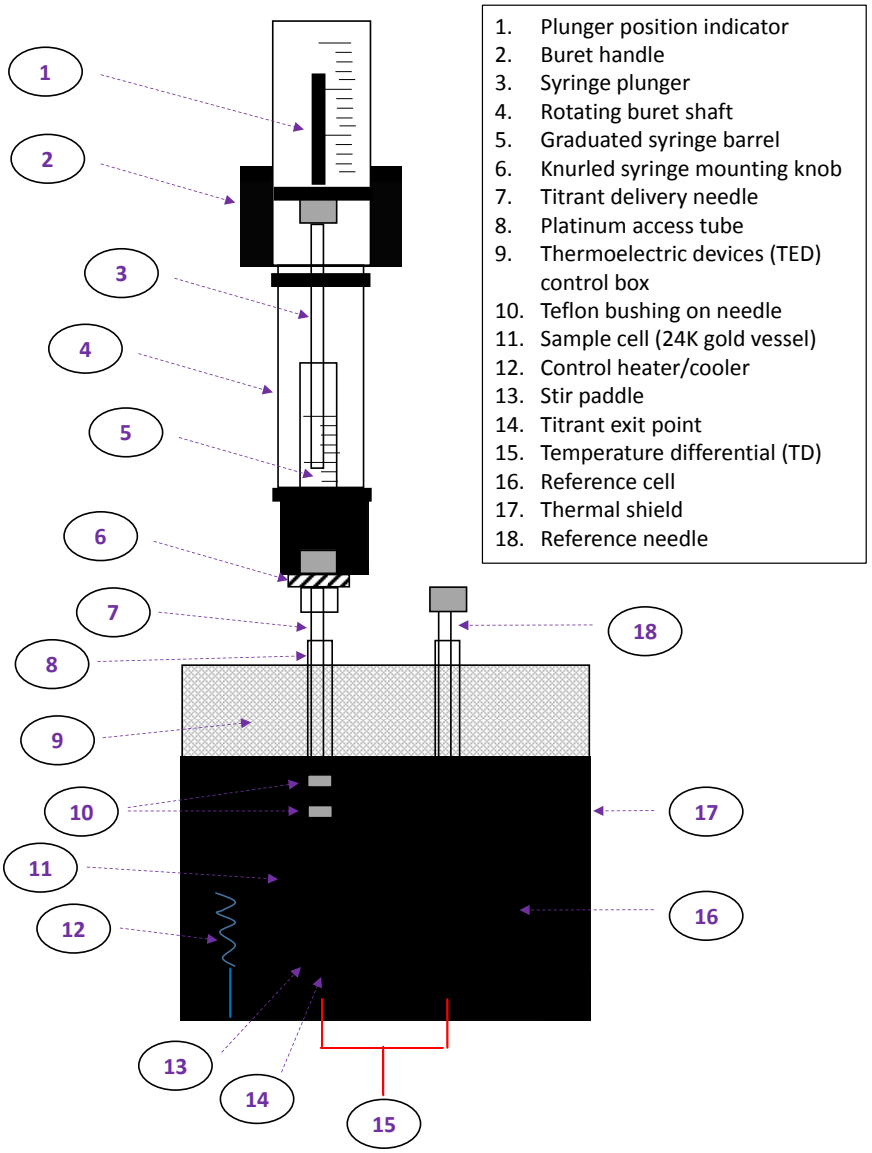

Figure 2.8 Schematic diagram of the low volume Nano-ITC with all the major component shown (not drawn to scale). Adapted from TA Instrument getting started guide [179].

The simplest of the ITC binding models is the single site independent binding model (so called "Wiseman Isotherm"), which assume a Langmuir type equilibrium (**Equation 2.6**) between a ligand (*X*) and receptor (*M*) with single set of identical binding sites [180]. Single site binding model is used for uniphasic sigmoidal ITC isotherms (only one exothermic or endothermic phase). For the binding reaction shown in **Equation 2.7**, overall mass balance (**Equation 2.8**) and energy balance (**Equation 2.9**) yield the amount of heat released presented in **Equation 2.10**.

$$K_a = \frac{\Theta}{(1-\Theta)[X]} \tag{2.6}$$

$$M + nX \leftrightarrow MX_n \tag{2.7}$$

$$[X]_t = [X] + n\Theta[M]_t \tag{2.8}$$

$$Q = n\Theta[M]_t \Delta HV_0 \tag{2.9}$$

$$Q = \frac{n[M]_t \Delta HV_0}{2}\left[1 + \frac{[X]_t}{n[M]_t} + \frac{1}{nK_a[M]_t} - \sqrt{\left(1 + \frac{[X]_t}{n[M]_t} + \frac{1}{nK_a[M]_t}\right)^2 - 4\frac{[X]_t}{n[M]_t}}\ \right] \tag{2.10}$$

where *n* is the number of binding sites, $[X]_t$ and $[X]$ are the total and equilibrium ligand concentration, $[M]_t$ and $[M]$ are the total and equilibrium receptor concentration, Θ is the fraction of binding site occupied by ligand, and V_0 is the active cell volume. For full derivation of **Equation 2.10**, interested readers can refer to the literature [180, 181]. **Equation 2.10** can be used to find the amount of heat released during the i^{th} injection by the following equation, derived from displaced volume.

$$\Delta Q_i = Q_i + \frac{\Delta V_i}{V_0}\left[\frac{Q_i + Q_{i-1}}{2}\right] - Q_{i-1} \tag{2.11}$$

where ΔV_i is the volume of ith injection. Now, three binding parameters ΔH, n and K_a can be fitted for each binding site using a least squared error curve fitting using the equations.

Biphasic binding isotherms (having two different exothermic or endothermic regions or one endothermic and one exothermic region), when produced by ITC interactions, usually indicate either a sequential binding or binding to two distinct types of sites. Both kinds of model have been used to analyze ITC data [182]. For binding with two sets of distinct sites, Langmuir equilibrium, mass balance and energy balance equation is provided below.

$$K_{a1} = \frac{\Theta_1}{(1-\Theta_1)[X]} \text{ and } K_{a2} = \frac{\Theta_2}{(1-\Theta_2)[X]} \tag{2.12}$$

$$[X]_t = [X] + (n_1\Theta_1 + n_2\Theta_2)[M]_t \tag{2.13}$$

$$Q = [M]_t V_0 (n_1\Theta_1\Delta H_1 + n_2\Theta_2\Delta H_2) \tag{2.14}$$

where, subscript "*1*" and "*2*" correspond to first and second types of binding sites. **Equation 2.12** to **2.14** can be solved numerically along with **Equation 2.11** to find the heat for every injection and fitted with experimental isotherms to estimate six thermodynamic parameters ΔH_1, n_1, K_{a1}, ΔH_2, n_2 and K_{a2} simultaneously.

Both single site and two site binding models are used in **Chapter 7**, for the analysis of thermodynamic interactions between RNA and MSNPA. Finally, mathematical derivation for other binding models such as sequential binding, three or more binding sites, dimer dissociation, cooperative binding *etc.* is available in literature but not presented here as they are not relevant to this dissertation.

2.4 Engineered Nanoparticle Interactions with Cells

Both nanoharvesting and delivery applications in this dissertation involve nanoparticle (ESNP) interaction with living cells and tissues. Hence, a thorough understanding is needed of detailed mechanisms of nanoparticle interaction with cells, pathways of engineered nanoparticles inside eukaryotic cells, and the ultimate fate of the nanoparticle (expulsion or entrapment). Major pathways (internalization or uptake, intracellular transport and expulsion or exit) of functionalized MSNP interaction with cell are depicted in **Figure 2.2** along with various surface modification performed in this dissertation to regulate the interactions with cells for nanoharvesting and delivery applications.

The response of biological systems (*esp.* cells) with engineered nanoparticles are widely varied, which mainly depend on the types of cells and/or the nature of the nanoparticles used [62]. Effects of nanomaterials in living cells and corresponding cell responses are indeed very complex depending mainly on the properties of nanomaterials such as shape, size, concentration, surface composition and pore size, and full knowledge of this field is still developing [36, 183, 184]. Nanoparticle interaction with biological systems are also complicated due to size and other property distribution among a population of particles, which renders it very difficult to establish a cut-off value for a certain response. Generally, nanoparticle interaction with cells can be explained from a broader energetic point of view, and the process which involves less energy penalty is ultimately favored [62, 184].

When nanoparticles were exposed to animal or plant cells (eukaryotic cells in general), they are generally internalized at first based on the surface properties and size of the nanoparticles and/or cell types. After uptake or internalization, nanoparticles are

transported *via* intra- or intercellular pathways and finally either get immobilized in/with certain organelles or exit *via* different expulsion mechanisms. During nanoparticle design, special emphasis should also be put on toxicity of nanoparticles after cellular uptake and uptake/ expulsion mechanisms, and a short residence time inside the cells is desirable to minimize toxicity.

The lipid bilayer cell membrane is the most important cellular component that nanoparticles encounter first during uptake and last during expulsion. Nanoparticle entry and exit mechanisms through cell membrane is a vast research area but can be divided into two major types: activated and non-activated. In order to show the difference between them, schematic diagrams for both are presented in **Figure 2.9**. Non-activated penetration (also called direct penetration) happens mainly for charged particles, which when comes in the vicinity of the membrane disturb the regular membrane orientation and can pass through the membrane, while the membrane itself recovers its regular orientation (**Figure 2.9a**). Direct membrane penetration mechanism should be the same during both uptake and expulsion. On the other hand, activated mechanisms during uptake and expulsion (endocytosis and exocytosis) are different fundamentally, as uptake involves wrapping the particles, while during expulsion wrapped vesicle gets fused with cell membrane (**Figure 2.9b**). Both endo- and exocytosis require energy to happen, as vesicle formation and merging both involve expenditure in energy.

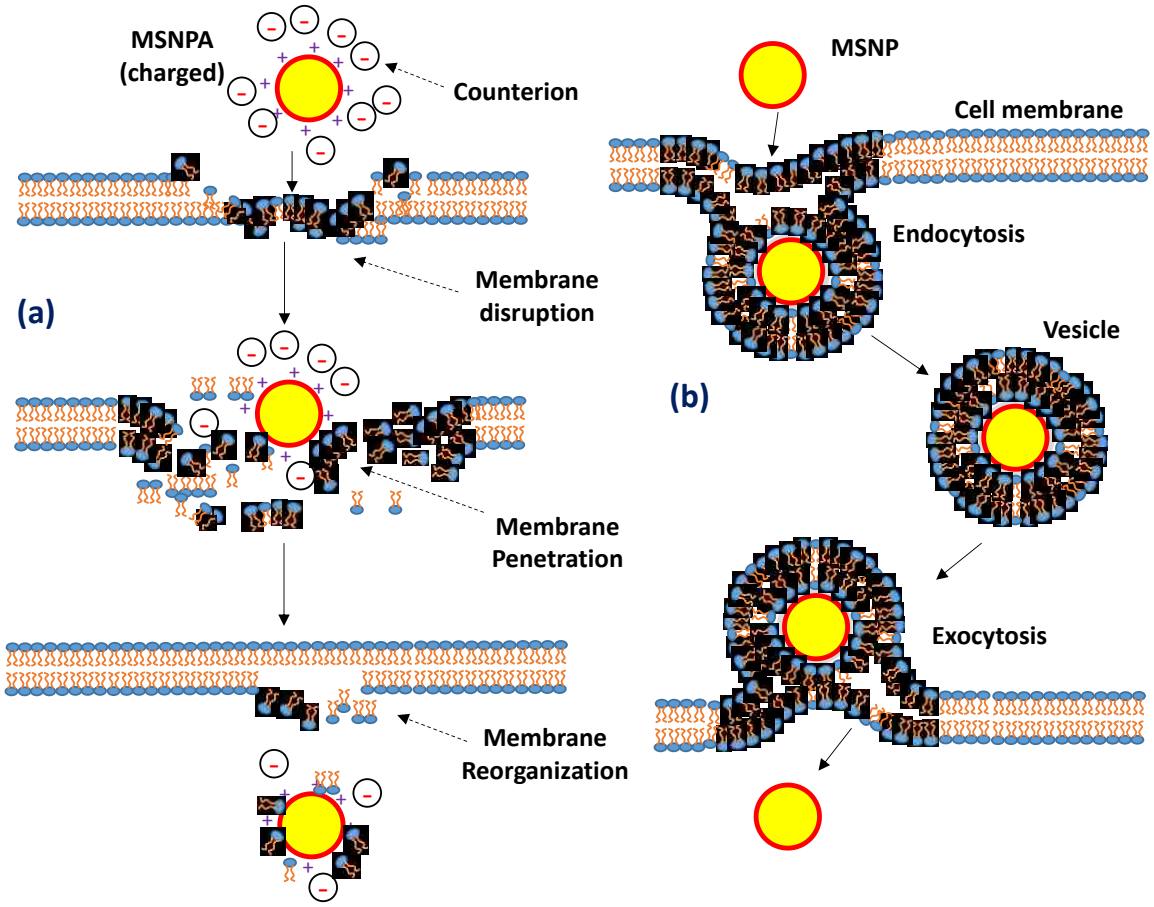

Figure 2.9 Schematic representation of (a) lipid exchange membrane penetration for charged MSNPs in comparison with (b) activated (energy-mediated) uptake and expulsion mechanism (endo- and exo-cytosis, respectively). Part (a) is adapted from Wong et al. [156].

2.4.1 Cellular Uptake

Nanoparticle internalization by cells is a complex process, far beyond relying on a simple factor like size of the nanoparticles [185]. Other factors contributing to cellular uptake of nanoparticles are surface chemistry and the shape of the particles. Uptake is also dependent on cell types (for example: plant and animal cells behave differently). It was reported that colloidal stability of the nanoparticles in cell media in addition to charge driven interaction with cell membrane is important for cellular uptake [36]. Nanoparticles

often bind to proteins in cell cultivation media (forming a protein corona), which sometimes stabilize the particles against weak aggregation forces [186]. As mentioned before, nanoparticles are often internalized by energy dependent (activated) mechanism or endocytosis similar to the internalization of nutrients and other biomolecules by the cells. Some endocytosis process involve taking up fluid and particles together (micropinocytosis and pinocytosis), which usually involve formation of vesicle with size ranging from 0.2 to 5 µm. Activated internalization get switched off at low temperature (4 ºC), which helps to identify and differentiate between active and passive uptake [26]. Cellular uptake is generally the first step for nanoparticle interaction with living cells, where nanoparticles are to be used as carrier for biomolecule transport and should be studied in detail. Below, an elaborated description is provided for nanoparticle uptake in plant cells (which is most relevant to nanoharvesting) along with a brief description on animal cell uptake for contrast.

2.4.1.1 Uptake in Plant Cells

Nanoparticle uptake mechanisms in living plants and plant cells are still a poorly understood topic and there are widespread disputes among researchers. As a whole, plant cells possess cell walls around their cell membrane (in contrast to protoplasts) and as a result show different behavior during nanoparticle uptake. Cell walls have pore with dimeter < 20 nm, and hypothetically any nanoparticle size greater than this should not be internalized by plants. However, researchers have reported internalization of larger sized MSNPs (up to 200 nm) inside whole plant tissue [26, 187]. Therefore, it was reasoned that larger nanoparticles have the ability to create pores in cell walls in order to penetrate [188].

Once cell walls are penetrated, nanoparticles interact with cell membrane by activated and passive mechanism (endocytosis and direct penetration, respectively), as mentioned before depending on the particle properties [26, 156] as found by nanoparticle internalization by isolated plant cells (protoplasts) [189]. Since activated mechanisms of uptake are energy dependent, they can be halted at 4 ºC and uptake experiment at different temperature (23 and 4 ºC) can be used to differentiate activated and passive mechanisms (**Chapter 5**). Nanoparticle uptake in plant roots are most relevant here, as hairy root cultures will be used for nanoharvesting of polyphenolic flavonoids. Nanoparticle uptake in plant roots is mostly associated with nutrient uptake, and since the primary uptake pathway of nanoparticles in plants are through roots, using hairy roots in nanoharvesting (**Chapter 4**) is inherently advantageous, as roots are already equipped to facilitate nanoparticle internalization. Nanoparticle uptake in hairy roots is also the first condition to be met during the nanoharvesting process. In this dissertation, ESNP uptake in hairy root is confirmed by fluorescence microscopy (**Chapter 4**) and quantified by Ti-content (present for target metabolite binding) analysis of calcined roots following exposure in **Chapter 5**.

2.4.1.2 Uptake in Animal Cells

Although not directly applied in this dissertation, uptake mechanisms and pathways in animal cells (especially human cell lines) provides a better-understood counterpart to uptake in plants during nanoharvesting. It is also important to study during nucleic acid delivery to animal cells using MSNPAs. Non-functionalized MSNPs internalization by animal cells (*esp.* human cell lines) is typically an energy dependent process with phagocytosis, micropinocytosis and clathrin-mediated processes being dominant [62, 183].

Internalization also happens by membrane penetration and passive diffusion, which is called direct penetration as described in **Figure 2.9a** [190]. Animal cells have shown faster internalization for large particles (> 500 nm) compared to small nanoparticles (~80 nm) [191] unlike plant cells. The cause of this is two-fold: larger particles create higher association force with lipid headgroups of cell membranes and it takes less energy to engulf larger particles due to small surface curvature [192], whereas in plant cells uptake of larger particles is slower probably due to an additional barrier in cell walls. This phenomena was also observed for uptake of differently sized particles in human melanoma cells; particles with larger aspect ratio (length:diameter) show higher degree of internalization due to more contact area (longitudinal) with cell membranes [193]. The internalization route also depends on the size of mesopores as shown for MCM-41 and SBA-15 types mesoporous silica [194]. Surface functionalization also plays a critical role during endocytosis of MSNPs in animal cells. It was reported that the mechanism of endocytosis of amine-functionalized MSNPs (receptor mediated) is different compared to bare MSNPs, which are internalized by nonspecific adsorptive route [195].

2.4.2 Nanoparticle Toxicity

During nanoparticle interaction with cells, they can produce mild to acute toxicity in the cells and the organism at large. At the sub-cellular level, toxicity arise from intracellular injuries through various interactive mechanisms of the nanoparticles with biological systems such as membrane disruption, antioxidant depletion, dysfunction and damage of vital part like mitochondria and DNA [62]. The size of nanoparticles is one crucial factor besides concentration that determines the toxicity of nanoparticles in

biological systems, and the general consensus is that smaller particles are generally more toxic than their larger counterparts due to exerting higher oxidative stress [191, 192, 196]. Toxicity is also dependent on the cell types being used because of different uptake and transport mechanism [62]. Plants suffer from two different types of toxicity upon particle uptake: cytotoxicity (toxicity toward cells) and phytotoxicity (toxicity toward plant growth). Phytotoxicity of plant seedlings and mature plants by engineered nanoparticles is widespread, stemming from the blockage of water uptake and transport pathways [197]. This effects is so multifaceted based on plant types and nanoparticle properties, it is recommended to study toxicity on a case-by-case basis [188]. MSNPs were also found to be less toxic to human cells compared to nonporous silica particles due less surface silanol groups in contact with the cell membrane surface [198]. Toxicity studies of hairy roots after exposure to engineered MSNPs are a vital and integral part of this dissertation as one of the requirements of nanoharvesting is the viability of hairy roots after exposure to nanoparticles. During nanoharvesting in **Chapter 4**, toxicity of hairy roots upon ESNP uptake were is studied by re-culturing and observing regrowth of the roots.

2.4.3 Nanoparticle Transport after Uptake

Transport route after uptake is important to determine the efficacy of designed nanoparticles for biomolecule delivery or other applications. For example, during nanoharvesting ESNP must travel to the biomolecule rich organs (primarily vacuoles) after uptake in order to gain access to target compounds. Similarly, during gene delivery particles need to reach the proximity of cell nuclei for targeted release. As mentioned before, nanoparticles internalized by activated mechanisms usually stay entrapped in a

vesicle, which then transforms into an endosome. Exit from the endosomal vesicles (endosomal escape) is important for the nanoparticles to reach targeted sites. Two kinds of nanoparticle transport happen after internalization: intracellular transport and transport outside cells (*a.k.a.* translocation) [199, 200]. Both are immensely important as they determine the ultimate fate of the particles, whether they will get entrapped inside or come out of the cell, which is tremendously important for minimal toxicity. After uptake in plants through the roots, nanoparticles can be transported through the transport tissues to other organs such as stems or leaves. Nanoparticles can also move from cell to cell through the space between the cell wall and membrane. Due to the importance with respect to this dissertation, intracellular transport, endosomal escape and extracellular transport are discussed separately below.

2.4.3.1 Intracellular Transport

Intracellular transport of nanoparticles consists of different steps from entry into the cell, which involve membrane penetration, vesicle entrapment, endosome creation and lysosomal degradation [62]. Particles taken up by active route (endocytosis) often exist in early endosomes, which then travel along microtubules and follow lysosomes to fuse with late endosomes and finally exit through fusion with the cell plasma membrane [201]. Some of the nanoparticles can escape from early endosomes and become free in the cytosol, which can get trapped inside various organelles subsequently. Intracellular transport and organelle distribution of nanoparticles are sometimes dependent on their uptake pathways, where vesicular contents can be secreted at different steps of endo-lysosome pathways [95]. The ability of designed particles to exit the intracellular vesicle are immensely important

for biomolecule delivery application and sometime particles are engineered to provide these capabilities. In the sub-section below endosomal escape is discussed separately. It should be noted that charged particles following their uptake by direct penetration travel freely through the cytoplasm and are not trapped in early vesicles. Their pathways inside the cells should be different as opposed to non-charged particles, whose only internalization mechanism is energy mediated [156].

2.4.3.2 Endosomal Escape

Endocytosed nanoparticles remain in the endosomal vesicles rather than roaming free in the cytoplasm, which creates a major issue for delivering biomolecules in the targeted intracellular sites [202]. However, the ability of the particles to penetrate out of endosomal vesicles is very important to obtain an efficacious delivery system, and research is still ongoing in his subject. Several methods of endosomal escape have been proposed in literature. As endosomal vesicles are acidic, disturbing the proton concentration is the most reliable method for obtaining endosome free nanoparticles [120]. Another approach is to functionalize the particles with polycationic cell-penetrating peptide (*e.g.* poly-arginine) or other positively charged group that shows capability of rupturing endosomal vesicles [95, 203]. The ability of particles functionalized with polycations to escape endosome has huge significance in this dissertation, as MSNPAs are positively charged and as a result should be able to escape the vesicles even if they are endocytosed. The size of nanoparticles also plays a crucial role in determining their endosomal escape capabilities, with larger sizes tending to escape more easily [204]. With relatively larger

size (~170 nm), positively charged particles in **Chapter 4** should be able to escape endosomal vesicles.

2.4.3.3 Extracellular Transport

Internalized nanoparticles in plants are often transported from roots to other parts (stem, leaves) through the transport (vascular) tissues and channels [197, 205]. In plants, once nanoparticles enter through the cell wall, they can be transported through the interconnected space between the cell wall and membrane. There can be repeated entry and exit from cell to cell for transport and localization. Extracellular transport in hairy roots is very important during nanoharvesting (**Chapter 4**), as cell-to-cell (repeated) transport is the way nanoparticles reach to the internal parts of the roots and come out in solution.

2.4.4 Nanoparticle expulsion after uptake

Much effort has been put into investigating nanoparticle uptake and transport throughout the years, but prolong exposure or entrapment of nanoparticles inside the cells are responsible for toxicity in both animal and plant cells [201]. Thus studying the underlying expulsion/exit mechanism of nanoparticles is also important in order to design smart nanoparticulate carriers that exit the cells swiftly after their intended purpose (biomolecule binding or delivery) is served. Golgi apparatus excretion or lysosomal exocytosis was described as a possible mechanism for MSNPs exit after internalization [206]. Nanoparticle recovery is also an essential component of biomolecule nanoharvesting and delivery processes, as expulsion of the nanoparticles is the final crucial steps during these applications.

Like uptake, expulsion of nanoparticles are equilibrium process as silica nanoparticle uptake and expulsion was found to reach equilibrium within 2 h of exposure [16]. Positive surface charge is very important for nanoparticle excretion, similar to nanoparticle internalization [207], where particles can penetrate out of the cell membrane directly (shown in **Figure 2.9a**). For non-charged particles, the major exit pathway is exocytosis, an activated mechanism where nanoparticle containing vesicles (late endosomes) get fused with the cell membrane to expel internal nanoparticles (**Figure 2.9b**). Like uptake, nanoparticle expulsion should be dependent on cell type and particle properties such as size, shape and surface properties. Another largely unexplored major factor is the intracellular interaction after uptake and before expulsion, and varieties of biomolecule adsorption (such as protein) inside cells [16]. We investigate the uptake, transport and expulsion pathways of engineered MSNPs inside hairy roots during nanoharvesting (**Chapter 4**) in order to identify the mechanism of uptake and exit.

2.4.4.1 Exocytosis

Nanoparticles after endocytosis are usually wrapped in vesicle (early endosome), which carry them towards lysosomes where degradation happens and non-degradable particles (silica) are eventually exocytosed. Exocytosis is often found associated with cellular waste-disposal systems, where nanoparticle-containing vesicles are transported to the cell membrane and turned inside out following fusion. This process is thought to be regulated by Lipid rafts (regularted by cholesterol) [208]. Exocytosis is also an energy dependent process (activated), and as a result can also be inhibited by metabolic inhibitors. The rate of exocytosis (along with endocytosis) is concentration dependent as they are

dynamic processes [201]. Exocytosis can also be stopped at 4 °C, to differentiate it from non-activated mechanism or direct expulsion (**Chapter 5**).

2.5 Designing Nanoparticulate Carriers for Biomolecule Delivery to Cells

Biomolecule targeted and controlled delivery to cells, tissues and organs has become an integral part of modern therapeutic and regenerative medicine. Due to their large size and structure as well as inherent immunity of cells towards foreign materials, biomolecules generally cannot penetrate and survive inside living cells in their active forms to produce intended results. Hence, inorganic, organic and polymeric carriers (nanoparticles) have emerged as delivery vehicles for numerous biomolecules such as proteins, nucleic acids and small/large molecular drugs [209]. During the past decades, numerous investigations were carried out in order to study the interactions between a wide variety of biomolecules and mesoporous silica systems for loading and controlled release of the molecules [65]. Based on nanoparticle interactions with molecules and cells, they can undergo binding with verities of compounds inside cells once internalized and generally stay inside vesicles and endosomes after activated uptake. In order to design perfect delivery vehicle, nanoparticles should have the capability to escape endosome, evade enzymatic hydrolysis and unwanted binding to other intracellular compounds, reach the target intracellular sites, and finally release their cargo in a controlled way [62]. An ideal drug delivery carrier should have the following characteristics: (i) sufficient loading, (ii) minimal toxicity, (iii) no premature release, (iv) release in targeted sites and (v) controlled release with a predetermined rate [24]. As mentioned before, surface functionalized MSNPs are good candidates for biomolecule delivery based on their tunable surface properties, pore size, particle size and surface functionalization. Part of this dissertation involves designing amine-functionalized MSNPs (**Chapter 7**) for nucleic acid delivery, where pore size dependent interaction of double stranded (ds) RNA is investigated by isothermal titration calorimetry (ITC) in order to understand the

fundamental physicochemical processes during delivering dsRNA using engineered MSNPs. As a result, fundamental understanding of nucleic acid (DNA/RNA) delivery processes and design requirements for ideal carrier design is very important, which will be introduced and discussed briefly.

2.5.1 Carriers for Nucleic Acid Delivery

Polynucleic acid (DNA/RNA) delivery to targeted intracellular sites is essential for gene therapies and selective gene expression/silencing for various diseases [210, 211]. However, nucleotides face tremendous odds in reaching the vicinity of cell nuclei (delivery sites) as almost all cells have intrinsic defense against foreign nuclear materials. There are mainly two kinds of barriers (extracellular and intracellular) a nucleic acid delivery system naturally encounters when it is introduce to the body [212]. To be successful, an ideal nucleic acid delivery vehicle in mammalian systems should have the following characteristics: (i) protection against blood serum nucleases, (ii) stealth properties against immunity, (iii) dodging non-specific binding, (iv) avoiding clearing mechanisms from body before delivery, (v) transport from blood vessel to target tissue, (vi) cellular uptake and (vii) reaching target intracellular sites to release nucleic acid [213]. Engineered MSNPs have been shown to possess properties to meet the criteria to be a perfect nucleic acid carrier and release agent. Useful MSNP properties for nucleic acid delivery are schematically presented in **Figure 2.10**, which mainly include tunable pore characteristics, easy surface functionalization, and lipid encapsulation for providing stealth properties. Two fundamentally different kinds of nucleic acid delivery systems exists based on the

properties of DNA and RNA, and their slightly different applications [214]. A brief discussion on DNA and RNA delivery is presented below separately.

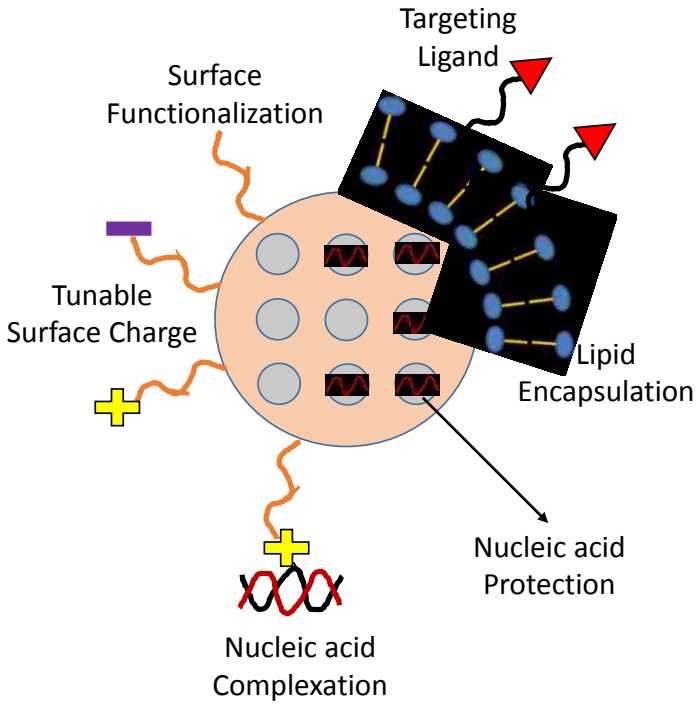

Figure 2.10 Conceptual representation of the tunable surface properties for nucleic acid loading, protection and release, and surface functionalization for cell targeting and internalization.

2.5.1.1 DNA Delivery

Nonviral carriers for DNA are important systems for delivery to affected cells to alter the function of that cell, tissue or organ in the human body to achieve gene therapy [212]. Naked or unprotected DNA delivery is the most used nonviral gene delivery systems [20]. During DNA delivery, the vehicle must deliver the DNA molecule inside the nuclei and should have the capability to pass through/penetrate nuclear pores/walls even when they are inside the cells [212]. After reaching into the nuclei, nanoparticles should then release the DNA, which then get transcribed to induce the intended response. Thus, there

are two kinds of efficiency that in combination determine the overall efficacy of DNA delivery process: the fraction of DNA transported to the target site, and the fraction DNA that transcribed in nuclei [215]. Thus, and ideal DNA carrier should have the capability of penetrating through both cell and nuclear membranes, and MSNPAs can serve this purpose as lipid membrane penetration mechanism by charged particles are universal regardless of their location.

2.5.1.2 RNA Delivery

Double stranded (ds) RNA delivery to silence certain gene expression is called RNA interference (RNAi), which is the most prominent RNA delivery reason to date. Using this technique, RNAi can be used to silence or alter virtually any gene expression and as a result has huge potential to treat some diseases that is otherwise considered untreatable [213]. Although longer dsRNA can be delivered, the overwhelming number of RNAi application involve small interfering RNA (siRNA), which generally inhibit protein translation selectively in order to silence gene expression. The steps and requirements for siRNA delivery are similar to that of DNA delivery, except that the delivery site is outside of cell nuclei. To date numerous nanoparticle-based siRNA delivery vehicles have been investigated in literature including functionalized MSNPs [216, 217]. Recent developments in making MSNPs with large pores (as described in **Section 2.1**) provide pore size-based protection along with high loading capacity of siRNA. Hence, RNA is selected as model compound in **Chapter 7** to study nucleic acid interaction with amine functionalized MSNPs.

2.5.2 Primary Requirements for Biomolecule Carriers in Cellular Delivery

As mentioned earlier, nucleic acids and other biomolecules by themselves cannot penetrate cell membrane (due to large size and negative charge) and as a result require a delivery vehicle to enter into living cells [218]. Efficiency of delivery system primarily depends on the quantity of biomolecules loaded for delivery, protection against intracellular enzymes (fraction actually reached to delivery sites) and delivery with appropriate rates. As a result, three primary necessities should be fulfilled by any delivery vehicle in order to act as proper carrier: loading, protection and release, which are discussed below in detail. MSNPAs also provide binding sites for fluorescent dye to be used for bio-imaging during targeted delivery.

2.5.2.1 Biomolecule Loading

Loading is the first step for biomolecule delivery, which is performed outside the cells in order to load a sufficient amount of biomolecules inside the porous space or cavities of nanocarriers. Biomolecule loading inside pores of MSNPs as a function of pore size and surface functionalities is highly explored research topics during the recent decades. Adsorption was found to be the most widespread method for protein and nucleic acid loading in bare and surface functionalized MSNPs [219, 220]. For example, nucleic acid interactions with the surface can be divided into three parts: electrostatic interaction, solvent reorganization and water release, and H-bonding formation [65, 165]. Conversely, protein and enzyme attachment techniques into MSNPs include covalent bonding, encapsulation and adsorption. When proteins do not naturally adsorb onto silica surface through electrostatic interactions, surface functionalization of MSNPs is used to load

proteins [221]. Sometimes loading inside the pores also provides biomolecules the conformational stability against adverse surroundings [222]. Another prevalent technique is to encapsulate biomolecules during particle synthesis by the addition in sol-gel solution with the help of stabilizing agent such as sugars or liposomes [223, 224]. Sometimes amine to amine covalent linking is used to load molecules on to silica surface following post synthesis amine functionalization of silica surface.

Normally biomolecule loading by adsorption is quantified by solution-depletion methods by UV-vis or fluorescence spectroscopy, whereas recent advances also allow us to directly visualize them and measuring their transport inside the pores using confocal microscopy [46, 59, 225-228]. Protein loading can also be quantified using standard protein assays but this method is not always applicable to short chain peptides. Fluorescently labeled biomolecules allow quantification of localization and transport, whereas naturally fluorescent compounds can be measured for their activity and transport.

2.5.2.2 Protection from Enzymatic Hydrolysis

Once inside living organisms, biomolecule can be degraded by protective enzymes (proteases, nucleases, *etc.*) either in the bloodstream or inside cells, and an ideal biomolecule carrier should protect against this action. While pore end capping of MSNPs after biomolecule loading was explored for protection, cap opening at target site is a significant challenge [229]. On the other hand, pore size dependent protection from enzymatic hydrolysis is carried out by selecting a pore size large enough to accommodate selected biomolecules while blocking degradation enzymes' entry into the pore [220]. Pore size-dependent nucleic acid protection is presented schematically in **Figure 2.11**, which

shows that an optimum pore size (larger than nucleic acid molecular diameter but less than the size of nuclease molecules) is required for protection. Smaller pore size only allows adsorption on outer surface of the particles, whereas very large pores permit enzymes to enter into the pores, and in both of these cases adequate protection is not provided.

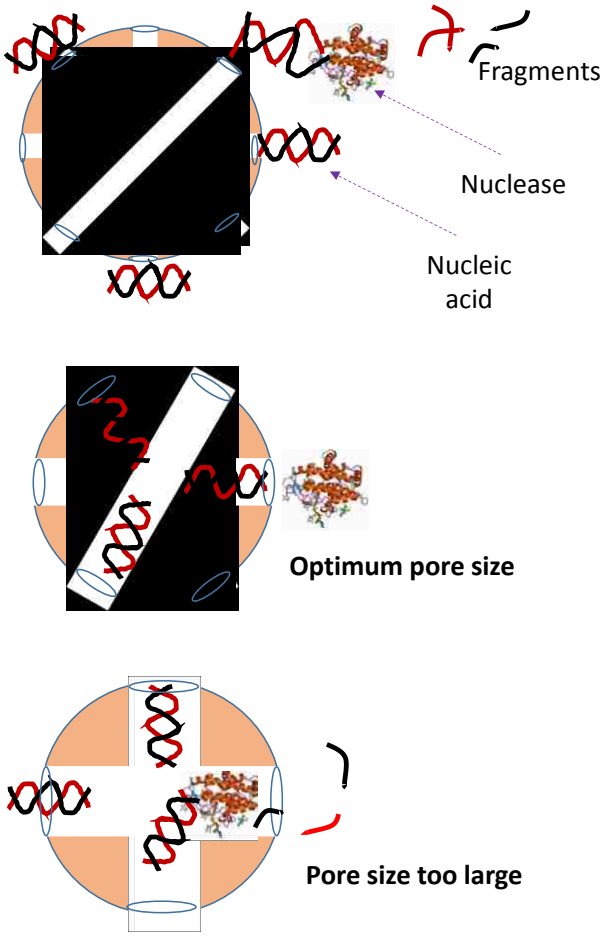

Figure 2.11 Schematic diagram of pore size dependent nucleic acid loading and protection from cellular enzymes.

2.5.2.3 Controlled and Targeted Intracellular Release

Release is the final step in the biomolecule delivery process that culminates a delivery process starting from nanoparticulate carrier design. Engineered MSNPs are potent controlled release carriers, in which controlled targeted release can be obtained by

pH, light, temperature, redox, competitive binding, biological inputs and chemical signal switched release [230]. Besides these single-responsive release systems, researchers have developed multiple responsive controlled release systems where two or more stimuli simultaneously trigger release [24]. Biomolecule release from bare MSNPs is highly dependent on the diffusional rate of drug release from the pores, so the pore structure and pore orientation are extremely important in designing MSNP-based delivery systems [18, 231-233]. However, non-functionalized MSNPs cannot block the pores to prevent premature drug release. Several surface engineering techniques have evolved to bind the molecule tightly or block the pores for cargo release upon responding to external stimuli. One strategy for controlled and targeted drug release is to use biodegradable polymeric drug carrier, where drug release is induced by hydrolytic degradation. Any surface functional group that has strong electrostatic interaction with a biomolecule slows down the release rate thus providing opportunity of a slow release, whenever needed [234]. Nucleic acids are primarily bound to MSNPAs using electrostatic interaction and surface bound nucleic acids are mobile, which should enable their release, with control based on loading quantity and surface functionalization. Double stranded (ds) RNA adsorption thermodynamics and its relationship to effective release will be explored further in **Chapter 7**.

CHAPTER 3. ADSORPTION AND RECOVERY OF POLYPHENOLIC FLAVONOIDS USING TiO_2 FUNCTIONALIZED MESOPOROUS SILICA NANOPARTICLES

3.1 Summary

Exploiting specific interactions with titania (TiO_2) has been proposed for the separation and recovery of a broad range of biomolecules and natural products, including therapeutic polyphenolic flavonoids which are susceptible to degradation, such as quercetin. Functionalizing mesoporous silica with TiO_2 has many potential advantages over bulk and mesoporous TiO_2 as an adsorbent for natural products, including robust synthetic approaches leading to high surface area, stable separation platforms. Here, TiO_2 surface functionalized mesoporous silica nanoparticles (MSNPs) are synthesized and characterized as a function of TiO_2 content (up to 636 mg TiO_2/g). The adsorption isotherms of two polyphenolic flavonoids, quercetin and rutin, were determined (0.05-10 mg/mL in ethanol), and a 100-fold increase in the adsorption capacity was observed relative to functionalized nonporous particles with similar TiO_2 surface coverage. An optimum extent of functionalization (approximately 440 mg TiO_2/g particles) is interpreted from characterization techniques including grazing incidence x-ray scattering (GIXS), high resolution transmission electron microscopy (HRTEM) and nitrogen adsorption, which examined the interplay between the extent of TiO_2 functionalization and the accessibility of the porous structures. The recovery of flavonoids is demonstrated using ligand displacement in ethanolic citric acid solution (20% w/v), in which greater than 90%

recovery can be achieved in a multistep extraction process. The radical scavenging activity (RSA) of the recovered and particle-bound quercetin as measured by 2,2-diphenyl-1-picrylhydrazyl (DPPH) radical scavenging assay demonstrates greater than 80% retention of antioxidant activity by both particle-bound and recovered quercetin. These mesoporous titanosilicate materials can serve as a synthetic platform to isolate, recover, and potentially deliver degradation-sensitive natural products to biological systems.

3.2 Introduction

The interaction of titania (TiO_2) with specific biomolecules (peptides such as histidine, catechols, dopamine, reactive dyes and various other nitrogen containing compounds) has been exploited for their analysis, separation and recovery [113, 235-238]. For example, concentration and subsequent analysis of phosphoproteins [239, 240], phosphopeptides [241, 242] and phospholipids [243] from mixtures has been achieved by exploiting the specificity of bidentate complexation of phosphates to TiO_2-based adsorbents. Similarly, the ability to selectively concentrate and separate some polyphenolic flavonoids (such as quercetin and its derivatives), presumably through bidentate coordination of the 3', 4'-dihydroxy (catechol) moiety with Ti, has also been demonstrated using bulk TiO_2 or TiO_2-functionalized platforms [15, 244, 245]. Designing processes for the recovery and delivery of therapeutic secondary plant metabolites, such as the anti-oxidant quercetin, is of particular interest on the basis of their anti-tumor, anti-thrombosis, anti-inflammatory, anti-cancer properties, and their applications to the reduction of oxidative stress and cardiovascular diseases [246-249]. The medicinal uses of quercetin and other secondary plant metabolites are of increasing interest due to recent advances in drug delivery that enhance their stability and bioavailability [250-252]. While TiO_2-based adsorbents can be used to recover compounds from plant extracts following conventional solvent extraction [253, 254], direct adsorption of polyphenolic flavonoids on TiO_2 nanoparticles in plant cell tissues suggests an alternative approach to metabolite recovery, a technique called “nanoharvesting” [15].

While bulk TiO_2 nanoparticles have been synthesized and demonstrated for biomolecule adsorption [236, 255], mesoporous TiO_2 nanomaterials with high surface area

are potentially a more efficient platform to achieve large scale biomolecule separation process. However, the synthesis of mesoprous TiO_2 nanoparticles is non-trivial due to rapid hydrolysis of TiO_2 precursors, uncontrollable crystallization during thermal treatment and structural breakdown at high temperature resulting in low specific surface area (~100 m^2/g) [256, 257]. To overcome this limitation of using TiO_2 alone, TiO_2 can be grafted onto mesoporous silica nanoparticles (MSNPs), which have high surface areas (> 600 m^2/g [258]), tunable pore structures and particle sizes, and are readily functionalized to tailor their surface properties. MSNPs are broadly applied in catalysis, chromatography, biomolecule loading, separation and drug-delivery based on advances in metal oxide synthesis and surface functionalization [29, 46, 59, 259]. To exploit the properties of hydrophilic silica nanoparticles for the recovery of hydrophobic plant metabolites, functionalization of silica with groups that specifically bind the metabolites is required [34, 260]. The current study combines the high surface area and controlled pore structure of MSNPs with the specificity of TiO_2 for polyphenolic flavonoids to design TiO_2-functionalized MSNPs (MSNPT) for biomolecule recovery.

Previous efforts to functionalize mesoporous silica with TiO_2 have primarily targeted the adsorption and photo-degradation of organic compounds such as pollutants [114, 258, 261, 262]. Thus, the incorporation of TiO_2 in MSNPs has involved high temperature calcination of the materials after composite formation to achieve maximum nanocrystalline anatase TiO_2, the most photo-catalytically active form. This crystallization process has the net effect of reducing the TiO_2 surface coverage. In contrast, highly dispersed amorphous TiO_2, which favors adsorption applications, can be obtained in the absence of calcination [263, 264]. In addition to post-synthesis surface modification,

alternative techniques for metal oxide incorporation in MSNPs include nanoparticle impregnation and metal oxide layer deposition inside the mesopores, processes that are complicated and expensive for the synthesis of bulk adsorbent materials [265-267]. In contrast, our laboratory has previously applied a TiO_2 functionalization procedure on nonporous Stöber silica nanoparticles (SNP, average particle diameter 450 nm) by following a modified version of the method reported by Hanprasopwattana et al. [268], in which TiO_2 was deposited on particle outer surface as a layer by one-pot hydrolysis of precursor titanium (IV) ethoxide (TEO) [244]. A maximum quercetin adsorption of 2 mg quercetin/g particle was observed at near-monolayer coverage for these TiO_2-functionalized SNPs (SNPT). Moreover, the radical scavenging activity of particle-bound quercetin was compared with that of free quercetin and the effect of binding with TiO_2 on quercetin activity was found to be minimal. However, desorption and recovery of active flavonoids from the TiO_2 functionalized surface was not investigated.

Here, TiO_2 functionalized mesoporous silica nanoparticles (MSNPT), broadly applicable as advanced adsorbents for biomolecules that interact with TiO_2 through bidentate binding, are synthesized and characterized with a goal of relating the extent of amorphous TiO_2 functionalization to TiO_2 accessibility and pore morphology. Specifically, the effects of functionalization on particle surfaces, pore order, and pore accessibility are studied by high resolution-transmission electron microscopy (HRTEM), grazing incidence small angle x-ray scattering (GISAXS) and nitrogen adsorption. Also, the amorphous nature of the incorporated TiO_2 (thought to indicate high dispersion for biomolecule adsorption) is confirmed by grazing incidence wide angle x-ray scattering (GIWAXS). For the model polyphenolic flavonoids, quercetin and rutin, the characterization techniques

were used to interpret the observed adsorption behavior as a function of extent of the TiO_2 functionalization. Solvent systems compatible with MSNPTs were developed for the recovery of flavonoid from the flavonoid-TiO_2 complexed nanoparticles using ligand displacement by ethanolic citric acid, expected to be a generalizable approach to biomolecule recovery. Specific to the stability concerns with flavonoids, the radical scavenging activity (RSA) of particle-bound and recovered quercetin shows the retention of activity throughout the adsorption and desorption steps.

3.3 Materials and Methods

3.3.1 Chemicals and Reagents

Tetraethyl orthosilicate (TEOS, 99%) and H_2O_2 (35 wt% in water) were obtained from Acros Organics; tri-block copolymer Pluronic F127 (bio-grade), quercetin (≥ 95%, HPLC grade), rutin (> 95%), citric acid (≥ 99.5%) and titanium (IV) ethoxide (TEO, technical grade) from Sigma-Aldrich; 2,2-diphenyl-1-picrylhydrazyl (DPPH, 95%) from Alfa-Aesar; cetyltrimethylammonium bromide (CTAB, 99.8%) from MP Biomedicals; ethyl acetate (≥ 99.5%) from EMD Millipore; acetone (≥ 99.5%) from BDH analytical; and Nochromix powder, titanium reference solution (1000 ppm in 10% HCl), ethanol (200 proof), acetonitrile (HPLC grade), methanol (HPLC grade), ultrapure deionized ultra-filtrated (DIUF) water, H_2SO_4 (95-98% in water), 12 N HCl (ACS grade), and 29.3 wt% NH_4OH solution from Fisher Scientific.

3.3.2 Mesoporous Silica Nanoparticle (MSNP) Synthesis

Ordered mesoporous silica nanoparticles were synthesized by a modified Stöber method based on the method of Kim et al. [69], where CTAB was used as a structure directing agent and TEOS and F127 as silica source and dispersing agent, respectively. Initially 0.5 g of CTAB and 2.05 g of F127 were dissolved in a mixture of 96 mL of DIUF water, 43.1 mL of ethanol and 11.9 mL of NH_4OH solution (29.3 wt%) and the solution was stirred until solutes dissolved completely. Then, 1.9 mL of TEOS was added to the solution and stirred vigorously for exactly 1 min at room temperature. The solution was then aged for 24 h without stirring at room temperature for complete silica condensation. The particles were removed from the solution using a high-speed centrifuge (Beckman-

Coulter) at 17,000 rpm and were washed 3 times with DIUF water and ethanol with intermittent centrifugation, and dried at 80 ºC in air overnight. Finally, template free silica particles were obtained by washing in 200 mL acidic ethanol (HCl, 1.5 M) for 24 h (acidic ethanol wash) followed by repeated centrifugation and washing with DIUF water and ethanol. Template free particles were dried overnight at 84 ºC.

3.3.3 Nonporous Stöber Particles (SNP) Synthesis

SNPs were synthesized according to the method reported by Bogush et al. [51]. 10 mL of DIUF water and 6.75 mL of 28.5% NH_4OH (0.5 M in ethanol) were added to 183 mL of ethanol. The solution was stirred for 5 min. Then, 7.6 mL of TEOS was added rapidly and the solution stirred for 24 h at room temperature. The particles were separated from the solution by centrifugation (17,000 rpm) followed by washing with DIUF water and ethanol 3 times. Finally, separated particles were dried in an oven at 84 ºC overnight**.**

3.3.4 TiO_2 Functionalization

MSNP were functionalized with TiO_2 according to a modified version of the method used by Schlipf et al. and originally reported by Hanprasopwattana et al., using TEO as the TiO_2 precursor [244, 268]. A 100, 400, 600, 900, 2000, or 2600 µL of TEO in 7.15 mL of ethanol were prepared in a nitrogen-filled glove bag. In a 250 mL round bottom flask, 500 mg MSNP was sonicated in 100 mL of ethanol for 15 min before 142.5 mL of ethanol was added and the solution in the round bottom flask was heated with continuous magnetic stirring. Once the solution started boiling, the previously prepared TEO solution and 1.62 mL of DIUF water were added to the flask and the solution was refluxed (78 ºC) for 1.5 h

under vigorous mixing. The particles were then removed from solution by centrifugation (17,000 rpm) and washed with ethanol 3 times. Final particles were washed in ethanol overnight to remove excess unbound TiO_2, and dried overnight at 84 ºC.

SNPs were functionalized by the same method as MSNPs but 100 μL or 600 μL of TEO were used instead. After functionalization, particles were centrifuged with repeated ethanol washing followed by overnight stirring in ethanol and drying overnight at 84 °C.

3.3.5 Nanoparticle Characterization

The morphology and shape of bare and functionalized particles were characterized using a Hitachi S-4300 Scanning Electron Microscope (SEM). The samples for SEM characterization were prepared by dispersing the particles onto double sided carbon tape attached to a 15 mm aluminum stub. Samples were dried in a desiccator for 24 h after excess silica materials were blown off with dry nitrogen gas. Prior to analysis, the samples were coated with Au-Pd alloy using an Emscope SC400 sputtering system. Average and standard deviation of particle diameters were calculated by considering 20 random particles analyzed using ImageJ Software. Transmission electron microscopy (TEM), high resolution (HR) TEM and scanning transmission electron microscopy (STEM) imaging were performed using a JEOL 2010F TEM at a voltage of 200 kV. Samples were prepared 3 days in advance by sonicating approximately 5 mg of particles in 2 mL of ethanol for 15 min. Then a lacey carbon 300 mesh copper grid (Ted Pella, 01895-F) was dipped into the particle solution for 2-3 seconds, briefly dried in air, and left in a desiccator for 3 days before analysis. Average pore diameter, pore size distribution and surface area were estimated from nitrogen adsorption conducted at -196 ºC using a Micromeritics TriStar 300

instrument. Samples were degassed at 135 ºC for a minimum of 4 h under flowing dry N_2 gas before the adsorption experiment. The specific surface area was estimated using the Brunauer, Emmett and Teller (BET) isotherm, and average pore diameter and pore size distribution were estimated by the method of Barrett, Joyner and Halenda (BJH) using the adsorption branch. Micropore volume and external surface area were estimated using the method described in Jaroniec et al. [269]. To confirm the successful removal of surfactant from MSNP pores, Fourier transform infrared (FTIR) spectroscopy was conducted using a Thermo Nicolet Nexus 470 with a deuterated triglycine sulfate (DTGS) detector before and after acidic ethanol wash. For the analysis, 0.5 g of anhydrous KBr was mixed with particles (0.5-1.0 wt %) and the mixture was crushed using a mortar and pestle. A small amount of sample was pressed in a die until it became a translucent, rigid pellet. The pellet was then placed in a FTIR pellet holder, purged with dry nitrogen, and a spectrum collected in transmission mode. Energy dispersive x-ray spectroscopy (EDS) elemental mapping were carried out for MSNPT using a Zeiss EVO MA-10 SEM. The samples for EDS measurements were prepared using exactly the same method as SEM samples, but 12.7 mm aluminum stubs were used instead of 15 mm. A Bruker-AXS D8 Discover diffractometer at a x-ray wavelength of 1.54 Å (scanning speed of 0.5 °/min in 2θ increments from 1.5º to 6º) was used to perform low angle XRD analysis after putting the particles in a powder sample holder and tapping flat with a spatula. The data was analyzed with the Bruker Diffrac-Suite software.

The grazing incidence small-angle x-ray scattering (GISAXS) and grazing incidence wide angle x-ray scattering (GIWAXS) patterns of particles were collected in order to determine the mesostructure and crystallinity of incorporated TiO_2. GISAXS and

GIWAXS experiments were conducted separately at the Advanced Photon Source at Argonne National Laboratory at beamline 8-ID-E using an x-ray wavelength of 1.148 Å (10.82 keV) [270]. Nanoparticle samples were prepared 3 days in advance by sonicating 5 mg of particles in 2 mL of water and dispersing the solution on a borosilicate glass slides (Fisher Scientific) cleaned with Nochromix solution, prepared by following the instructions of the supplier. The samples were mounted on the sample holder and the holder was put in a vacuum chamber. X-rays were allowed to enter the chamber through a mica window and was incident on the samples. Scattered x-ray exited the chamber through a Kapton window and data were collected with a Pilatus 1M pixel array detector for 10 sec exposure time. The sample to detector distance was 2185 and 228 mm for GISAXS and GIWAXS, respectively. GISAXS and GIWAXS patterns were collected at 0.20° and 0.17° incident angle, respectively, at room temperature. The beam size was 100 μm × 50 μm (H×V) and 200 μm ×20 μm (H×V) for GISAXS and GIWAXS, respectively. Images were corrected for detector nonuniformity and converted to *q*-space using the GIXSGUI package for MATLAB [271]. Integrated profiles of x-ray intensity vs. *q* were computed from the 2D GISAXS and GIWAXS patterns after integration along the polar angle in the detector plane (ϕ) using the GIXSGUI package.

3.3.6 Chemical Analysis of Titanium Content

The amount of TiO_2 on the functionalized particles (both MSNP and SNP) surface was quantified by a sulfuric acid / hydrogen peroxide assay [244, 272]. 25 mg of TiO_2-functionalized particles were mixed vigorously with 25 mL of 2 M H_2SO_4 for 20 min at 90 ^oC and then the solution was filtered through a PTFE syringe filter (0.02 μm). 1μL of H_2O_2

solution was added to 1 mL of the resulting filtrate, and the mixture was allowed to sit. After 10 min, the absorbance of the resultant yellow solution was measured using a BioTek (Winooski, VT) plate reader at 407 nm. The absorbance was compared with a calibration curve previously prepared with titanium reference solution, to find the amount of TiO_2 on silica particles. Particles were named according to the measured amount of TiO_2 (mg/g particle) for convenience, *i.e.* when X mg TiO_2 is present per g MSNP, it is called MSNPT-X and Y mg TiO_2 is present per g SNP, it is called SNPT-Y. To quantify the potential leaching of TiO_2 from the functionalized MSNPs into solution during quercetin recovery, fuming sulfuric acid was added to particle free solution to achieve a final solution concentration of sulfuric acid of 2 M. After 30 min of digestion, the amount of TiO_2 in solution was determined by UV-Vis spectrophotometry by the same method used after particle dissolution in 2 M H_2SO_4.

3.3.7 Flavonoid Adsorption

Adsorption of flavonoids quercetin and rutin on MSNPTs was measured by following similar procedure used by Schlipf et al. [244]. The UV-Vis absorbance of quercetin and rutin (371 and 369 nm, respectively) in ethanol was used to quantify the concentration of flavonoids in solution. For adsorption experiments, 25 mg of particles were pre-wetted under vortex mixing in a series of 2 mL centrifuge tubes with 1 mL of ethanol for 24 h, centrifuged for 5 min at 17000×G in an AccuSpin Micro 17 centrifuge (Fisher Scientific) and supernatants were discarded. Then, 1 mL of flavonoid solutions in ethanol (0.05-10 mg/mL) were added to these pre-wetted particles. After vortex mixing for 24 h in the dark, the particles were centrifuged again and 200 µL of supernatant was

analyzed using the plate reader. The initial flavonoid solution was also analyzed in the same way and a calibration curve was plotted, which was used to find the amount of adsorbed flavonoid on to the particle surface by solution depletion using **Equation A.1 (Appendix A)**.

3.3.8 Quercetin Recovery from MSNPs

Quercetin loaded particles were re-suspended in 1 mL of different solvents (ethyl acetate, acetone, acetonitrile, 1% w/v HCl in ethanol, 1% w/v HCl in methanol and 1-40% w/v citric acid in ethanol) intended for quercetin recovery. After 24 h of vortex mixing, the particles were centrifuged and the supernatant was analyzed in the well plate reader by same method as adsorption. The amount of quercetin retained on the particles and percent recovery was estimated by subtracting the recovered amount from the initial amount of quercetin present on the particle using **Equation A.2** and **A.3**.

3.3.9 Activity Determination for Free, Particle Bound and Recovered Quercetin

The activity of quercetin in ethanol solution (fresh quercetin), was determined by mixing 100 µL of quercetin solution in ethanol (0-0.5 mg/mL) with 1 mL of 2,2-diphenyl-1-picrylhydrazyl (DPPH) solution (0.1 mg/mL) in ethanol in 2 mL vials. The vials were covered and after 10 min of reaction in the dark, the absorbance was measured at 517 nm (DPPH solution absorbance peak). The initial DPPH absorbance was measured by adding 100 µL of ethanol with 1 mL of DPPH solution (0.1 mg/ml). Radical scavenging activity (RSA) was calculated from the percent decrease in DPPH absorbance according to **Equation A.4**. The activity of quercetin recovered from MSNPTs in 20% w/v ethanolic citric acid solution (recovered quercetin) was measured by an identical procedure, where

the quantity of quercetin in the ethanolic citric acid solution was known (**Section 3.3.8**). Control experiments were performed with only ethanolic citric acid solution (20% w/v) to demonstrate that citric acid in ethanol does not possess any RSA. For RSA measurement of particle-bound quercetin, quercetin-containing particles with a known amount of quercetin were dispersed in ethanol (1 mL) by sonication so that the final concentration of quercetin in the particle solution is known. 100 µL of the particle solution was added to DPPH solution and activity of particle bound flavonoid was measured using the same method. RSA of MSNPTs (without quercetin) were also measured for comparison and the activities of recovered and particle-bound quercetin reported relative to the corresponding amount of fresh quercetin. Adsorption, desorption and activity measurements were performed in triplicate.

3.4 Results and Discussion

3.4.1 Material Characterization

MSNPs were synthesized by a modified Stöber method using CTAB as structure directing compound, and TEOS and pluronic F127 as silica precursor and dispersing agent, respectively. Successful removal of the surfactants was confirmed by FTIR analysis (**Appendix Figure A.1**). The disappearance of CH_2 stretching bands (2800-3000 cm^{-1}) from CTAB after acidic ethanol washing indicates the complete removal of the surfactant. Specific surface area, average pore diameter and pore volume of the particles were determined using nitrogen adsorption (**Table 3.1**). The average pore diameter was 2.8 ± 0.23 nm, which is in the expected range of literature values when CTAB is used as structure directing agent [273]. The specific surface area determined by the BET method was 950 ± 51 m^2/g and the BJH pore volume from the adsorption branch was 1.21 ± 0.09 cm^3/g for non-functionalized MSNP.

Table 3.1 BET specific surface area, BJH pore volume and average pore diameter of TiO_2 functionalized and non-functionalized mesoporous silica nanoparticles.

Particle Type	**BET Surface Area (m^2/g)**	**BJH Pore Volume (cm^3/g)**	**Average Pore Diameter (nm)**
MSNP	950 ± 51	1.21 ± 0.09	2.8 ± 0.23
MSNPT-59	850	1.03	2.6
MSNPT-140	790	0.81	2.5
MSNPT-162	780	0.77	2.4
MSNPT-270	640	0.57	2.4
MSNPT-425	630	0.59	2.2
MSNPT-636	260	0.23	2.1
SNP	16	-	-

Following template removal, MSNPs were functionalized with TiO_2 by the hydrolysis of TEO, yielding MSNPTs. Different degrees of functionalization were

achieved by varying the amount of TEO. The quantity of grafted TiO_2 on the MSNP surface was determined following chemical dissolution of the particles, and by EDS elemental analysis of the MSNPTs (results reported in **Appendix Table A.1**). Both methods agree within statistical limits, but EDS measurements had greater uncertainty. Thus, the reported extents of TiO_2 functionalization are based on the bulk measurement of TiO_2 content determined from chemical analysis (see **Section 3.3.6** for the naming convention of functionalized particles).

The amount of TiO_2 incorporated on the particles (mg TiO_2/g particle) after functionalization are reported in **Figure 3.1**. An approximately linear relationship between the amount of TEO used and degree of functionalization on nonporous silica particles (SNPs) has been observed previously [244] and appears to describe the extent of functionalization of MSNP up to 4.3 g TEO/g particle. A greater degree of functionalization is found for 5.7 g TEO/g particle.

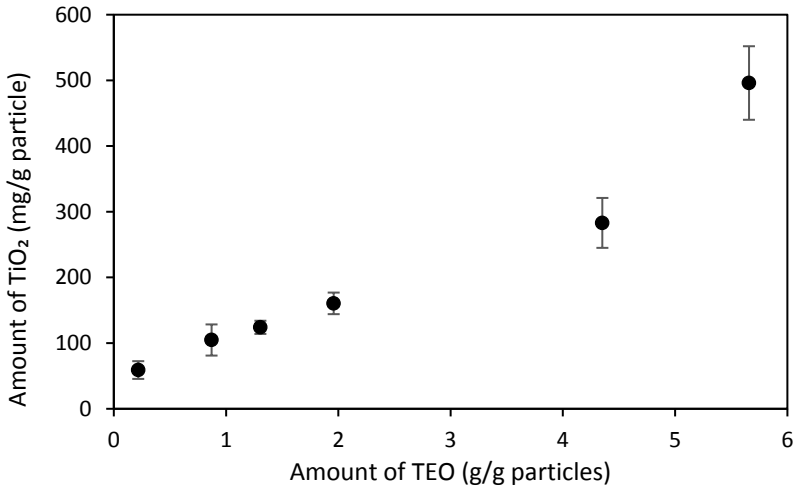

Figure 3.1 Amount of TiO_2 grafted onto MSNPTs as a function of the amount of precursor (TEO) used for functionalization. Results were measured in triplicate by chemical analysis of dissolved MSNPTs.

The effect of the degree of TiO_2 functionalization on particle morphology was examined using scanning electron microscopy (SEM). MSNPs before and after TiO_2 functionalization were spherical in shape (**Appendix Figure A.2**). Changes in the average diameter of the MSNPs with functionalization were within the batch to batch variation of the synthesized MSNPs, with an initial diameter of 165 ± 19 nm (**Table A.1**). From TEM images of bare and functionalized particles (**Figure 3.2**), nonfunctionalized MSNPs show highly ordered cubic structures. This ordered mesostructure was also visible for lower degree of functionalization (MSNPT-59 and MSNPT-110), but is not apparent with higher incorporation of TiO_2 in the nanostructures (MSNPT-270 (**Figure 3.2d**) and greater). Starting with MSNPT-110, increasing TiO_2 functionalized resulted in increasing nanocrystal growth at the exterior of the nanoparticles. In the case of MSNPT-636 (**Figure 3.2e**), a continuous outer layer of TiO_2 is observed. The size of the nanocrystals was observed to increase with increasing TiO_2 functionalization, as determined by high resolution (HR) TEM (**Appendix Figure A.3**). Dark-field STEM, in conjunction with EDS spectral line scan was used to further verify the uniform distribution of TiO_2 inside the particles (**Appendix Figure A.4** for MSNPT-110). Although uniformly distributed, the presence of the outer nanocrystals/layer complicates a straightforward quantification of TiO_2 only inside the mesopores. The effect of porosity on functionalization was examined by incorporating TiO_2 on the surface of nonporous SNPs (190 ± 30 nm), at both 5.4 mg and 13.7 mg of TiO_2/g particles. At similar grafting conditions, the nonporous particles incorporated an order of magnitude less TiO_2 than MSNPs (**Appendix Figure A.5**). TEM images for SNPT-13.7 shows no nanocrystal growth for nonporous particles (**Figure 3.2f**)

or corresponding increase in particle diameter, and the smoothness of the surface of SNPT-13.7 was verified using HRTEM (**Appendix Figure A.6**).

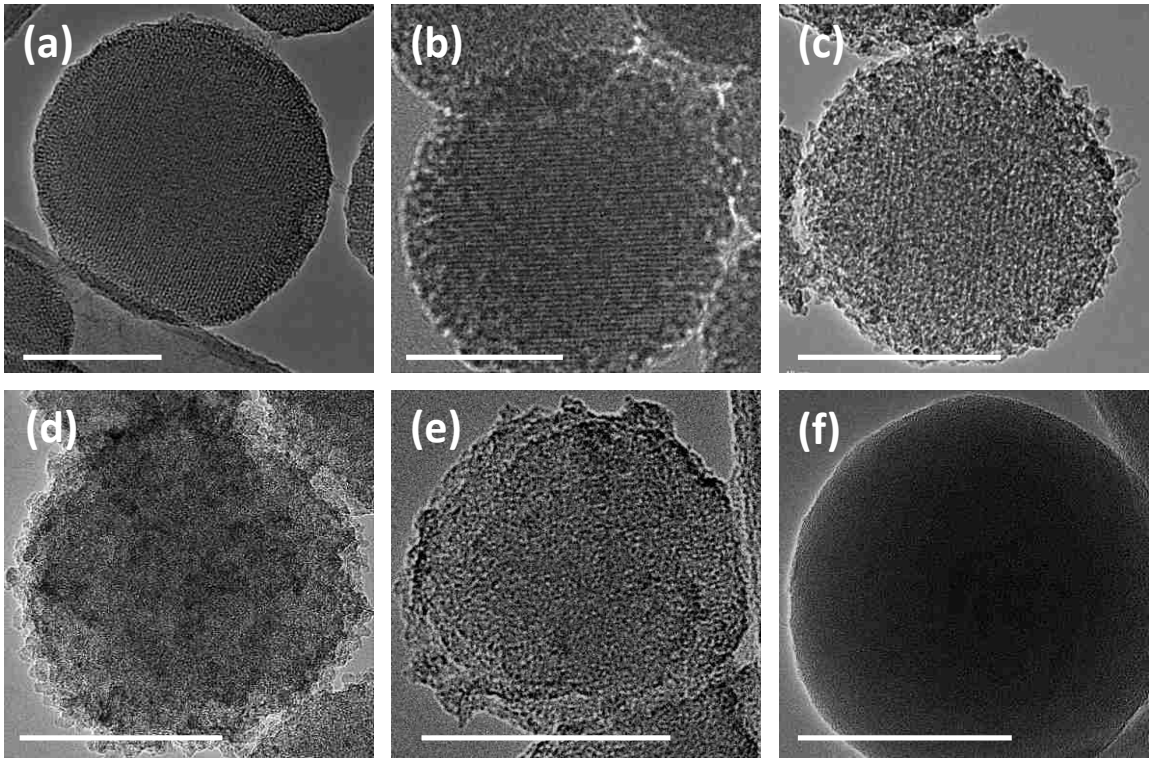

Figure 3.2 TEM images of (a) bare MSNP, (b) MSNPT-59, (c) MSNPT-110, (d) MSNPT-270, (e) MSNPT-636 and (f) SNPT-13.7 (scale bar = 100 nm for all images).

The analysis of surface area, pore properties and TEM images of MSNPTs provide a consistent picture of the effect of increasing TiO_2 grafting in these porous materials. N_2 sorption analysis of the MSNPTs indicates that the surface area, average pore diameter, and pore volume decrease with increasing TiO_2 loading (**Table 3.1**). **Figure A.7a** shows that the N_2 sorption isotherm for MSNP is a type IV isotherm with clear capillary condensation, which indicates uniform mesoporosity [69]. The capillary condensation step was retained for MSNPT-59, but for all other MSNPTs, a sharp capillary condensation step was not evident, consistent with broadening and a reduction in total pore volume in the pore size distributions (**Figure A.7b**). Standard reduced adsorption (α_s) plots drawn using

literature procedures [269, 274] (**Figure A.7c)** indicate no micropores (< 2 nm [274]) in any MSNPTs, and the external surface area decreases gradually with increasing TiO_2. The gradual reduction in surface area and pore diameter and absence of microporosity with increasing functionalization are consistent with monolayer-like coverage in the pores, and the TEM images of MSNPT-110 (**Figure 3.2c**) indicates uniform incorporation of TiO_2 inside of its mesopores. **Table 3.1** also shows that BET surface area and BJH pore volume decrease dramatically for MSNPT-636 (to 255 m^2/g and 0.23 cm^3/g) after decreasing gradually up to MSNPT-425 (to 629 m^2/g and 0.59 cm^3/g). From TEM images (**Figure 3.2e**), we can see that a full layer of TiO_2 encapsulates MSNPT-636, leading to a large drop in pore accessibility. Prior studies of TiO_2 loading onto mesoporous silica mostly used high temperature calcination to obtain anatase TiO_2, but consistent with our observations, they show that surface area, pore size and pore volume decrease with higher TiO_2 loading [258, 261, 275]. Complete encapsulation with a high amount of amorphous TiO_2 loading is surprising, and has not previously been reported for anatase TiO_2, even when use of a large amount of precursor (10 g per g particles) caused a precipitous drop in surface area (987 to 157 m^2/g), as reported by Chendrowski et al. [276].

Mesostructure disruption within mesoporous silica after anatase TiO_2 loading has been reported based on a reduction in intensity of the small angle XRD peak after loading [258, 272, 275]. Here, only low temperature treatments were used, and GISAXS experiments were conducted to observe the effects of amorphous TiO_2 loading on mesopore ordering. **Appendix Figure A.8** shows GISAXS patterns of MSNPs before and after functionalization with different amounts of TiO_2. For bare MSNP, the GISAXS

pattern shows concentric semicircular rings of uniform intensity (also inset of **Figure 3.3a**) as expected for a layer of isotropically oriented particles on the glass substrate.

Integrated 1D patterns were extracted from 2D GISAXS images by angular integrating ($0^o < \phi < 180^o$) using GIXSGUI MATLAB software, and intensity was plotted as a function of the magnitude of the scattering vector q in **Figure 3.3a**. The integrated GISAXS profile for MSNPs showed diffraction peaks at $q = 0.18$ Å^{-1} and 0.21 Å^{-1}, indexed to the (211) and (220) reflections, which in conjugation with the small angle XRD profile (**Appendix Figure A.9**, indexed as 211, 220, 321, 400, 420 and 332 reflections) indicative of a Ia$\bar{3}$d cubic mesoporous structure [277], (**Figure 3.3a**) consistent with other reports of cubic mesostructure prepared using CTAB [69]. GISAXS peaks diminish in intensity gradually with increasing TiO_2 loading. This may be caused both by a reduction in contrast between silica framework and (TiO_2-coated) pores, and a reduction in long-range order. The curve for MSNPT-59 is similar to MSNP, except with broader peaks and smaller d-spacing. MSNPT-110 is a mixture of poorly resolved phases (two broad peaks overlapping) and no mesophase could be assigned at higher TiO_2 loadings (**Figure 3.3a**). Peak broadening indicates that the coherence length contributing to scattering decreases with increasing TiO_2 functionalization. The average number of layers contributing to a diffraction peak, N, was quantified by Scherrer analysis adapted to GISAXS [278]. For MSNP, N was calculated to be 29, while N decreased to 16 for MSNPT-59, and even further (N = 12) for higher functionalization (MSNPT-110 and higher). Although the presence of TiO_2 reduced diffracted intensity for higher functionalization (> MSNPT-59), cubic structures are assumed for quantification of structural properties for all particles.

The d-spacing, lattice constant and pore wall thickness calculated from GISAXS peaks and BJH pore diameter for MSNP and MSNPTs are presented in **Appendix Table A.2**. The reduction in coherent scattering length and d-spacing suggests some degree of restructuring of the silica matrices during the solvothermal functionalization process. The estimated wall thicknesses calculated for cubic mesostructures [69] were validated by measuring them directly from TEM images as shown in **Appendix Figure A.10** and were in good agreement. The cubic lattice constant and pore wall thickness decrease gradually with increasing TiO_2 functionalization (**Appendix Table A.2**). Since all MSNPTs underwent the same hydrothermal treatment but different pore sizes and wall thicknesses were found, the changes in these characteristics were caused by the presence of TiO_2, which is consistent with TiO_2 being deposited into the mesopores of the MSNPTs.

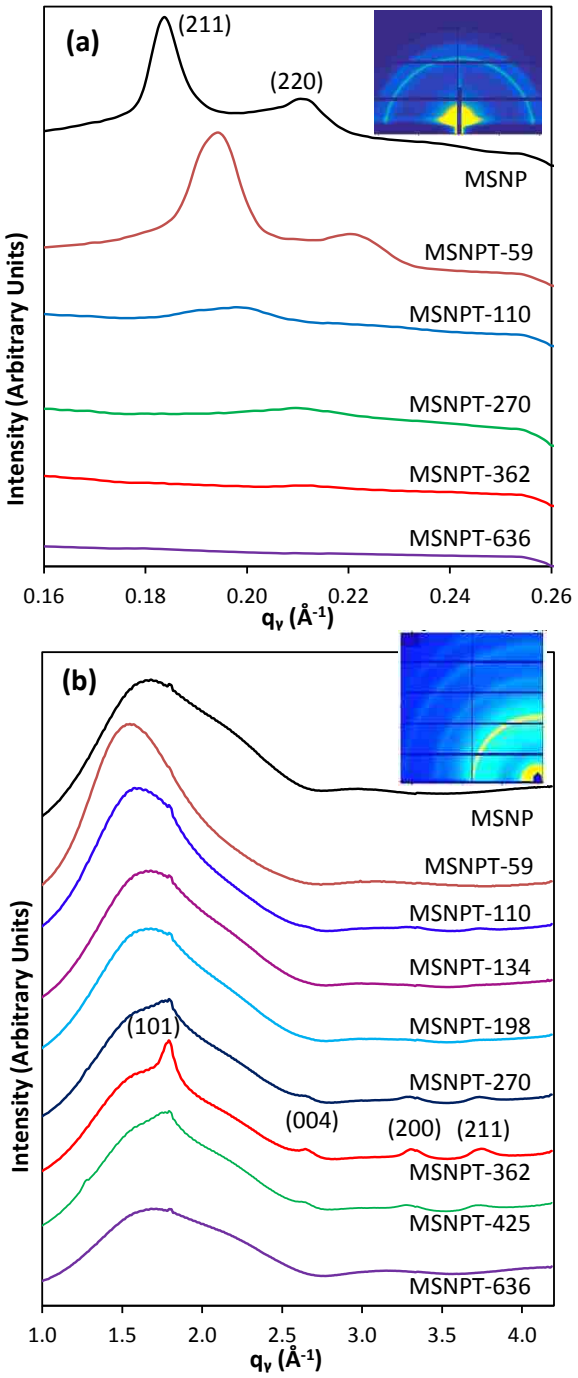

Figure 3.3 Integrated data from (a) GISAXS and (b) GIWAXS pattern (incident angles, α_i = 0.20º and 0.17º, respectively) showing change of mesostructured and crystallization of MSNP after TiO_2 functionalization. The insets show (a) the 2D GISAXS pattern of non-functionalized MSNP and (b) 2D GIWAXS pattern of TiO_2 functionalized MSNP with highest crystallization (MSNPT-362). Miller indices are for (a) cubic mesostructure and (b) anatase TiO_2 crystalline phase, respectively.

Among possible modes of metal oxide incorporation into mesoporous materials, formation of a dispersed amorphous oxide layer inside the mesopores is highly desirable for biomolecule adsorption, but difficult to synthesize and characterize [264, 265]. In order to ensure maximum dispersed phase, we identified and evaluated the crystalline phase of TiO_2 after functionalization using GIWAXS. Although TEM images indicate some TiO_2 nanocrystallites in MSNPT-110 (**Figure 3.2c** and **Figure A.3b**), 2D GIWAXS patterns (**Appendix Figure A.11**) do not indicate significant crystallinity up to MSNPT-198, suggesting that those samples contain primarily amorphous TiO_2. With increasing TiO_2 functionalization, GIWAXS crystallinity was first found for MSNPT-270, intensified for MSNPT-362 and diminished slightly for MSNPT-425. For MNSPT-636, no crystallinity was detected. This observation is in contrast with the literature involving anatase TiO_2 loading on mesoporous silica, where crystallinity generally continues to increase with increasing TiO_2 [258, 261, 262, 272]. Integrated GIWAXS patterns are presented in **Figure 3.3b**. The broad feature in the GISAXS profiles from $1.0 \leq q_y \leq 2.6$ is from amorphous material combined with the borosilicate glass slide (**Appendix Figure A.12**). The integrated profiles for MSNPT-270, 362 and 425 contain sharp diffraction peaks at q values of 1.79 $Å^{-1}$, 2.66 $Å^{-1}$, 3.30 $Å^{-1}$ and 3.73 $Å^{-1}$, indexed to the (101), (004), (200) and (211) planes of anatase TiO_2, respectively [279]. GIWAXS analysis of SNPT showed no crystallinity for any degree of functionalization (data not shown), indicating that crystalline TiO_2 is able to form at the exterior of MSNPT at high loadings due to the presence of mesopores.

Average crystallite size was calculated using the Scherrer equation modified for an area detector as described by Smilgies [278]. The average nanocrystal sizes were estimated

to be 7.4 nm, 10.3 nm and 6.2 nm for MSNPT-270, MSNPT-362 and MSNPT-425, respectively. Since the calculated average nanocrystal size is larger than the average pore diameter of bare MSNP and no crystallinity was detected for the highest loading (636 mg TiO_2/g particles), anatase TiO_2 formed only on the outer MSNP surface. In contrast, TiO_2 deposited inside the mesopores (*e.g.* MSNPT-59, **Figure 3.2b**) is not crystalline and perfectly suitable for biomolecule adsorption.

3.4.2 Flavonoid Adsorption on MSNPTs

The effect of extent of functionalization on the performance of the MSNPTs as adsorbents for biomolecules was examined for the model system of quercetin, a plant-derived polyphenolic flavonoid which is capable of bidentate binding with TiO_2 *via* the catechol moiety, resulting in a color change upon binding [15]. Binding of a second plant-derived flavonoid, rutin (quercetin-3-o-rutinoside, **Appendix Figure A.13**), was also investigated to understand the effect of glycosylation. Flavonoid adsorbed on MSNPTs was quantified by solution depletion and adsorption isotherms constructed as a function of equilibrium concentration. **Figure 3.4** presents the adsorption results for both quercetin and rutin on MSNPT-86 per g particle. The isotherms exhibit saturation behavior, as described by Langmuir isotherms (**Equation A.5** and summarized in **Table A.3**), where q_m accounts for maximum monolayer sorption and K_L accounts for solute-solid binding affinity. Similar binding constants were determined for quercetin and rutin adsorption on MSNPT-86 (K_L of 10.6 mL/mg and 13.2 mL/mg, respectively). This similarity is consistent with literature indicating that flavonoids do not use the 3-hydroxy group in the C-ring (where rutin is glycosylated) for TiO_2 chelation [280], unlike some other metal

complexation (*i.e.* quercetin-Ag chelation reported by Jurasekova et al. [281]). The maximum loading of rutin was approximately 40% of that of quercetin on a molar basis, which may reflect its larger size and therefore the larger surface area it occupies relative to quercetin. Given that the isotherms suggest a similar mechanism of binding of the two flavonoids, quercetin is the focus of the remaining binding studies.

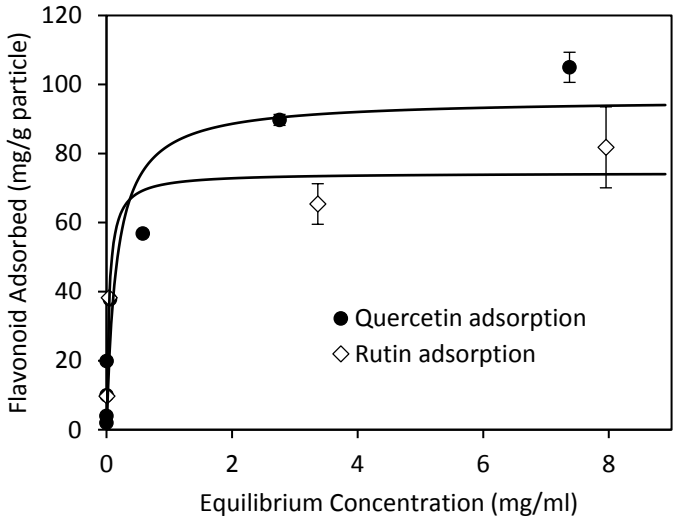

Figure 3.4 Comparison between quercetin and rutin adsorption isotherms for MSNPT-86 (data points and solid line represent experimental values and corresponding Langmuir fit, respectively).

Quercetin adsorption isotherms on MSNPT of varying TiO_2 content are presented in **Figure 3.5a**. Bare silica nanoparticles have very little affinity towards hydrophobic polyphenolic flavonoids (maximum capacity 0.7 mg quercetin/g particle). The adsorption capacity of the particles increases steadily with the grafted TiO_2 amount up to a maximum of 232 mg quercetin/g particle for MSNPT-440 (**Figure 3.5a**). Beyond this TiO_2 content (*i.e.,* MSNPT-636), the specific adsorption capacity decreased consistent with the reduction in accessible surface area. The maximum quercetin loading observed for MSNPT-440 is about 100 times the value reported for nonporous SNPT [244], and is

attributed to the high dispersion of TiO_2 over a large surface area in MSNPT. When the quercetin capacity is normalized by the specific surface area of the particles (**Figure 3.5b**), the areal capacity is found to increase with TiO_2 loading up to MSNPT-440, and then to decrease for MSNPT-636. Normalizing the adsorption capacity by the amount of TiO_2 grafted provides a measure of the accessibility of the TiO_2. The adsorption capacity per mass of TiO_2 on particle surface decreases with increasing loading (**Figure 3.5b**). This trend is consistent with the morphology of TiO_2 present in the MSNPTs, going from well dispersed monolayers to surface-bound nanocrystals to a pore blocking layer as TiO_2 loading increases, which is also evident from **Figure A.14 (**normalization by both surface area and TiO_2 amount). The adsorption isotherms for MSNPT were fit with the Langmuir model and the best-fit parameters are presented in **Appendix Table A.3**. The binding constant, K_L, found for MSNPT-59 is 8.8 mL/mg, and increases with TiO_2 loading up to 21.1 mL/mg for MSNPT-162. This is consistent with strong binding of quercetin with the highly dispersed amorphous TiO_2 present at loadings below 200 mg/g. For higher functionalization (MSNPT-362 or higher), the binding affinity is lower, even though capacity continues to increase up to a maximum at MSNPT-440. This lower affinity can be explained by more of the TiO_2 in these materials being present in crystallites and encapsulating layers that bind quercetin less efficiently.

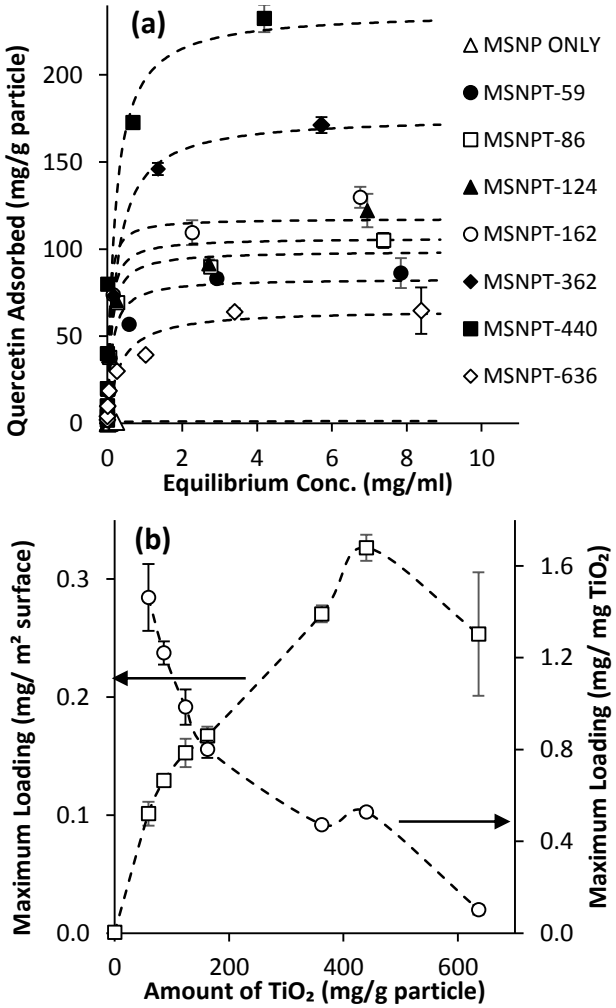

Figure 3.5 Quercetin adsorption isotherms and Langmuir model fitting on TiO_2 functionalized MSNP: (a) measured quercetin adsorption isotherms (points) for MSNPT with varying TiO_2 content and corresponding Langmuir fits (dashed curves), and (b) maximum areal quercetin loading (open squares) and quercetin loading per TiO_2 (open circles) with curves as visual guides.

The role of porosity on TiO_2 functionalization and subsequent quercetin binding can be examined by comparing the adsorption behavior of flavonoids on MSNPTs with that of SNPTs reported by Schlipf et al [244]. Given the small surface area of SNP (**Table 3.1**), it is not surprising that specific quercetin adsorption of SNPT particles is much lower than that of MSNPT. However, the areal capacities for quercetin reported by Schlipf et al. increase with TiO_2 loading from 0.09 mg/m^2 to 0.27 mg/m^2, and the capacity per TiO_2

values decrease from 1.7 to 0.17 mg quercetin/mg TiO_2 [244]. Both ranges and trends are similar to those found in **Figure 3.5b** but absolute magnitudes are much greater due to the high surface areas of the MSNPT samples. MSNPTs also showed 10 times greater flavonoid adsorption capacity compared to a recent report using mesoporous amine-functionalized silicates [282] because of the superior binding capability of TiO_2 for flavonoids compared to amines [244]. For flavonoid adsorption, there is a trade-off between increasing capacity by adding TiO_2 to the surface and losing capacity by aggregation of and pore blocking by excessive TiO_2. These factors lead to the maximum in specific capacity in **Figure 3.5a**.

3.4.3 Quercetin Recovery from MSNPTs

The Langmuir parameters, K_L in **Table A.3** indicate a strong interaction between TiO_2 and flavonoids when adsorbed from ethanol – on the order of 10^4 mL/mmol for well-dispersed samples containing less than 200 mg TiO_2/g and 10^3 mL/mmol for higher TiO_2 loading. This is very useful for harvesting of flavonoids, but to design a successful flavonoid isolation process, an approach to recovery has to be developed. In addition, quercetin is potentially unstable and susceptible to activity loss depending on the solvent used [254]. Solvents such as ethyl acetate, acetone, acetonitrile and acidic (HCl) alcohol that were used to recover polyphenolic compounds from other solid matrices [283-285] might not be able to displace strongly bound flavonoids from TiO_2. Moreover, while addition of HCl can be used for extraction from non-metal matrices, it has the potential to leach TiO_2 from MSNPTs [286]. Hence, an alternative compatible solvent system for quercetin desorption from TiO_2 was sought. Zhao et al. studied rutin extraction from plant

sources using deep eutectic solvents, and reported that those containing citric acid exhibited efficient extraction [287]. Also, as a biocompatible ligand, citric acid binds with metal oxides such as TiO_2 without causing TiO_2 leaching in a wide range of pH (2.0 to 7.5) [288, 289]. Thus, it can be hypothesized that citric acid, being a polydentate ligand with strong chelating capability with TiO_2, can aid flavonoid recovery process by displacing flavonoids from the particle surface without leaching TiO_2. Also, adsorption of citric acid on TiO_2 is a strong function of solution pH, with highest adsorption (> 0.25 mg/m^2 surface) found at pH 2.0 [288]. Thus at low pH (2.0-3.0) citric acid will have the most potential to displace flavonoids from the TiO_2 surface.

When several polar organic solvents were screened at 1 mL/25 mg of quercetin-bound MSNPTs, very small flavonoid recovery was obtained (< 5%) as seen in **Figure 3.6a**. Acidic methanol and ethanol increased recovery, but in the case of acidic ethanol, the solution turned reddish orange instead of the light yellow color of dissolved quercetin. The most likely cause for this color shift was leaching of quercetin-bound Ti^{4+} which is known to produce a reddish orange complex [15, 244]. When MSNPTs were tested for TiO_2 leaching in acidic ethanol, 9 mg TiO_2/g particle was leached from MSNPT-270 after 24 h of mixing. The peak for quercetin in the UV-vis spectrum after acidic ethanol recovery (**Appendix Figure A.15)** showed a significant red shift due to Ti complexation. On the other hand, citric acid did not produce measurable TiO_2 leaching from MSNPT, and no shift was observed in the position of the UV-vis peak of the quercetin recovered by ethanolic citric acid (**Appendix Figure A.15**), consistent with no TiO_2 leaching.

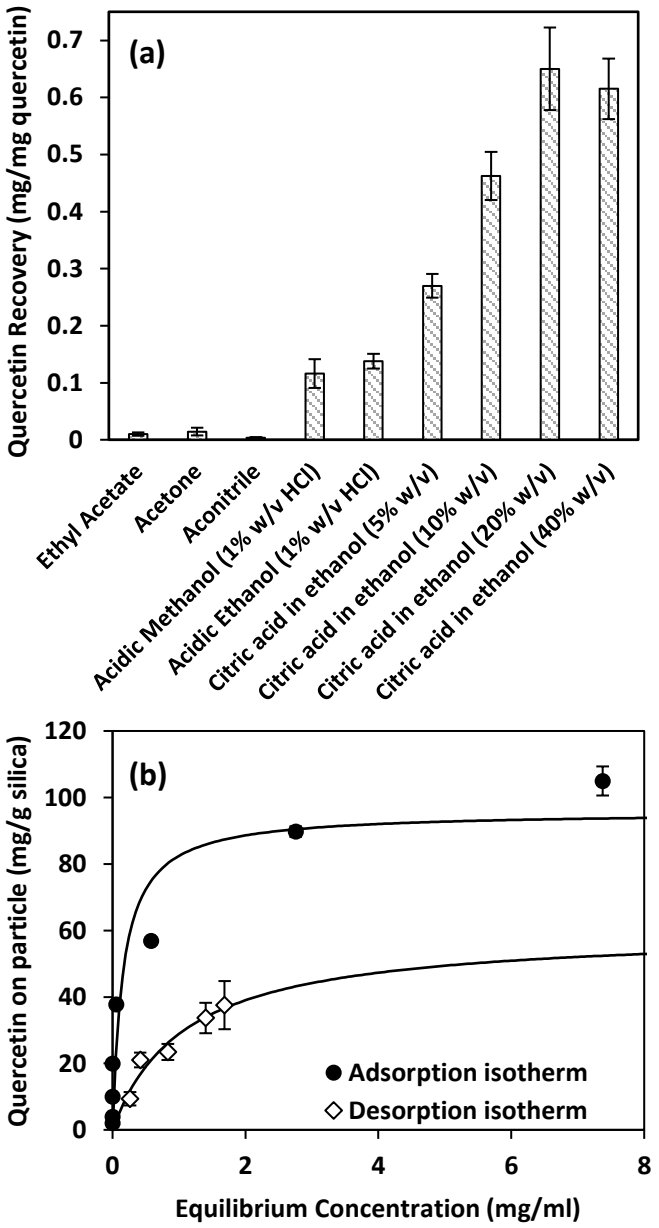

Figure 3.6 Recovery of quercetin from TiO_2 functionalized MSNP (MSNPT-86) using various solvents: (a) Comparison of recovery using different solvents when 1 mL was used for 25 mg quercetin adsorbed particles, and (b) Quercetin desorption isotherm in 20% w/v ethanolic citric acid solution compared to adsorption isotherm from ethanol solution (points and curves represent experimental data and Langmuir fit respectively).

When 1 mL of ethanolic citric acid solution was used at pH 2-3 for quercetin desorption from 25 mg of MSNPT-86 after saturation adsorption, **Figure 3.6a** shows that quercetin recovery (estimated using **Equation A.3**) increased with increasing citric acid

concentration up to 20% w/v citric acid in ethanol, but did not increase for 40% w/v citric acid presumably because TiO_2 surface was saturated with citric acid. Moreover, **Figure 3.6b** compares the desorption isotherm of quercetin in 1 mL of 20% w/v ethanolic citric acid from MSNPT-86 compared to adsorption isotherm onto MNSPT-86 in 1 mL ethanol solution. The isotherm shows that in the presence of the citric acid solution, the particles retained 37 mg/g particle, which is 35% of the maximum quercetin loading (105 mg quercetin/g particle) in ethanol. The Langmuir model fit to the desorption data (solid curve in **Figure 3.6b**) gave K_L = 0.93 ml/mg in ethanolic citric acid - much less compared to in ethanol (10.6 mL/mg). Thus the interaction between TiO_2 and quercetin is, as hypothesized, disrupted in the presence of citric acid and quercetin can be recovered in solution. Using the desorption isotherm, recovery processes can be designed based on the ratio of ethanolic citric acid solution:particles and the number of recovery stages used. For example, in a multistep recovery process with 1 mL of 20% w/v citric acid used per 25 mg particles at each stage, 91% recovery of quercetin can be achieved from saturated MSNPT-86 in 5 stages. The effect of the extent of TiO_2 functionalization on quercetin recovery was examined. The maximum quercetin loading on MSNPT-362 is higher (171 mg/g particle) than that of MSNPT-86, but the recovery using a single 20% w/v ethanolic citric acid solution extraction step was 47%, compared to 65% for MSNPT-86. However, the corresponding absolute recoveries for MSNPT-362 relative to MSNPT-86 were greater (80 mg/g particle compared to 68 mg/g particle).

To determine the mechanism by which citric acid promotes desorption, linearized Langmuir plots ($1/q_e$ vs. $1/C_e$) were analyzed (**Appendix Figure A.16**) for the adsorption (in ethanol) and desorption (in 20% w/v citric acid) of quercetin on MSNPT-86 and

MSNPT-362. They gave the same y-intercept values with and without citric acid (0.01 g particle/mg quercetin for MSNPT-86 and 0.006 g/mg for MSNPT-362, respectively), which indicates that quercetin and citric acid compete for adsorption on the same surface sites [290]. Thus, citric acid competes with and displaces quercetin molecules from already occupied TiO_2 surface sites to allow for recovery from MSNPT surfaces.

3.4.4 Activity of Particle Bound and Recovered Quercetin.

Radical scavenging activity (RSA) is the ability of a flavonoid to neutralize the free radicals produced in a cellular environment to prevent cellular oxidative stress. Here, RSA values of MSNPT bound quercetin and quercetin recovered using ethanolic citric acid were measured and compared with those of fresh quercetin in ethanol (0-0.5 mg/ml). The RSA of recovered quercetin is only slightly lower than that of fresh quercetin (**Figure 3.7**), showing that adsorption on particles and citric acid recovery does not significantly alter the activity of quercetin. The reduction after recovery in citric acid can be explained by the low pH of the solution, which reduces the favorability of proton donation, resulting in slightly reduced RSA. Both electron donation from C-ring double bond and proton donation from hydroxyl group contribute to the antioxidant activity of flavonoids, and thus the radical scavenging activity of flavonoids decreases with decreasing pH [291, 292].

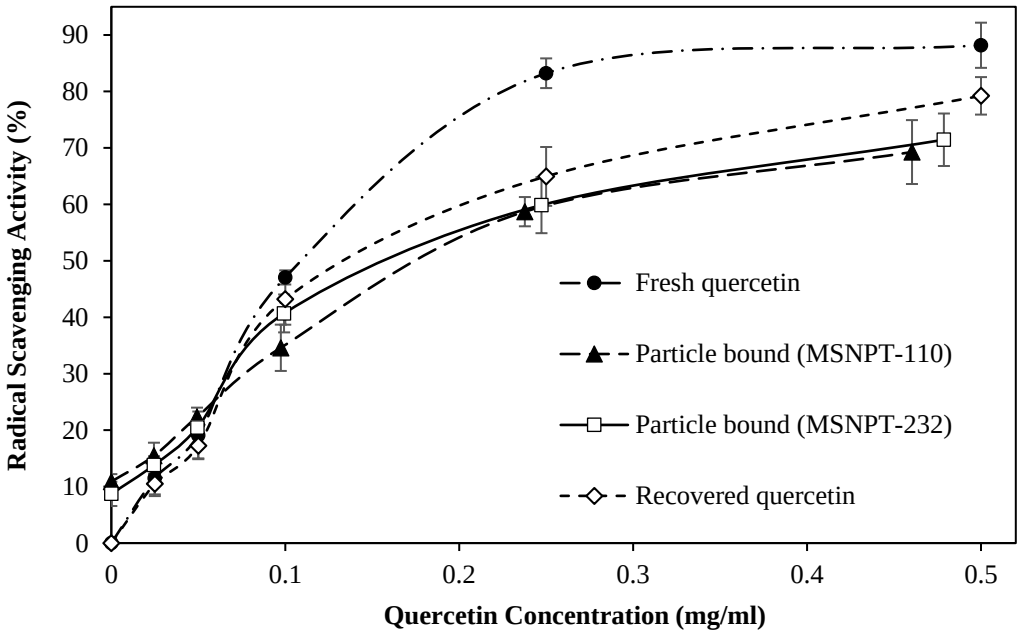

Figure 3.7 Radical scavenging activity of particle bound quercetin on MSNPT-110 and MSNPT-232 (particle solution in ethanol) and recovered quercetin in ethanolic citric acid solution (20% w/v) compared to the fresh quercetin solution in ethanol (curves are visual guides).

Quercetin activity also measured when it is bound to MSNPT (**Figure 3.7**). Two different TiO_2 functionalized particles (MSNPT-110 and MSNPT-232) were selected to determine whether TiO_2 loading affects flavonoid activity. Activity profiles for particle bound quercetin showed that the amount of TiO_2 does not affect flavonoid activity but that the RSA activity of particle-bound quercetin is lower compared to fresh quercetin, as observed previously for non-porous TiO_2 functionalized silica particles [244]. Previous investigations of the activity of flavonoids complexed with metals have concluded that metal flavonoid complexes maintain radical scavenging activity but in reduced quantity, as both the metal and the free radical compete for the hydroxyl groups in flavonoids [293]. Thus, when quercetin is bound to TiO_2 through its two hydroxyl groups, the reduced proton donating ability translates to reduced radical scavenging activity. It is very important to

note that MSNPT alone has some apparent RSA (about 9% and 11% for MSNPT-110 and MSNPT-232), which is also in accordance with the previous study with SNPT, where bare particles showed 2% RSA [244]. Since nonporous silica nanoparticles possesses much less surface TiO_2 their RSA was lower than that of MSNPT. TiO_2 can produce $OH^{\bullet}$ and $O_2^{\bullet-}$ reactive oxygen species, which have the potential to bind with the DPPH free radicals in the RSA assay [294, 295].

3.5 Conclusion

TiO_2 functionalized mesoporous silica nanoparticles were synthesized using surfactant-modified Stöber method followed by TiO_2 deposition on the silica surface. Different degrees of TiO_2 grafting were achieved by varying amount of TiO_2 precursor. Surface area, pore volume and average pore diameter decreased with increasing TiO_2 grafting. TEM images showed the TiO_2 nanocrystal formation outside the particles for moderately high loadings of TiO_2 but STEM images indicated the presence of highly dispersed TiO_2 throughout the particles. Peak intensity decreases observed in GISAXS pattern after functionalization suggested reduction in contrast and possible restructuring during the solvothermal functionalization process due to the grafting of TiO_2 inside the mesopores. GIWAXS provides evidence for anatase formation only with TiO_2 particles on their outer surface, while TiO_2 mainly dispersed in mesopores was amorphous. The alteration of the form of the deposited TiO_2 with extent of functionalization was demonstrated, which complements existing knowledge on the formation of mesoporous titanosilicate materials previously focused on maximizing the formation of photocatalytic anatase.

The functionalized and non-functionalized MSNP were used to adsorb a polyphenolic flavonoid quercetin and its derivative rutin dissolved in ethanol. Bare MSNPs showed very little affinity towards flavonoids and flavonoids adsorption capacity increased with increasing TiO_2 functionalization up to a maximum (440 mg TiO_2/g particle), a trend that is attributed to highly dispersed amorphous TiO_2 first forming within the pores followed by crystallite formation at the surface, and finally pore blocking with increasing TiO_2 grafting. Accessibility of Ti-sites was preserved due to the high level of dispersion in the particles, thus giving as much as 100 times the capacity of nonporous particles,

demonstrating the superiority of TiO_2-functionalized mesoporous particles in designing large scale flavonoid isolation processes.

The suitability of quercetin recovery using ethanolic citric acid (20% w/v) was demonstrated, in which citric acid produced high recovery by acting as a displacing ligand for flavonoids. Radical scavenging activity (RSA) of the recovered and particle-bound quercetin was measured for various quercetin concentration and compared with the activity of free quercetin. Quercetin retains most of its RSA in particle-bound form irrespective of TiO_2 loading, and also when recovered using ethanolic citric acid. The results presented here confirm that TiO_2 functionalized nanoparticles have strong affinity towards polyphenolic flavonoids, and that the high surface area of MSNP can be employed to isolate large amount of flavonoids in order to design efficient and economically viable process. The knowledge gathered for adsorption and recovery of flavonoids on MSNPTs will provide background for the isolation of numerous biomolecules that bind with TiO_2 and facilitate using the nanoparticles to directly isolate biomolecules *in situ* from living plant cells.

CHAPTER 4. NANOHARVESTING OF BIOACTIVE MATERIALS FROM LIVING PLANT CULTURES USING ENGINEERED SILICA NANOPARTICLES

4.1 Summary

Plant secondary metabolites are valuable therapeutics not readily synthesized by traditional chemistry techniques. Although their enrichment in plant cell cultures is possible following advances in biotechnology, conventional methods of recovery are destructive to the tissues. Nanoharvesting, in which nanoparticles are designed to bind and carry biomolecules out of living cells, offers continuous production of metabolites from plant cultures. Here, nanoharvesting of polyphenolic flavonoids, model plant-derived therapeutics, enriched in *Solidago nemoralis* hairy root cultures, is performed using engineered mesoporous silica nanoparticles (MSNPs, 165 nm diameter and 950 m^2/g surface area) functionalized with both titanium dioxide (TiO_2, 425 mg/g particles) for coordination binding sites, and amines (NH_2, 145 mg/g particles) to promote cellular internalization. Intracellular uptake and localization of the nanoparticles (in Murashige and Skoog media) in hairy roots were confirmed by tagging the particles with rhodamine B isothiocyanate, incubating the particles with hairy roots, and quenching bulk fluorescence using trypan blue. Nanoharvesting of biologically active flavonoids was demonstrated by observing increased antiradical activity (using 2, 2-diphenyl-1-picrylhydrazyl radical scavenging assay) by nanoparticles after exposure to hairy roots (indicating general antioxidant activity), and by the displacement of the radio-ligand [^{3}H]-methyllycaconitine from rat hippocampal nicotinic receptors by solutes recovered from nanoharvested particles (indicating pharmacological activity specific to *S. nemoralis* flavonoids). Post-

nanoharvesting growth suggest that the roots are viable after nanoharvesting, and capable of continued flavonoid synthesis. These observations demonstrate the potential for using engineered nanostructured particles to facilitate continuous isolation of a broad range of biomolecules from living and functioning plant cultures.

4.2 Introduction

Plant cells are capable of synthesizing valuable secondary metabolites, in the form of small organic molecules that are potential and proven therapeutics that cannot readily be made by traditional synthetic chemistry [2, 9, 296]. Recent progress has been made in increasing the yields of target metabolites in plant cell cultures with genetic or environmental modification. Genetic sequencing and manipulation of biosynthetic pathways provide a vast resource of potential therapeutic agents [8, 11-13, 297]. It is also possible to select mutant plant cells for survival on the basis of their overproduction of bioactive metabolites to generate a population of mutants with a specific pharmacological phenotype [298]. Flavonoids, a class of secondary metabolites known to be active antioxidants with medicinal, therapeutic and pharmacological applications, have recently been enriched in hairy root cultures by genetic transformation [14, 246-248, 299, 300]. However, these potential therapeutics are usually present in low concentrations, making recovery and purification expensive and complicated. The shortage of commercially viable separation technologies is a main bottleneck in the discovery and application of plant metabolites [301-305]. The conventional method of recovery of natural products from plant cells is to harvest the whole tissues and chemically recover the targeted materials from macerated tissues, usually by solvent extraction. Besides the destruction of the expensive genetically modified plant cell cultures, the activity of labile biomolecules can be reduced depending on the solvent used for the extraction process [254]. Thus, new techniques are required to continuously isolate metabolites from living plant cultures without whole tissue harvesting.

Nanoharvesting, in which nanoparticles are used to carry biomolecules out of living plant cells, can provide continuous harvesting from living and functioning source plants. This is the reverse process of the delivery of bioactive materials (drugs, nucleic acids, *etc.*) to cells [213, 215, 306], but is guided by the same principles in that a nanoparticle must gain entry to the cell with minimal toxicity. Kurepa et al. [15] reported the use of nonporous 2.8 ± 1.4 nm TiO_2 nanoparticles to harvest quercetin-derived flavonoids directly from *Arabidopsis thaliana* plants based on a high degree of chelation of these molecules by TiO_2 [113, 235], but this is the only report of nanoharvesting to date.

While they are effective in nanoharvesting, nonporous TiO_2 nanoparticles lack the high surface area desirable for adsorption, and mesoporous TiO_2 nanoparticles are not readily synthesized as a robust, stable platform [256, 257]. Additionally, requirements for stabilization of small nanoparticles limit the functional groups that can be utilized, and the recovery of 3 nm TiO_2 particles from solution is difficult due to their small size [307]. To overcome these limitations, TiO_2 can be dispersed on mesoporous silica nanoparticles (MSNPs) using post-synthesis TiO_2 functionalization [258, 262, 266, 272]. MSNPs, which include both nanosized and nanostructured silica particles, have high surface area (~1000 m^2/g) and tunable pore size, and silica surface can be easily modified with other functional groups as necessary. Moreover, MSNPs can be synthesized with a magnetic metal oxide core, which provides the opportunity for facile recovery of the particles using an external magnetic field [30].

Although MSNPs are broadly applied in catalysis, chromatography, and biomolecule loading and cellular delivery [26, 29, 34, 46, 59, 308], hydroxyl-terminated bare silica has limited, nonspecific affinity for most plant metabolites. Thus, to exploit the

surface properties of MSNPs for nanoharvesting, functionalization of silica with a metabolite binding group such as TiO_2 is necessary. Previous efforts to incorporate TiO_2 in MSNPs have primarily focused on the adsorption and/or photo-degradation of organic compounds using large-size silica nanoparticles and non-spherical silica mesotructures [114, 258, 261, 262, 309, 310], which are not suitable for cellular internalization. In contrast, we recently demonstrated facile TiO_2 functionalization of MSNPs (average particle diameter ~170 nm), where TiO_2 was deposited inside the mesopores by hydrolysis of a TiO_2 precursor [38]/**Chapter 3**. TiO_2 functionalized MSNPs exhibited a high capacity for the model flavonoid quercetin, over 100 times greater than functionalized nonporous silica. A solvent-based ligand displacement method was developed for flavonoid recovery after binding, and quercetin was found to retain most of its antiradical activity throughout the adsorption and desorption steps. Hence, these particles are hypothesized to be capable of isolating flavonoids in high quantity if internalized in flavonoid-rich cells during nanoharvesting, and to provide for the recovery of active flavonoids.

In addition to binding and releasing active flavonoids, an ideal nanoharvesting process should also provide for efficient uptake of nanoparticles into plants with minimal toxicity. Internalization of MSNPs by plant cells were primarily investigated for gene/protein delivery using MSNP carriers [25, 26, 311, 312], where valuable guidance can be found for the design of nanoparticles for internalization. The interaction of the particles with plant cells and the ability to extract metabolites depends on the particle shape, size, surface area, adsorption capacity, degree of aggregation, and bulk pH and ionic strength [313]. Particle size and surface chemistry are two critical properties for nanoparticle cellular uptake. Nanoparticle uptake is also dependent on the plant species

[314, 315], and the uptake mechanisms are still under investigation. Endocytotic uptake in root cells is believed to occur through a variety of mechanisms sometimes associated with nutrient uptake [184, 189]. Nanoparticles smaller than the pores in plant cell walls (5-20 nm) can directly pass into the cell membrane. Larger particles can be internalized through endocytosis or direct penetration [26, 312]. Further, surface functionalization of MSNPs with amine ($-NH_2$) groups is often used to promote cell membrane penetration through charge interactions, to enhance their colloidal stability, and thus - facilitate their internalization by living cells [35, 36]. Amine groups not only provide positive charge for lipid cell membrane penetration during uptake [156, 184], but also act as binding sites for fluorescent molecules [316], which are used for visualization of cellular uptake *via* fluorescence imaging.

Nanoharvesting also requires that the internalized nanoparticles be recovered from the living plant cells. Internalized particles can escape from cellular systems using vesicle fusion with cell membranes or through direct membrane penetration (probably due to electrostatic interactions) [201, 317]. Moreover, plant cells must remain viable and capable of re-synthesizing the target biomolecule (*i.e.*, flavonoids) after nanoparticle uptake and release to maintain a continuous nanoharvesting system. Prolonged interaction between particles and plants has been reported to create toxicity in some cases [197]. The effect of silica nanoparticle concentration on the cell viability of *A. thaliana* plant root cells was studied by Slomberg and Schoenfisch, who observed that particles between 14 and 200 nm in diameter are taken up and not phytotoxic at concentrations up to 1 mg/mL [187]. *A. thaliana* roots were also found to be viable after 7 days of uptake of anatase TiO_2

nanoparticles [15, 318]. The toxicity of MSNPs functionalized with TiO_2 and/or amines to hairy root cultures is unknown.

In this study, the application of high surface area engineered MSNPs are reported for the nanoharvesting of polyphenolic flavonoids from living *Solidago nemoralis* hairy roots. Dual surface functionalization (with TiO_2 and amines) is used to facilitate metabolite binding and cellular uptake, respectively. The accessibility and order of mesopores of the MSNPs (designed with 2.8 nm diameter pores for loading and 170 nm diameter to permit uptake) after surface functionalization are studied by scanning electron microscopy (SEM), X-ray diffraction (XRD) and nitrogen adsorption. Quercetin is used as a model flavonoid to evaluate the adsorption capacity and the subsequent recovery of active biomolecules from particle surfaces using ligand displacement (in 20% w/v ethanolic citric acid solution). Cellular uptake and localization of engineered nanoparticles fluorescently labeled with rhodamine B isothiocyanate (RITC) from Murashige and Skoog (MS) media by *S. nemoralis* hairy root cultures are visualized using fluorescent microscopy, using trypan blue (TPB) to quench extracellular fluorescence [319, 320]. Nanoparticles from the hairy root cultures are isolated using centrifugation. Antiradical activity and radio-ligand displacement activity ([^{3}H]-methyllycaconitine) - from rat hippocampal nicotinic receptor membranes (characteristics of *S. nemoralis* flavonoids [321]) are measured to demonstrate the presence of active surface-bound flavonoids and flavonoids recovered in solution. Hairy roots are re-cultured following nanoharvesting to examine continued cell viability and the ability of the cultures to re-synthesize flavonoids, as measured by antiradical activity of root extracts. All of these studies provide proof of concept that engineered MSNPs represent a promising platform for *in situ* recovery of small molecule drug

candidates from living plant cell tissues, and thus are a viable route to advance the concept of nanoharvesting.

4.3 Materials and Methods

4.3.1 Chemicals and Reagents

Tetraethyl orthosilicate (TEOS, 99%), sucrose (grade I, ≥ 99.5%), 2-(N-morpholino) ethanesulfonic acid hydrate (MES hydrate, ≥ 99.5%) and H_2O_2 (35 wt% in water) were purchased from Acros Organics; Pluronic F127 (tri-block copolymer, bio-grade), quercetin (> 95%), trypan blue (TPB, 0.4% in 0.81% NaCl and 0.06% K_2HPO_4), titanium (IV) ethoxide (TEO, technical grade), (3-Aminopropyl)triethoxysilane (APTES, 99%), ethylenediaminetetraacetic acid (EDTA, ≥ 99%), citric acid (CA, ≥ 99.5%), nicotine (≥ 99.5%), sodium azide (NaN_3, 99%), phenylmethanesulfonyl fluoride (PMSF, ≥ 98.5%), phosphate buffer saline tablets (PBS, pH 7.4) and rhodamine B isothiocyanate (RITC, mixed isomers) from Sigma-Aldrich; cetyltetramethylammonium bromide (CTAB, 99.8%) from MP Biomedicals; [^{3}H]-methyllycaconitine (^{3}H-MLA) from American Radiolabeled Chemicals; 2,2-diphenyl-1-picrylhydrazyl (DPPH, 95%) and fluorescamine from Alfa-Aesar; NaOH pellets (≥ 97%) from EMD Millipore; Acetone (≥ 99.5%) from BDH analytical; Ti reference solution (1000 ppm in 10% HCl), ultrapure deionized ultra-filtrated (DIUF) water, methanol (HPLC grade, 99.9%), ethanol (200-proof), 36 N H_2SO_4 (95-98% in water), tris-HCl buffer (molecular biology grade, ≥ 99%), NaH_2PO_4 (certified ACS grade), 12 N HCl (ACS grade) and 29.3 wt% NH_4OH solution from Fisher Scientific; and Murashige and Skoog (MS) media supplemented by vitamin B5 and antibiotic cefotaxime sodium (~ 95%) from PlantMedia (BioWorld, Dublin, OH, USA).

4.3.1.1 Solidago nemoralis Hairy Roots

Hairy roots were generated from stem explants of seedlings using *Agrobacterium rhizogenes* mediated genetic transformation reported earlier in detail [14]. After *Agrobacterium* treatment, explants were transferred onto half-strength MS media in agar plates supplemented with 400 mg/L cefotaxime and 3% sucrose, where hairy roots were generated within 2 to 3 weeks. Roots were than excised and maintained in continuous culture on MS media supplemented with 250 mg/L cefotaxime and 3% sucrose.

4.3.1.2 Animals

Adult, male Sprague-Dawley rats (body weight approximately 200-225 g) were purchased from Harlan Laboratories (Indianapolis, IN, USA). Handling, care and use of animals were performed according to the National Institute of Health Guide for Care and Use of Laboratory Animals after the approval of all protocols by the Institutional Animal Care and Use Committee (IACUC) at the University of Kentucky.

4.3.1.3 Engineered Silica Nanoparticles

Functional mesoporous silica nanoparticles were synthesized using a surfactant templated sol-gel process and post-synthesis grafting with TiO_2 and amine, successively, using techniques previously established in literature [38, 69, 125, 322]. Some of the particles were tagged with fluorescent RITC for visualization after internalization by the hairy roots [94, 323]. The detailed procedures for particle synthesis, functionalization, and fluorescent group attachment are provided in **Appendix B**).

4.3.2 Material Characterization

A Hitachi S-4300 Scanning Electron Microscope (SEM) was used to examine the particle morphology. Particles were mounted onto a 15 mm aluminum stub using double sided carbon tape, excess materials were blown off with dry N_2, and the samples were stored in a desiccator for 24 h. Prior to SEM analysis, the particles were coated with conductive Au-Pd alloy using an Emscope SC400 sputtering system. Average and standard deviation of particle diameters were calculated using 20 random particles with ImageJ Software. Surface characterization was performed from nitrogen adsorption conducted at -196 ºC using a Micromeritics TriStar 3000. Samples were degassed at 135 ºC for 4 h under flowing N_2 gas before analysis. The specific surface area, average pore diameter and pore size distribution were estimated using the Brunauer, Emmett and Teller (BET) isotherm and by the method of Barrett, Joyner and Halenda (BJH), respectively. Micropore volume and external surface area were estimated using the comparative adsorption method described by Jaroniec et al. [269, 274]. Fourier transform infrared (FTIR) spectroscopy was conducted by a Thermo Nicolet Nexus 470 spectrometer with a deuterated triglycine sulfate (DTGS) detector. 0.5 g of anhydrous KBr and particles (0.5-1.0 wt %) were crushed with a mortar-pestle, and some of this powder was pressed into a pellet for transmission analysis with N_2 purging. XRD was performed using a Bruker-AXS D8 Discover diffractometer with a Cu K_α source (λ = 1.54 Å) at 0.5 °/min for 2θ from 1.5° to 6º. XRD samples were prepared in a powder sample holder and tapped flat with a spatula.

4.3.2.1 TiO_2 Quantification

The amount of TiO_2 on the particle surface was determined using an H_2SO_4/H_2O_2 assay [244, 272]. 25 mg of TiO_2-functionalized particles were mixed vigorously with 25 mL of 2 M H_2SO_4 for 20 min at 90 ºC and then the solution was filtered through a PTFE (0.02 µm) syringe filter. 1 µL of H_2O_2 was added to 1 mL of the resulting filtrate, and after 10 minutes, the absorbance was measured using a BioTek plate reader (Winooski, VT) at 407 nm in a 96 well plate. The absorbance was calibrated using samples prepared using a Ti-reference solution.

4.3.2.2 Amine Quantification

The amount of amine groups on the functionalized particle surface was determined by a previously reported fluorescamine assay after particle dissolution [324, 325]. 30 mg of particles were dissolved over an 8 h period in 30 mL of 0.02 M NaOH at room temperature under vigorous stirring. 100 µL of this solution and 1.0 mL of 1.0 mM fluorescamine in acetone were mixed with 2.0 mL of PBS solution at pH 7.4. The emitted fluorescence intensity of this solution was measured at 480 nm after excitation at 366 nm using a Varian Cary Eclipse fluorescent spectrophotometer. The calibration curve was prepared using known amounts of APTES.

4.3.3 Adsorption and Recovery of the Flavonoid Quercetin

Quercetin adsorption onto particles was measured using the method of Schlipf et al. [244]. For each measurement, 25 mg of particles was pre-wetted under vortex mixing with 1 mL of ethanol for 24 h in a 2 mL tube, centrifuged for 5 min at 17,000×g (AccuSpin

Micro 17, Fisher Scientific), and the supernatant was discarded. Then, 1 mL of quercetin solution in ethanol (0.05-10 mg/mL) was added to the pre-wetted particles for vortex mixing (24 h) in the dark. The particles were centrifuged again and 200 µL of supernatant was analyzed using the plate reader. A calibration curve was plotted using known concentrations of quercetin, and was used to find the amount of adsorbed flavonoid on to the particle surface by the solution depletion method. For quercetin recovery, quercetin-loaded particles were re-suspended in 1 mL of recovery solvent (20% w/v ethanolic CA). After 24 h of vortex mixing, the particles were centrifuged and the supernatant was analyzed in a plate reader.

4.3.4 Nanoparticle Uptake in Hairy Roots

Hairy roots cultures which overproduce flavonoids, obtained from stem explants of seedlings using *A. rhizogenes* induced genetic transformation, were studied in continuous culture for a period of 4-6 weeks [14]. Roots were periodically checked for flavonoid content indicated by radical scavenging activity, and only those found to be overproducing flavonoids were used for nanoharvesting experiments. Sterile nanoparticles of desired functionalization were sonicated in MS media for 1 h to make a uniform 10 mg/mL master solution, which was diluted to different concentrations (1 µg/mL, 10 µg/mL, 100 µg/mL, 1 mg/mL and 2.5 mg/mL) for root uptake experiments. Growing portions of *Solidago nemoralis* hairy roots were cut from agar plate cultures and rinsed carefully with sterile water. Roughly 500 mg of hairy roots were placed in sterile Nalgene^{TM} centrifuge tubes and 10 mL of a desired nanoparticle solution and the antibiotic cefotaxime (200 mg/L)

were added, followed by vortex shaking in the dark for 48 h. Uptake experiments for each concentration of nanoparticles were performed in triplicate.

4.3.4.1 Fluorescence Imaging

Fluorescence microscopy of RITC tagged amine-functionalized nanoparticles was performed using a Nikon Ti-U inverted microscope. Half of the roots exposed to fluorescent nanoparticle solutions were submerged in trypan blue (TPB) solution (0.04 %) for 10 min and then rinsed with water. Roots with and without TPB treatment were sliced in petri dishes using razor blades, and smashed gently onto glass slides with cover slips before bright field and fluorescence imaging. For some of the roots, a drop of TPB solution was added on top of the sliced roots and the images were taken when the roots were in TPB solution.

4.3.5 Nanoparticle Separation and Flavonoid Recovery

After 48 h exposure, nanoparticles were recovered from hairy roots by centrifugation (7,000 rpm) for 15 min. Whole roots were then separated and kept in sterile conditions for viability studies. The remaining solution was centrifuged again at high speed (17,000 rpm) and the pellets re-suspended in 1 mL of ethanol for particle activity measurements. Flavonoids were recovered from the particle surface by suspending nanoharvested particles in ethanolic CA solution (20% w/v) followed by 24 h of vortex shaking (see **Section 4.3.3**).

To verify that the centrifugation step was not responsible for antioxidant activity on recovered particles, one experiment was performed in which hairy roots and particles were centrifuged for 15 min (without prior incubation in the vortex mixer).

4.3.6 Hairy Root Extract Preparation

Solidago nemoralis hairy roots extract was prepared using the method discussed elsewhere [12]. Briefly, roots were removed from the cultures, rinsed with growth medium, flash frozen in liquid nitrogen, and lyophilized for 24 h and stored at -80 ºC. For extraction, 100 mg/mL lyophilized tissue was shaken overnight in extraction solvent (0.1 M HCl in methanol) and the extracts were filtered to remove remaining plant material and dried in a Labconco rotary evaporator (Kansas City, MO, USA) under reduced pressure and stored at -80 ºC.

4.3.7 Activity Determination

4.3.7.1 Radical Scavenging Activity (RSA)

For RSA determination, 100 µL of the flavonoid solution in ethanol (0-0.5 mg/mL) was mixed with 1 mL of DPPH solution (0.1 mg/mL in ethanol) in a 2 mL vial. The vials were covered immediately and after 30 min the absorbance was measured at 517 nm. The initial DPPH absorbance was measured by adding 100 µL of ethanol with 1 mL of DPPH solution, and RSA was calculated from the percent decrease in DPPH absorbance. RSA of flavonoids recovered by ethanolic CA was determined using the same procedure. For RSA of particle-bound flavonoids, particles with a known amount of bound flavonoids (**Section**

4.3.3) were dispersed in 1 mL of ethanol by sonication and 100 µL of the solution was added to DPPH.

For RSA measurement of plant extracts, 50 µL of 2 mg/mL extract solution in methanol was added to 450 µL of tris-HCl buffer and 50 µL of the resultant solution were added to a 96 well plate in triplicate. 100 µL of 0.1 mM DPPH solution in methanol was added to each well and the plate was then kept in the dark for 30 min. Absorbance was measured at 517 nm and RSA of root extracts calculated from the percent decrease in DPPH absorbance.

4.3.7.2 Specific Radio-Ligand Binding Displacement Activity

Radio-ligand binding displacement activity of nanoharvested particles and their eluents was performed by displacing ^{3}H-MLA from rat hippocampal membranes [321, 326]. Membranes were prepared from freshly harvested hippocampal tissues from adult, male Sprague-Dawley rats by homogenizing the tissues in sucrose buffer (0.32 M sucrose with 50 mM NaH_2PO_4, 0.1 mM EDTA, 0.1 mM PMSF and 0.01% w/v NaN_3) at pH 7.4 using a glass homogenization tube and Teflon pestle. The homogenate was washed two times at 1000×g for 10 min and the supernatants re-centrifuged at 50,000×g for 20 min. The pellet was re-suspended in ice-cold buffer and the protein content was determined by the Pierce Method in Bicinchoninic Acid Kit (Sigma-Aldrich). Final protein content was adjusted to 3 mg/mL using extra buffer solution and samples were frozen at -80 ºC before use. Individual samples were screened for displacement activity in quadruplicate against 2 nM solution of ^{3}H-MLA. 100 µL of samples containing nanoparticles or nanoparticle eluents were added in quadruplicate to a 96 well plate containing membranes (1 mg/mL

protein content). After 15 min of incubation, ^{3}H-MLA was added and the plate was incubated for further 2 h, before harvesting onto a 96 well GF/B filter array and rapidly washed 3 times with 350 μL of 50 mM tris-HCl buffer (pH 7.4) and dried overnight. Finally, 35 μL of scintillation fluid (Microscint 20, Packard Inc.) was added to each filter and the plate was counted using a scintillation counter (Packard TopCount NXT). Non-specific binding in the presence of 300 μM nicotine was subtracted from total binding to find specific binding.

4.3.8 Viability and Flavonoid Synthesis of Hairy Roots after Nanoparticle Exposure

Viability of *Solidago nemoralis* hairy roots after exposure to particles was studied by re-culturing them (at least 10 roots for each nanoparticle type and concentration) on agar plates containing MS media supplemented by 3% sucrose and 250 mg/L cefotaxime. Re-cultured root growth and viability were observed after every week up to four weeks. To measure the flavonoid re-synthesis capability of nanoharvested roots, extracts were prepared in triplicate after regrowth and RSA of the extracts measured and compared to a control (roots not treated with nanoparticles).

4.4 Results and Discussion

4.4.1 Nanoparticle Characterization

Spherical MSNPs (approximately 170 nm diameter) were synthesized by a modified Stöber method using CTAB, TEOS and Pluronic F127 as structure directing agent, silica precursor, and dispersant, respectively. Complete removal of the organic surfactants was confirmed by FTIR analysis by the disappearance of the peak corresponding to CH_2 stretching (2800-3000 cm^{-1}) after acidic ethanol wash (**Figure B.1** in **Appendix B**) [38], thus preventing any toxic effects of surfactants from impacting cell viability. Surface characteristics (BET area, average pore diameter and BJH pore volume) of the dried particles were determined using nitrogen adsorption and are presented in **Table 4.1**. Average pore diameter (2.76 ± 0.23 nm) falls in the expected range of values obtained from the literature when CTAB is used as a templating agent [273]. The BET specific surface area and BJH pore volume were 953 ± 51 m^2/g and 1.21 ± 0.09 cm^3/g for non-functionalized MSNPs, confirming their potential as high surface area platforms for biomolecule adsorption. In a previous study, MSNPs were functionalized with a range of TiO_2 amounts *via* the hydrolytic condensation of TEO, and optimum capacity for the model flavonoid quercetin (in mg quercetin/g particle) was observed at a TiO_2 incorporation of 425 ± 9.2 mg/g particles [38]. This sample is labeled MSNPT in **Table 4.1**. TEM and STEM imaging of these particles shows that there is a tradeoff between the creation of binding sites with by TiO_2 functionalization in the mesopores of ordered cubic MSNPs and the blocking of pores with increased TiO_2 functionalization, where the sample with the greatest quercetin loading (MSNPT) has titanium both inside the pores and at the particle surface [38]. The average nanocrystal size for MSNPT is larger than the average pore

diameter from nitrogen adsorption, which suggests that nanocrystallites form only on the particle outer surface, and that TiO_2 in the pores is amorphous (a suitable form for adsorption). Reduction in pore diameter occurred not only due to TiO_2 deposition but also due to restructuring and contraction of silica matrices (indicated by reduced d-spacing) resulting from the solvothermal functionalization process. The presence of uniformly distributed amorphous TiO_2 (confirmed by wide angle XRD [38]) was also evident from peak broadening and reduced contrast in low angle XRD patterns after TiO_2 loading, consistent with other literature for TiO_2 incorporation in mesoporous silica [258, 272, 275].

Both MSNPs and MSNPTs were functionalized by amine ($-NH_2$) groups using an aminosilane precursor, APTES, resulting in materials referred to as MSNPA and MSNPTA, respectively. For MSNPA and MSNPTA, the amount of amine on the particle surface (presented in **Table 4.1**) corresponds to 0.0038 mmol/m^2 and 0.0012 mmol/m^2 on bare silica and TiO_2-functionalized silica, respectively. Based on the reported area of an amine group in monolayer coverage (50 $Å^2$ surface area/amine functional group) [324], the particle coverage of amines corresponds to 114% and 37% of monolayer coverage for MSNPA and MSNPTA, respectively. The reduced monolayer coverage on TiO_2 (MSNPTAs) is probably due to smaller surface area and lower pore size of MSNPTs compared to bare MSNPs. After amine functionalization, XRD peaks were broadened and less resolved (**Figure B.2**), but this effect was not as drastic as after TiO_2 functionalization [38]. MSNPs retain their mesostructure after amine functionalization, which is in agreement with literature observation for other types of mesoporous silica [100, 101].

Similarly, MSNPs retained their spherical shape after TiO_2 and/or amine functionalization (**Figure 4.1**) and functionalization did not measurably affect particle

diameter (**Table 4.1**). The effect of functionalization on the surface properties of MSNP was studied using nitrogen sorption isotherms, BJH pore size distribution, and α_s-plots, as shown in **Figure B.3**. The nitrogen sorption isotherm for MSNPs is a type IV isotherm with clear capillary condensation, which indicates a well-ordered mesostructure [69]. For all functionalized particles, the capillary condensation step was not evident, suggesting mesopore disruption in presence of TiO_2 and amine groups. The pore size distribution of MSNPs showed a clear peak at around 2.2 nm, but for all types of functionalized particles, the peak sharpness (**Figure B.3b**) and the average pore diameter decreased, as reported in **Table 4.1**. Prior studies of TiO_2 [258, 261, 275] or amine [103, 327] loading onto mesoporous silica are consistent with our observations, where surface area, pore size and pore volume decreased after functionalization. MSNPTAs are less common, and in this case showed an additional surface area reduction (approximately 50%) relative to the starting MSNPTs. The standard reduced adsorption (α_s) plots (**Figure B.3c**) [269, 274] show no micropore formation (pores < 2 nm). The external surface areas were also measured from α_s-plots to be 137.2 m^2/g for MSNP, and were reduced to 120.8 m^2/g, 77.9 m^2/g and 65.3 m^2/g for MSNPT, MSNPA and MSNPTA, respectively. The gradual reduction in surface area and pore diameter and the absence of microporosity after both functionalization steps are consistent with monolayer-like coverage in the pores, providing surfaces appropriate to provide positive charge (to promote cell uptake) and adsorption sites for biomolecule binding.

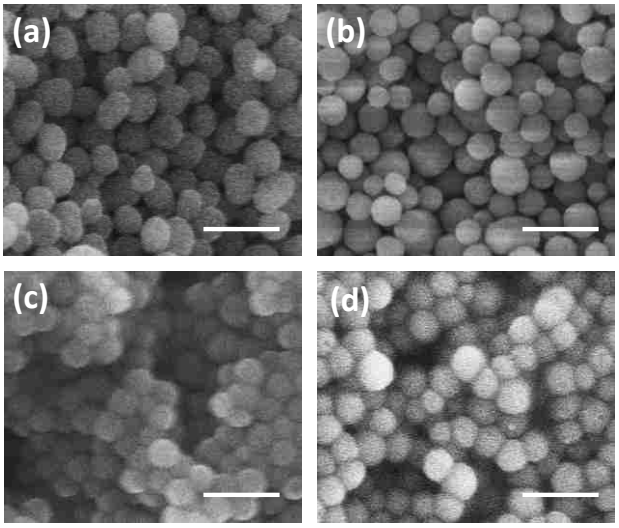

Figure 4.1 SEM image of (a) MSNP, (b) MSNPT, (c) MSNPA and (d) MSNPTA (scale bar 500 nm for all images).

Table 4.1 BET specific surface area, BJH pore volume and average pore diameter of TiO_2 functionalized, amine functionalized, and TiO_2-amine functionalized mesoporous silica nanoparticles (MSNPs) with optimum TiO_2 content compared to non-functionalized MSNPs.

Particle types	**Average particle diameter**	**Amount of TiO_2**	**Amount of amine**	**BET surface area**	**BJH pore volume**	**Average pore diameter**
	nm	**mg/g particle**	**mmol/g particle**	**m^2/g**	**cm^3/g**	**nm**
MSNP	165 ± 19[a]	-	-	953	1.21	2.76
MSNPT	185 ± 29	425 ± 9.2[b]	-	629	0.59	2.21
MSNPA	172 ± 26	-	2.00 ± 0.16[b]	400	0.57	2.50
MSNPTA	174 ± 32	407 ± 13	0.65 ± 0.07	325	0.33	1.97

Standard deviation values resulted from [a]measurement of 20 particles selected randomly (using ImageJ Software) and [b]quadruplicate measurement for chemical analysis.

4.4.2 Nanoparticle Uptake in Hairy Roots and Hairy Root Viability

Plant cells are inherently different from animal cells in that they have rigid cell walls. It has been proposed that the cell wall may place a size limit on nanoparticle uptake based on the size of naturally occurring pores [189, 197, 312]. Silica nanoparticles with much larger size (up to 200 nm [187]) than the pores were shown to be internalized by

plant cells, but the penetration mechanism through plant cell walls is still unknown. Enlargement of pores or new pores/channel creation after the disruption of cell wall proteins and polysaccharides are speculated to be the pathways for nanoparticle entry [312]. The exact uptake mechanism of nanoparticles through the cell membrane is also still unknown or disputed; endocytosis, direct penetration and pore creation by nanoparticles have all been proposed as mechanisms for nanoparticle uptake in plant cells [26, 189, 314]. Direct penetration occurs for strongly positively charged nanoparticles (creating a hole in the membrane is universal for positively charged particles, regardless of shape, size and chemical composition) and after that the nanoparticle can localize in lysosomes, endosomes, cytoplasm, mitochondria, endoplasmic reticulum and cell nuclei [184]. Although nanoparticle transport through a cell membrane reaches equilibrium given sufficient time [184], smaller particles are transported faster than larger ones [328]. Bare and/or amine-functionalized silica nanoparticles (< 200 nm) or TiO_2 nanoparticles (< 140 nm) were reported to be internalized by plant cells [26, 187, 329, 330], but the effect of combined amine and TiO_2 functionalization on internalization of nanoparticles is unknown. Thus, MSNPTAs were tagged with RITC for visualization of uptake in hairy roots by fluorescence microscopy. To confirm internalization, fluorescence of RITC on particles outside of cells [320] was quenched by trypan blue (TPB) added after uptake and fluorescence microscopy was performed, by rinsing off TPB from the roots [331] and also without rinsing [320].

At 100 μg/mL MSNPTA loading, fluorescent images (**Figure 4.2**) showed evidence for nanoparticle internalization. The bright field images (**Figure 4.2a** and **c**) show clear outlines of cells with green chloroplasts inside. The corresponding fluorescent image

(**Figure 4.2b**) of the root cells after 24 h of nanoparticle exposure showed bright fluorescence, which remained after TPB treatment (**Figure 4.2d**), conclusively indicating nanoparticle association and partial internalization by the cells. In contrast, the images of root cells that were not exposed to nanoparticles (**Figure B.4b**) without TPB addition showed no fluorescence. The faint red fluorescence (much less intense than fluorescence of labelled nanoparticles in **Figure 4.2d**) observed when TPB solution was added to the roots without any nanoparticle treatment (**Figure B.4d**), is attributed to the auto-fluorescence of TPB in contact with outer cell membranes [331, 332].

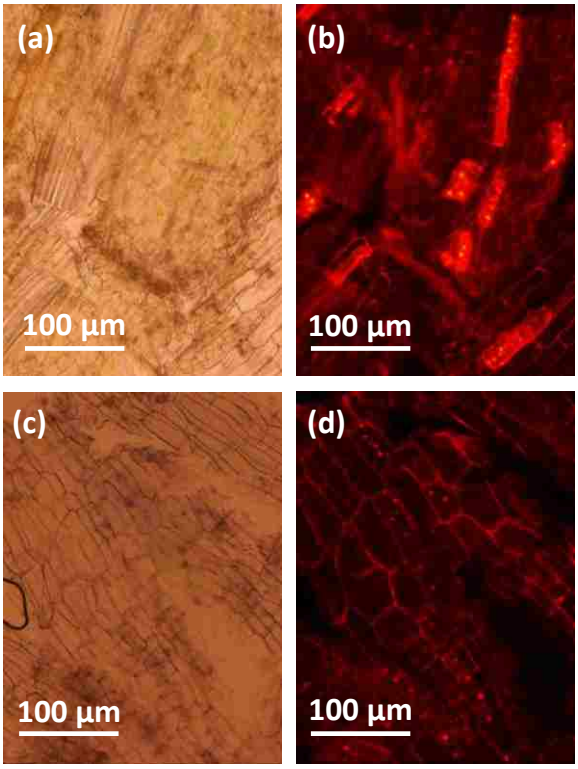

Figure 4.2 Bright field (left) and corresponding fluorescence microscopic image (right) of *Solidago nemoralis* hairy roots after RITC-tagged MSNPTA uptake: (a) & (b) without and (c) & (d) with trypan blue addition for 100 µg/mL nanoparticle solution (exposure time 150 ms).

The fluorescent image presented in **Figure 4.2b** shows some nanoparticles in aggregates, also visible in less quantity after TPB treatment (**Figure 4.2d**). These particles were observed more closely to verify internalization and localization in magnified fluorescence images with or without TPB (**Figure 4.3**). Nanoparticles were found in clusters as well as scattered throughout the cells (**Figure 4.3a**). After TPB addition and rinsing, images of the roots (**Figure 4.3b**) still show intracellular localization, but the reduction in the number of fluorescent spots indicates some particles (or clusters) were quenched. Particle entry into the plant cells and cluster formation inside the cells has been reported based on particle surface chemistry (hydrophobicity) [205]. For MSNPs, Torney et al. found endocytosis clusters inside tobacco plant protoplasts [25], whereas Chang et al. reported direct penetration (energy independent) for amine functionalized MSNPs into *Arabidopsis* plant roots [26]. It is also possible that TPB entered and neutralized RITC in some of the viable cells, which can explain reduced intracellular fluorescence after TPB treatment. When particles enter plant cells, the cell membrane structures can be disrupted, increasing the cell wall permeability [189], and allowing TPB entry.

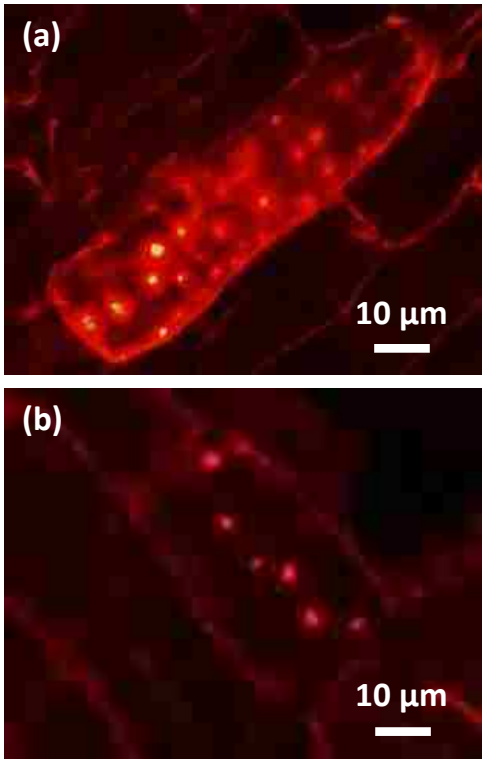

Figure 4.3 Magnified fluorescence image showing intracellular localization of MSNPTAs for 100 µg/mL nanoparticle concentration (a) in absence of trypan blue and (b) in the presence of trypan blue.

At a higher particle concentration (1 mg/mL), the fluorescent images were too bright for individual clusters to be seen (**Figure B.5** in **Appendix B**). After TPB addition, almost all of the cells were still very brightly fluorescent, suggesting a higher amount of particle internalization, which indicates a concentration-dependent equilibrium in particle uptake. Finally, because imaging in the presence of a TPB-containing solution has been used to confirm particle internalization [333], fluorescent images were collected after adding a drop of TPB solution to the roots to ensure quenching of extracellular particles (**Figure B.6**). The bright field images in TPB solution are bluish in color suggesting cells are completely covered with TPB solution. The corresponding fluorescent images appear similar to those for which TPB was rinsed before imaging. Since extracellular particle

fluorescence quenching by TPB is very fast (< 2 min [331]), images taken after rinsing the TPB solution provided additional evidence for particle internalization and localization.

Another requirement for the nanoharvesting process is to not only isolate flavonoids from hairy root cultures but also to maintain viable roots capable of regrowth. Uptake and translocation of engineered nanomaterials in vascular plants, and associated phytotoxicity and cytotoxicity were discussed by Miralles et al. [189], where several factors were identified as contributors to toxicity, such as nanoparticle surface characteristics and possible metal ion leaching. They advise that viability should be studied case-by-case. TiO_2 nanoparticles have been reported to inhibit plant leaf growth and transpiration by reducing root water transport, to delay photosynthesis by acting as photocatalysts, and to disrupt cell function and microtubule networks by generating reactive oxygen species (ROS) [315, 334, 335]. Cell membrane disruption during the uptake process can also lead to cellular dysfunction [184].

The viability of hairy roots exposed to 2.5 mg/mL nanoparticle concentration, the same experimental conditions used for nanoharvesting experiments, was demonstrated over a period of two weeks after particle exposure and reculturing in petri dishes containing agar (**Figure 4.4**). The results are consistent with the absence of an effect on root growth after exposure to nanoparticles. This is shown in **Figure B.7** (**Appendix B**), where data are shown for hairy roots treated with 0 (control), 10 µg/mL, and 1 mg/mL nanoparticle solutions after 0, 2 and 4 weeks of re-culturing. Root viability is similar to the control over the concentration range tested.

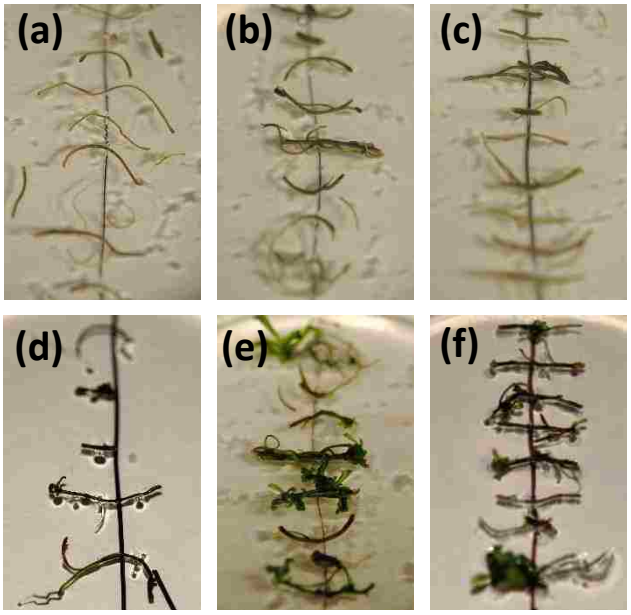

Figure 4.4 Viability of *Solidago nemoralis* hairy roots culture after exposure to 2.5 mg/mL functionalized MSNPs for 48 h and re-culturing: (a) control after 0 week, (b) only TiO_2 functionalized MSNPs after 0 weeks, (c) TiO_2-amine functionalized MSNPs after 0 week, (d) control after 2 week, (e) only TiO_2 functionalized MSNPs after 2 weeks and (f) TiO_2-amine functionalized MSNPs after 2 weeks.

4.4.3 Nanoparticle Recovery and Flavonoid Activity Measurements

Genetically modified *S. nemoralis* hairy roots synthesize polyphenolic flavonoids that are detectable from their radical scavenging activity RSA (antiradical activity using DPPH assay), a broad measure of their ability to reduce oxidative stress [336]. Also, flavonoids from *S. nemoralis* have demonstrated specific bioactivity in their ability to displace ^{3}H-MLA from nicotinic receptors [321]. After the nanoharvesting process, nanoparticles were recovered from the solution in contact with the hairy root cultures by centrifugation. Particles were analyzed for RSA directly. Particles were also washed with ethanolic citric acid (CA) and the activity of flavonoids recovered in the solution was tested. We have previously demonstrated ethanolic CA for the effective recovery of

flavonoids from TiO_2-functionalized mesoporous silica [38], presumably by ligand displacement of the chelated flavonoid. CA is ubiquitous in nature (found blood plasma at ~1 mM) and has tremendous advantages over other extraction agents for its excellent biocompatibility. For these reasons, CA is widely used in living systems for mineral dissolution and detoxification [288]. Moreover, the citrate ion provides very good surface binding, enhances water solubility and reduces aggregation [289], and as a result can increase the bio-availability of hydrophobic flavonoids.

RSA was measured directly from solutions containing suspended MSNPTs or MSNPTAs recovered from the nanoharvesting process (**Figure 4.5**). Both MSNPTs and MSNPTAs were used in nanoharvesting, where the positive charge of the amine groups (in MSNPTAs) is expected to be necessary for localization in the cell. Additional control experiments included RSA measurements for particles exposed only to the media, and particles exposed to media in which hairy roots has been grown (but not incubated with hairy roots directly). All particles were vortexed in their respective solution (media only, media after 24 h of incubation with hairy root cultures (left-over media), and media in which particles and hairy roots were incubated together for 24 h). For MSNPTAs, nanoparticles exposed to roots showed a statistically significant increase in activity compared to particles exposed to leftover solution after shaking with roots and control (no roots), consistent with the color change of the particles after exposure to roots (**Figure B.8** in **Appendix B**). This color change suggests that active metabolites bound to the particles. For MSNPTs, no significant activity difference was found among particles exposed to roots, particles exposed to leftover solution, and particles exposed only to media (**Figure 4.5**). Thus, internalization of the nanoparticle, which was mediated by the amine

functionalization on the particle surface, is necessary for nanoharvesting of these flavonoids to occur. Flavonoids in plants are localized throughout plant cells, with quercetin derivatives accumulating in the plasma membrane, but also found in the nucleus [337]. The mechanism of nanoparticle uptake and release are investigated in **Chapter 5**, but positively charged particles have previously been shown to be taken up by direct penetration of cell membranes [156, 184]. After particles are internalized, flavonoids bind to the TiO_2 groups of the particles [38], presumably through complexation of their cis-diol group with Ti, and then carried out of the cells during particle expulsion.

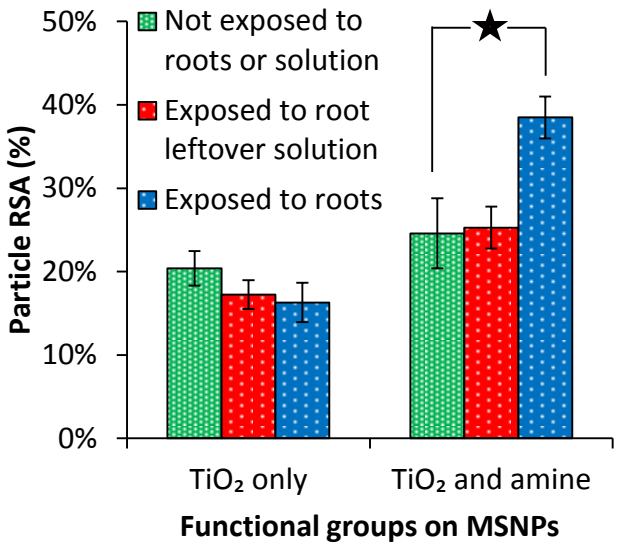

Figure 4.5 Radical scavenging activity (RSA) of MSNPs functionalized with only TiO_2 and TiO_2-amine group when nanoparticles (25 mg, 2.5 mg/mL in MS media) were exposed to 500 mg hairy roots, leftover solution and control solution (error bars are standard deviation from quadruplicate measurements and statistically significant difference in mean ($p \leq 0.05$) from unpaired t-test shown by 'asterisk').

Several additional controls were investigated to demonstrate that uptake of particles in the hairy root cultures was necessary to observe RSA. Centrifugation of particles in the presence of hairy roots (without incubation of the roots and particles) did not result in any increase in particle activity (data not shown), suggesting that prolonged interaction during

vortex shaking is necessary to allow particles to enter and leave cells. Roots were also subject to vortex shaking and centrifugation in the absence of nanoparticles. No measurable RSA was found in the supernatant of any of the experiments conducted, which proves that metabolites were not secreted by the roots and subsequently bound to the particles in solution. Metabolites chelating to MSNPTAs inside of cells is consistent with the elemental analysis of internalized $NaYF_4$ nanoparticle clusters, which provided evidence for phosphate attachment to the particle surface [338]. Similarly, silica nanoparticles were shown to adsorb nutrients from the cellular environment [187], thus making the nutrients unavailable to plant cells. Regarding potential mechanisms of particle recovery from the hairy root cultures, there is an strong tendency in cells with internalized nanoparticles towards cell membrane regeneration and repair, leading to the spontaneous direction of some of the endocytosed materials towards the cell membrane [339]. Also, endosomal and recycling pathways often gradually reduce the intracellular concentration of internalized materials [339, 340]. Particles inside endocytotic vesicles can be removed by fusion with the cell membrane [201] or can become free in the cytoplasm after endosomal escape, which is reported to happen within 12 h for endocytosed mesoporous silica nanoparticles [183]. These free particles, along with those that directly penetrate the cell membrane, can be steadily exocytosed from the cellular interior by secretary vesicles formation and fusion with the cell membrane [341]. Exocytosis, like endocytosis, reaches thermodynamic equilibrium, but is faster for smaller nanoparticles [184, 186]. More than 50% of internalized nanoparticle were observed to be transported to the cell periphery and subsequently expelled out of mammalian cells within one to two hours [186, 342].

To show that biologically selective compounds could be nanoharvested using MSNPTAs (since both amine and TiO_2 are required for nanoharvesting), we demonstrated that eluted flavonoids specifically bind *α–7* nicotinic receptors in rat hippocampal cell membranes. Root extracts from the genetically modified *S. nemoralis* hairy roots used in this study were previously shown to contain specific flavonoids that selectively bind *α–7* nicotinic receptors [321]. Binding to *α–7* receptors is presented as the percent displacement of ^{3}H-MLA from hippocampal membrane and compared to the binding of only ^{3}H-MLA without adding anything (as control). Non-specific binding was measured in the presence of excess nicotine and subtracted from total binding to find the specific binding. Specific binding of ^{3}H-MLA in the presence of extract or nanoharvested compounds (nanoparticle and recovered in solution) is presented as percent of specifically bound ^{3}H-MLA in the control. The percentage of specifically bound ^{3}H-MLA (**Figure 4.6a**) decreased in the presence of increasing plant extract concentration, showing that flavonoids present in the extract have nicotinic receptor activity as predicted for specific flavonoids from *S. nemoralis* [321].

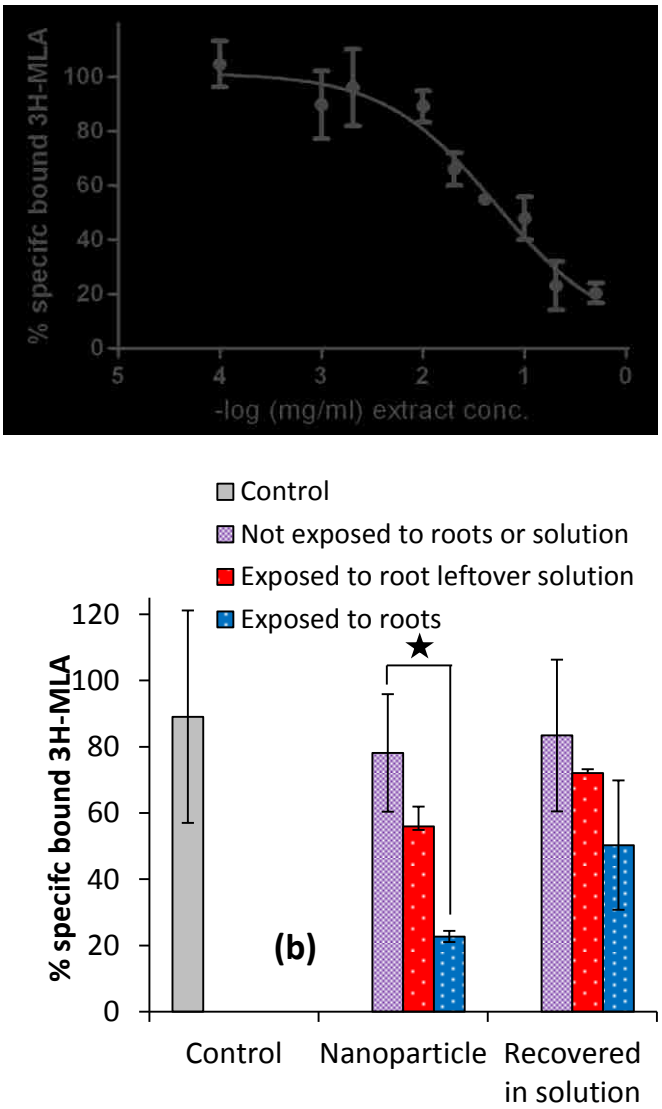

Figure 4.6 [^{3}H]-methyllycaconitine (^{3}H-MLA) binding displacement activity of (a) *Solidago nemoralis* hairy root extracts and (b) TiO_2 and amine functionalized MSNPs (25 mg, 2.5 mg/mL) and their eluent in ethanolic citric acid (20% w/v) exposed to 500 mg hairy root compared to control (error bars are standard deviation from quadruplicate measurements and statistically significant difference in mean ($p \leq 0.05$) from unpaired t-test shown by 'asterisk').

MSNPTAs exposed to hairy roots show a high degree of displacement of ^{3}H-MLA, but nanoparticles that were not exposed to roots or exposed to only leftover solution show no statistically significant displacement of ^{3}H-MLA compared to control (**Figure 4.6b**),

suggesting that polyphenolic flavonoids active towards *α–7* nicotinic receptors are present on only the particle surface that was able to enter into and bind metabolites from hairy roots. The displacement is the same as a solution containing 0.16 mg/mL of root extract (**Figure 4.6a**). Similarly, the average displacement by compounds recovered in solution (ethanolic CA) from nanoparticles exposed to roots was higher compared to that of the nanoparticles not exposed to roots or exposed to root left-over solution only (**Figure 4.6b**), although the differences are not as high as the activity measured directly from the particles. The single washing step by ethanolic CA may not have been sufficient to remove all the flavonoids from the particle surface [38].

4.4.4 Flavonoid Re-Synthesis Potential of Roots after Nanoharvesting

We have shown that *S. nemoralis* hairy roots remain viable and capable of regrowth after exposure to 2.5 mg/mL MSNPs, irrespective of the type of functionalization (TiO_2 and/or amine). To determine whether nanoharvested roots have the ability to synthesize new flavonoids, we made extracts of nanoharvested roots after 2, 10 and 17 days of re-culturing. Extracts from fresh roots were prepared to measure concentration-dependent RSA, which shows RSA increases with increasing extract concentration (data not shown). RSAs of roots exposed to nanoparticles are presented in **Figure 4.7**, where roots exposed to MSNPT (TiO_2 only) and MSNPTA (TiO_2 and amine) along with control roots (no particles) were re-cultured. After 2 days of exposure, roots exposed to MSNPTA (but not MSNPT) gave an extract showing less RSA activity suggesting that a fraction of the metabolites were nanoharvested, which again supports our hypothesis that both amine and TiO_2 functional groups are required for flavonoid removal from plant cells. The root extract

activity remained roughly the same after 10 days, which probably is due to the readjustment of roots to the new culturing environment. After 17 days of exposure, roots exposed to MSNPTA regained their original activity (higher than after 2 and 10 days), and RSA was statistically the same when compared to control roots and roots exposed to MSNPT. This increase in activity of root extracts indicates flavonoid re-synthesis after nanoharvesting. Thus, *in situ* product removal from plant culture, hypothesized as one way to increase the rate of production of secondary metabolites by biosynthesis in plants [305], has been demonstrated.

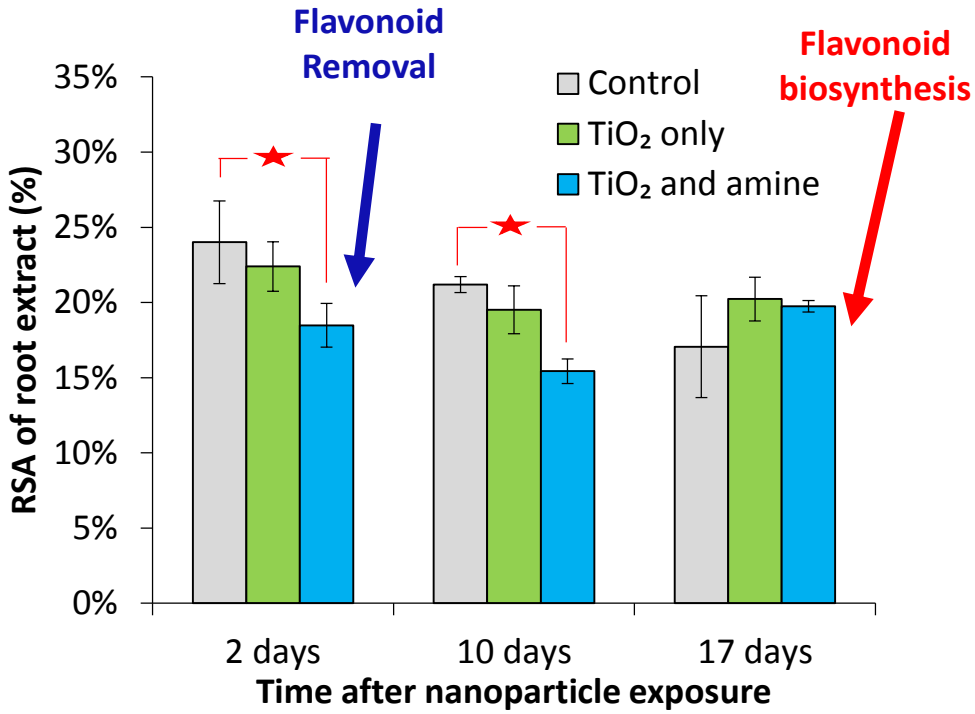

Figure 4.7 Comparative radical scavenging activity (RSA) of *Solidago nemoralis* hairy root extracts after exposure to control (no nanoparticles), only TiO_2 functionalized MSNPs and TiO_2-amine functionalized MSNPs (error bars are standard deviation from triplicate measurements and statistical difference in mean ($p \leq 0.05$) from unpaired t-test represented by 'asterisk').

4.5 Conclusion

The use of engineered mesoporous silica nanoparticles in a nanoharvesting process, which is broadly applicable for several classes of biomolecules, was demonstrated for *Solidago nemoralis* plant hairy root cultures. MSNPs with uniform, well-defined pores were successfully synthesized and functionalized with amines and TiO_2 to promote both cellular nanoparticle uptake and polyphenolic compound binding (respectively).

The first requirement for nanoharvesting, the uptake of functionalized nanoparticles in hairy roots was demonstrated by fluorescence microscopy of RITC-tagged MSNPTA. To further demonstrate that particles are indeed internalized within root cells, the fluorescence of extracellular particles was quenched by trypan blue (TPB) solution. The next requirements for nanoharvesting were demonstrated by showing that the particles could be readily recovered after hairy root uptake, and that the roots were viable and capable of synthesis of new flavonoids after nanoharvesting, as demonstrated by post-uptake growth studies and plant extract activity analysis. Finally, to demonstrate that the compounds recovered on the surface of the MSNPTAs are active flavonoids, the increase in radical scavenging activity (RSA) was analyzed after nanoharvesting. Nanoparticles exposed to roots and their eluents in ethanolic citric acid solution were also tested for biological activity, where both particles and recovered compounds were able to displace radiolabeled ^{3}H-MLA from rat hippocampal cell membrane nicotinic receptors. ^{3}H-MLA displacement from nicotinic receptors proves that the nanoharvested compounds are polyphenolic flavonoids that exhibit the type of bioactivity found in plant extracts.

The ability of particle-bound flavonoids from *S. nemoralis* to bind to nicotinic receptors on synaptic membranes suggests a new direction for treatment, where particles after nanoharvesting can be directly applied for biomolecule delivery to their cellular

targets [321]. Furthermore, mesoporous silica layers can be coated onto magnetic nanoparticles to create functional magnetic core-shell particles, for enhanced recovery [30, 87]. The magnetic core will facilitate particle recovery from living plant cells, while the TiO_2 functionalized mesoporous silica coating can act as a high surface area adsorbent in separation processes. The synthesized engineered particles are expected to represent a platform technology for the isolation and delivery of a broad range of therapeutic biomolecules in living tissues.

CHAPTER 5. MECHANISM OF ENGINEERED SILICA NANOPARTICLE INTERACTION WITH LIVING PLANT CULTURES DURING NANOHARVESTING OF BIOMOLECULES

5.1 Summary

Cellular uptake, intracellular transport and expulsion mechanisms of engineered silica nanoparticles (ESNP) are important to understand when designing novel processes involving biomolecule isolation and delivery. Nanoharvesting, where ESNP nanocarriers are used to transport and isolate valuable therapeutics out of living plant cell cultures (*e.g.* hairy roots), is an example of a developing technology to obtain biomolecules such as secondary metabolites that are most effectively synthesized in plants. Feasibility of nanoharvesting with ENSP has been demonstrated, but the mechanisms of ESNP entry and transport in, and expulsion from plant cells are still unknown, which makes optimization of the particle properties difficult. Here, by changing external variables temperature and properties of ESNP (surface functionalization and charge), insights into the ESNP uptake and recovery process in hairy root cells are revealed. The ESNP uptake into hairy roots is quantified *via* Ti-content (part of the ESNP), and time-dependent expulsion from the roots using fluorescence spectroscopy of particles labeled with rhodamine B isothiocyanate (RITC). The results suggest that functionalization and surface charge (regulated by the attachment of amine groups) play the biggest role in the effectiveness of uptake and recovery. Comparison of ESNP interactions at 4 ºC and 23 ºC (thought to differentiate between activated process and direct cell wall penetration) show that ESNP functionalized only with Ti are taken up and expelled by thermally activated mechanisms, while amine-functionalized, positively charged particles are taken up and expelled mainly by non-activated routes (such as direct penetration of cell walls). Amine-functionalized ESNP

were also found to be transported spontaneously into and out of plant cells by the dynamic exchange experiment between fluorescent and non-fluorescent particles, suggesting tremendous promise as a biomolecule delivery systems as well as for isolating therapeutics from plant cell cultures.

5.2 Introduction

A number of valuable therapeutics can only be economically synthesized in plant cell cultures, but development of this technology requires new methods of product isolation that do not destroy valuable and slow-growing cultures [343]. A novel process called nanoharvesting offers such an approach for isolation of biomolecules from living and functioning plant cultures using nanoparticulate carriers. Kurepa et al. first reported nanoharvesting of flavonoid compounds from plant cultures using small titania (TiO_2) nanoparticles without significant harm to the host plants [15]. Subsequently, our group developed engineered silica nanoparticles (ESNP) functionalized with TiO_2 and demonstrated their high capacity for flavonoids [38]. Addition of amine functionalization gave ESNP highly positive charge, which was shown to be active for nanoharvesting of polyphenolic flavonoids from *Solidago nemoralis* hairy roots, where TiO_2 and amine functional groups were hypothesized to bind flavonoids and facilitate internalization by root cells, respectively (**Chapter 4**) [39]. Consistent with this concept, particles were able to harvest active metabolites only when both functional groups were present. However, the mechanism of this process (entering into plant cells and emerging with bound target compounds) has not been explored. Understanding particle uptake, intracellular transport, and expulsion is important to the development of nanoharvesting as a plant biotechnology platform, and also for designing vectors for delivery of biomolecules (such as polynucleic acids) to plants by these ESNP [344].

ESNP have been investigated extensively as advanced materials, including for delivering drugs, proteins, and nucleic acids into cells due to their high surface area and tunable characteristics including size, shape, pore structure, and surface functionalization [62, 345, 346]. However, ESNPs are just beginning to be explored for selective removal

of compounds from biological systems, such as the extraction of proteins and peptides from HeLa cells recently reported by Slowing et al. [16] and Zhang et al. [347]. Most of the work regarding plant cells (in particular) has focused on environmental and toxicological implications of nanoparticles for plants [188, 189, 197, 348] and polynucleic acid delivery to plants, and also isolating plant produced metabolites using nanoparticles [25, 26, 312, 349].

The interaction of nanoparticles with plant cells is a complex process, which has been demonstrated to be dependent upon particle shape, size, surface charge, composition, degree of aggregation, concentration, adsorption capacity for intracellular compounds, and ionic strength and pH of the bulk solution [193, 197, 313, 314, 328]. Although particle size and surface properties (charge) are the two most critical factors for cellular uptake, the extent of uptake still depends heavily on the plant species [314]. However, silica particles up to 200 nm in diameter have been shown to be taken up by *Arabidopsis thaliana* root cells without significant cytotoxicity up to large particle concentrations (1000 ppm) [187], and amine-functionalized MSNPs are readily internalized by *A. thaliana* roots [26].

The presence of cell wall primarily represents the main difference between uptake in animal and plant cells, as larger particles were reported to be internalized faster in the former [191, 192], while smaller particles are taken up faster in plants [328]. Although some articles performed uptake and release studies on plant cell protoplasts by removing cell walls [25, 339, 350], protoplasts are very poor representative of plant cells in actual living tissues [351], and interaction of nanoparticles with whole plant tissues should be studied for nanoharvesting and other applications. Plant cell walls possess rigid structures with pores ranging from 5 to 20 nm, but nanoparticles much larger than this were reported

to enter into plant cells. Pore creation or enlargement, piercing and loosening of the cell wall matrix by free radicals generated by the particles have been proposed as mechanisms for the internalization of particles larger than intrinsic cell wall pores [188, 189, 312, 352, 353]. Nanoparticle entry through cell membranes is also a complex process and a variety of activated and passive mechanisms have been proposed similar to animal cell studies [314]. Nanoparticle uptake is often associated with nutrient uptake and controlled by plasma membrane receptors for regulation in roots [189]. Surface functionalization of particles with positively charged groups has been shown to promote lipid membrane [62] and plant cell wall penetration [26], and has been found essential in nanoharvesting. A mechanistic investigation of our ESNP and hairy roots interaction should be carried out in order to identify complete route in and out of plant cells [39].

In addition to uptake, intracellular transport and expulsion of nanoparticles are important to reduce prolonged plant cell exposure to nanoparticles (and potential resulting toxicity), ensure plant viability, and carry away desired compounds – all requirements established for viable nanoharvesting and delivery applications [39]. Most nanoparticles adsorb proteins and lipids from plant media or once inside the cells. Hence, during transport and expulsion one should consider the protein corona around the nanoparticles rather than the pristine particles themselves [201]. Like uptake, excretion mechanisms depend on cell types and species, and on nanoparticle size, shape and surface modification. However, surface charge is probably the decisive factor governing transport and expulsion [201]. Secretary vesicle formation (lysosomal excretion) and fusion with the cell membrane is the mechanism for activated expulsion of nanoparticles, whereas passive penetration is thought to happen through electrostatic interactions in the reverse process of internalization.

Once particles get expelled from root cells during nanoharvesting, they can undergo repeated internalization-expulsion cycles or travel through the intercellular space, and finally exit the roots themselves into the medium [16]. Nanoparticles have been found to travel from cell to cell by either repeated uptake-expulsion cycles or through intercellular spaces [205, 330]. ESNP were also found to travel from plant roots to aerial tissues by transport tissues [354]. Particle localization in root parts away from the tips can be ascribed to intercellular migration following uptake inside the roots [26]. In plant roots, vascular tissues can aid nanoparticle transported from root tips to other parts [355], but the kinetics of uptake and localization of ESNP in hairy roots remains to be investigated. Although there have been some studies involving nanoparticle uptake and translocation inside plants as mentioned above, there is still a need for better mechanistic understanding of nanoparticle expulsion, and the comprehensive interaction (in and out) between ESNP and plant tissues. The kinetics of nanoparticle uptake and expulsion, and the underlying mechanisms and pathways for nanoparticle excretion are still elusive [197, 201].

Here, the kinetics and mechanisms of ENSP uptake and release from hairy roots of *Solidago nemoralis* are investigated. Fluorescently tagged particles are used to qualitatively monitor particle uptake in the root cells. Uptake is quantified by taking advantage of the presence of Ti in the particles (present for nanoharvesting of flavonoids containing enediol groups). This avoids the limited sampling possible using microscopy-based techniques, and the need for digestion of whole plant tissues [187, 356, 357]. Ti content is measured after calcination of tissues and dissolution of the resulting ash. Expulsion following uptake in solution is measured using fluorescence spectroscopy of RITC-tagged particles in solution. Temperature dependent quantification of ESNP uptake

and release at 4 ºC and 23 ºC is used to differentiate between activated pathways and direct penetration. Also, novel exchange experiments involving recovery of RITC-tagged particles in solutions of untagged particles are used to demonstrate continuous replacement by the uptake of ESNP and the dynamic nature of particle-cell interactions for nanoharvesting. Regarding the effects of surface charge on uptake and release, ESNP without amines (functionalized with only Ti, expected to give a mild negative surface charge) are compared using the methods described above.

5.3 Materials and Methods

5.3.1 Chemicals and Reagents

Tetraethyl orthosilicate (TEOS, 99%), grade I sucrose (≥ 99.5%), and hydrogen peroxide (35 wt% in H_2O) were obtained from Acros Organics. Tri-block copolymer Pluronic F127 (bio-grade), (3-aminopropyl)triethoxysilane (APTES, 99%), titanium (IV) ethoxide (TEO, technical grade) and rhodamine B isothiocyanate (RITC) mixed isomers were purchased from Sigma-Aldrich. Acetone (≥ 99.5%) from BDH analytical; NaOH pellets (≥ 97%) were obtained from EMD Millipore; cetyltrimethylammonium bromide (CTAB, 99.8%) from MP Biomedical; and fluorescamine from Alfa-Aesar. Ultrapure deionized ultra-filtrated (DIUF) water, Ti-reference solution (1000 ppm dissolved in 10% HCl), 200-proof ethanol, fuming H_2SO_4 (95-98% in water), 12 N HCl (ACS grade), and 29.3 wt% NH_4OH solution were purchased from Fisher Scientific. For root growth, Murashige and Skoog (MS) media with vitamin B5 and antibiotic cefotaxime sodium supplement (~ 95%) was obtained from PlantMedia (BioWorld, Dublin, OH, USA).

5.3.1.1 Solidago nemoralis Hairy Roots.

Hairy roots of *S. nemoralis* (goldenrod) were generated from seedlings stem explants following genetic transformation mediated by *Agrobacterium rhizogenes* infection reported in an earlier study [14]. After *Agrobacterium* treatment, explants were re-cultured onto 1/2-strength MS media in agar plates containing 400 mg/L cefotaxime and 3% sucrose supplement. Generation of hairy roots was observed within 2 to 3 weeks, which were than excised and cultivated in continuous culture on MS media with 250 mg/L cefotaxime and 3% sucrose supplement until use.

5.3.1.2 Engineered Silica Nanoparticles

Synthesis of functional mesoporous silica nanoparticles (MSNPs) was carried out using a surfactant templated sol-gel procedure and functionalized post-synthesis by grafting with TiO_2 and amine, successively. MSNPs with highly ordered pore structure were synthesized by a modified Stöber method first reported by Kim et al. using CTAB as templates [69]. Initially, 2.05 g of F127 and 0.5 g of CTAB were dissolved in 96 mL of DIUF water mixed with 43 mL of ethanol, and 11.9 mL of 29.3% ammonia. The solution was stirred continuously at room temperature until complete dissolution of the surfactants occur. 1.9 mL of TEOS was added dropwise to the clear solution with vigorous stirring and the solution was kept mixing for exactly 1 min at room temperature (RT) after TEOS addition. The solution was then kept stationary at RT for a period of 24 h for silica condensation to complete. Synthesized particles were separated and washed 3 times with water and ethanol each using repeated ultrahigh speed centrifugation (Beckman-Coulter) at 17,000 rpm before drying at 84 ºC in air overnight. Lastly, surfactant template was removed from the silica matrices of the particles by washing them in 200 mL of 1.5 M HCl solution in ethanol for 24 h (termed acidic ethanol wash) followed by repeated high-speed centrifugation and washing with water and ethanol overnight drying at 84 ºC.

Particles were functionalized with TiO_2 using TEO as precursor to obtain TiO_2 functionalized MSNPs (MSNPTs) according to post-synthesis procedure reported earlier [38]. Initially, 500 mg of MSNPs were sonicated in 100 mL of ethanol for 15 min in a 250 mL round bottom flask. Separately, 2.6 mL of TEO was added to 7.15 mL of absolutely dry ethanol in a nitrogen glove bag following multiple purging with dry N_2. 142.5 mL of ethanol was added to the particle solution before heating the flask with continuous

magnetic stirring. Once boiling of the solution began, the previously prepared TEO solutions and 1.6 mL of DIUF water were added to the flask. The solution was refluxed for 1.5 h under magnetic stirring for the functionalization to complete. Functionalized particles were recovered by high-speed centrifugation at 17,000 rpm for 5 min and washed in 100 mL of ethanol for 24 h to remove excess and unbound TiO_2 before drying in an oven at 84 ^oC.

Both bare MSNPs and MSNPTs were functionalized with amine to obtain amine functionalized MSNPs (MSNPA) and TiO_2-amine functionalized MSNPs (MSNPTAs), by APTES condensation on the particle surface using a modified version of literature procedures [101, 125, 322, 358]. At first, 200 mg of MSNPs/MSNPTs were dispersed uniformly in 25 mL of absolutely dry ethanol by ultra-sonication for 15 min. 0.5 mL of APTES was added dropwise to the particle suspension under constant stirring in a dry nitrogen glove bag. The solution was stirred in a sealed flask for 24 h at room temperature for APTES condensation. Following amine grafting, particles were recovered using centrifugation and after repeated washing with ethanol, kept in an oven at 84 ^oC for 24 h for curing of functional groups. After curing, particles were stirred in excess ethanol (100 mL) for 24 h to remove any loosely-bound or adsorbed amine functionalities. Washed particles were again rinsed 3 times with ethanol using high-speed centrifugation and dried at 84 ^oC overnight to obtain final functionalized particles.

5.3.1.3 Fluorescent Tagging

To add RITC on their surface, 200 mg of amine-functionalized particles (both MSNPAs and MSNPTAs) were suspended in 25 mL of ethanol by ultra-sonication for 15

min. 3.2 mg of RITC was added to particle suspension and the resultant mixture was stirred for 24 h for RITC attachment. After 24 h, the brightly red particles were obtained by high-speed centrifugation and repeated washing in ethanol until completely clear supernatant was observed. The particles were dried in an oven at 84 ºC and then washed in water and ethanol for 24 h each to remove any excess dye before final drying in the oven overnight.

5.3.2 Material Characterization

Particle morphology was examined by using a Hitachi S-4300 Scanning Electron Microscope (SEM) by dispersing the particles onto a 15 mm aluminum stub using a double sided carbon tape (Ted Pella). After dispersing, excess particles were blown off the carbon tape surface with dry N_2, and the stubs were kept in a desiccator for 24 h. Before SEM analysis, the particles were sputter-coated with a conductive film of Au-Pd alloy using an Emscope SC400 sputtering instrument. From SEM images, average and standard deviation of particle diameters were measured using ImageJ Software by randomly selecting 20 individual particles. Nitrogen adsorption experiments conducted at -196 ºC using a Micromeritics TriStar 300 apparatus were used to characterize surface area, pore volume and average pore size of bare and functionalized particles. Before nitrogen adsorption, trace moisture was removed from the particle samples by degassing at 135 ºC for 4 h under flowing dry N_2 gas. The specific surface area was estimated using the Brunauer, Emmett and Teller (BET) isotherm and average pore diameter and pore size distribution were obtained by the Barrett, Joyner and Halenda (BJH) method. To demonstrate successful removal of surfactants from particle pores during acidic ethanol wash, Fourier transform infrared (FTIR) spectroscopy was carried out using a Thermo Nicolet Nexus 470

spectrometer along with deuterated triglycine sulfate (DTGS) detector. Sample preparation for FTIR analysis involve crushing 0.5 g of anhydrous KBr and particles (0.5-1.0 wt %) together with a mortar and pestle, and pressing some of the powder into a pellet. Zeta potentials of the particles were measured by dynamic light scattering (DLS) using an Anton-Paar Lightsizer 500 instrument. Around 0.1 mg/mL of homogeneous particle suspension (by ultrasonication) in acetate buffer (pH = 4.0) was placed in an omega cuvette (inverted Ω-shaped capillary tube) for measurement. During placement of solution inside the capillary tube, extreme care was taken to exclude air bubbles.

5.3.2.1 TiO_2 Quantification.

The amount of TiO_2 grafted on the particle surface was quantified using a sulfuric acid/hydrogen peroxide assay reported elsewhere [244, 272]. For analysis, 25 mg of particles were stirred vigorously for 20 min in 25 mL of 2 M H_2SO_4 solution at 90 ºC to induce complete dissolution of surface TiO_2. After cooling, the solution was filtered through a polytetrafluoroethylene (PTFE) syringe filter with pore size of 0.02 µm. 1 mL of the filtrate (with dissolved TiO_2) was taken to a vial and 1µL of H_2O_2 was added. After 10 minutes, the absorbance was measured at 407 nm in a 96 well plate using a BioTek plate reader (Winooski, VT). Amount of TiO_2 on the particles was determined using an absorbance calibration curve made from Ti-reference solution.

5.3.2.2 Amine Quantification

Amine groups on MSNPA and MSNPTA surface was determined chemically by dissolving the particles in alkaline solution and using a fluorescence assay as reported

earlier [324, 325]. 30 mg of amine functionalized particles were stirred in 30 mL of 0.02 M NaOH at room temperature over an 8 h period with vigorous stirring. After 8 h (complete particle dissolution), 100 μL of this solution was mixed with 1.0 mL of 1.0 mM fluorescamine in acetone and 2.0 mL of PBS solution at pH 7.4. The emitted fluorescence intensity of this solution was measured immediately at 480 nm emission with excitation wavelength of 366 nm using a Varian Cary Eclipse fluorescence spectrophotometer. Amount of amine was calculated by comparing with a calibration curve prepared using known amounts of APTES.

5.3.3 Nanoparticle Uptake in Hairy Roots

Hairy roots cultures obtained from stem explants of seedlings genetically transformed using *A. rhizogenes* were studied in continuous culture for a period of 4-6 weeks [14]. Sterile nanoparticles of desired functionalization were sonicated in MS media for 1 h to make a uniform 10 mg/mL master solution, which was diluted to different concentrations (1 μg/mL, 10 μg/mL, 100 μg/mL, 1 mg/mL and 2.5 mg/mL) for root uptake experiments. Growing portions of *S. nemoralis* hairy roots were cut from agar plate cultures and rinsed carefully with sterile water. Roughly 300 mg of hairy roots were placed in sterile Falcon centrifuge tubes and 15 mL of a desired nanoparticle solution and the antibiotic cefotaxime (200 mg/L) were added, followed by vortex shaking in the dark for 24 h. For time dependent uptake experiment, multiple batches of roots were exposed to 1 mg/mL MSNPTAs for different times (15 min – 48 h).

5.3.3.1 Fluorescence Imaging

Fluorescent microscopy of roots after RITC tagged MSNPTAs was performed using a Nikon Ti-U inverted microscope. Roots were sliced in petri dishes using razor blades, and smashed gently onto glass slides with cover slips before bright field and fluorescence imaging.

5.3.3.2 Uptake Quantification

The amount of MSNPT(A) taken up by hairy roots was quantified by calcining the roots following exposure to the particles and analyzing the Ti-content in the ash using the Ti analysis described earlier (**Section 5.3.2.1**). After nanoparticles exposure at 4 ºC and 23 ºC for 24 h (for temperature dependent uptake), roots were initially cleaned with fresh plant media and then rinsed repeatedly with water to remove non-internalize particles adhering on root surface. Roots were then calcined in a muffle furnace at 500 ºC (with 1 ºC/min ramp) for 10 min under air following drying at 120 ºC for 8 h. Ashes were collected carefully and dissolved in 2 mL of 2M H_2SO_4 for 30 min at 90 ºC in a water bath. Ti-content and corresponding amount of particles taken up by the roots were calculated by hydrogen peroxide assay using a calibration curve prepared in presence of root ash from 300 mg roots and known amount of MSNPTAs.

5.3.4 Nanoparticle Recovery and Retention after Internalization

After 24 h of exposure to 15 mL of 2.5 mg/mL RITC-tagged MSNPTAs, roots were rinsed with fresh plant media and water repeatedly to remove surface adhering non-internalized particles. The roots are then placed in 15 mL of fresh plant media either at 4

ºC or 23 ºC (for temperature dependent recovery) in Falcon tubes, which were vortex-shaken in the dark at the desired temperature, and the solution was analyzed periodically to quantify time dependent particle recovery (see below). For one set of experiments, roots were put in 15 mL of MS media containing 2.5 mg/mL of untagged (non-fluorescent) MSNPTAs at 23 ºC to test and quantify the dynamic nature of nanoparticle uptake and recovery.

5.3.4.1 Recovery Quantification

The amount of RITC-tagged MSNPTAs recovered in solutions with or without untagged particles were determined by analyzing a 300 µL aliquot of solutions by fluorescent spectroscopy after first saturating the roots with tagged MSNPTA. Samples were collected periodically after 15 min to 28 h, and analyzed quickly for fluorescent intensity at 582 nm (peak fluorescence) after excitation at 557 nm (peak absorbance) and then replaced to the original solution. The amount of particles recovered was estimated by constructing a calibration curve of fluorescence intensity vs. concentration with a known amount of fluorescently-tagged particles in the respective exchange solution (fresh plant media or untagged particle solution).

5.3.4.2 Retention after Recovery Quantification

After recovery, the amount of particles retained by the roots was estimated by analyzing Ti-content in the roots following calcination and acid dissolution. Roots were taken out from recovery solutions and rinsed repeatedly with water to remove any adhering

particles, calcined at 500 ºC for 10 min following drying at 120 ºC, and analyzed for Ti using the sulfuric acid-hydrogen peroxide assay (see **Section 5.3.3.2**).

5.4 Results and Discussion

In our previous work [39]/**Chapter 4**, amine and TiO_2 functinalized MSNPs (MSNPTAs) were used to harvest polyphenolic flavonoids from living and viable *S. nemoralis* hairy roots. TiO_2 functionalization was used to provide binding sites for the flavonoids and amine functionalization to promote cellular internalization and expulsion. Uptake and intracellular localization was qualitatively demonstrated using fluorescence microscopy by tagging the particles with RITC. Active flavonoids were harvested only when the particles were functionalized by both TiO_2 and amine groups, but not particles functionalized with only Ti (*i.e.* MSNPTs). The presence of flavonoids harvested by MSNPTA was determined by antiradical activity (common to many flavonoids), and displacement of ^{3}H-methyllycaconitine from rat hippocampal tissue by nicotinic receptor-active flavonoids specifically found in *Solidago nemoralis*.

Before functionalization, mesoporous silica nanopartilces (MSNPs) were synthesized using surfactant templated sol-gel synthesis technique using CTAB as structure directing agent. After synthesis, surfactant was removed by acidic ethanol washing and complete removal was confirmed by FTIR analysis [38], thus ruling out effects of residual surfactants or other organics on nanoparticle-cell interactions. MSNPs were functionalized with TiO_2 and/or amine following synthesis using post-synthesis grafting of TEO and APTES, respectively. SEM images of the particles before and after functionalization are presented in **Figure C.1** of the **Appendix**. The particles retain their spherical shape after functionalization, and their average diameter is similar within statistical limits (**Table C.1**) – close to 170 nm before and after functionalization. The size of the particles determines their ability not only to be taken up by cells, but also to permeate through tissues [185], which is important for nanoharvesting. Silica nanoparticles up to 200

nm in diameter have been shown to be taken up and transported in *A. thaliana* [187]. Pore properties (specific surface area, pore volume and average pore size) are presented in **Appendix Table C.1** along with amounts of TiO_2 and amine grafted on particle surfaces. Reductions in surface area and pore volume are consistent with the addition of mass to the pore walls by functionalization with both Ti and aminopropyl groups, but the pore diameter is not severely affected (2.8 nm for MSNP and 1.97 nm the smallest pore diameter for MSNPTAs). These pore texture and loading indicate successful loading of accessible Ti-sites for flavonoid complexation and amines to impart a positive surface charge (**Table C.1**) [39]. We have utilized the unique opportunities provided by the functional groups of MSNPTAs to quantify the amount of nanoparticles internalized into hair roots, recovered after switching to fresh media, and retained by the roots after recovery. The concentration of particles in the roots was quantified by using Ti as a chemical tracer, and the concentration of particles in solution using fluorescence spectroscopy of particles tagged with RITC *via* amines.

Before providing the results of internalization and expulsion studies, we present a brief overview of possible interactions and pathways of nanoparticles through plant root cells. Engineered nanoparticle interaction with cells can primarily be divided into three parts: uptake (or internalization), intracellular transport, and release (or expulsion) from the cells. A conceptual diagram is presented in **Figure 5.1** showing all possible major pathways for ESNP in and out of plant cells. Entry into the cells occurs through two main routes: activated uptake (endocytosis) and direct penetration by passive diffusion [184, 190]. Wong et al. recently proposed a mechanism for direct penetration in which nanoparticles of a critical magnitude of surface charge accentuate the local electrical field

near the bilayer and pass through by softening the lipid and exchanging some lipid onto the nanoparticle surface [156]. Immediately after activated internalization, particles usually stay inside of lipid vesicles (early endosomes), while for direct penetration, particles enter into the cytoplasm. Inside the cells, early endosomes usually mature into late endosomes while retaining nanoparticles taken in by endocytosis, and entry into the cytoplasm requires endosomal escape. Maturation of endosomes is associated with increasing interior acidity, and fusion of lysosomes introduces hydrolytic enzymes to degrade foreign materials [201]. Depending on their properties, nanoparticles can interact with intracellular organelles and get entrapped [188], and a good deal of work has been directed towards engineering nanoparticles for endosomal escape or targeting organelles [359]. Non-degradable particles (silica) that are not able to escape the endosome are usually transported to and expelled by fusion with the cell membrane (exocytosis), sometimes by the formation of exosomes [95]. Free particles internalized by direct penetration or escaped from endosomes can also undergo exocytosis (activated expulsion) by means of secretary vesicle formation in the Golgi apparatus. Golgi apparatus excretion and lysosomal exocytosis (fusion of lysosome the with cell membrane) are two distinct events in this mechanism [206]. A final route to exit available to charged particles is to escape the cell membrane directly by passive diffusion and membrane penetration (similar to direct penetration for particle uptake).

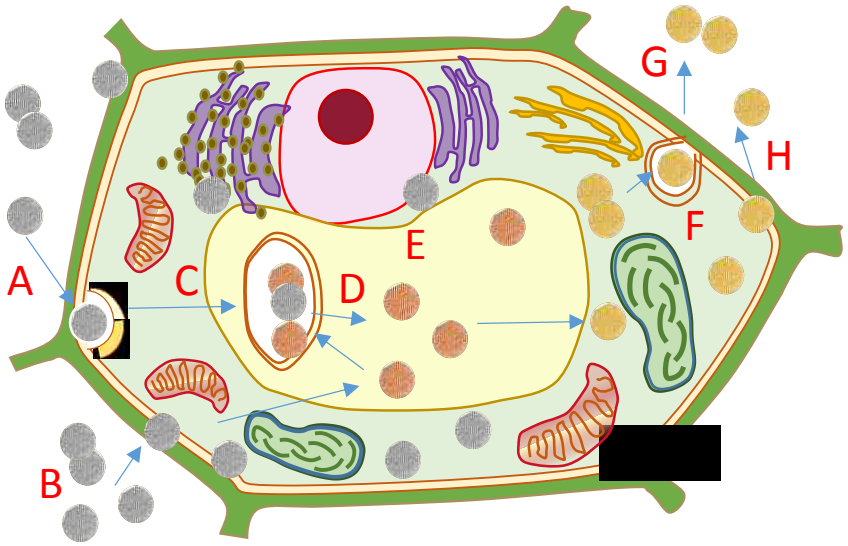

Figure 5.1 Schematic representation of possible pathways of MSNPTAs in and out of hairy root cells during nanoharvesting with uptake, intracellular transport and expulsion. Capital letters indicate a certain mechanism for uptake: (A) endocytosis and (B) direct penetration; for transport: (C) vesicle formation, (D) endosomal escape, (E) organelle entrapment and (F) secretory vesicle formation; and for expulsion: (G) exocytosis and (H) direct escape through passive diffusion.

The ESNP used for nanoharvesting were designed to have a positive surface charge to facilitate both entry and release from plant cells. First, both the plant cell wall [360] and plasma membrane are negatively charged [361], so positive nanoparticles would be expected to accumulate at the cell exterior which aids in cellular internalization [36]. Some organic character to the functional groups (in our case, aminopropyl) promotes association with lipids to help ESNP transport through membranes [184]. Positively charged particles have also been shown to induce endosomal escape, often achieved by functionalizing MSNPs with amines or polycations [62, 95, 202, 203]. The drop in pH during endosome aging causes protonation of amine groups, leading to destabilization of the endosomal membrane and nanoparticle escape [95]. Particle size is also important for endosomal

escape and 200 nm was established as maximum value for effective endosomal escape [183].

Positive charge has been associated with more effective particle expulsion from cells by both activated and passive mechanisms. Although nanoparticle expulsion mechanisms are not yet fully understood and differ among species [16], they are different from internalization – for example, smaller nanoparticles have been shown to be expelled faster while larger nanoparticles of the same type were taken up the fastest for a single cell type [186]. If particles are expelled by passive mechanisms, a high positive particle charge will aid in this route (just as for uptake). Positively charged surface functionalization also enhances activated exocytosis [207]. During exocytosis following endocytosis or direct penetration, vesicles containing nanoparticles are transported close to the cell membrane, and fusion causes the nanoparticles to be expelled. It was reported that positively charged particles bind with intracellular proteins and thus can aid in activated excretion as cells recognize them as foreign bodies. Polycation (amine and chitosan) functionalized silica nanoparticles have been shown to produce multiple vesicles highly prone to cellular secretion [95].

Based on these considerations, positively charged particles (MSNPTAs) were used to study concentration and time dependent uptake in *S. nemoralis* hairy root cells. **Figure 5.2** shows the fluorescence microscopy images along with bright field images for concentration dependent uptake of RITC-tagged MSNPTAs in the hairy roots after 24 h of exposure. The control (0 mg/mL) showed no fluorescent signal, and only a faint glow could be observed for 0.1 mg/mL MSNPTA concentration. For 0.5 mg/mL particle concentration, significant amount of particles were observed inside the root tissues. The most prevalent

location is in the cell walls, which glow uniformly and brightly in all images. The distribution of fluorescence in the interior of the cells is more heterogeneous, with only some of the cells showing bright interiors with both individual particles and clusters of particles. The intensity of both the walls and cell interiors increased at higher particle concentration (1 mg/mL and 2.5 mg/mL).

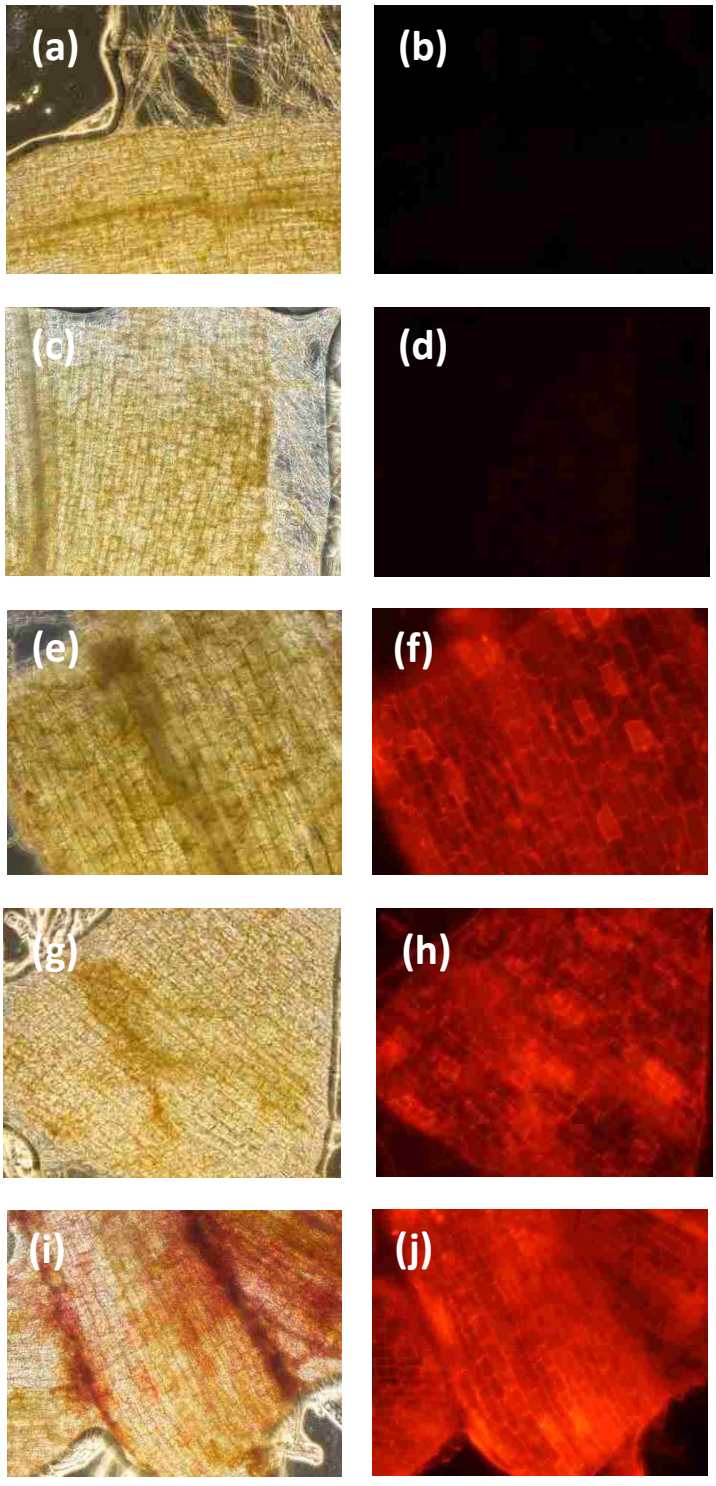

Figure 5.2 Concentration dependent bright field (left) and corresponding fluorescence microscopic image (right) of *Solidago nemoralis* hairy roots after RITC-tagged MSNPTA uptake for 24 h: (a) & (b) 0 mg/mL (control), (c) & (d) 0.1 mg/mL, (e) & (f) 0.5 mg/mL, (g) & (h) 1.0 mg/mL and (i) & (j) 2.5 mg/mL (exposure time 150 ms).

Time dependent (15 min to 48 h) fluorescent microscopy is presented in **Figure 5.3** for 1 mg/mL particle concentration. Initially (at 15 min), particles accumulate along the cell walls, and a few cells show more intense outlines indicating that particles begin to move inside at 1 h. More and brighter cells in the sample are observed due to internalization at 4 to 8 h. At 24 h, a large number of bright cells are observed, and by 48 h so many particles are taken up that it is difficult to distinguish cell walls – this may be because constant acquisition time was used for all images to give semi-quantitative information about the progress of particle uptake. These observation support the idea that particles initially undergo charge driven adsorption into cell walls and membranes and then get internalized [36].

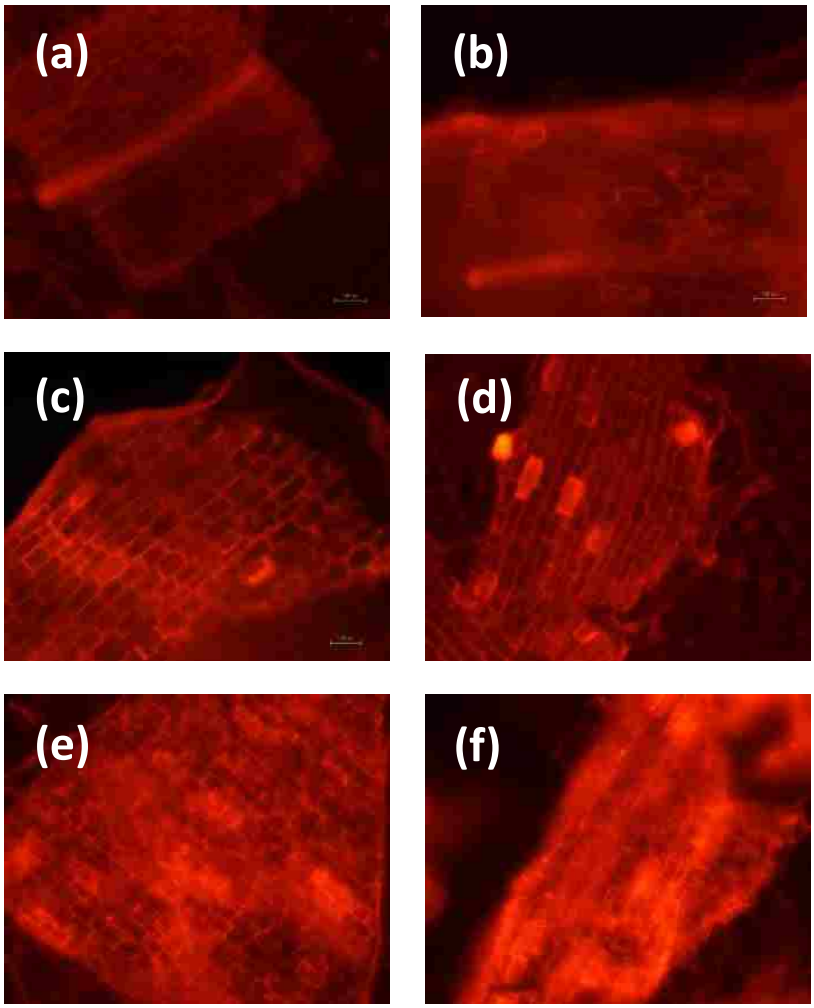

Figure 5.3 Fluorescence image of hairy roots showing time dependent uptake of MSNPTAs for 1.0 mg/mL nanoparticle concentration after an incubation time of: (a) 15 min, (b) 1 h, (c) 4 h, (d) 8 h, (e) 24 h and (f) 48 h (exposure time 150 ms).

Uptake of MSNPTAs into *S. nemoralis* roots was quantified by collecting root samples after 24 h of uptake, calcining the roots, and using the Ti-content to determine nanoparticle uptake, as summarized in **Table 5.1**. Internalized particles per gram roots were measured by dissolving the ashes (containing particles) in sulfuric acid and using a hydrogen peroxide assay for Ti. A calibration curve was constructed with constant amounts of root ash and known amounts of particles (**Appendix Figure C.1**). Consistent with the fluorescence microscopy presented in **Figure 5.2**, the amount of particles taken up by the

roots is concentration dependent, with 2.5 mg/mL (used previously for nanoharvesting [39]) initial particle concentration induces an uptake after 24 h of 2.6 ± 0.13 mg particles/g roots. The uptake appears to reach a plateau as particle concentration increases, and applying a Langmuir model to the data (**Appendix Figure C.2**) gives an equilibrium coefficient for particle uptake of 0.26, and a maximum of 6.0 mg/g. These values are much smaller than literature results for non-functionalized nonporous silica nanoparticles (70-150 mg/g roots for 0.25-1 mg/mL [187]). While there might be species-dependent variation (*A. thaliana* in the prior work), this primarily suggests that continuous expulsion of charged particles may be occurring along with uptake such that internalization-expulsion is a dynamic phenomenon during nanoharvesting with an equilibrium coefficient < 1.0. Zeta potential of the MSNPTAs (with uptake experiments performed at various concentration) is also provided in **Table 5.1**, which shows change in negative direction after exposure to the roots, consistent with when MSNPTAs were attached with flavonoid quercetin (zeta potential -1.5 mV at pH 4.0), suggesting active metabolites being isolated from the roots.

Table 5.1 Concentration-dependent MSNPTA uptake at 23 ºC in hairy roots following 24 h exposure determined by calcination and Ti-content analysis and the zeta potential of the particles following exposure to the roots.

Nanoparticle concentration (mg/mL)	0.10	0.50	1.0	2.5	10
Particle in roots (mg/g roots)	0.20	0.36	1.1 ± 0.08[a]	2.6 ± 0.13[a]	4.24
Zeta potential at pH 4.0 (mV)	+5.4	-1.7	-6.8	+4.3	+30.1

[a] The range is determined from triplicate measurements.

To differentiate between activated and passive penetration during internalization, uptake experiments was performed at 4 ºC and 23 ºC and the results are presented in **Table 5.2** (first row). It should be noted that results in **Table 5.2** are from a different set of experiments, thus slightly different from that presented in **Table 5.1** for 1 mg/mL particles. It was reported that all activated mechanisms for uptake in plant cells are effectively stopped at 4 ºC because of the large activation energy of protein-mediated endocytosis [26, 350]. Here, the amount of MSNPTA taken up after 24 h was reduced by roughly half (1.2 ± 0.14 mg/g) at 4 ºC compared to at 23 ºC (2.6 ± 0.15 mg/g), suggesting that activated and passive uptake occur in parallel for MSNPTAs. In contrast, for only TiO_2 functionalized particles (MSNPTs), 1.17 ± 0.08 mg particles were measured inside the roots at 23 ºC after 24 h of exposure to 2.5 mg/mL solution of particles, whereas only about 15% of this value was observed at 4 ºC (**Table 5.3**), suggesting primarily an activated nanoparticle uptake mechanism in the absence of amine groups. These results support the idea that for weakly charged particles (MSNPT charge shown in **Table C.1**), the predominant mechanism of uptake is endocytosis [351], which is consistent with the uptake of unmodified particles in plant roots for both TiO_2 nanoparticles with average diameter of 140 nm and silica nanoparticles with average diameter up to 200 nm [187, 330]. Xing et al. also showed that silica-terminated nanoparticles are taken up by endocytosis [362].

Table 5.2 Effect of temperature on the uptake, recovery and retention of MSNPTAs by hairy roots as measured from calcined roots following 24 h of exposure and from fresh recovery solution after 24 h of recovery, respectively. Initial particle concentration of 2.5 mg/mL in 15 mL MS media supplemented by sucrose and antibiotics was exposed to 300 mg roots.

Uptake temperature	4 ºC	23 ºC		
Amount taken up (mg/g roots)	1.2 ± 0.14	2.2 ± 0.15		
Recovery temperature	4 ºC	4 ºC	23 ºC	
Recovery media	Fresh solution	Fresh solution	Fresh solution	Solution containing 2.5 mg/mL particles
Amount recovered (mg/g roots)[b]	1.15 ± 0.096	2.04 ± 0.23	2.01 ± 0.14	1.93 ± 0.069
Amount retained (mg/g roots)	0.087 ± 0.023	0.17[c]	0.16 ± 0.027	2.3 ± 0.13

[a] The range is determined from multiple (triple or quadruple) measurements, [b] recovery is the average value ≥ 4 h and [c] single measurement.

Table 5.3 Effect of temperature on the uptake and retention of MSNPTs by hairy roots as measured from calcined roots following 24 h of exposure and 24 h of recovery, respectively. Initial particle concentration of 2.5 mg/mL in 15 mL MS media supplemented by sucrose and antibiotics was exposed to 300 mg roots.

Uptake temperature	4 ºC	23 ºC	
Amount taken up (mg/g roots)	0.17 ± 0.063	1.2 ± 0.081	
Recovery temperature	4 ºC	4 ºC	23 ºC
Amount retained (mg/g roots)	0.049 ± 0.022	1.1[b]	0.064 ± 0.041

[a] The range is determined from multiple (triple or quadruple) measurements and [b] single measurement.

Time dependent recovery of particles into fresh medium after uptake was measured by fluorescence spectroscopy of RITC-labeled particles in solution. Initially a calibration curve was constructed in plant media (also used for the recovery experiments) with known amounts of RITC-tagged MSNPTAs (**Appendix Figure C.4**). **Figure 5.4** shows time and temperature-dependent recovery after uptake from a 2.5 mg/mL solution of RITC-tagged MSNPTA for 24 h. Similar to uptake, activated expulsion of nanoparticles (exocytosis) is also energy dependent and can be switched off at 4 ºC, which can be used to identify dominant mechanism for both nanoparticle internalization and expulsion [26]. Three different recovery experiments were performed in which particle-loaded roots were rinsed and placed into fresh solution (plant media): 4 ºC recovery after uptake at 4 ºC, 4 ºC recovery after uptake at 23 ºC and 23 ºC recovery after uptake at 23 ºC. Another recovery experiment was performed (termed "Exchange") in which MSNPTA-RITC were recovered from hairy roots into a solution of non-fluorescent MSNPTA solution (2.5 mg/mL), to see whether non-fluorescent particles can replace and exchange with fluorescent particles inside the root cells. It can be seen from **Figure 5.4** that more than 90 % of the fluorescent particles inside the hairy roots after uptake were expelled within 2 h, regardless of temperature or the presence of untagged MSNPTA in the media.

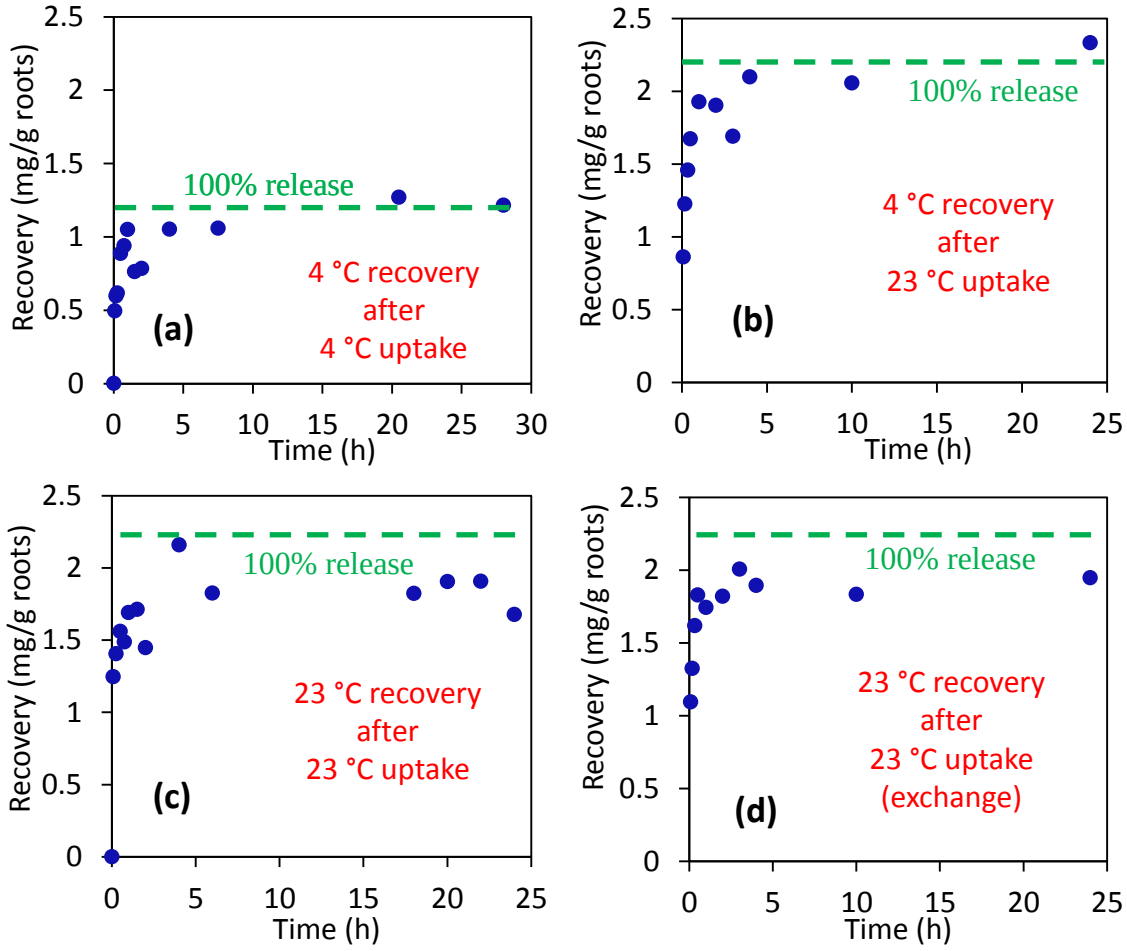

Figure 5.4 Time dependent recovery of fluorescently tagged MSNPTAs in MS media after 24 h of uptake with initial particle concentration of 2.5 mg/mL: (a) recovery at 4 ºC in fresh solution after uptake at 4 ºC, (b) recovery at 4 ºC in fresh solution after uptake at 23 ºC, (c) recovery at 23 ºC in fresh solution after uptake at 23 ºC, and (d) recovery at 23 ºC in non-fluorescent particle solution (2.5 mg/mL) after uptake at 23 ºC.

It has been reported that nanoparticle internalization or recovery reaches thermodynamic equilibrium within a certain timeframe [184], which was shown to be 20 min for single wall carbon nanotube [363]. Cells with internalized nanoparticle have a strong tendency to repair their damaged membrane and spontaneously send vesicular materials towards the cell membrane [339], where particles can be steadily exocytosed by secretary vesicle formation [341]. In mammalian cells, more than half of the internalized particles were reported to be transported to the cell membrane and steadily expelled,

reaching steady state within 1-2 h [186, 342]. Similar dynamics were found here (**Figure 5.4**), suggesting a similar spontaneous particle release process.

The average recovery of RITC-labeled MSNPTA from roots at steady state (after 4 h for each time-dependent recovery plot) is presented in **Table 5.2** for MSNPTAs to elucidate this point more clearly. Regardless of temperature and the presence of untagged particles, roughly 90% of the particles inside the roots were expelled at steady state. This is roughly consistent (within experimental uncertainty) with the steady-state Langmuir constant of 0.26, which would imply about 80% particle expulsion at equilibrium. Comparable recovery at 4 ºC and 23 ºC indicates a non-activated mechanism of particle expulsion. We were not able to measure the time dependent recovery of particles without amine groups (MSNPT), since there were no fluorescent binding groups their surface, but the amounts recovered for MSNPT samples can be inferred from the amount retained by the roots after recovery experiments were complete (see below).

After the recovery experiment was complete, the amounts of particles retained by the roots were quantified by calcining the roots followed by dissolving the ash in sulfuric acid and using the hydrogen peroxide Ti-assay. Regardless of recovery temperature, a small amount of MSNPTA was found inside the roots after recovery (**Table 5.2**), which is consistent with the recovered amount found in solution within the experimental uncertainty. On the other hand, for MSNPT samples (**Table 5.3**), although small fractions of particles were retained by the roots at 23 ºC, almost all of the particles were retained by the roots at 4 ºC (no expulsion) suggesting primarily an activated mechanism of expulsion for MSNPT. This result provides important insights into what was found during nanoharvesting, where no flavonoid isolation was found in the absence of amine groups

(**Chapter 4**/[39]). This is not because MSNPT are not taken up at all by the root cells; rather **Tables 5.2 and 5.3** suggests that the difference in uptake (and expulsion) mechanism in the absence of amines is responsible for the difference in nanoharvesting effectiveness.

The distribution of nanoparticles inside cells and their ability to access the cytosol prior to excretion depends largely on the uptake pathway [201]. In plant cells, the vacuole is the primary place where cells store metabolites and other hydrophobic compounds [339], but quercetin derivatives were reported to accumulate in the nucleus, plasma membrane and in several endomembrane systems [337], so nanoparticles should be able to travel there in order to bind flavonoids during nanoharvesting. The inability of MSNPT to gain access to flavonoids can most likely be ascribed to their lack of endosomal escape, which turns out to be tremendously important in nanoharvesting. Since MSNPTs are only internalized and excreted through activated mechanisms, they probably remain mainly associated with endosomes and are not able to fully explore organelles with high flavonoid content. The cationic nature of MSNPTA is found to allow the particles to enter and leave the cell by direct penetration. This allows the particles to explore the cytosol, endomembrane systems and potentially vacuoles of plant cells, thus giving them the opportunity to bind significant concentrations of flavonoids prior to release. A first order kinetic analysis is performed on the nanoparticle recovery data of **Figure 5.4** (see **Appendix Figure C.5** and **Table C.2**), which gives an overall first order kinetic constant of 2.5-3.7 h^{-1} and an average residence time inside the cells 16-25 min. Because the steady-state root binding constant is < 1.0, the time of interaction with the cell is dominated by expulsion dynamics, with an average residence time of < 0.5 h in hairy root tissue prior to release.

Both endo- and exocytosis as well as non-activated penetration are dynamic processes that occur simultaneously and depends on the particle concentration inside and outside of the cells [201]. Uptake and release occur at different sites and through different molecular interactions, so the process is not at equilibrium, but the process reaches steady state with kinetics consistent with first-order uptake and release. To demonstrate the dynamic exchange of particles, roots loaded with RITC-tagged MSNPTA (from 2.5 mg/mL solution after 24 h) were placed into plant medium containing 2.5 mg/mL of untagged MSNPTA. The dynamics of release of the fluorescent particles were the same as for fresh medium (**Figure 5.4d**), and just like for the experiment with fresh medium, 90% fluorescent particles were recovered in solution (**Table 5.2**). The hypothesis for this experiment was that there would be simultaneous uptake of untagged particles at the same time that fluorescently tagged particles were expelled. The population of RITC-tagged particles reached the same dynamic equilibrium as in the absence of fresh particles, and untagged particles continued to be taken up as well. The total amount of particles inside the roots after the "exchange" experiment (measured by calcination of the roots and Ti-assay) was found to be statistically the same as the amount of tagged particles initially in the roots (**Table 5.2**), showing that dynamic exchange happens between non-fluorescent and fluorescent particles. This demonstrates definitively that internalization and expulsion processes during nanoharvesting of flavonoids from roots are continuous dynamic processes with an average residence time in the roots of 1-2 h. Surface functionalization with amine groups was found to provide a non-activated route for uptake and release of the particles into root cells, while activated endo- and exo- cytosis mechanisms dominated in the absence of amines. This suggests that particles with amines are able to directly explore

the cytoplasm and flavonoid-containing organelles of plant cells during nanoharvesting, thus giving positively charged particles an opportunity to bind and remove metabolites from plant cells prior to being excreted.

5.5 Conclusions

The interaction of engineered silica nanoparticles (ESNP, functionalized with TiO_2 and amine groups) with *S. nemoralis* hairy root cultures was investigated in detail, in order to elucidate the mechanism of nanoparticle entry and exit during nanoharvesting of polyphenolic flavonoids. The mechanism of nanoparticle uptake and recovery was studied by chemical analysis of particles internalized in roots with Ti as a tracer, and by fluorescence spectroscopy of RITC-tagged particles recovered solution. Intracellular transport and fate of the particles were interpreted from temperature and surface charge dependent uptake and recovery experiments.

Fluorescence microscopy showed strong dependence of particle uptake on concentration that followed a Langmuir-like dependence with a steady-state equilibrium coefficient of 0.26 and a maximum MSNPTA uptake of 6 mg/g of roots. Time dependent uptake imaging showed initial distribution of particles along the cell walls (consistent with electrostatic interactions between cell wall components and the cationic particles) followed by intracellular localization after 4 to 8 h. When quantified, the amounts of MSNPTAs inside the root cells were significantly less than prior literature values for non-functionalized particles in whole plants, which suggests a dynamic process of the functionalized particles in hairy roots involving continuous expulsion as well as uptake of particles.

When particle recovery in solution after uptake was quantified by fluorescence spectroscopy, the results showed that around 90% of internalized particles were spontaneously expelled from the root cells within 1-2 h. Uptake and recovery experiments were also conducted at 4 °C and 23 ºC in order to understand and differentiate between possible mechanism of transport (activated or non-activated). With amines present (for

MSNPTAs), parallel activated (endocytosis) and non-activated (direct penetration) mechanisms were indicated by a reduction by about half in the amount of particles taken up at 4 °C. On the other hand, only activated internalization happens for solely TiO_2 functionalized particles (MSNPTs) without any amine groups. The particle escape mechanism from the roots was also found to be surface charge dependent. With amines, only non-activated (temperature independent) particle recovery was observed, while in the absence of amines only an activated mechanism was observed. This is a significant finding which provides valuable insights into the importance of particle surface charge for successful nanoharvesting, as found for polyphenolic flavonoids previously. These results suggest that without amines, particles can enter and leave plant roots, but because they are associated with endosomes for most of the time, they are unable to explore the cell interior. With amines, however, the particles enter cells by direct penetration, giving them access to the cytosol, and organelles where flavonoids are located, thus allowing them to bind target compounds to Ti before they are spontaneously excreted. Dynamic exchange between fluorescent and non-fluorescent MSNPTAs was also observed during recovery in a solution containing non-fluorescent particles, which suggests continuous uptake and expulsion processes that facilitate biomolecule nanoharvesting using engineered silica nanoparticles (ESNP) with both surface charge modifying amines and flavonoid-binding Ti-sites.

CHAPTER 6. CONJUGATION STRATEGY FOR OLIGOPEPTIDES TO MESOPOROUS SILICA NANOPARTICLES USING DIAZIRINE-BASED HETEROBIFUNCTIONAL LINKERS

6.1 Summary

Successful strategies for attachment of oligopeptides to mesoporous silica having sufficient pore size to load biomolecules should utilize the high surface area of pores to provide an accessible, protective environment. Many functionalization strategies involving peptide linkers have been proposed, but the resulting functionalization is often not robust or well-suited to attachment within within mesopores. A two-step oligopeptide functionalization strategy is examined here using diazirine-based heterobifunctional linkers. Mesoporous silica nanoparticles (MSNPs) with average pore diameter of ~8 nm and surface area of ~730 m^2/g were synthesized and amine functionalized. Tetrapeptides Gly-Gly-Gly-Gly (GGGG) and Arg-Ser-Ser-Val (RSSV), and a peptide comprised of 4 copies of RSSV (4RSSV) were covalently attached *via* their N-terminus to the amine groups on the particle surface by a heterobifunctional linker, sulfo-succinimidyl 6-(4,4'-azipentanamido)hexanoate (sulfo-NHS-LC-diazirine, or SNLD). SNLD consists of an amine-reactive NHS ester group and UV-activable diazirine group, providing precise control over the sequence of attachment steps. Attachment efficiency of RSSV was measured using fluorescein isothiocyanate (FITC)-tagged RSSV (RSSV-FITC). TGA analysis shows similar efficiency (0.29, 0.31 and 0.26 mol peptide/mol amine, respectively) for 4G, RSSV and 4RSSV, suggesting a generalizable method of peptide conjugation. The oligopeptide-functionalized nanoparticles have increased capacity to adsorb β-estradiol adsorption relative to nonfunctionalized or amine-functionalized MSNPs, confirming accessibility of the peptides. The technique developed here for the

conjugation of peptides to MSNPs provides for their attachment in pores and can be translated to selective peptide-based separation and concentration of therapeutics from aqueous process and waste streams.

6.2 Introduction

Synthetic organic functional groups that can mimic biological specificity of host-guest interactions have been used for analysis, sensing and isolation of different biomolecules, especially in affinity column chromatography [364-367]. Recent progress in supramolecular chemistry has resulted in tailor-made organic functionalities with high selectivity and specificity toward an array of biomolecules and therapeutic ligands, which can be used for their selective separation [368, 369]. Synthetic peptides, in particular, have tremendous molecular recognition and selective binding capabilities and a large volume of peptide libraries with different binding properties has been developed during the last two decades [370-372]. Oligopeptide mimics of biological binding sites (of longer proteins) on solid supports are durable, reusable and cost-effective for affinity separations [370].

Mesoporous silica materials are an ideal support for high affinity functional groups due to their high surface area, tunable pore size and ease of surface modification [125, 373]. Use of mesoporous silica functionalized with affinity binding sites is widespread in chromatography [374, 375]. We hypothesize that functional oligopeptide attached or conjugated MSNPs can also be used to selectively harvest specific metabolites from living plant cells. This would be the reverse process of biomolecule delivery to cells using functional peptide or protein conjugated nanoparticles [120, 125, 376, 377]. Plants are the natural factories of various therapeutic molecules, which are difficult to synthesize by chemical methods, and conventional extraction process involves maceration of the host plant cultures in order to gain access to the metabolites [39]/(**Chapter 4**). During nanoharvesting, functionalized nanoparticles enter the plant cell tissue, bind the target molecule, and are excreted into the media while keeping the valuable plant cell culture viable. A potential benefit of oligiopeptide binding of plant metabolities relative to general

chelation to TiO_2 (**Chapter 4**) is specificity. In extending the concept of nanoharvesting to specific compounds, conjugation of these organic functionalities (oligopeptide) inside the pores of MSNPs should provide high stability and capacity.

The most common biomolecule linking strategy is to functionalize the silica surface with amine groups and then to covalently link the amine moieties with the N-terminus of peptide/protein molecules. Bifunctional linkers [121, 378-380] for amine-amine conjugation can be mainly divided into two types: homo-bifunctional and hetero-bifunctional. Homo-bifunctional linkers such as bis(sulfosuccinimidyl)suberate (BS^3) have two amine-reactive NHS ester groups at the either end, which can react with amine functionalized particles at one end and with the amine terminal group of a peptide at the other [121, 381, 382]. During peptide conjugation to porous particle surface using homo-bifunctional linkers containing amine reactive NHS groups at both end, competitive rapid hydrolysis of ester groups poses huge problems during attachment, and proteins may be physically adsorbed rather than attaching covalently [128, 383, 384], unlike simultaneous cross-linking of two proteins or peptides in solution. Controlling the rate of reaction of the linker with both the peptide and the surface is also challenging and homo-bifunctional linkers lack the specificity and precise control of attachment orientation.

A hetero-bifunctional linker containing an amine reactive end and a UV-activable end during peptide conjugation overcomes the limitations of homo-bifunctional linkers. The activation of the UV active group by a light source provides precise control over the attachment mechanism and location. One of the most common hetero-bifunctional linkers for peptide/protein conjugation is phenyl azide based: sulfosuccinimidyl 6-(4-azido-2-nitrophenyl-amino) hexanoate (sulfo-SANPAH) [383, 385, 386]. The UV-activable end of

sulfo-SANPAH is activated at a wavelength < 320 nm (as low as 260 nm) [121, 387], which can cause denaturation of proteins. Also, the larger size of the aromatic photoactive group in sulfo-SANPAH can create steric hindrance [388]. On the other hand, the diazirine group is activated at higher wavelength (340-370 nm), and thus does not cause denaturation of proteins/peptides. As a result, diazirine has been used extensively in photolabeling agents for proteins [387, 389, 390]. Diazirine-based photoreactive linkers have better stability compared to commonly used aromatic azide photo-linkers [391, 392]. The linkers can also be designed to provide optimal peptide orientation for ligand attachment from the bound surface using spacers. For example, succinimidyl 6-(4,4'-azipentanamido) hexanoate (NHS-LC-diazirine) provides a sufficient spacing arm for the biomolecule to avoid effects of surface interactions on its properties [393]. The NHS-LC-diazirine linker has been shown to be stable under ambient lighting conditions [393, 394]. The derivative sulfo-NHS-LC-diazirine (SNLD) contains a charged sulfate group that enhances its aqueous solubility and as a result can be used in physiological media [395].

Covalently linking peptides on the inner surface of the pores of mesoporous silica nanoparticles using hetero-bifunctional linkers has not been reported, most likely due to the insufficient pore size (< 4 nm) in previously synthesized silica nanoparticles. Large pores are required for peptides and linkers to infiltrate the interior surface without pore blockage. Surfactant templating with cationic surfactants such as alkyltrimethylammonium salts typically produces pore sizes around 3 nm in diameter [38, 69, 71]. Only recently, surfactant templated synthesis of MSNPs with < 170 nm particle diameter and pore sizes of 4.5 nm to 8 nm has been reported by using pore expanding agents [83, 84]. These particles facilitate the conjugation of long peptide sequences and proteins along with

sufficient spacer arms to prevent strong surface effects. A study of peptide conjugation to the inner surface of silica microbubbles (cavity size 0.55-0.65 mm) using NHS-diazirine has been reported [396]. However, the pore size of microbubble is thousands of times larger than MSNPs, so there is a need to investigate the use of NHS-diazirine linkers in pores comparable in size to peptides and proteins. Based on previous studies [383, 396, 397], we hypothesize that oligopeptides will preserve their solution binding properties in expanded mesopores (> 4 nm diameter) when a spacer of 1.25 nm (SNLD arm length [398]) is provided between surface functional group and the peptide N-terminus.

This work examines strategies to conjugate functional oligopeptides to large-pore amine-functionalized MSNPs (~ 8 nm diameter pores) using diazirine based hetero-bifunctional linker sulfo-NHS-LC-diazirine (SNLD). The four-amino acid peptide RSSV (Arg-Ser-Ser-Val) was selected for this application from a combinatorial peptide library based on its ability to bind *β*-estradiol (equilibrium constant, $K = 6 \times 10^4$ M^{-1}) *via* column chromatography with good selectivity versus other steroids [141]. Conjugation of the peptide 4RSSV (Arg-Ser-Ser-Val-Arg-Ser-Ser-Val-Arg-Ser-Ser-Val-Arg-Ser-Ser-Val), a four-repeat peptide of the original RSSV 4-mer, and 4G (Gly-Gly-Gly-Gly) to the nanoparticles is investigated to test the versatility of the conjugation strategy for peptides of varying length and amino acid sequence. Two conjugation strategies based on first attaching the linker to either the particle or peptide are proposed. For Type-1 attachment, the linker is first attached to the surface amine group using NHS-ester and then the peptide amine group is attached to the linker using UV-activation of diazirine. For Type-2 attachment, the linker is first attached linker to peptide using NHS-ester followed by attachment to surface using UV-activation (**Figure 6.1**). The anticipated advantage of

Type-1 attachment is that unbound linkers can be removed by washing after the first step and before attachment to peptides. However, activated diazirine is indiscriminate toward N-H or O-H moieties and can result attachment to either terminus of the peptide. Activation of the diazirine group under UV light has also been shown to bind the carboxyl moieties of proteins to some degree [399]. Another problem with Type-1 attachment in a porous system is the possible attachment of the diazirine moiety with another amine group inside the pores. Specific attachment of the peptide N-terminus to the linker during first step is the main advantage of Type-2 attachment. In addition, the peptide-attached linker can diffuse into the pore prior to the photoactived conjugation to the surface, promoting reactions within the pores and not just at the surface. Attachment of diazirine to O-H moieties of particles provide no disadvantages (in fact it is probably advantageous in keeping some of amine groups unattached and positively charged) compared to Type-1 attachment. However, during the second step of Type-2 attachment, the activated diazirine of the peptide-attached linker can react with the C-terminus of another peptide. These solution-based complexes would be removed during washing but would result in inefficient use of peptide and linker. Considering these *pros and cons*, the attachment efficiency is examined for both of these methods using fluorescent spectroscopy of fluorescein isothiocyanate (FITC)-labeled peptide and TGA analysis. The binding capacity of peptide-conjugated particles for estrogen is measured by β-estradiol adsorption, where the ability to increase binding capacity of 4RSSV relative to RSSV is examined.

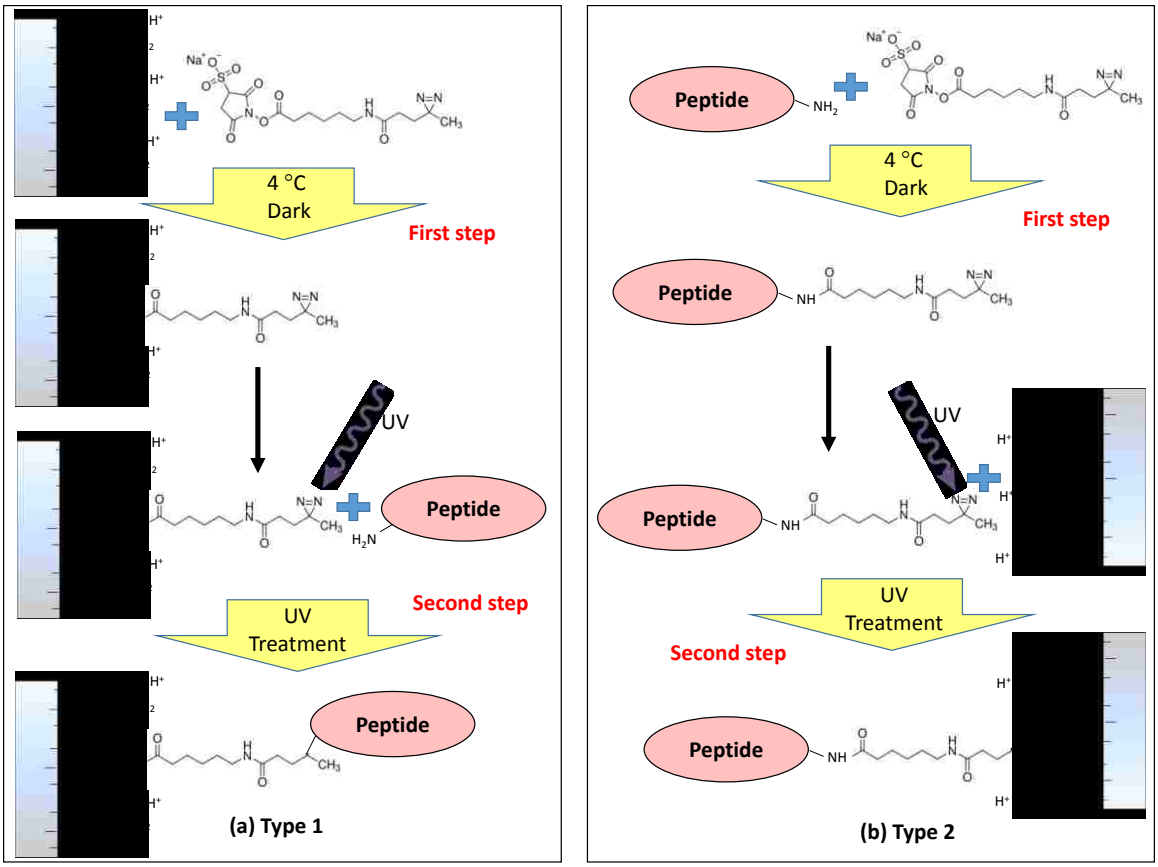

Figure 6.1 Schematic diagram of the peptide attachment strategies using hetero-bifunctional cross-linker Sulfo-NHS-LC-Diazirine (SNLD): (a) Type 1 – attaching the linker to the particle amine group first using the NHS group and then attaching to peptide amine group using the UV-reactive diazirine group and (b) Type 2 - attaching the linker to the peptide amine group first using the NHS group and then attaching to particle amine group using the UV-reactive diazirine group.

6.3 Materials and Methods

6.3.1 Chemicals and Reagents

Tetrapropyl orthosilicate (TPOS, 95%), phosphate buffer saline (PBS) tablets, (3-aminopropyl) triethoxysilane (APTES, 99%) and N, N-dimethylformamide (DMF, molecular biology grade) were purchased from Sigma-Aldrich. Cetyltrimethylammonium bromide (CTAB, 99.8%) was purchased from MP Biomedicals; NaOH pellets (≥ 97%) from EMD Millipore; Acetone (≥ 99.5%) from BDH analytical; 1,3,5-triisopropylbenzene (TIPB, > 95%), triethanol-amine (TEA, > 98%) and fluorescamine from Alfa-Aesar; ultrapure deionized ultra-filtrated (DIUF) water, ethanol (200-proof), 12 N HCl (ACS grade) from Fisher Scientific. Heterobifunctional linker sulfo-NHS-LC-diazirine (SNLD, Pierce™) was purchased from Thermo-Fisher Scientific and used for peptide conjugation.

6.3.1.1 Oligopeptide synthesis

Peptides 4G (GGGG) was obtained from Sigma-Aldrich; RSSV and 4RSSV were synthesized by Genscript (Piscataway, NJ), and RSSV-FITC was synthesized by Lifetein (Hillsborough, NJ) using solid-phase peptide synthesis and purified to > 95% yield using reverse phase high pressure liquid chromatography (RP-HPLC). RSSV-FITC was designed (sequence Arg-Ser-Lys(FITC)-Val) by replacing the serine at position 3 with a lysine to incorporate the fluorescein isothiocyanate (FITC) fluorescent label while maintaining the peptide arginine positive charge for peptide function and the single free amine (N-terminus) for attachment. All peptide sequences were confirmed to be of the correct molecular mass by LC-MSMS analysis following purification. Lyophilized peptide was

resuspended in PBS buffer (pH 7.4) to a final concentration of 1.7 mg/mL 4G, 3 mg/mL RSSV and 12 mg/mL 4RSSV before conjugation to particles.

6.3.2 Mesoporous Silica Nanoparticle (MSNP) Synthesis

MSNPs were synthesized using a modification of the method described by Yamada et al. [84], where TIPB was used to swell the CTAB micelles, the pore forming agent, during surfactant-templated synthesis. Initially, 0.56 ml of TEA and 3.0 g of CTAB was added to 360 mL of DIUF water. The solution was kept stirring at 80 ºC for 2 h for complete mixing and emulsion formation and 16 mL of TIPB was added under vigorous mixing. After 30 min, a complete colloidal state (oil-in-water) was obtained and 4.77 mL of TPOS was added with constant stirring. Then, the solution was stirred vigorously for 12 h to obtain white solid particles. The particles were then separated by repeated centrifugation and washing and the surfactant was removed by acidic ethanol (2 M HCl in ethanol) washing before drying at 84 °C overnight.

6.3.3 Amine Functionalization and Quantification.

Amine functionalized MSNPs (MSNPAs) were obtained by condensing APTES on the particle surface using modified literature procedures [101, 125, 322, 358]. 200 mg of MSNPs were uniformly dispersed in 25 mL of dry ethanol by sonication for 15 min. 0.5 mL of APTES was added dropwise under constant stirring, and the solution was kept stirring in a closed vessel for 24 h at RT. Particles were centrifuged with repeated ethanol washing, and cured at 84 ºC for 24 h. After curing, particles were stirred in excess ethanol

for 24 h to remove any remaining loosely-bound amine species. The functionalized particles were again washed 3 times with dry ethanol and dried at 84 ºC.

6.3.3.1 Amine Quantification

The amount of amine groups on the functionalized particle surface was determined by a previously reported fluorescamine assay after particle dissolution [324, 325]. 30 mg of particles were dissolved over an 8 h period in 30 mL of 0.02 M NaOH at room temperature under vigorous stirring. 100 μL of this solution and 1.0 mL of 1.0 mM fluorescamine in acetone were mixed with 2.0 mL of PBS solution at pH 7.4. The emitted fluorescence intensity of this solution was measured at 480 nm after excitation at 366 nm using a Varian Cary Eclipse fluorescent spectrophotometer. The calibration curve was prepared using known amounts of APTES.

6.3.4 Peptide Attachment to MSNPAs

For Type-1 attachment, 10 mg of MSNPAs were sonicated in 1 mL of PBS solution (pH 7.4) for 15 min to make a uniform dispersion and mixed with 3 mg of SNLD in 100 μL DMF at 4 ºC. The mixture was allowed to stir at 4 ºC overnight and the particles were centrifuged afterwards. Particles were washed with fresh PBS solution three times to remove excess and unbound linkers and then dispersed in 2 mL of PBS solution containing 3 mg of RSSV peptide at room temperature with vortex mixing. The solution was then stirred overnight to allow adsorption of peptide on particle surface and finally treated with UV light (Thorlabs M00284926, λ=365 nm, 1.2 A) with continuous stirring for 60 min, which was selected based on a series of attachment experiments using RSSV-FITC with

different UV treatment time (0, 10, 30, 45, 60, 90 and 120 min) (see **Section 6.3.6** for quantification). After UV treatment, peptide attached particles (MSNPA-RSSV) were separated by centrifugation and washed 5 times with fresh PBS solution and dried overnight in vacuum at room temperature.

For the Type-2 attachment, 3 mg of SNLD in 100 μL DMF is mixed with 3 mg of RSSV peptide in 1 mL PBS solution first at 4 ºC and the mixer is allowed to stir at 4 ºC overnight for the completion of linking with the amine terminal of peptide. 10 mg of MSNPAs were dispersed uniformly in 1 mL PBS with sonication and added to the peptide-linker solution. The combined mixture was allowed to stir overnight for adsorption of peptide-linker conjugation on the particle surface and then UV treated for 60 min with continuous stirring for the attachment to the particle surface. Finally, peptide attached particles were separated by centrifugation, washed thoroughly with fresh PBS solution and dried overnight in vacuum at room temperature. 4G and 4RSSV attachment using the Type-2 method is similar, but 1.7 mg of 4G or 12 mg of 4RSSV was used to keep the molar ratio of peptide:amines approximately the same as for RSSV.

6.3.5 Materials Characterization

A Hitachi S-4300 Scanning Electron Microscope (SEM) was used to examine the particle morphology. Particles were dispersed onto a 15 mm aluminum stub using double sided carbon tape, excess materials were blown off with dry N_2, and the samples were stored in a desiccator for 24 h. Prior to SEM analysis, the particles were coated with conductive Au-Pd alloy using an Emscope SC400 sputtering system. Average and standard deviation of particle diameters were calculated using 20 random particles using ImageJ

Software. Surface characterization was performed using nitrogen adsorption conducted at -196 ºC with a Micromeritics TriStar 3000 gas sorption instrument. Samples were degassed at 135 ºC for 4 h under flowing N_2 gas before analysis. The specific surface area, average pore diameter and pore size distribution were estimated using the Brunauer, Emmett and Teller (BET) isotherm and by the method of Barrett, Joyner and Halenda (BJH), respectively. To confirm the covalent linkage of peptides, Fourier transform infrared (FTIR) spectroscopy was conducted by a Thermo Nicolet Nexus 470 spectrometer with a deuterated triglycine sulfate (DTGS) detector. 0.5 g of anhydrous KBr and particles (0.5-1.0 wt %) were crushed with a mortar and pestle, and some of this powder was pressed into a pellet for transmission analysis. Dynamic light scattering (DLS) was used to measure the zeta potential of the particles in an Anton-Paar Lightsizer 500 instrument. Initially, a 1 mg/mL of uniform particle suspensions was made in DIUF water with sonication and diluted to around 0.1 mg/mL concentration before measurement. The pH of the solutions were adjusted by adding very small amount of 0.1 N of either HCl or NaOH solution in water as required to obtain desired pH, which were checked before every measurement with a benchtop pH-meter (Accumet Research AR25 dual channel). For measurements, the solutions were carefully placed in an Omega Cuvette consisting of an inverted Ω-shaped capillary tube without any air bubbles.

6.3.6 Quantification of Peptide Attachment

Fluorescein isothiocyanate (FITC) labeled RSSV peptide (RSSV-FITC) was used to quantify RSSV attachment efficiency to the particle amine groups by solution depletion with fluorescence spectroscopy. During quantification of peptide attachment, the amount

of particles and linkers and the solution volume were the same as during RSSV attachment. The amount of RSSV-FITC was adjusted to 5.5 mg (instead of 3 mg RSSV) to keep the molar ratio of peptide:amine the same. Fluorescence intensity of the solution after attachment was measured at an emission wavelength of 520 nm (peak fluorescence) after excitation at 495 nm (peak absorbance) and compared to a calibration curve prepared with known amounts of RSSV-FITC. Type-1 attachment was quantified using the calibration curve of RSSV-FITC (only peptide) fluorescence intensity, whereas Type-2 attachment was quantified using the calibration curve of SNLD-RSSV-FITC (peptide conjugated with linker) after correcting to account for photo-bleaching (intensity reduction) during the UV treatment period.

Thermogravimetric analysis (TGA) was performed to quantify the amount of organic groups (peptides) conjugated to the particle surface with a TA-SDT-Q600 simultaneous TGA/DSC instrument (TA Instruments). Particle samples were dried at 50 °C under vacuum overnight before performing TGA analysis from 25 °C to 500 °C with a ramp rate of 10 °C/min with constant dry air flow of 100 mL/min. Mass loss due to thermal decomposition and combustion of organics were analyzed for MSNPA, MSNPA-4G, MSNPA-RSSV and MSNPA-4RSSV compared to bare MSNP from 150 °C to 500 °C to determine the amount of amine grafting and peptide conjugation, respectively.

6.3.7 Estradiol Adsorption to Peptide Attached Particles.

β-estradiol binding to the particles was carried out in PBS buffer by solution depletion with LC-MS measurements. Particles (10 mg) were sonicated in 1 mL of PBS buffer (pH 7.4) until a uniform suspension of master solution obtained. A 100 µL aliquot

of 1 mg/mL particle suspension was placed in a 500 µL vial and 125 µL of PBS buffer added. Subsequently, 25 µL of 10 µM *β*-estradiol solution in ethanol was added and the mixture was incubated for 24 h with constant shaking. After 24 h, particles were separated by centrifugation and supernatants were analyzed by LC-MS (QExactive orbitrap mass spectrometer equipped with a Shimadzu Nexera UPLC). *β*-estradiol adsorption on the particle surface was quantified by depletion in concentration after exposure to the particles and depletions for all particles were normalized with respect to the depletion for MSNPA-RSSV.

6.4 Results and discussion

MSNPs with large pores (~8 nm average pore size) were synthesized by the method of Yamada et al. [84], where CTAB surfactant template was used to create pores and TIPB served to expand the micelle pore templates. After synthesis, the surfactants were removed from the pores by acidic washing. Particles were then functionalized with amine groups using APTES condensation. Spherical particles with average diameter of 146 ± 27 nm were obtained after template extraction, as seen in the SEM image presented in **Figure 6.2**. This particle size is suitable for cell uptake [184]. Surface characterization (surface area, pore volume and average pore size) was performed using nitrogen adsorption before and after amine functionalization (**Figure 6.3** and **Table 6.1)**. Nitrogen sorption of particles showed Type-IV isotherms (**Figure 6.3a**), consistent with the presence of mesopores. X-ray diffraction pattern did not show any peaks (data not shown), as the orientation of the pores is reported to be radial [84], which limits the size of oriented domains. The average pore diameter, as determined by the BJH method, was reduced with functionalization (7.9 nm to 7.6 nm) (**Figure 6.3b**). The surface area and pore volume were also reduced after functionalization, consistent with amine grafting inside the mesorpores. The large pore size of the particles (relative to CTAB-templating alone) allows the amine functional groups in the pores to be accessible for covalent attachment to the linkers and peptides. The amount of amines on particle surface was estimated by chemical analysis to be 1.53 mmol amine/g silica, corresponding to 64% of a monolayer coverage on the particle surface considering the projected area per aminopropyl group on the surface [324].

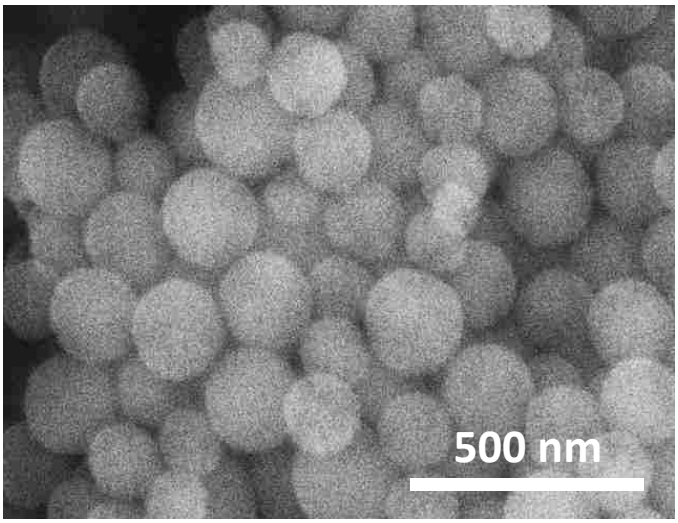

Figure 6.2 SEM image of bare MSNPs (large-pore) showing spherical particles with average particle diameter 146 ± 27 nm (average pore size ~8 nm from nitrogen adsorption).

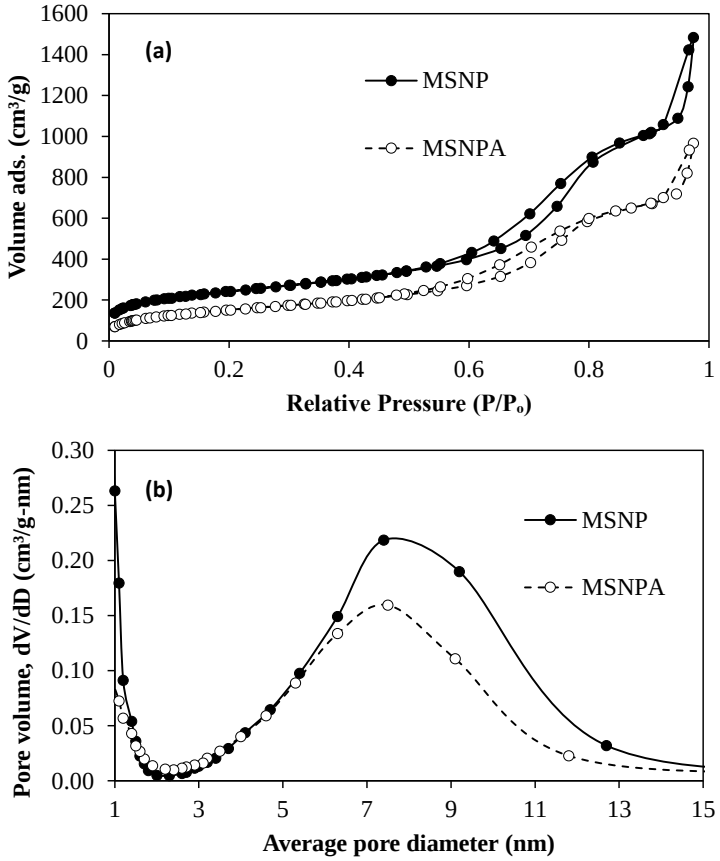

Figure 6.3 Surface property characterization of non-functionalized and amine functionalized MSNPs: (a) Nitrogen sorption isotherms, (b) BJH pore size distribution.

Table 6.1 Surface properties of MSNPs from nitrogen adsorption before and after amine functionalization.

Particle type	BET surface area (m^2/g)	Total pore volume (cm^3/g)	Average pore diameter (nm)[a]
MSNP	729	2.32	7.9 ± 2.2
MSNPA	469	1.50	7.6 ± 1.9

[a] The range is determined from the full width at half maximum (FWHM) of BJH pore size distribution.

Oligopeptides RSSV, 4G and 4RSSV were conjugated to amine functional groups on the particle using hetero-bifunctional linker SNLD, which provides a combination of amine-reactive chemistry with the photochemistry of diazirine groups for UV-activation. The silica pore walls should not hinder UV light within the particles; silica cavities with pore walls of much greater thickness (2 μm) have been functionalized using same UV treatment process [396]. UV activated conjugation is relatively rapid and efficient compared to NHS conjugation [400], and was determined to be optimum for 60 min using RSSV-FITC attachment (data not shown).

For RSSV, two different peptide conjugation strategy were used when a bifunctional linker is used as shown in **Figure 6.1**. For Type-1 attachment, SNLD was first conjugated to amine groups on the particles by using amine-reactive NHS moieties, and then the peptide N-terminus was attached to the linker using the diazirine end under UV treatment. The Type-2 attachment sequence was the opposite of this and the peptide N-terminus was first attached to the linker NHS end before attaching the diazirine end to particle amine groups by UV treatment. FITC-conjugated RSSV (RSSV-FITC) was used to evaluate these two oligiopeptide attachment strategies. Fluorophore-tagged peptides/proteins are widely used to calculate the attachment efficiency using homo- or

hetero-bifunctional linkers [401]. The UV-vis absorbance spectra of RSSV-FITC was measured (**Figure D.1** of **Appendix D**), where the absorbance intensities do not change with UV treatment up to 120 min of treatment. Fluorescence intensities were used to measure RSSV-FITC attachment by solution depletion, while accounting for photobleaching of the fluorescent moiety (using a control UV treatment in absence of any particles) during the functionalization process. UV illumination caused 25% and 35% reduction in intensity for RSSV-FITC and SNLD-RSSV-FITC after 60 min of treatment for Type-1 (**Figure D.2** and **D.3**) and Type-2 attachment (**Figure D.4** and **D.5**), respectively.

Based on the calculation of solution depletion after peptide attachment, attachment efficiency of Type-2 conjugation was found to be 0.43 mol peptide/mol amine, whereas for Type-1 conjugation it was 0.24 mol peptide/mol amine. Better efficiency of Type-2 attachment is consistent with literature involving antibody conjugation to polyamine yarns using NHS-LC-diazirine [402]. Part of the reason may be the high concentration of diazirine groups accessible to amine group in the pores during Type-2 attachment. Thus along with lower attachment efficiency, possible attachment to another amine group or the wrong peptide moiety makes Type-1 less attractive option. During Type-2 attachment, activated diazirine can attach to the carboxyl moiety of another peptide. However, if any activated diazirine binds with the C-terminus of another peptide, both of them will be removed during particle washing steps. Thus, Type-2 attachment is preferable to preserve the functionality of peptide. UV-vis absorbance and fluorescence intensity of the particles and the supernatant after Type-2 conjugation using RSSV-FITC with UV treatment is provided in **Figure 6.4**, compared to attachment without UV treatment. The absorbance

and fluorescence intensity of the particles increased only when they underwent UV treatment, whereas absorbance and fluorescence intensity decreased in the supernatant, consistent RSSV-FITC attachment to the particles. It should be noted that the particle external surface represents less than 2% of the total surface area and as a result peptide attachment should be only 0.02 mol peptide/mol amine if peptides only attach to the outer surface amine of the particles. Considering the relative amount of peptide attachment, the peptides are conjugated primarily to the amines inside the pores, as hypothesized.

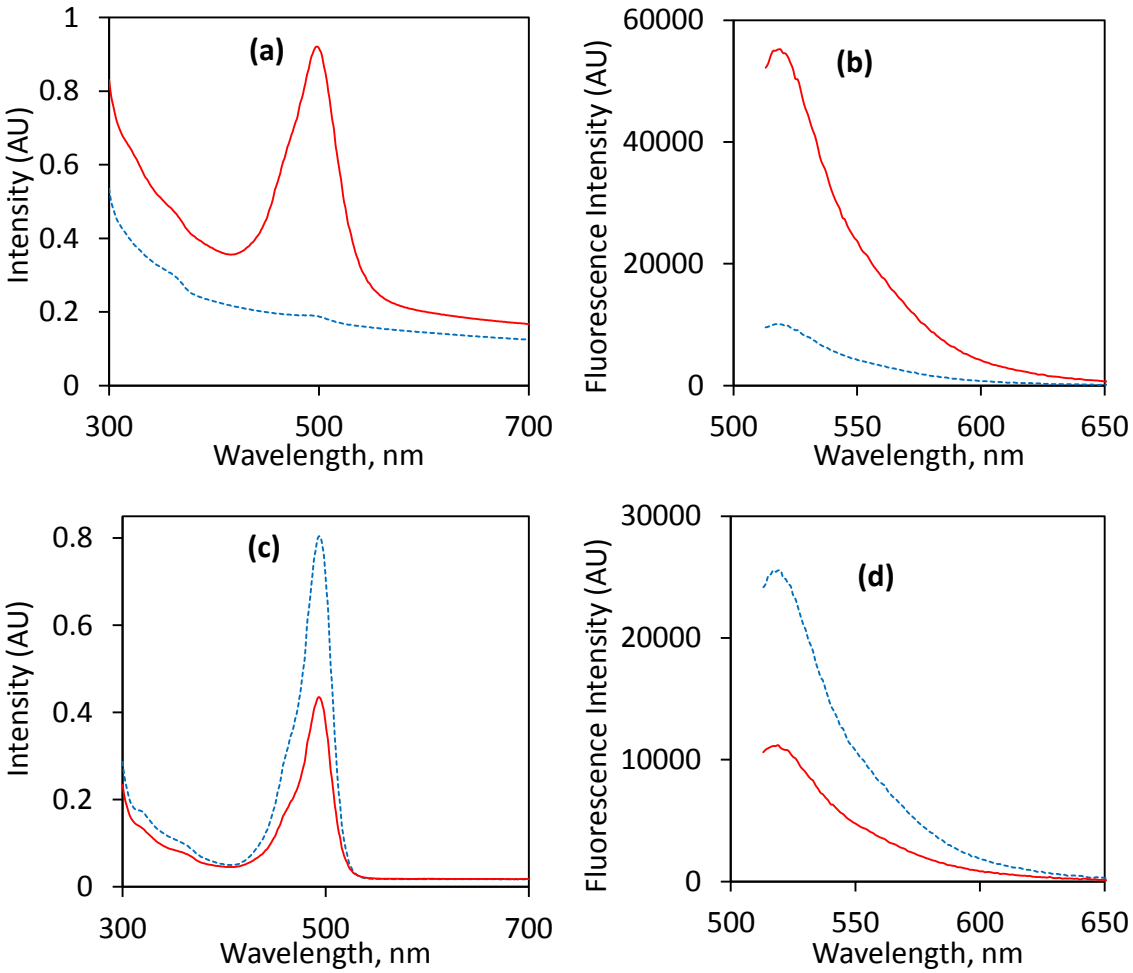

Figure 6.4 UV-vis absorbance (left) and fluorescence intensity (right) of (a) & (b) particles and (c) and (d) supernatant after RSSV-FITC attachment to the particles. Solid red lines and dashed blue lines represent results with or without UV treatment, respectively.

To show covalent linkage (not merely physical adsorption), FTIR spectra of the particles after peptide attachment were measured. The FTIR spectra of MSNPs (bare, amine functionalized, RSSV-functionalized and 4RSSV-functionalized prepared by Type-2 attachment) are compared in **Figure 6.5**, along with the spectra of fresh linker and peptides. The FTIR spectra of the bare MPSNs does not contain a peak due to $–CH_2$ stretching (2800-3000 cm^{-1}), suggesting complete removal of the organic template following particle synthesis. For bare MSNPs and MSNPAs, the most prominent peaks

were bands corresponding to Si-O-Si and Si-OH vibration, located at 1080 and 960 cm^{-1}, respectively [46]. Primary amine peaks are not visible, but amine functionalization was quantified by chemical analysis as described previously. The linker, SNLD, has symmetric and asymmetric (-C=O from the ester) stretching vibrations at 1788 and 1736 cm^{-1}, respectively, whereas peaks at 1223 and 1051 cm^{-1} can be assigned as asymmetric C-N-C and N-C-O stretching vibrations [128]. There are also two peaks correspond to diazirine (N=N stretching at 1643 and N-H amide bond stretching 1540 cm^{-1}) [403-406]. After peptide attachment, the intensity of $–CH_2$ stretching vibrations (2800-3000 cm^{-1}) increase, which indicates the presence of linking spacer between particle surface and peptide, whereas peaks corresponding to NHS ester and diazirine group disappeared suggesting their conversion during the attachment process. Both MSNPA-RSSV and MSNPA-4RSSV showed increased intensity corresponding to arginine side chain stretching vibration, which confirms peptide attachment to the particle surface. Specifically, the spectra of the RSSV oligopeptides have a characteristic peaks from the arginine side chain ($CN_3H_5^+$) (asymmetric and symmetric stretching vibrations of 1673 and 1586 cm^{-1}, respectively), -CH_3 bending vibration at 1460 cm^{-1} from valine and C-OH bending vibration from serine side chain (1181 cm^{-1}) [407]. On the other hand, characteristic peaks of the inner groups from 4G (CH_2 bending at 1435 cm^{-1}, COO- symmetric and asymmetric stretching at 1788 and 1736 cm^{-1}, and C=O stretching at 1637 cm^{-1} [408]) remains, while N-H symmetric and assymetric stretching peaks (at 3311 and 3276 cm^{-1} [409]) disappeared., suggesting covalent linkage through the N-terminus.

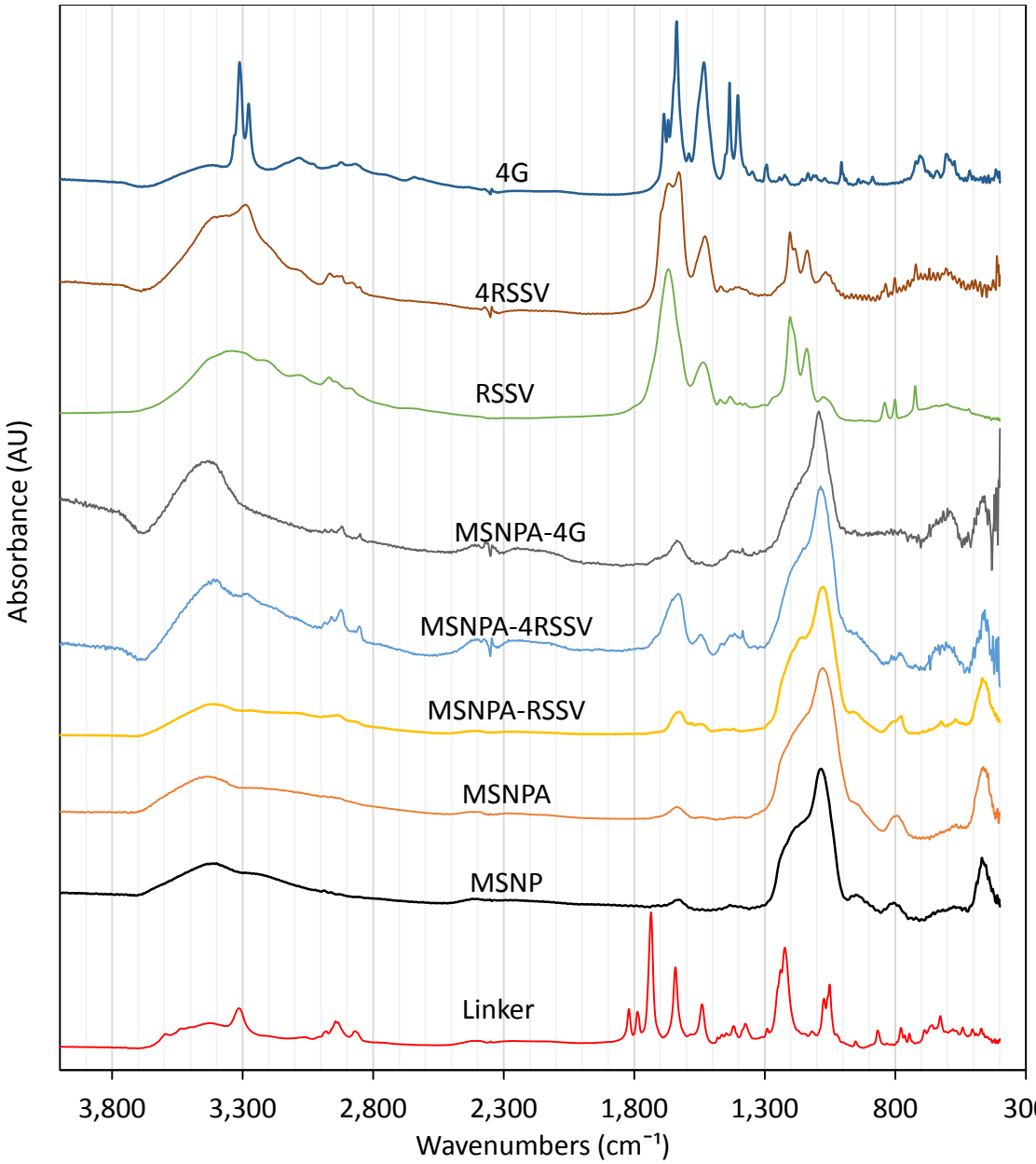

Figure 6.5 FTIR spectra of peptide functionalized particles relative to bare MSNPs and MSNPAs, as well as fresh linker (sulfo-NHS-LC-diazirine) and peptides.

In order to directly quantify and compare the attachment efficiency of non-fluorescently labelled peptides (required to show that the conjugation strategy is generalizable), TGA analysis was carried out to find the weight loss during thermal degradation and combustion of organic groups for peptide-attached MSNPs. The mass of

peptide (RSSV, 4G and 4RSSV) / linker conjugated MSNPAs (using Type-2 attachment) was quantified by comparing their mass loss from 150 ºC to 500 ºC to MSNPs and MSNPAs (**Figure 6.6**). For bare MSNPs, 2.6% mass is lost from 150 to 500 ºC (0.278 mg/mg silica; representing impurities such as residual template and further temperature-induced condensation of silica) and is subtracted before calculating the organic content of the other particles based on mass loss in this temperature range. The amount of aminopropyl groups on MSNPAs was found to be 0.494 mg/mg silica (1.04 mmol amine/g silica). Hence, TGA analysis underestimates the amount of amine by a factor of 0.67 compared to that of chemical analysis (see above). The reason for this underestimation may be due to the carbon residue on particle surface (which was visually observed on the particles). After subtraction of the weight loss of organics for MSNPAs, an additional 0.132, 0.208 and 0.516 mg/mg silica weight loss (due to removal of peptides and linkers) was observed for MSNPA-4G, MSNPA-RSSV and MSNPA-4RSSV, respectively. This corresponds to 0.300 mmol 4G/g silica, 0.324 mmol RSSV/g silica and 0.267 mmol 4RSSV/g silica. The molar attachment efficiency with amine is similar for the three peptides: 0.288, 0.311 and 0.257 mol peptide/mol amine for 4G, RSSV and 4RSSV, respectively. It is usually difficult to estimate protein length due to the presence of different secondary structures, but for oligopeptides an average length of 1.5 Å can be assumed per amino acid [410]. Thus a length of 0.6 nm, 0.6 nm and 2.4 nm can be approximated for 4G, RSSV and 4RSSV, respectively, in addition to 1.25 nm of spacer length from linker [398]. Hence, the method of peptide attachment to MSNPAs is robust to amino acid sequences and oligopeptide length. It should also be noted that TGA analysis underestimated RSSV estimation by a factor of 0.72 compared to estimation by fluorescent

measurements, which is close to aminopropyl underestimation for MSNPAs, again due to carbon residue on particle surface. Thus, chemical methods are more accurate in estimation of peptide attachment, but TGA can provide a reasonable estimation of relative attachment.

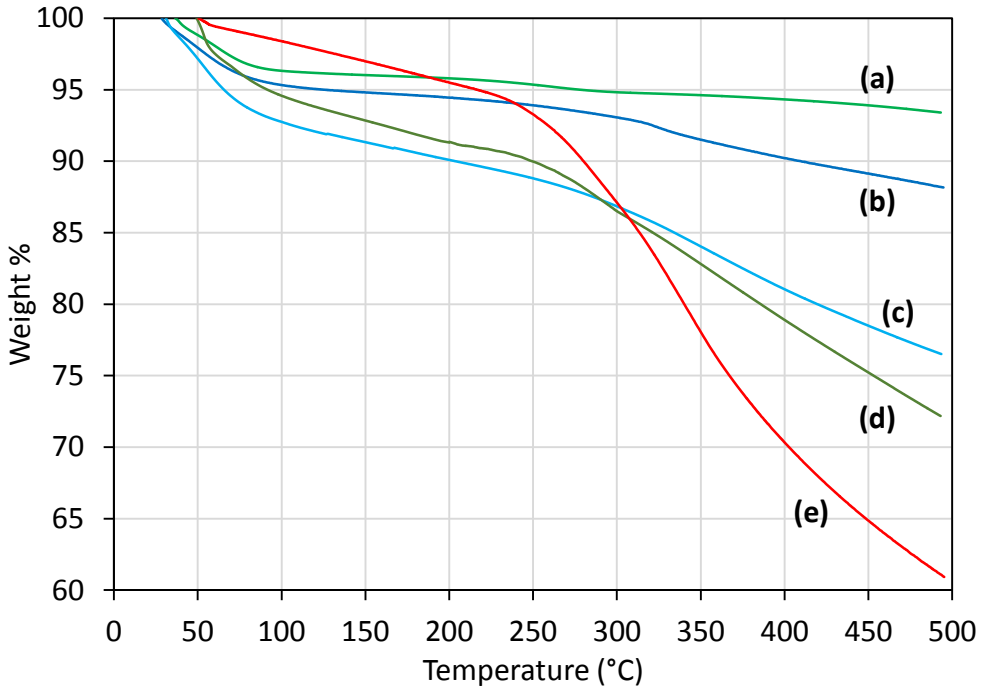

Figure 6.6 Thermogravimetric analysis (TGA) profiles of particles showing relative mass loss with temperature increase for (a) MSNP, (b) MSNPA, (c) MSNPA-4G, (d) MSNPA-RSSV, and (e) MSNPA-4RSSV.

All the particles after peptide conjugation (MSNPA-4G, MSNPA-RSSV and MSNPA-4RSSV) remain positively charged at physiological pH (**Figure D.6**), consistent with the unreacted surface amine groups. MSNPA-4G has slightly lower zeta potential compared to bare MSNPAs, but MSNPA-RSSV and MSNPA-4RSSV have comparable charge to MSNPAs. Possible charge reduction after reaction of surface amine groups due to peptide conjugation may be offset by the charge of the positive moieties of arginine side chain for MSNPA-RSSV and MSNPA-4RSSV. Positive charge is important for the colloidal stability of the particles during the suspension and re-suspension. Due to high

positive charge, these particles should be appropriate for intracellular penetration during nanoharvesting or biomolecule delivery applications, where positive charge has been shown to be beneficial (**Chapter 4**).

A challenge of covalent immobilization of peptides on surfaces is the possible loss of the desired selective ligand binding functionality after attachment [370]. Here, functionality of surface conjugated peptides were demonstrated from their increased binding to β-estradiol (E2) compared to bare MSNPs and MSNPAs, as peptide RSSV was shown to have high affinity for E2 [141]. β-estradiol binding to the particles was determined by the depletion from 10% ethanolic solution of PBS in the presence of particles. Relative depletion of E2 in the presence of MSNPs, MSNPAs, MSNPA-RSSVs and MSNPA-4RSSVs compared to that of MSNPA-4G are presented in **Figure 6.7**, where depletion corresponding to MSNPA-4G was assumed as 100%. Although there is high non-specific binding to bare particles, a statistically significant differences in E2 adsorption between peptide-conjugated particles and unconjugated MSNPAs were found. E2 binding to only peptide groups was estimated in comparison with binding to only amine groups (non-specific adsorption) from the differences in **Figure 6.7**. Considering the mol peptide/mol amine bound on particle surface (from TGA analysis), the binding of E2 per mol of 4G, RSSV and 4RSSV peptides is calculated to be 2.16, 2.20 and 3.05 times the E2 bound per amine group (**Figure 6.8**). Statistically significant higher binding to 4RSSV on the particle surface compared to RSSV validates our hypothesis that repeating a selective peptide sequence increases the binding stoichiometry. However, high background binding to both MSNPs and MSNPAs shows the difficulties in measuring the selective binding of a hydrophobic molecule like E2 in aqueous solution, where their natural abhorrence

towards water drives them out of solution. Although hydrophobic interactions are the main driving force, hydrogen bonding with silica and aminopropyl groups may also be present [411, 412], which make the binding more complicated. However, the difference in binding capacity of peptide conjugated particles will be more pronounced compared to MSNPAs (and between MSNPA-RSSV and MSNPA-4RSSV) if an affinity chromatographic column functionalized by the same peptide is used, as demonstrated for the fractionation of other biomolecules [413-415]. High β-estradiol binding capacity also provides an opportunity for the removal of these types of compounds from polluted water sources, which are notorious endocrine disrupting compounds [416].

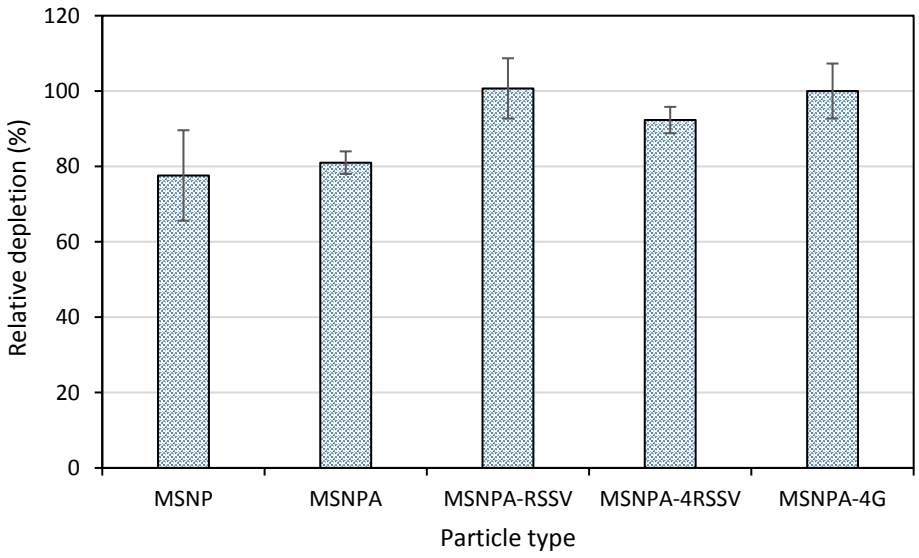

Figure 6.7 Adsorption of β-estradiol on particle surface relative to MSNPA-4G from solution depletion by adding 25 µL of 10 µM β-estradiol in ethanol to 0.1 mg particle in 225 µL PBS (10% ethanol in PBS).

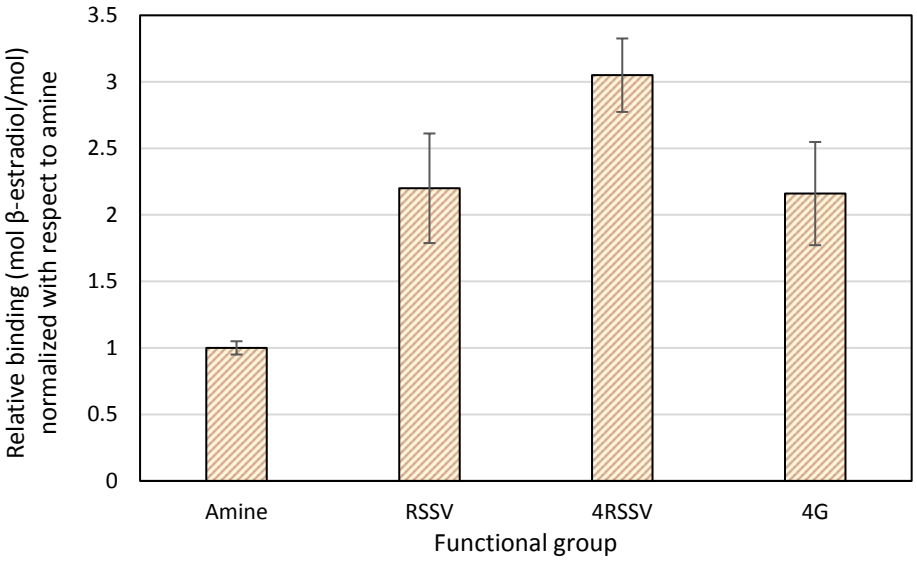

Figure 6.8 Capacity differences in β-estradiol binding (mol/mol functional group) normalized relative to amine group as calculated from β-estradiol adsorption.

6.5 Conclusions

Functional oligopeptide 4G (Gly-Gly-Gly-Gly), RSSV (Arg-Ser-Ser-Val) and 4RSSV were attached to large pore (7.9 nm diameter) amine functionalized MSNPS using a hetero-bifuntional linker, sulfo-NHS-LC-diazirine (SNLD), which contains an amine reactive NHS ester group and UV-activable diazirine group. Hetero-bifunctional peptide linkers containing a diazirine group provide precise control of the mechanism and orientation during attachment with a high activation wavelength (365 nm), which is more benign to the protein/peptide compared to other linkers that are activated at lower wavelength. Two different conjugation schemes were compared to attach oligopeptide RSSV to the MSNPs based on the order of addition (Type-1: functionalize particle with linker and then attach the peptide and Type-2: attach the linker to the peptide and then functionalize the particle with peptide-linker conjugate). The efficiency of peptide attachment was measured by fluorescence spectroscopy using FITC-labeled peptides (RSSV-FITC). Higher attachment efficiency per mol amine groups was found for Type-2 attachment (0.43 mol RSSV/mol amine) compared to Type-1 attachment (0.24 mol RSSV/mol amine). Type-2 attachment efficiencies of 4G, RSSV, and 4RSSV on particles, as determined by TGA analysis, were similar. This demonstrates that the attachment strategy is generalizable and can be used to attach a range of sizes of oligopeptide to MSNPA. An increase in capacity of the oligopeptide-functionalized MSNPs for a target molecule (β-estradiol) was demonstrated compared to only MSNPAs, although significant background adsorption of this hydrophobic molecule was observed.

The functional oligopeptide conjugation to “large pore” MSNPs appropriate for biomolecule loading was demonstrated using a versatile and robust hetero-bifunctional linking strategy, which provides precise control of binding moieties of peptide molecule.

High capacity platforms for selective separation of biomolecules with therapeutic value can be designed by selecting oligopeptides that mimic the specific binding sites of biomolecules. For example, MSNPAs can be used to selectively isolate different small molecular therapeutics from living plants, a technique recently demonstrated by using engineered silica nanoparticles. Further, high capacity adsorbents for the removal of specific therapeutics in polluted water sources can be developed based on oligopeptide-functionalized silica particles.

CHAPTER 7. THERMODYNAMIC INTERACTION OF RNA WITH AMINE FUNCTIONALIZED MESOPOROUS SILICA NANOPARTICLES

7.1 Summary

Functionalized mesoporous silica nanoparticles (MSNPs) are ideal carriers for nucleic acids and oligonucleotides for gene delivery and RNA interference (RNAi) applications due to their low toxicity, tunable pore and particle morphology, high loading capacity and ease of surface modification. As one example, MSNPs have been proposed as carriers for the delivery of double stranded (ds) RNA in insects for RNAi mediated pest control. With the advent of MSNPs with pores large enough for biomolecule access, RNA loading, release and mobility in cationic, amine functionalized MSNPs (MSNPAs) have been demonstrated to be strongly dependent on pore diameter and RNA length. This investigation examines the thermodynamic driving force for RNA-MSNPA interactions and the nature of binding of RNA, extending knowledge of solution-based nucleic acid-polycation interactions to RNA confined in nanopores. The interactions of 84 and 282 base pair (bp) dsRNA with MSNPAs of varying pore diameter (nonporous, 1.6 nm, 3.2 nm and 7.6 nm) are studied using isothermal titration calorimetry (ITC). RNA interactions with the porous particles occur through a two-step process, where the first is an initial endothermic interaction driven by entropic contribution from counterion (and water) release from positively charged amine moieties and negatively charged RNA molecules. The second step is an exothermic regime dominated by short range interactions of RNA within the pores. The exothermic heats evolved are significantly larger for 84 relative to 282 bp RNA for MSNPAs with 1.6 nm pores, consistent with hindered pore loading of the larger RNA. Within 3.2 nm pore particles, the initial entropic contributions are more dominant for 84 bp RNA, while greater exothermic heat is associated with 282 bp RNA. At the largest pore

diameter (7.6 nm), similar interactions with MSPNPAs are found for both 84 and 282 bp RNA. Reduction of both endothermic and exothermic enthalpies in the presence of salt for both lengths of RNA indicates that electrostatic interaction contribute to both regimes of binding. Thermodynamic binding energies (ΔH and ΔG), as determined from fitting binding models to the ITC data, are consistent with previous investigations of nucleic acid interaction with polycations, suggesting high conformation change and significant desolvation during binding. Knowledge of the size-dependent nature of the interactions between RNA and functionalized porous nanoparticles will aid in the design of porous nanocarriers suitable for functional RNA and functionalized porous nanoparticles will aid in the design of porous nanocarriers suitable for functional RNA loading and release.

7.2 Introduction

Nucleic acid (DNA/RNA) research has revolutionized their biomedical applications and opened a new horizon for treatments for numerous recalcitrant diseases [417-420]. Delivery of oligonucleotides of DNA to targeted intracellular sites (especially cell nuclei) is extremely important for gene therapy and associated technologies involving genetic interference [210, 211, 421]. Similarly, RNA-based therapy that includes regulation of gene expressions involves delivery of RNA to the vicinity of cell nuclei [212, 218, 422]. A prominent type of RNA delivered for RNA-based treatments is small interfering (si) RNA, which is notable for its gene silencing or knocked down capability. siRNA is small double-stranded RNA (dsRNA, 20-25 base pair (bp)), delivered to cells for targeted silencing of genes (called RNA interference (RNAi)) responsible for varieties of hereditary and transmittable diseases, as well as cancer [23, 423]. RNAi technology is also developing rapidly for bio-based management of agricultural pests [27], where specific insect genes responsible for vitality and mortality can be suppressed and/or switched on, respectively, by delivering respective larger dsRNA sequences (up to 1000 bp) [28]. Efficient delivery of the nucleic acids to the intracellular target sites is limited by the inability of free polynucleic acids to penetrate cell membranes (both are negatively charged) and their rapid degradation by the nucleases present in cells [210, 211]. As a result, designing protective nanocarriers to efficiently deliver functional nucleotides in cells has become the principal challenge in the application of oligonucleotides in areas including bio-insecticides [424], genetic manipulation of food crops [425], fighting multidrug resistance [426], and gene silencing therapies [427, 428].

A limitation of many of the types of nucleic acid carriers (including exosome nanoparticles, polymers, lipid and lipoloid nanoconjugates [22, 213, 215, 429, 430]) has been their unacceptable toxicity and poor structural tunability [431]. Thus, mesoporous silica nanoparticles (MSNPs) have emerged as promising carriers of nucleic acids and polynucleotides based on their tunable pore morphology, high surface area, low toxicity, and ease of surface modification [308, 432-435]. Nucleic acid loading is generally achieved by functionalizing the silica surface with positively charged groups such as amines (using aminopropylsilanes), metal ions, cationic polymers or peptides to adsorb the negatively charged nucleic acid through electrostatic interactions and to promote cellular internalization [211, 436]. Multiple surface functional groups on siRNA-loaded MSNPs have been used to augment binding to specific cells (through targeted ligand and peptide moieties [432]) and to prevent particle aggregation (polyethyleneimine (PEI) [437, 438] or lipid bilayers [439]).

Initial studies of MSNPs for oligopeptide and nucleic acid delivery and protection focused on surfactant templated materials with typical pore sizes < 4 nm [440-442]. Reliable synthesis procedures for MSNPs with larger pores capable of accommodating proteins, larger DNA and RNA molecules have only recently been developed [435, 443-445]. Prior studies have suggested an optimal mesopore size for functional siRNA delivery (7-10 nm) [85] and optimal functional group (amine) grafting density to balance loading and release [446], but a fundamental basis for these carrier design parameters for large pore amine functionalized MSNPs (MSNPAs) has not been developed. The adsorption and release of stiff polyelectrolytes such as RNA confined in pores remains an incompletely

understood subject, as indicated by a number of recent theoretical and computational studies [447-450].

Previously, we have studied the dependence of mobility of RNA confined in nanopores on RNA length (84 bp (24 nm) and 282 bp (80 nm)), and pore size (nonporous, 3.6 nm, 7.4 nm and 11.8 nm) in amine-functionalized mesoporous silica microspheres (MSMs). The diffusivities of these fluorescently labeled dsRNA of inhibitor of apoptosis (IAP) genes of *Spodoptera frugiperda* were measured by fluorescence recovery after photo-bleaching (FRAP) using confocal laser scanning microscopy (CLSM) imaging of the micron-sized particles [61]. Pore size dictates length-dependent loading of dsRNA, where combination of the largest dsRNA (278 bp) and smallest pore size (2.2 nm) results in only surface-bound RNA. The mesoporous structure also provides a mobile network of dsRNA; the diffusivity of RNA was similar at the surface and in the porous interior of MSMs in which RNA length and pore size resulted in significant RNA loading [61]. Only MSMs with measurable diffusivity effectively released dsRNA, an important element of functional RNA delivery.

Understanding the nature of the binding between nucleic acid and MSNPAs and the associated thermodynamic parameters is vital for the design of effective nanocarriers for loading and targeted release. Isothermal titration calorimetry (ITC) is a highly sensitive and versatile technique that can be used to determine enthalpies, entropies and equilibrium association/ dissociation constants of binding, and has been broadly applied to biomolecule interactions such as protein/ligand binding [163]. Previously, interaction of nucleic acids with polycations in solution has been investigated by ITC to design complexed particles and polymeric vehicle for gene delivery, new diagnostic agents, and for the understanding

of DNA packaging in cell nuclei and RNA-protein interactions [171, 172, 174, 451-456]. Nucleic acid interactions with polycations are multifaceted, involving electrostatic forces, protonation and hydrogen bonding, with a strong contribution of entropy, and sometimes without any defined stoichiometry [171, 174]. The ability to extend interpretations of solution-based nucleic acid and polycation interactions obtained from ITC to RNA confined in charged nanopores has not been explored previously.

The pore-size dependent interactions of dsRNA with functionalized mesoporous silica nanoparticles (MSNPAs) were investigated for dsRNA of two lengths (84 bp and 282 bp) and over a range of silica pore sizes, (nonporous, 1.6 nm, 3.2 nm and 7.6 nm). The nominal dimensions (2.6 nm diameter) of dsRNA are larger than the smallest pore dimension of the MSNPAs here, making this pore size range relevant to understanding the insertion of dsRNA in a pore. The enthalpic contributions to binding are interpreted directly from ITC heat profiles (integrated heat vs. mole bp RNA/mole amine on particle surface) after injecting dsRNA (0.334 to 4.5 mM bp) into an aqueous (unbuffered) particle suspension of known total amine concentration on particles (0.2 to 3.2 mM amine). The nature of the dsRNA-MSNPA surface interactions were further probed by conducting ITC experiments for RNA (both lengths) with 7.6 nm porous MSNPAs in 30 mM NaCl, which is used to suppress the electrostatic and ionic interactions. Appropriate binding models are used to fit the ITC heat profiles, yielding thermodynamic binding parameter (enthalpy, entropy and free energy) that allow comparison of thermodynamic driving forces for RNA binding across pore sizes and relative to solution-based interactions with polycations.

7.3 Materials and Methods

7.3.1 Chemicals and Reagents

Tetraethyl orthosilicate (TEOS, 99%) was obtained from Acros Organics. Tri-block copolymer Pluronic F127 (bio-grade), phosphate buffer saline (PBS) tablets, (3-Aminopropyl) triethoxysilane (APTES, 99%) and tetrapropyl orthosilicate (TPOS, 95%) were purchased from Sigma-Aldrich. Cetyltetramethylammonium bromide (CTAB, 99.8%) and nuclease free water (molecular biology grade) was purchased from MP Biomedicals; NaOH pellets (≥ 97%) from EMD Millipore; Acetone (≥ 99.5%) from BDH analytical; 1,3,5-triisopropylbenzene (TIPB, > 95%), triethanol-amine (TEA, > 98%) and fluorescamine from Alfa-Aesar; ultrapure deionized ultra-filtrated (DIUF) water, ethanol (200-proof), 12 N HCl (ACS grade), NaCl (99.7%) and 29.3 wt% NH_4OH solution from Fisher Scientific. N,N-dimethylhexadecylamine (DMHA, ≥ 98%) was purchased from TCI America. Octadecyltrimethylammonium bromide (OTAB) was purchased from Chem-Impex International. Synthesis of dsRNA with 84 and 282 base pair (bp) length was performed in Dr. Webbs's laboratory in Entomology Department and discussed elsewhere in detail [457].

7.3.2 Nanoparticle Synthesis

7.3.2.1 Nonporous Stöber Particle (SNP) Synthesis

SNPs were synthesized according to the method reported by Bogush et al. [51]. 10 mL of DIUF water and 6.75 mL of 29.3% NH_4OH were added to 183.25 mL of ethanol. The solution was stirred for 5 min. Then, 7.6 mL of TEOS was added rapidly and the solution was stirred for 24 h at room temperature. The particles were separated from the

solution using high speed centrifugation (17,000 rpm) followed by washing with DIUF water and ethanol 3 times each. Finally, separated particles were dried in an oven at 84 ºC overnight**.**

7.3.2.2 Mesoporous Silica Nanoparticles (MSNPs) Synthesis

Ordered mesoporous silica nanoparticles with small pores (2-3 nm) were synthesized by a modified Stöber method reported earlier [38] and originally based on Kim et al. [69], in which CTAB was used as a structure directing compound and TEOS and Pluronic F127 as the silica source and dispersing agent, respectively. Initially 0.5 g of CTAB and 2.05 g of F127 were dissolved in 96 mL of DIUF water, followed by the addition of 43 mL of ethanol and 11.9 mL of NH_4OH solution (29.3 wt%) and the solution was stirred until complete dissolution of solutes. Then, 1.9 mL of TEOS was added to the solution and stirred vigorously for exactly 1 min at room temperature. After that, the solution was aged for 24 h without any stirring at room temperature for complete silica condensation. The particles were removed from the solution by ultrahigh speed centrifugation (Beckman-Coulter) at 17,000 rpm and were washed 3 times with DIUF water and ethanol with repeated centrifugation and dried at 84 ºC in air overnight. Finally, template free silica particles were obtained by washing in 200 mL acidic ethanol (HCl, 1.5 M) for 24 hours (acidic ethanol wash) followed by repeated centrifugation and washing with DIUF water and ethanol. Template free particles were dried overnight at 84 ºC.

Synthesis of medium pore MSNPs (4-5 nm) was achieved by following the method reported by Gu et al. [83]. Initially, 0.4 mL of DMHA and 0.1 g of Pluronic F127 were mixed with 1.02 g of OTAB and 364 mL of water was added. 3.5 mL of 2 M NaOH solution

was then added under stirring. The solution temperature was raised to 80 ºC, and kept stirring under constant temperature until a clear homogeneous solution was obtained. Then, 5.0 mL of TEOS was added dropwise. The solution was stirred at 80 ºC for 2 h and cooled to room temperature afterwards. The particles were separated by centrifugation and repeated washing with water and ethanol. Template-free particles were achieved by the acidic ethanol wash described earlier.

Large pore MSNPs (*ca.* 8 nm) were synthesized using a modified method described by Yamada et al. [84], where TIPB was use as a CTAB pore expanding agent. Initially, 0.56 mL of TEA and 3.0 g of CTAB was added to 360 mL of DIUF water. The solution was kept stirring at 80 ºC for 2 h for complete mixing and emulsion formation and 16 mL of TIPB was added under vigorous mixing. After 30 min, complete colloidal state (oil-in-water) was obtained and 4.77 mL of TPOS was added with constant stirring. Then, the solution was stirred vigorously for 12 h at 80 °C to obtain white solid particles. The particles were then separated by repeated centrifugation and washing and the surfactant was removed by acidic ethanol washing.

7.3.3 Amine Functionalization

Amine functionalized SNPs and MSNPs were obtained by condensing (3-aminopropyl)triethoxysilane (APTES) on particle surfaces using a modified version of the methods reported in the literature [101, 358]. 200 mg of the particles (either SNPs or MSNPs) were sonicated in 25 mL of dry ethanol for 15 min and a uniformly dispersed solution was obtained. 0.1 mL or 0.5 mL of APTES (for SNPs or MSNPs, respectively) was added drop wise under constant stirring in nitrogen environment and the solution was

kept stirring overnight in a closed environment at room temperature. Particles were centrifuged at 17,000 rpm followed by repeated washing with dry ethanol and cured at 84 ºC overnight. After curing, particles were stirred in excess ethanol for 24 h to remove any remaining, loosely bound amine groups. The functionalized particles were again washed 3 times with dry ethanol and dried in an oven at 84 ºC. Amine functionalized nonporous and porous particles were denoted as SNPA and MSNPA-x, respectively, where "x" denotes approximate mean pore size.

7.3.4 Materials Characterization

The morphology and shape of bare and functionalized particles were characterized using a Hitachi S-4300 Scanning Electron Microscope (SEM). The samples for SEM characterization were prepared by dispersing the particles onto a double sided carbon tape attached on a 15 mm aluminum stub. Samples were put in a desiccator for 24 h after excess silica materials blown off with dry nitrogen gas. Prior to analysis, the samples were coated with gold-palladium alloy using an Emscope SC400 with a gold-palladium alloy sputtering. Average and standard deviation of particle diameters were calculated by considering 20 random particles throughout the SEM image using ImageJ Software. Transmission electron microscopy (TEM) imaging were performed using a JEOL 2010F TEM at a voltage of 200 kV. Samples were prepared 3 days in advance by sonicating approximately 5 mg of particles in 2 mL of ethanol for 15 min. Then a Lacey carbon 300 mesh copper grid (Ted Pella, 01895-F) was dipped into the particle solution for 2-3 seconds and left in a desiccator before analysis.

Average pore diameter, pore size distribution and surface area were estimated from nitrogen sorption conducted at 77 K using Micromeritics TriStar 300. Samples were degassed at 135 ºC for a minimum of 4 h under flowing dry N_2 gas before the nitrogen sorption experiment. The specific surface area was estimated using the Brunauer, Emmett and Teller (BET) isotherm, and average pore diameter and pore size distribution were estimated by the method of Barrett, Joyner and Halenda (BJH) for adsorption branch. To confirm the successful removal of surfactant from MSNP pores, Fourier transform infra-red (FTIR) spectroscopy was conducted using Thermo Nicolet Nexus 470 with a deuterated triglycine sulfate (DTGS) detector before and after acidic ethanol wash. For the analysis, 0.5 g of anhydrous KBr was mixed was the particles (0.5-1.0 wt %) and the mixture was crushed using a mortar and pestle. A small amount of the sample was put into the FTIR pellet dye to press until samples became translucent, rigid, and solid. The pellet was then put in FTIR pellet holder in the sample chamber under a constant flow of dry nitrogen and infra-red radiation was allowed to pass through it. The FTIR spectra were recorded using Thermo OMNIC software.

7.3.4.1 Amine Quantification

The amount of amine group on the particle surface was determined by a modified version of the previously reported method [324], where primary amine groups in aminosilane following dissolution in alkaline solution react with fluorescamine to produce fluorescent pyrrolinone [325]. 30 mg of functionalized particles were dissolved over an 8 h period in 30 mL of 0.02 M NaOH solution at room temperature under vigorous stirring. 100 μL of this solution and 1.0 mL of 1.0 mM fluorescamine in acetone solution were

mixed with 2.0 mL of PBS solution at pH 7.4. Maximum fluorescence intensity of this solution was measured at emission wavelength of 480 nm after excitation at 366 nm using a Varian Cary Eclipse fluorescence spectrophotometer with both excitation and emission slits held at 5 nm. Calibration curve was prepared using the same procedure by dissolving known amounts of APTES and 30 mg of non-functionalized respective particles.

7.3.5 Isothermal Titration Calorimetry (ITC)

Isothermal titration calorimetry (ITC) experiments were performed in a Low Volume Nano-ITC instrument (TA Instrument). A suspension of amine functionalized nanoparticles was made in nuclease-free water by ultra-sonication for 15 min. dsRNA (84 and 282 bp) solutions were diluted to desired concentrations using nuclease-free water and injected to the nanoparticle solution in a 300 µL ITC sample cell using the injection syringe. Both nanoparticle suspension and RNA solution were degassed under vacuum for 15 min before ITC experiments to remove any gas bubbles. The reference cell was filled with degassed DIUF water, which was replaced after every 3 days with fresh water. In a typical experiment, 50 µL of RNA solution (0.334 to 4.5 mM bp) was injected into the ITC cell containing 300 µL of nanoparticle suspension (0.2 to 3.2 mM amine on particles) with 20 distinct injections (2.5 µL per injection) sequentially 300 s apart with a stirring rate of 350 rpm. The cell temperature was maintained at 25 ºC. For ITC experiments in the presence of salt, both nanoparticle suspension and RNA solution were made in 30 mM NaCl in nuclease-free water. To avoid any minute difference in NaCl concentration between syringe and cell, both RNA and nanoparticle solutions were prepared using aliquots of same NaCl solution.

Before starting the injections, the baseline of heat signal was allowed to stabilize for at least an hour to absolutely minimize noise and drift in the baseline level. Raw heat data with the injections was recorded with ITCRun™ software (TA Instruments) as raw heat rate in μJ/s versus time in seconds. For every RNA concentration (both 84 and 282 bp), dilution experiments were performed by injecting RNA solution in a cell containing 300 μL of respective solvent (nuclease-free water with/without NaCl) without any nanoparticles. Raw data (thermograms) are presented after correction for baseline drift in heat signal by NanoAnalyze™ software (TA Instruments).

7.3.6 ITC Data Analysis and Fitting of Binding Models

After recording raw data, integrated heats (μJ) are calculated for each injection from its starting point to its finish, as determined from the return of the heat signal to the baseline using NanoAnalyze software. Integrated heats for the corresponding dilution of RNA (RNA into corresponding water or aqueous buffer) was also calculated and subtracted from the heat of RNA into particles to find the heat of interaction at each injection point. Finally, integrated heat profiles (heat/mol bp versus mol bp/mol amine), which are also called isotherms, were calculated by dividing the integrated heats (with dilution subtracted) at each injection point by the number of mole bp per injection. As standard procedure, the first injection point is removed to avoid artifacts arising from initial equilibration and void in the syringe tip.

Independent single or two-site thermodynamic binding models were fitted to uni-phasic or bi-phasic binding curves, respectively, of the integrated heat profiles using NanoAnalyze software. Thermodynamic parameters of binding (association/dissociation

constant (K_a/K_d), number of binding sites (n), and enthalpy change (ΔH)) are determined by non-linear least squared regression, where there are 3 fit parameters per binding site. Initially, n, ΔH and K_a are considered as floating variables during least square fitting according to a Wiseman isotherm (single site binding model) [180] or modified Wiseman isotherm for two distinct binding sites [174, 453]. ΔG and ΔS are estimated using the thermodynamic relation presented in **Equation 7.1**:

$$\Delta G = -RT*ln(K_a) = \Delta H - T\Delta S \tag{7.1}$$

where T is the isothermal temperature of the experiments.

When the fitting of the biphasic ITC isotherms using two site models produces unrealistic values of parameters (especially ΔH), the enthalpy for one phase of isotherm is constrained following the suggestions of previous literature [182]. An isotherm that is nearly uniphasic was fit to a one-site independent binding model to roughly estimate either ΔH_1 or ΔH_2 and these values were constrained during two-site model fitting.

7.4 Results and Discussion

7.4.1 Nanoparticle Characterization

Nonporous silica nanoparticles (SNPs) and mesoporous silica nanoparticles with different pore diameter (MSNPs) were synthesized by a silica alkoxide hydrolysis technique (modified Stöber method) coupled with surfactant templating and hydrophobic pore swelling agents [51, 69, 83, 84]. After synthesis, template surfactants and other organics were removed by washing in acidic ethanol and removal was confirmed by FTIR analysis (data not shown). Average particle diameter and spherical shape of the particles were determined by SEM imaging (**Figure 7.1** and **Table E.1** in **Appendix E**). The nanoparticles size (< 200 nm) is suitable for cellular internalization and delivery of dsRNA.

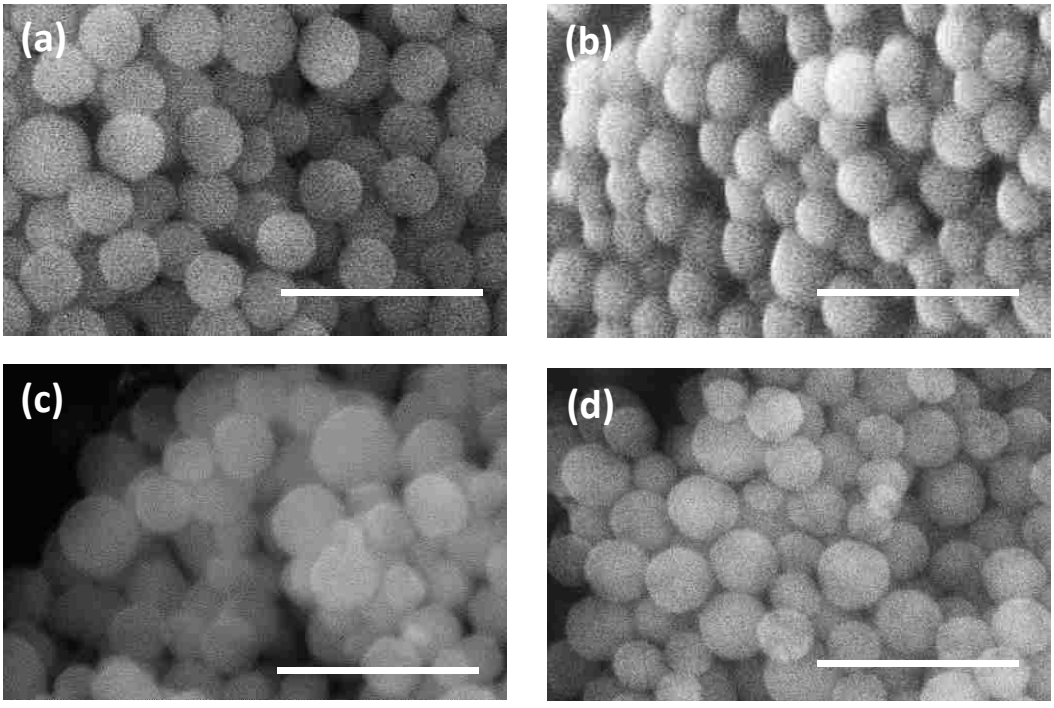

Figure 7.1 SEM images of nonporous silica nanoparticles (SNPs) along with mesoporous silica nanoparticles (MSNPs) with different pore sizes: (a) SNP, (b) MSNP-2.2, (c) MSNP-4.1 and (d) MSNP-7.9. Scale bar is 500 nm for all images.

Surface characterization was performed by nitrogen adsorption and was used to determine BET surface area, total pore volume and average pore diameter (**Table 7.1)**. Porous particles synthesized with varying pore diameters (2.2 nm, 4.1 nm, and 7.9 nm) possess high surface area and pore volume, which is needed to provide a large capacity for RNA loading. Ordered accessible interconnected pores, required for loading RNA, can also be observed from TEM images of the particles (**Figure E.1**). MSNPs are named according to their average pore size, for example: MSNP-2.2 means mesoporous silica nanoparticles with mean pore size of 2.2 nm.

Table 7.1 Surface properties characterization results from nitrogen adsorption experiments before and after amine functionalization.

Particle type	BET surface area (m^2/g)	Total pore volume (cm^3/g)	Average pore diameter (nm)[b]
SNP	14.4[a]	-	-
SNPA	14.4 [a]	-	-
MSNP-2.2	953	1.21	2.2 ± 0.16
MSNPA-1.6	585	0.57	1.6 ± 0.14
MSNP-4.1	862	1.37	4.1 ± 0.35
MSNPA-3.2	366	0.66	3.2 ± 0.38
MSNP-7.9	729	2.32	7.9 ± 2.2
MSNPA-7.6	469	1.50	7.6 ± 1.9

[a]Surface area determined by considering all particles as regular spheres, [b]The average and range were determined from the peak and full width at half maximum (FWHM) of the BJH pore distribution, respectively.

Particles were functionalized with amines using APTES to provide a positive surface charge for anionic dsRNA loading. A previous study [446] involving low extent of amine functionalization only on the exterior surface of silica particles or lightly

functionalized pores resulted in dsRNA adsorption only on the particle surface, which does not offer adequate protection of dsRNA from nucleases during delivery. A modified version of the amine functionalization procedure of Schlipf et al. [324] was used to achieve amine coverage close to a monolayer on the silica surface, which is not expected to change the accessibility of the pores for RNA loading [358]. For comparison, nonporous silica nanoparticles that allow only dsRNA adsorption on their surface were synthesized and functionalized with amines using the same method. The amine amount used for functionalization of nonporous particles was reduced by a factor of five to avoid depositing a thick polyaminosiloxane layer.

The extent of amine modification was determined by dissolution of the particles in alkaline solution, followed by reaction with fluorescamine, which produces fluorescent pyrrolinone [324, 325]. The specific extent of amine functionalization (mmol/g) and silica surface coverage compared to a monolayer decreases with increasing pore size (**Table E.1**). The extent of aminosilane grafting on silica supports, state of grafted amine (isolated, layer, branched and ladder type oligomers) and uniformity varies depending on the amount of trace water present during the hydrolysis process and the nature of the solvent [94, 102]. Cross-linked oligomeric structures form in the presence of significant water, whereas non-hydrated surfaces can allow isolated tridentate aminosilane grafting (at less than monolayer coverage). Layer uniformity also depends on the solvent used; polar solvents like ethanol (used here), which induce higher mobility inside of pores, tend to produce more uniform functionalization throughout. Based on the volume ratio of precursor to solvent (1 APTES:50 ethanol) in our functionalization procedure, linear and a few ladder-like oligomeric (6-8 repeat units) cross-linked aminopropylsiloxanes are expected, with some

tridentate isolated grafted aminopropyl groups [102], consistent with our amine coverage which ranges from 64% to 114% of monolayer coverage for MSNPs and 272% for SNPs (**Table E.1**).

BJH pore size distribution before and after amine functionalization (**Figure 7.2**) as well as surface area, pore volume and average pore diameter after amine functionalization (**Table 7.1**) demonstrate that these particles have uniform and accessible mesoporous structures and interconnected pores throughout the particles, which is expected to allow for uptake of dsRNA. All MSNPs have characteristic Type-IV nitrogen sorption isotherms with clear capillary condensation indicating uniform mesoporosity (**Figure E.2**). The introduction of amine groups caused the reduction of mean pore diameter and BET surface area, consistent with the incorporation of the amine groups in the pores of particles. Sharp capillary condensation step was only retained for MSNPA-7.6, but not for MSNPA-1.6 and MSNPA-3.2, consistent with peak broadening and reduced pore volume. Amine-functionalized nonporous and mesoporous silica particles are indicated with the prefix SNPA and MSNPA-x, respectively, where "x" is the mean pore size of the particles after functionalization. dsRNA has been estimated to have a width of 2.6 nm [458], a length per base pair of 0.28 nm/base pair (bp) and a persistence length of 64 nm [459]. This would mean that an 84 bp and 282 bp dsRNA would be ~24 nm and ~80 nm long, respectively, which is 38% and 125% of the persistence length. Both types of RNAs are much longer than the largest pore size investigated here.

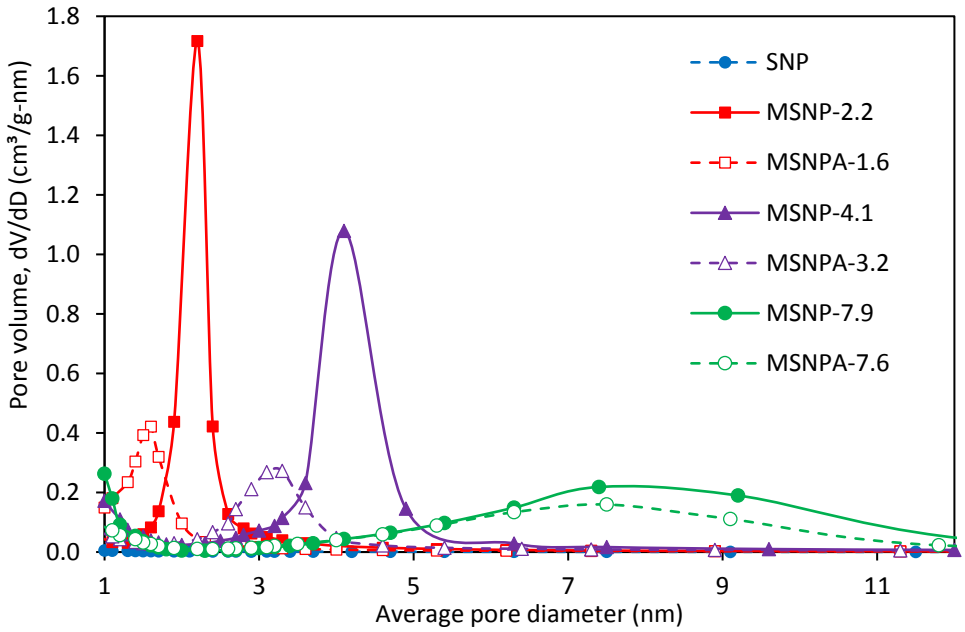

Figure 7.2 Pore size distribution of the particles before and after amine functionalization using BJH method from nitrogen adsorption.

7.4.2 RNA Interactions with Functionalized Nanoparticles

The thermodynamic interaction and loading behavior of dsRNA (84 and 282 bp) with amine functionalized nanoparticles as a function of pore size (nonporous, 1.6 nm, 3.2 nm and 7.6 nm) were investigated by isothermal titration calorimetry (ITC). RNA was injected into a cell containing particle suspension, unlike nucleic acid-polycation ITC studies in solution [172, 174, 451, 453, 460-462] in which the polycation solution was injected into the cell containing RNA. Our approach is similar to previous investigations of biomolecule (protein) interaction with nanoparticles [147, 463, 464]. The solution-based ITC results for nucleic acid interactions with polycations containing amine groups are routinely expressed as the molar ratio of mole amine:mole phosphate (N/P) over the course of injecting the cationic polymer into the ITC cell containing nucleic acid [174, 453, 465]. Since we are injecting RNA into a suspension of the amine functionalized nanoparticles,

the isotherm is expressed as a function of mol base pair:mol amine on particles (P/N ratio). ITC profiles for dilutions of 84 bp RNA and 282 bp RNA with different concentration of bp are presented in **Figure E.3** and **Figure E.4**, respectively. The exothermic dilution of both RNAs, increasing with concentration, is as expected. RNA remains surrounded by counterions in water. Dilution results in interactions between fewer RNA molecules, which is enthalpically favorable due to more hydrogen bond formation between RNA and water in a relatively free environment. The heat of dilution per base pair is less for 282 bp compared to 84 bp RNA, probably due to higher degree of solvation of the shorter RNA.

During interactions of amine-functionalized porous particles with 84 bp RNA (**Figure E.7, E.9 and E.11**), the ITC thermogram consists of at least one region dominated by endothermic contributions followed by a region dominated by exothermic contributions. At intermediate concentrations, both endothermic and exothermic heats are present in a single injection. For 282 bp RNA (**Figure E.8, E.10 and E.12**), endothermic components are not as prominent from the thermogram peaks but they exist nonetheless. ITC isotherms for dsRNA (both 84 and 282 bp) interaction with SNPA and MSNPAs are presented in **Figure 7.3**. The smallest amount of heat was evolved for SNPAs due to the low surface area and corresponding limited amine groups for interaction with RNA. The observed heat of interaction with SNPA are slightly exothermic for 84 bp RNA and slightly endothermic for 282 bp RNA (**Figure 7.3a**). The large conformational change and bending of 282 bp RNA bound the particle surface may contribute to endothermic interactions.

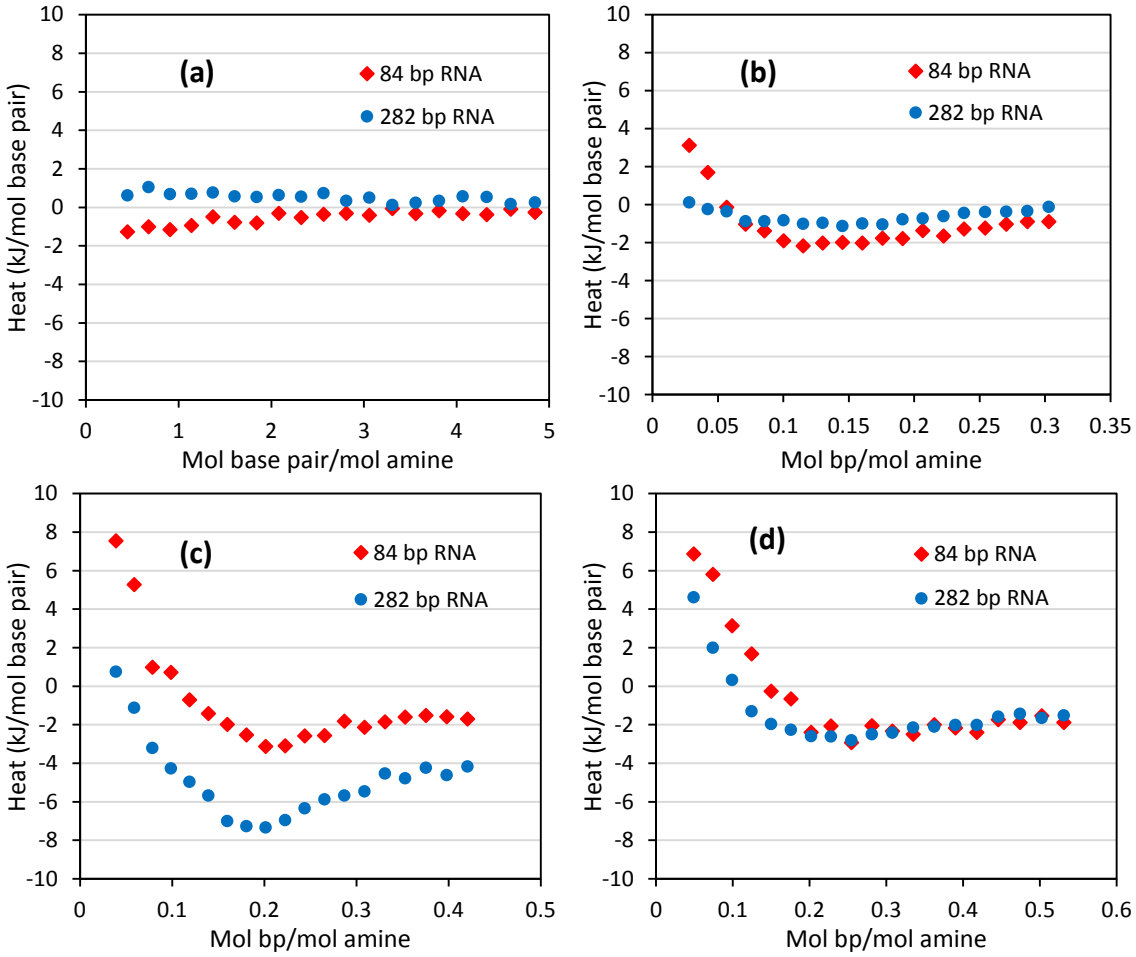

Figure 7.3 Integrated heat profiles after subtraction of dilution heat plotted against molar ratio of bp RNA and amine group in particles: (a) SNPA, (b) MSNPA-1.6, (c) MSNPA-3.2 and (d) MSNPA-7.6. First injection points were removed from thermodynamic analysis.

The interaction of dsRNA with MSNPAs (all three pore sizes) are biphasic as seen in **Figure 7.3b-d**, which means there are two distinct step-wise binding phases (as opposed to uniphasic ITC isotherms, where only one saturable interactaction is observed). Hence, ITC results can clearly be bifurcated into two different regions: (i) an initial endothermic dominant region, followed by (ii) an exothermic dominant region. The endothermic portion of the isotherms can be described as an entropy driven ionic binding process associated with large amount of counterion release, along with hydration water, from the surface of

porous particles as the RNA binds to the amine groups. This endothermic regime was observed previously for solution-based nucleic acid and polycation interactions [453, 465]. During the first binding step, unfavorable enthalpy change from the RNA-countercation and amine-counteranion electrostatic bonds is largely counteracted by the highly favorable entropy change of water release. The exothermic heat prevalent in the second phase is due to short-range local electrostatic interactions and hydrogen-bonding between deprotonated amines and nucleobases [174, 453]. Based on previous interpretations of interactions in solution, we infer that deprotonation of some amine groups upon charge-neutralization was responsible for enhancing H-bonding during later phase of binding. It should be kept in mind that even though one or the other process dominates at various steps during titration, these two interactions happen simultaneously and straightforward deconvolution is not possible. The second binding regime ultimately reached saturation around 1.5 mol bp/mol amine ratio (**Figure E.11d**), which marks the end of all thermodynamic interactions between RNA and MSNPAs.

Unlike some other studies involving polycations in solution with nucleic acid, there is no third endothermic region due to aggregation of cationic polymers after charge neutralization upon binding to nucleic acid [453, 466, 467]. Thus, the particles remain as a stable colloidal suspension, presumably due to their positive charge, a surface property that promotes cellular internalization during RNA delivery. The nature of the ITC isotherms is also different than those of 2-propylpentanoic acid titrated into amine functionalized mesoporous silica nanoparticles (average pore diameter ~ 6 nm), where only exothermic heats were measured [463]. Moreover, for nucleic acid bound to both cationic polymer and polyamine dendrimers, the end of the first binding phase is associated with phosphate

saturation, which marks the dynamic equilibrium between bound and free RNAs in solution [453, 468]. Phosphate saturation (end of first phase) is important, as the dynamic exchange of RNAs between the surface and surroundings can be achieved using the same particle to RNA ratio to induce RNA release.

The heat of interaction for 84 and 282 bp RNA is different for the smaller-pore materials (MSNPA-1.6 and MSNPA-3.2) but more similar for MSNPA-7.6 (**Figure 7.3b-d**). For MSNPA-1.6, the heat is large for 84 bp RNA compared to 282 bp RNA in both endothermic and exothermic regions, although the transition point on the isotherm from first to second phase was similar (0.11-0.13 mole bp/mole amine). For MSNPA-3.2, the shape of isotherms for both 84 bp and 282 bp RNA is similar, with a transition around 0.2 mole bp/mole amine, but the interaction with the 282 bp RNA is more exothermic compared to 84 bp RNA in both regions. Although 84 bp and 282 bp heat of interaction with MSNPA-7.6 is similar in the exothermic region, it differs slightly in the first endothermic region with 84 bp RNA being comparatively more endothermic.

The difference in heat as a function of RNA length for MSNPA-1.6 can be attributed to the effect of pore size and structure orientation. While RNA would not be expected to enter the pores based on its diameter (2.6 nm), the reported pore size of the functionalized materials (1.6 nm) represents an average of the pore distribution and pore loading is evident relative to the nonporous material. However, the bicontinuous cubic structure ($Ia\bar{3}d$) of MSNPA-1.6 [38, 69] has high tortuosity, which prevents 282 bp RNA from entering the pores completely. MSNPA-3.2 has 2D hexagonal pore structure (p6mm) [83] and larger pores, allowing both lengths of RNA to enter the pores more readily. The interaction for 282 bp RNA in MSNPA-3.2 is more exothermic (offset in **Figure 7.3c**)

compared to 84 bp RNA because there is relatively little entothermic recovery during each injection (**Figure E.10**), suggesting that its stiffness limits the ability of the 282 bp RNA to full enter and explore the pore space. For MSNPA-3.2 (average pore diameter 3.2 nm) the pore size is well matched to the RNA molecular diameter for binding the phosphate groups to amines on the particle, which may cause steric constraints. For MSNPA-7.6, the pore size is large compared to RNA diameter so that the length of RNA is not a factor and the heat of interaction per bp is roughly similar.

7.4.3 Thermodynamic Properties

Thermodynamic binding parameters for the endothermic and exothermic regions of the ITC isotherms were determined from model fitting, with a goal of more clearly elucidating the impact of pore size and RNA length on the interactions with MSNPAs. A biphasic binding isotherm fits two site binding models, which is equivalent to assuming a Langmuir-type equilibria of a macromolecule with two distinct and independent association sites for receptors [174]. Two binding site models have been applied to interpret nucleic acid interaction with polycations in solution [469]. The accuracy of binding parameter estimation (single or double binding site) from ITC data is largely dependent on the Wiseman "c-value", which is the product of the number of binding sites, receptor (nanoparticle) concentration and association constant (K_a) [167]. When the c-value is low (low affinity systems), it can be difficult to fit models to ITC data, as the proper sigmoidal shaped isotherms for saturable binding (one sigmoidal curve per binding site modelled) cannot be achieved. Capturing the first sigmoidal curve (for the endothermic region of the isotherm) would require lowering the mol bp:mol amine ratio by reducing the RNA

concentration titrated into the ITC or increasing the particle concentration. Lowering RNA concentration reduces the heat signal and the isotherms at low mole ratio is very noisy (for example **Figure E.9a**). Increasing the concentration of particle (receptor) suspension also increases the noise. However, Turnball and Daranas have shown that reasonable estimation of thermodynamic binding parameters is possible for an incomplete isotherm provided that a sufficient portion of isotherm is used for model fitting [470].

Thermodynamic binding parameters for 84 and 282 bp RNA interaction with SNPAs derived from ITC isotherms by fitting a single site binding model are presented in **Table 7.2**. The value of enthalpy and entropy is in the same range (ΔH = -4 to +10 kJ/mol and ΔS = 80 to 130 J/(mol K)) when nucleic acid interacts with other polycations in solution [453], and the stoichiometry (n = 1.84 and 3.55 for 84 and 282 bp, respectively) is inverse compared to the same literature (n = 0.2 to 0.9), which titrated polycations into nucleic acid. The value of n is consistent with the uniphasic isotherm for interactions of aqueous DNA (~2000 bp) with poly(diallyldimethylammonium chloride)-modified nonporous silica nanoparticles (mean particle diameter 25 to 40 nm) [471]. Using a one binding-site model, the binding of DNA to these nonporous particles was slightly exothermic (ΔH = -5 to -8 kJ/mol charge group) with a value of "n" of 1.2 to 1.8 charge group/base pair.

Table 7.2 Thermodynamic parameters for 84 and 282 bp RNA interaction with SNPAs as determined using a one-binding site model for nonporous particles.

RNA length	n	K_a (M^{-1})	K_d (M)	ΔG (kJ/mol)	ΔH (kJ/mol)	$-T\Delta S$ (kJ/mol)	ΔS (J/mol.K)
84 bp	1.84	2.04×10^{4}	4.91×10^{-5}	-24.6	-1.74	-22.8	76.6
282 bp	3.55	9.17×10^{3}	1.09×10^{-4}	-22.6	+1.33	-23.9	80.3

Estimated thermodynamic parameters for RNA interactions with MSNPAs are presented in **Table 7.3**, and were obtained by fitting two site binding models to biphasic ITC isotherms. Following the fitting procedure, the "c-value" was calculated for both binding sites using the model parameters and found to be in an acceptable range ($1 < c < 1000$ [167]) for estimating thermodynamic binding parameters from ITC data. As stated previously, the binding stoichiometry "*n*" is very low (0.03-0.10) for the first binding phase of MSNPAs without a full sigmoidal ITC isotherm, which is consistent with entrance of dsRNA into mesopores which are able to accomodate many base pairs while releasing a large concentration of counterions in response. The initial region described by the first binding site accounts for the high amount of water released as counterion, associated with a high entropy change. ΔH is positive because of the disruption of DNA-countercation interactions, and release of anions from the double layer inside of amine-modified silica mesopores. To compensate, ΔS is higher during the first phase of binding, but the positive entropy change for both binding steps is consistent with a large amount of water release upon binding in both regimes [472]. A similar entropy-driven binding process was observed for other polyelectrolyte interactions, such as poly(styrene sulfonate) and poly(allylamine hydrochloride) [473]. Similar ΔS and ΔG values were calculated for two different binding modes of DNA interactions with linear or branched polyethylenimine (PEI), where the endothermic region of the isotherm was attributed to deprotonation and water release and the exothermic region was described as interactions of amine groups with the phosphate backbone [460, 461].

Table 7.3 Thermodynamic parameters for 84 and 282 bp RNA interaction with MSNPAs as determined using an independent two-binding site model for porous particles.

MSNPA type		MSNPA-1.6		MSNPA-3.2		MSNPA-7.6			
RNA length		84 bp	282 bp	84 bp	282 bp	84 bp	282 bp	84 bp	282 bp
Salt addition		No Salt						30 mM NaCl	
First binding event	n	0.030	0.040	0.072	0.048	0.109	0.060	0.061	0.052
	K_a (M^{-1})	1.93×10^{6}	1.06×10^{6}	1.92×10^{6}	1.83×10^{5}	2.34×10^{5}	1.02×10^{5}	3.50×10^{6}	4.86×10^{6}
	K_d (M)	5.19×10^{-7}	9.39×10^{-7}	5.20×10^{-7}	5.45×10^{-6}	4.27×10^{-6}	9.76×10^{-6}	2.86×10^{-7}	2.06×10^{-7}
	ΔG (kJ/mol)	-35.8	-34.4	-35.8	-30.0	-30.6	-28.6	-37.2	-38.1
	ΔH (kJ/mol)	9.98	1.56	7.13	5.92	10.14	6.51	4.65	1.58
	$-T\Delta S$ (kJ/mol)	-45.8	-34.9	-43.0	-35.9	-40.8	-35.1	-41.9	-39.7
	ΔS (J/mol.K)	154	121	144	120	137	118	141	133
Second binding event	n	0.221	0.177	0.432	0.347	0.313	0.374	0.370	0.486
	K_a (M^{-1})	9.83×10^{4}	1.15×10^{5}	3.64×10^{4}	7.00×10^{3}	6.38×10^{3}	9.90×10^{3}	1.67×10^{5}	2.33×10^{5}
	K_d (M)	1.01×10^{-5}	8.67×10^{-6}	2.75×10^{-5}	1.43×10^{-4}	1.57×10^{-4}	1.01×10^{-4}	5.98×10^{-6}	4.29×10^{-6}
	ΔG (kJ/mol)	-28.5	-28.9	-26.0	-21.9	-21.7	-22.8	-29.8	-30.6
	ΔH (kJ/mol)	-2.71	-1.46	-3.87	-13.8	-8.45	-5.04	-0.863	-0.943
	$-T\Delta S$ (kJ/mol)	-25.8	-27.4	-22.1	-8.18	-13.3	-17.8	-29.0	-29.7
	ΔS (J/mol.K)	86.5	92.0	74.3	27.4	44.5	59.6	97.2	99.8

The second phase of binding of RNA to amine funtionalized particles is characterized by significantly higher values of binding stoichiometry, where *n* is around 0.2 for MSNPA-1.6 and from 0.3 to 0.43 for MSNPA-3.2 and MSNPA-7.6. Estimated parameters (n = 0.18 to 0.43, ΔH = -13.8 to -1.5 kJ/mol and ΔS = 27 to 92 J/mol/K) for the second binding phases are in the range of literature values for polycationic (polyaminated polymers) interactions with plasmid (p) DNA, dsDNA and siRNA, which was attributed mainly to short-range electrostatic interactions and H-bonding [174, 453, 455, 465]. Gourishankar et al. studied the interaction of nucleobases separately with Au nanoparticles and found only exothermic (H-bonding) interactions with an enthalpy of -1 to -3 kJ/mol [474]. Thus, the major contributions of the second phase interaction are short-range electrostatic interactions and hydrogen bonding of nucleobases with deprotonated amine group and surface. Holzerny et al. investigated dsRNA (~240 bp) interaction with chitosan in solution and found exothermic interaction (uniphasic) with an enthalpy of -84 to -102 kcal/mol RNA (-1.5 to -1.8 kJ/mol bp) [454]. These values also match our estimated parameters for second phase binding and suggest that it is dominated by H-bonding and short-range electrostatic interactions, which is responsible for threading of RNA further and deeper into the pores.

7.4.4 Effect of Salt Addition

The presence of salts in solution is known to suppress polyionic interactions due to charge shielding. Heat of interactions, either endothermic or exothermic are reduced when ionic strength increases [171]. The exothermic heats of dilution are greater in presence of salts for both lengths of RNA (**Figure E.13**) due to a higher concentration of counterions

in solution and more opportunity for hydration of salt ions. ITC isotherms for 84 bp and 282 bp RNA interacting with MSNPA-7.6 in the presence of 30 mM NaCl are presented in **Figure 7.4**. The magnitudes of both the endothermic and exothermic regions of the isotherm are reduced in the presence of salt, highlighting the contribution of electrostatic interactions in both regimes. Following the fit of the data with a two-site binding model, the magnitude of the resulting ΔH's for both sites decreases considerably (**Table 7.3)**, as suggested by the raw data. The enthalpy (ΔH) of the second binding phase is reduced by 4-6 kJ/mol in the presence of salts. This is consistent with the effect of salt on plasmid-DNA interactions with poly-lysine, which reduced the enthalpy of binding by 2-6 kJ/mol [469]. The contribution of entropy change to binding in the presence of salts increases slightly in the endothermic regime, but increases significantly during the exothermic regime. Higher entropy change in presence of salts can be attributed to salt ion induced breaking of well-ordered ionic shells in water in the presence of additional cations [451, 475]. The net effect also increases binding free energy (ΔG) in the presence of salt. Lower enthalpy and higher free energy of binding in presence of NaCl indicates the opportunity of salt mediated loading and release of RNA, which was demonstrated for DNA [165].

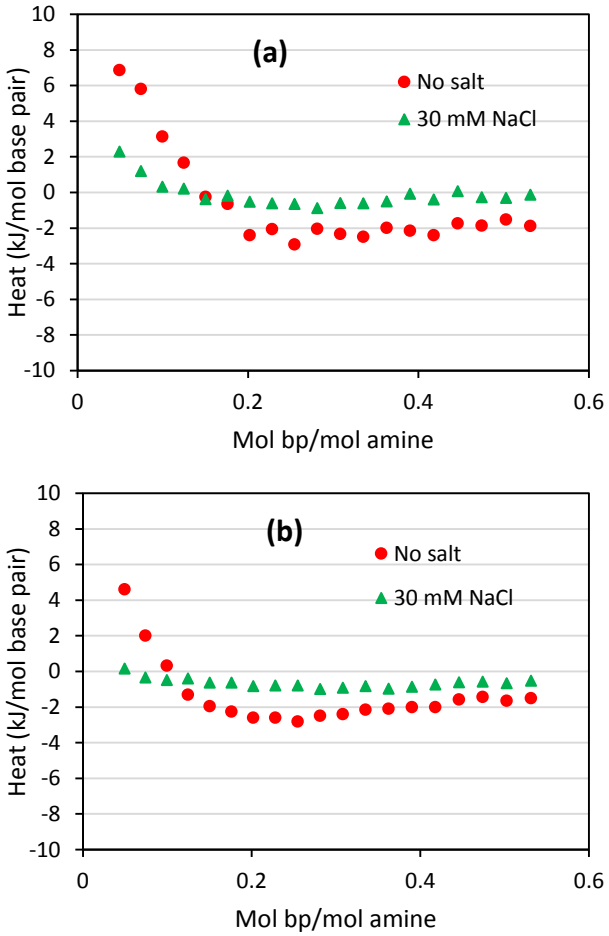

Figure 7.4 Integrated heat profiles after subtraction of dilution heat plotted against molar ratio of bp RNA and amine group in particles in absence and presence of salt for 1.67 mM bp into 0.57 mM amine on particles (0.5 mg/mL MSNPA-7.6): (a) 84 bp RNA and (b) 282 bp RNA interaction with particles.

7.4.5 Enthalpy-Entropy Compensation

As observed from the results in **Table 7.3,** higher unfavorable enthalpies for dsRNA interaction with MSNP particles tend to be balanced by higher entropic favorability and *vice versa*. Thus, enthalpy-entropy compensation exists during these interactions. Enthalpy-entropy compensation is frequently observed for thermodynamic interactions in aqueous solution, including DNA interaction with polycations cobalt(III)hexamine and spermidine^{3+} [476], as analyzed by Ball and Maechling [171]. The physical meaning of

enthalpy-entropy compensation can be interpreted from a plot of $T\Delta S$ versus ΔH, which produces a straight line [147, 163] expressed as:

$$T\Delta S = \alpha\Delta H + T\Delta S_0 \quad (7.2)$$

where α is the slope of compensation curve and $T\Delta S_0$ is the y-intercept. The slope, α, represents the contribution of enthalpic gain to the change in ΔG, as strongly binding processes usually restrict the mobility of molecules bound and thus associated with accompanying entropy loss and *vice versa*, whereas the intercept, $T\Delta S_0$ represents the stability of the complex formed in the absence of any enthalpic stabilization (ΔH = 0). These values of slope and intercept are used as a quantitative, empirical measure of conformational changes and desolvation (water release) upon binding [147, 477]. For a rigid cation-binding ligand, α = 0.45-0.65 with $T\Delta S_0$ = 8-13 kJ/mol was reported to be suggestive of no conformational change and small water release, whereas flexible protein interaction with ligands, peptides and Au nanoparticle involve α = 0.9-1.1 and $T\Delta S_0$ = 27-45 kJ/mol (high water release) [147]. A slope value of ~2.0 and $T\Delta S_0$ value of 20-30 kJ/mol were found during DNA interaction with polycations in solution [171], demonstrating significant conformational change with high water release.

It is also interesting to note that enthalpy-entropy compensation has been observed in the ion pairing/electrostatic interaction regime during DNA binding with polycations, but not during DNA aggregation (after phosphate saturation) [171, 476]. In **Figure 7.5**, all $T\Delta S$ from **Table 7.3** (for both the one phase and two phase binding models of RNA to MSNPAs with and without salt present) are plotted versus ΔH resulting in a linear fit of (R^2 = 0.87). The slope (α = 1.6) and intercept ($T\Delta S_0$ = 30 kJ/mol) are consistent with the ion pairing/electrostatic interaction regime of solution-based interactions of nucleic acids

and polycations. A high values of the slope (α = 1.6) compared to unity indicates a high conformational change of the system (including dsRNA, counterions and hydration water) upon binding, whereas large value of $T\Delta S_o$ indicates a significant amount of desolvation and water release [147], consistent with the explanation of the nature of binding involving counterion release with hydration water. Hence, the interpretation for solution based nucleic acid binding to polycations remain unchanged for the binding of RNA confined in mesopores.

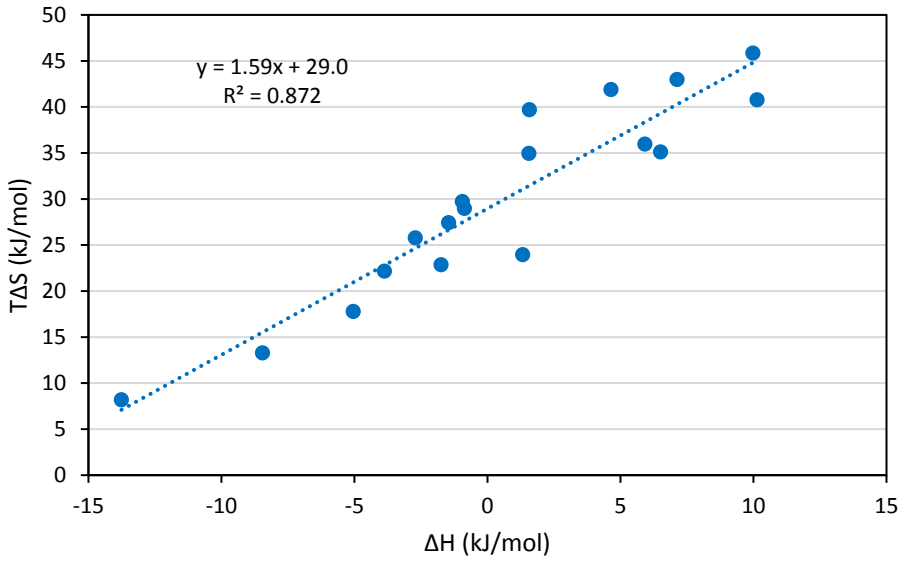

Figure 7.5 Enthalpy-entropy compensation diagram (plot of $T\Delta S$ vs. ΔH) for dsRNA (both 84 and 282 bp) interaction with amine functionalized nonporous and mesoporous nanoparticles (SNPAs and MSNPAs).

7.5 Conclusions

Length- and pore size-dependent dsRNA interaction with amine-functionalized mesoporous silica nanoparticles (MSNPAs) and adsorption of dsRNA inside nanopores were investigated using ITC. Although 84 bp dsRNA (2.6 nm × 24 nm rods) was able to load into 1.6 nm, 3.2 nm and 7.6 nm MSNPA pores, 282 bp dsRNA (2.6 nm × 80 nm) was found incapable of loading inside 1.6 nm pores, interpreted from their very low heat of interaction with MSNPA-1.6, but able to enter 3.2 nm and 7.6 nm pores. Significant difference between heat of interactions of 84 and 282 bp RNA was observed for MSNPA-3.2 due to greater steric constraints for pore exploration by the longer RNA. In contrast, similar heats of interaction were observed for dsRNA in the pores of MSNPA-7.6. This is the first study reporting direct measurements of the heat of interaction of dsRNA into MSNPA pores based on the relative dimension of dsRNA in comparison to pore diameter. The observations suggest that it should be possible to design efficient dsRNA nanocarriers by creating pores that are small enough to protect the RNAs from nucleases during delivery, while also providing enough space for dsRNA threading into the pores.

The interaction of RNA with porous particles is characterized by an initial endothermic heat followed by an exothermic region. These ITC data were fit to a two-site binding model. This first regime of the interaction of RNA with cationic amine functionalized porous particles is attributed to phosphate-amine binding inside of nanopores, resulting from the release of large amounts of counterion (and water) associated with the RNA and the electrical double layer inside of the pores. The second exothermic regime, while still dominated by entropic contributions, involves exothermic hydrogen bonding and short range electrostatic interactions between RNA and amine groups. Only one binding regime is observed for the interaction of RNA with nonporous particles; this

regime mimics the exothermic regime of porous particles. The contribution of electrostatic interactions during both binding phases is demonstrated by the enthalpy reduction in solutions of high ionic strength.

This work has implications to the design of RNA/mesoporous silica particles as nanocarriers, specifically with respect to the loading, protection, and release of RNA. This work identifies concentration regimes where the initial loading of RNA into nanopores of the particles becomes saturated, and regimes where confined RNA continues to interact through hydrogen bonding and short-range electrostatic interactions with external and internal particle surfaces. Since equilibrium between bound and unbound RNA is attained, RNA inside the pores remains mobile, as demonstrated by confocal microscopy and FRAP technique previously. These results also support the idea that the mobility of dsRNA confined in pores is dependent on the dsRNA loading, which can only be observed after a certain amount of local charge neutralization. As a result, the identification of the thermodynamic interactions and related parameters will aid in designing effective porous nanocarriers for loading and delivery of nucleic acid to target intracellular sites during a number of genetic manipulation strategies.

CHAPTER 8. OVERALL CONCLUSION AND FUTURE DIRECTIONS

8.1 Overall Conclusion

This dissertation addresses engineered silica nanoparticle design principles for bioactive materials nanoharvesting and delivery applications, with emphasis on underlying molecular and cellular interaction mechanisms. Mesoporous silica nanoparticles (MSNPs) were used as a high surface platform and support for biomolecule loading and transport across the cellular plasma membrane. Particle surfaces were functionalized by various active groups to provide affinity and specificity toward biomolecules as well as positively charged groups to facilitate membrane penetration. Initially, in **Chapter 3**, a nonspecific high binding ligand (TiO_2) was attached to the MSNP surface by post-synthesis functionalization for the adsorption and separation of polyphenolic flavonoids. The high loading capacity is utilized for the *in vitro* loading and release of model flavonoid quercetin and its derivatives, which are known for their therapeutic properties. Key findings were the determination of conditions to give optimal loading of amorphous, dispersed Ti-sites (required for adsorption) inside silica mesopores, and development of a novel flavonoid recovery process using citric acid to displace bound flavonoids. The high binding capacity of the particles for polyphenolic flavonoids provides the opportunity to isolate them from living plant cultures, circumventing both the need for costly chemical synthesis and maceration of expensive genetically modified plants during conventional extraction.

Particles with optimized surface properties (TiO_2 for metabolite binding and positively charged amine for cell membrane penetration) were used for nanoharvesting of flavonoid metabolites from living and functioning *Solidago nemoralis* hairy root cultures in **Chapter 4**. Particles were shown to penetrate inside root cells and carry the metabolites

out, while plant cultures remained viable for continuous bio-synthesis of metabolites. All of these features are required for the nanoharvesting application. Harvesting of active metabolites was confirmed by observing increased radical scavenging activity (characteristic of flavonoids) and nicotinic receptor-related ligand displacement activity of the particles after exposure to roots. The concept of nanoharvesting is new and using functionalized MSNPs with high surface area is novel, which provides opportunities for the selective isolation of many varieties of biomolecules from transgenic plant cultures. The ability of these particles to harvest biologically active therapeutics also points to another dimension for treatment, where recovered particles after nanoharvesting can be directly applied for intracellular biomolecule delivery.

As a follow-up to the nanoharvesting work, mechanisms of nanoparticle internalization into and expulsion from root cells during nanoharvesting was investigated in **Chapter 5**. Uptake of nanoparticles, when quantified using a Ti-assay, showed a Langmuir-type relation with concentration. Nanoparticle internalization was also found to be time dependent, interpreted from the fluorescent microscopy of roots after exposure to particles. Temperature dependent uptake and recovery, which distinguishes between activated and non-activated mechanisms, showed different uptake and expulsion process based on the presence of positively charged amine group on particle surface. The importance of positively charged group in gaining access to metabolites inside the cells during nanoharvesting is explicated as a result. Kinetics of nanoparticle uptake and expulsion processes during the exchange of non-fluorescent particles and fluorescent particles shows a spontaneous reversible particle exchange process during nanoharvesting. This study disentangles the inherent interactions of engineered silica nanoparticles with

plant cells and whole tissue, providing insights into transport and expulsion mechanisms not only during nanoharvesting but also in designing novel biomolecule delivery processes. Particle surface properties were found to be important for both cellular internalization and exit, and influences on both of them should be considered during optimum design of particles as nanocarriers.

It is possible to selectively isolate and separate a compound of interests from a biological mixture or plant cultures during nanoharvesting by selecting a surface functionality that selectively binds to the molecule in a specific host-guest interaction. In order to provide specific surface functionality to MSNPs for selective separation and isolation of β-estradiol, an oligopeptide that mimics human estrogen binding sites was conjugated to the particle surface in **Chapter 6** using a hetero-bifunctional linker sulfo-NHS-LC-diazirine. This linker is used to link amines on the particle surface to amines at the N-terminus of peptides. Preservation of peptide functionality after conjugation was demonstrated by increased β-estradiol binding ability of peptide-conjugated particles. The hetero-bifunctional linker consisting of UV-activable diazirine group at one end and amine reactive NHS ester at the other end provides separate control over diffusion of the peptide into pores and its reaction with the surface. Binding efficiency and applicability to different peptide sequences were demonstrated by fluorescence spectroscopy and TGA. General applicability of this attachment strategy between amines provides the opportunity to incorporate any known peptide to target specific biomolecule products. These peptide-attached particles are also viable candidates for selective nanoharvesting of valuable therapeutics from plants as the unconjugated amine groups (roughly 50%) provide the

necessary positive charge for cellular internalization and expulsion. Nanoharvesting using these particles allows for simultaneous harvesting and separation of target molecules.

Finally, the thermodynamic interaction between nanoparticles and biomolecule is immensely important for the loading and controlled release of the molecules during nano-delivery applications. The thermodynamic interaction between amine functionalized MSNPs and double-stranded RNA was investigated using isothermal titration calorimetry as a function of pore size (0, 1.6, 3.2 and 7.6 nm) and RNA length (84 and 282 base pairs) in order to promote facile RNA delivery (**Chapter 7**). Complex and biphasic interactions between porous particles and RNA were found, initially dominated by entropic favorability (endothermic heat) from a large amount of water release, followed by exothermic (still entropy-dominant) binding arising from short-range electrostatic interactions. On the other hand, interaction with nonporous particles were mainly uniphasic and dominated by short range electrostatic interactions. The inability of larger RNA (282 base pair) to enter smallest pores, consistent with a previous confocal microscopy study, is indicated by very low heats of interactions in both phases. In contrast, 84 base pair RNA was able to enter all pore sizes, and 282 base pair RNA in 3.2 nm and 7.6 nm pores. Heats of interactions reduce for both binding phases in the presence of salt, suggesting electrostatic interaction throughout the binding process. The interaction showed entropy-enthalpy compensation due to conformation change of RNA and behaving as a flexible host during binding. The end of first endothermic phase marks the end of phosphate saturation on the RNA molecule and at this point equilibrium is reached between surface-bound and free RNA consistent with high mobility of RNA molecule previously demonstrated by photobleaching. The enthalpy and entropy of interaction and saturation points are important parameters for

designing mesoporous carriers for loading, protection from enzymatic hydrolysis, and controlled release during intracellular nucleic acid (DNA/RNA) delivery.

8.2 Future Directions

There are a number of ways the findings in this dissertation can be expanded into new directions in future. As mentioned earlier, the overall goal of this dissertation is to design nanoparticulate carriers based on engineered silica nanoparticles (ESNP) with optimum properties for biomolecule harvesting and delivery from and to living cells. For these purposes, a robust TiO_2 surface functionalized MSNP platform was developed with high adsorption capacity of polyphenolic flavonoids (**Chapter 3**) and the same particles were utilized for nanoharvesting of flavonoids from living plants enabled by positive surface charge (**Chapter 4**). The mechanisms of nanoparticle entry and exit during nanoharvesting were also investigated (**Chapter 5**). Specific functional oligopeptides were conjugated inside of MSNP pores for the selective separation of biomolecules (**Chapter 6**), which provides the opportunity to nanoharvest a vast number of therapeutics. Lastly, thermodynamic interactions of double stranded RNA with amine functionalized MSNPs were studied in detail using isothermal titration calorimetry (ITC) (**Chapter 7**) for designing ideal carriers for delivery. Obviously, there is room for some improvements in each of the projects, but future directions from this dissertation should primarily involve selective nanoharvesting of high-value therapeutics from plant cultures and RNA delivery using functionalized MSNPs. Specific suggestions are provided below.

In **Chapter 3**, MSNPs were functionalized by the TiO_2 using post-synthesis grafting by hydrolysis of a Ti-precursor. Although the adsorption capacity of the particles increased a hundred-fold at the optimum degree of functionalization (~ 430 mg/g particles) compared to nonporous particles, all Ti-sites were probably not fully accessible based on surface area reduction and crystallite formation on the outer particle surface. To provide better Ti-dispersion, a ligand-assisted functionalization strategy can be adopted, where Ti-

precursor will be pre-complexed with the maltoside head-group of a sugar-surfactant before functionalization. Previously, our group reported a procedure for the synthesis of silica thin film with isolated Ti-sites by using ionic and sugar surfactant n-dodecyl β-D-maltopyranoside ($C_{12}G_2$) mixed micelle templating of the pores, where $C_{12}G_2$ was pre-complexed with titanium (iv) isopropoxide (TIP) [117]. A similar procedure can be developed for post-synthesis functionalization of MSNPs. An ionic surfactant CTAB should be used together with complexed sugar surfactant to enhance its adsorption on silica [478]. This functionalization strategy can be extended to MSNPs for the creation of isolated Ti-sites on the silica surface. A general schematic diagram of the proposed study is presented in **Figure 8.1**, depicting the process of ligand assisted post-synthesis functionalization strategy. After functionalization the degree of Ti-grafting as a function of precursor used can be analyzed by chemical analysis (see **Chapter 3** to **5**), and flavonoid adsorption can be performed on the functionalized particles to find the efficiency of surface TiO_2 coverage.

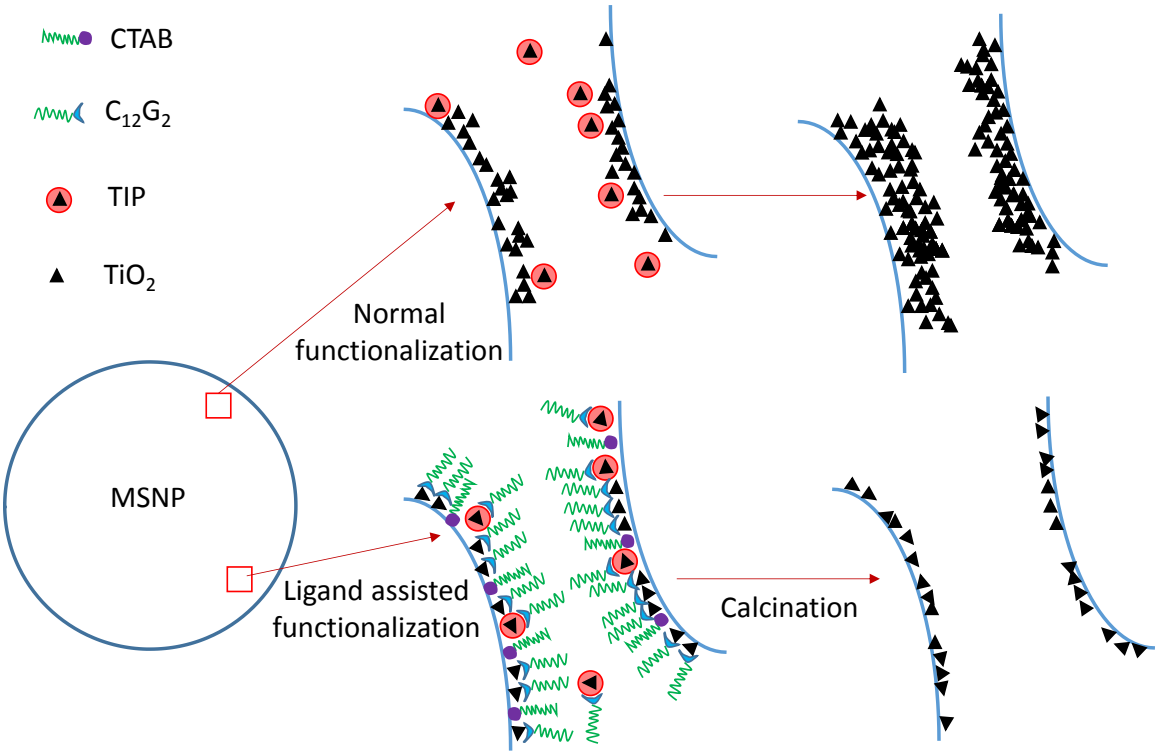

Figure 8.1 Schematic diagram of the proposed ligand assisted TiO_2 functionalization of MSNP pores as compared to normal functionalization by simple Ti-precursor hydrolysis.

The signature project of this dissertation is to harvest biomolecules from living plant cultures using ESNP carriers, as presented in **Chapter 4**. Particles were functionalized with TiO_2 and amine to provide binding sites and positive charge, respectively, and as a result, can be utilized to harvest other biomolecules that have affinity towards TiO_2. Several classes of metabolites such as phosphopeptides and amino acids, phospholipids, catechol derivatives, dopamine derivatives and alkaloids have been investigated for their attraction toward Ti [113, 235, 236], in addition to other flavonoids. All of this compounds can be potential targets for nanoharvesting using the ESNP developed here. In **chapter 6**, a strategy of functional oligopeptide/protein attachment to MSNPs was developed for the selective isolation of estrogen-like biomolecules, as demonstrated for β-estradiol. As mentioned before, oligopeptide conjugated particles can

be utilized for the selective nanoharvesting of other classes of biomolecules from transgenic plant cultures. For example, preliminary research work has been done for the selective separation of monoclonal antibodies from mutant tobacco hairy roots using protein A/G conjugated MSNPs.

We have investigated surface charge dependent nanoparticle entry, transport and exit mechanism in plant root cultures during nanoharvesting (**Chapter 5**). Temperature dependent (4 ºC and 23 ºC) uptake and expulsion of particles were studied in order to distinguish between activated and passive pathways (energy dependent/independent mechanisms) for both nanoparticle internalization and expulsion. Positively charged particles (amine functionalized) showed mostly passive uptake and exit, whereas energy dependent (endocytosis and exocytosis) mechanisms were prevalent in the absence of positive charge. However, the specific endocytosis and exocytosis mechanism was not investigated. Endocytosis mechanism usually involve micropinocytosis, pinocytosis, phagocytosis and receptor (clathrin/caveolin) mediated processes, whereas exocytosis usually happens through late endosome fusion with cell membrane or secretary vesicle formation. All of these processes have specific inhibitors, which block only a particular pathway that can be used to identify the most important uptake and expulsion mechanisms. Pinocytosis, micropinocytosis and clathrin-mediated uptake usually produces intracellular vesicles that transform into early endosomes, and without charge mediated endosomal escape, particles have no way to gain access to the metabolites. Thus, inhibitor dependent identification of mechanisms will help to elucidate why non-charged particles were not able to harvest metabolites more clearly.

In order to use the peptide conjugated particles (synthesized in **Chapter 6**) for selective nanoharvesting, it is necessary to study whether the particles can be internalized in plants and excreted following uptake. Fluorescence microscopy and spectroscopy were used to study internalization and expulsion mechanisms in **Chapter 5** for TiO_2 and amine functionalized MSNPs. However, in **Chapter 6** we used FITC-tagged peptide to quantify binding efficiency, and the same particles can be used to quantify uptake and recovery in plants. As a preliminary measure, RSSV-FITC conjugated MSNPAs were used for fluorescence microscopy of roots after exposure to the particles. Internalization inside *S. nemoralis* hairy roots is indicated by green fluorescence (**Figure 8.2**). This result is promising to show that fluorescent peptide/protein attached particles can be used to quantify uptake and recovery of polypeptide-conjugated MSNPs in other species.

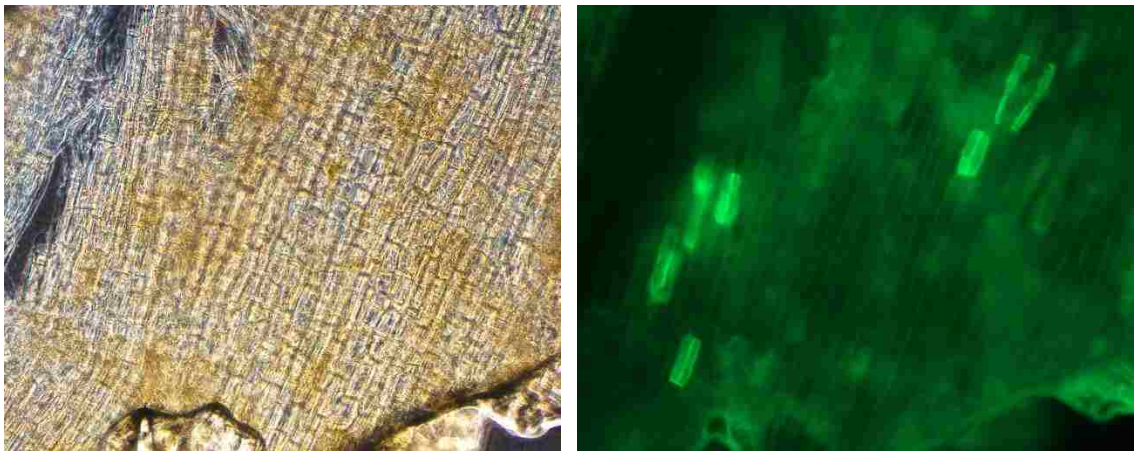

Figure 8.2 Bright field and corresponding fluorescence microscopic image of roots after exposure to RSSV-FITC conjugated MSNPAs (1 mg/mL) show uptake in *S. nemoralis* root cells.

In **Chapter 7**, thermodynamic interactions of RNA binding with amine functionalized MSNPs (MSNPAs) were investigated using ITC. The nature of the interactions largely validate previous observation regarding mobility of RNA in mesopores

once binding saturation is reached [61]. Loading of dsRNA is highly dependent on pore diameter and an optimum pore size is necessary based on the size of cell nucleases to induce pore size dependent protection. The natural progression of this project will be to deliver nucleic acids using MSNPAs and determining the optimum pore size based on delivery efficiency. Our collaborators (Dr. Bruce Webb's laboratory) at the Entomology Department of University of Kentucky have demonstrated the efficacy of MSNPA-mediated delivery of 84 and 282 base pair RNA to insect cells by silencing inhibition of apoptosis (IAP) genes [457]. However, RNA delivery to live insects remains to be investigated. One of the major route of nucleic acid delivery to insects is oral [479], which necessitates protection by MSNPAs to avoid nucleases in the insect gut. Nucleic acid delivery to plants for genetic modification, and to mammals for therapeutic purposes is also a natural ramification from this work.

Another important modification during particle design would be the introduction of magnetic core-mesoporous silica shell nanoparticles for nanoharvesting and delivery applications. Magnetic core-silica shell mesoporous silica nanoparticles (CSNPs) with various sizes have been investigated for bio-separation, small molecule isolation, magnetic resonance imaging (MRI) and drug delivery purposes, where an external magnetic field was employed for the confinement and controlled movement of nanoparticles [480-482]. As a preliminary study, CSNPs with average particle size of 70 nm were synthesized by surfactant (CTAB) templated sol-gel coating of magnetic iron oxide nanoparticles. Scanning electron microscopic images of the particles are presented for bare magnetic particles (**Figure 8.3**). Particle surface characterization was performed by nitrogen adsorption, which provided a surface area of 381 m^2/g, pore volume of 0.4 cm^3/g and

average pore diameter of 2.4 nm. In the future, these particles can be engineered to be functionalized with active groups for nanoharvesting and delivery applications, where particle movement and transport can be controlled by using an external magnetic field.

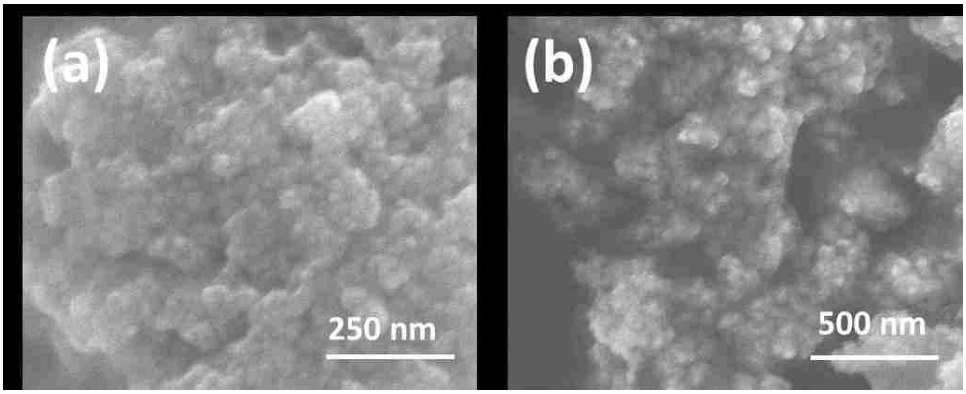

Figure 8.3 Scanning electron microscopic (SEM) images of (a) magnetic Fe_3O_4 nanoparticles and (b) Magnetic Fe_3O_4 core-silica shell mesoporous nanoparticles (CSNPs).

Finally, ESNP developed in this dissertation can be utilized as a combined nanoharvesting-nanodelivery platform where nanoharvested compounds bound to the particle surface from plants will be directly applied to the cellular targets in humans. For example, flavonoids bound to ESNP in **Chapter 4** showed binding to nicotinic receptors in rat hippocampal membranes, suggesting that they can be used directly to alleviate neuro-inflammation [321]. Delivery of the nanoharvested compounds using the same carrier ESNP will be possible and desirable due to silica's low human toxicity, for which they are heavily investigated in nano-delivery applications. It should be noted that, although the ESNP developed and designed in this dissertation are utilized for nanoharvesting of biomolecules from living plants and nucleic acid delivery, they hold tremendous promise in the broad field of chemical and materials engineering including bionanotechnology, biomaterials and advanced medicine as well as environmental engineering. High surface

platform of functionalized silica and associated physicochemical processes involving them can be the harbinger for numerous bioactive interfaces in the field of nanotechnology, from catalysis and bio-catalysis for reactive separation to drug delivery applications.

APPENDICES

APPENDIX A. SUPPLEMENTARY MATERIALS OF CHAPTER 3

A.1 Calculations for Flavonoid Adsorption, Recovery and Activity

The amount of adsorbed flavonoid on to the particle surface, $q_{e(ads)}$ (mg quercetin/g particles) was calculated by the depletion method using **Equation A.1**.

$$q_{e(ads)} = \frac{C_i - C_{e(ads)}}{m_p} V \times 1000 \quad \text{(A.1)}$$

where C_i is the initial concentration (mg/ml); $C_{e(ads)}$is the equilibrium concentration (mg/ml) after adsorption; and m_p and V are the mass of particle (mg) and volume of the flavonoid solution (in ethanol, mL) used for adsorption experiment, respectively.

The amount of quercetin retained onto the particles after recovery, $q_{e(des)}$ was estimated by subtracting the recovered amount from the initial amount of quercetin presents on the particle using **Equation A.2**.

$$q_{e(des)} = q_{e(ads)} - \frac{C_{e(des)}}{m_p} V \times 1000 \quad \text{(A.2)}$$

where $C_{e(des)}$is the equilibrium concentration (mg/ml) in desorption; and m_p and V are the mass of particle (mg) and volume of solvent (ml) used for desorption experiment, respectively. The percent recovery, η (%) was calculated by **Equation A.3**.

$$\eta(\%) = \frac{q_{e(ads)} - q_{e(des)}}{q_{e(ads)}} \times 100 \quad \text{(A.3)}$$

Radical scavenging activity (RSA) was calculated by the formula presented in **Equation A.4**.

$$RSA(\%) = \frac{A_i - A_f}{A_i} \times 100 \quad \text{(A.4)}$$

where A_i and A_f are the initial and final absorbance of DPPH solution, respectively.

A.2 Sorption Isotherm Models

Langmuir isotherm model equation (**Equation A.5**):

$$q_e = \frac{q_m K_L C_e}{1 + K_L C_e} \tag{A.5}$$

where q_e is the amount of solute adsorbed at equilibrium; q_m is the maximum monolayer sorption capacity; K_L is the Langmuir constant or binding constant and C_e is the equilibrium concentration in solution.

Table A.1 Comparison of amount of TiO_2 determined by chemical analysis and EDS analysis along with average particle diameter of MSNPTs.

Particle types	Average particle diameter (nm)	TiO_2 determined by chemical analysis (mg TiO_2/g particles)	TiO_2 determined by EDS elemental analysis (mg TiO_2/g particles)
MSNP	165 ± 19[a]	-	-
MSNPT-59	164 ± 30	59 ± 1.8[b]	53 ± 7.6[c]
MSNPT-124	199 ± 36	124 ± 3.9	110 ± 22
MSNPT-162	190 ± 24	162 ± 2.7	160 ± 11
MSNPT-440	185 ± 29	440 ± 11	380 ± 31

Standard deviation values resulted from [a]measurement of 20 particles selected randomly (using ImageJ Software) [b]triplicate measurement for chemical analysis and [c]multiple area scanning for EDS analysis.

Table A.2 Scattering vector (*q*-values), full width at half maximum (FWHM), d-spacing of (211) planes, lattice constant and pore wall thickness calculated from GISAXS peaks and BJH pore diameter.

Particle Types	q-value of (211) peak ($Å^{-1}$)	FWHM* of (211) peak ($Å^{-1}$)	q-value of (220) peak ($Å^{-1}$)	FWHM* of (220) peak ($Å^{-1}$)	(211) plane d-spacing, d_{211} (nm)	Lattice constant, a*** (nm)	Wall thickness, w** (nm)
MSNP	0.184	0.0064	0.210	0.0044	3.42	8.38	1.33
MSNPT-59	0.194	0.0122	0.220	0.0059	3.23	7.91	1.27
MSNPT-110	0.198	0.0156	-	-	3.17	7.76	1.25
MSNPT-270	0.210	0.0159	-	-	3.00	7.35	1.17
MSNPT-362	0.212	0.0176	-	-	2.96	7.25	1.20

*FWHM: Full width at half maximum of GISAXS peaks

Wall thickness, $w = \frac{a}{3.092} - \frac{BJH\ pore\ diameter}{2}$, * Lattice constant, $a = \sqrt{6}d_{211}$ [69].

Table A.3 Optimized Langmuir model parameters (q_m and K_L) found using nonlinear regression for MSNPT samples.

Particle Type	**Maximum capacity q_m (mg/g particle)**	**Langmuir constant, K_L (mL/mg)**
MSNPT-59	82.7	8.8
MSNPT-86	98.7	10.6
MSNPT-124	106	14.2
MSNPT-162	117	21.1
MSNPT-362	176	4.1
MSNPT-440	236	5.0
MSNPT-636	65.0	3.1

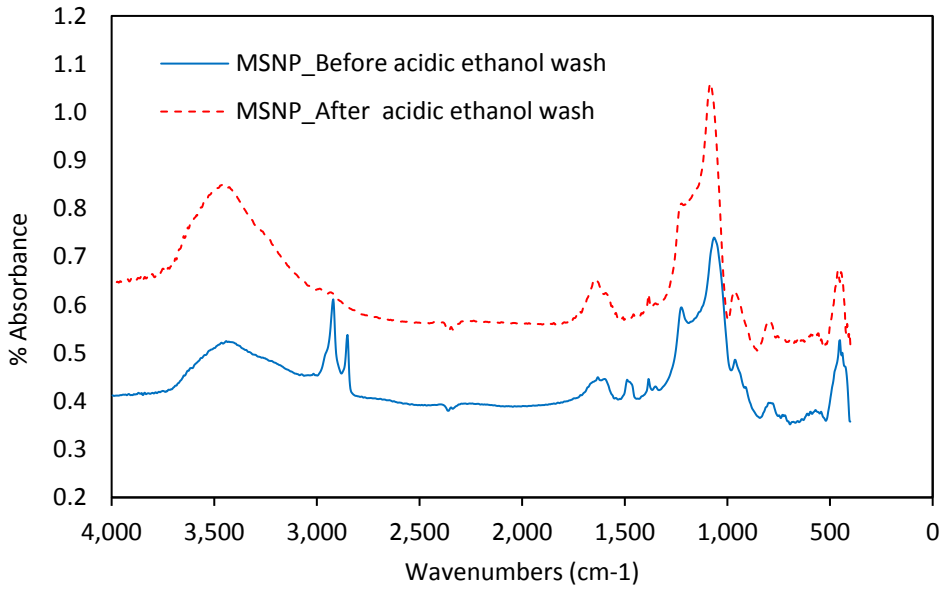

Figure A.1 FTIR analysis showing complete removal of surfactant CTAB (indicated by loss of C-H stretching bands from 2800 to 3000 cm^{-1}) during acidic ethanol washing of synthesized nanoparticles.

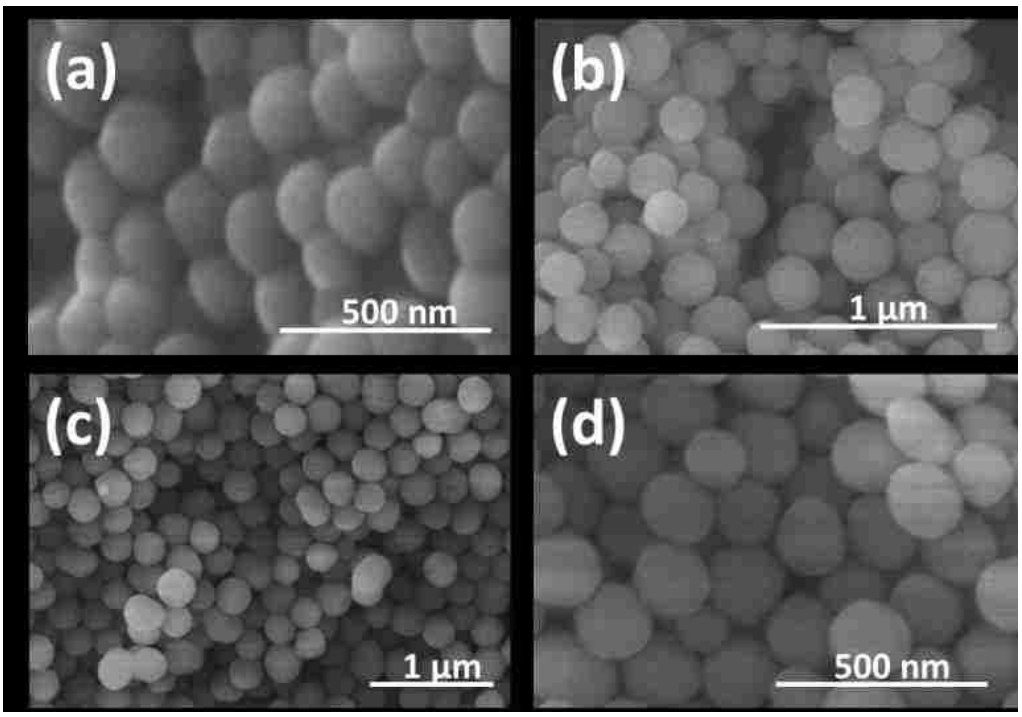

Figure A.2 SEM images of TiO_2 functionalized and non-functionalized mesoporous silica nanoparticles (MSNPT and MSNP, respectively): (a) MSNP, (b) MSNPT-59, (c) MSNPT-124 and (d) MSNPT-440.

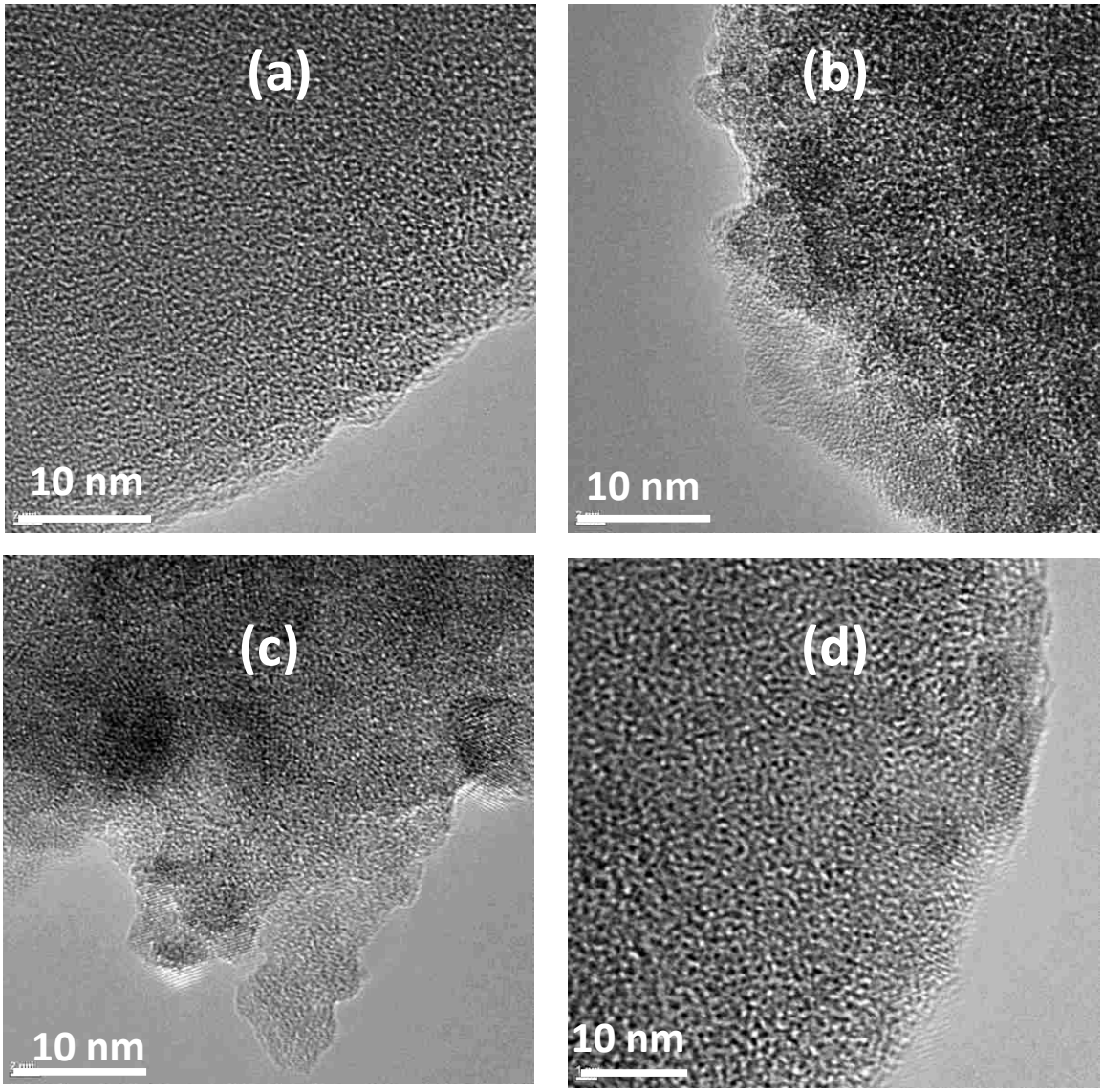

Figure A.3 High resolution TEM (HRTEM) images of (a) non-functionalized MSNP, (b) MSNPT-110, (c) MSNPT-270 and (d) MSNPT-636 showing the formation of nanocrystals with increasing TiO_2 content.

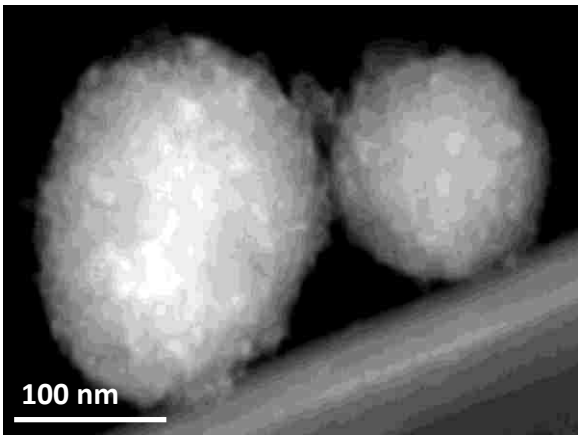

Figure A.4 Dark-field scanning-transmission electron microscope (STEM) image of MSNPT-110. Due to its high electron density relative to SiO_2, TiO_2 gives the bright spots throughout the particles.

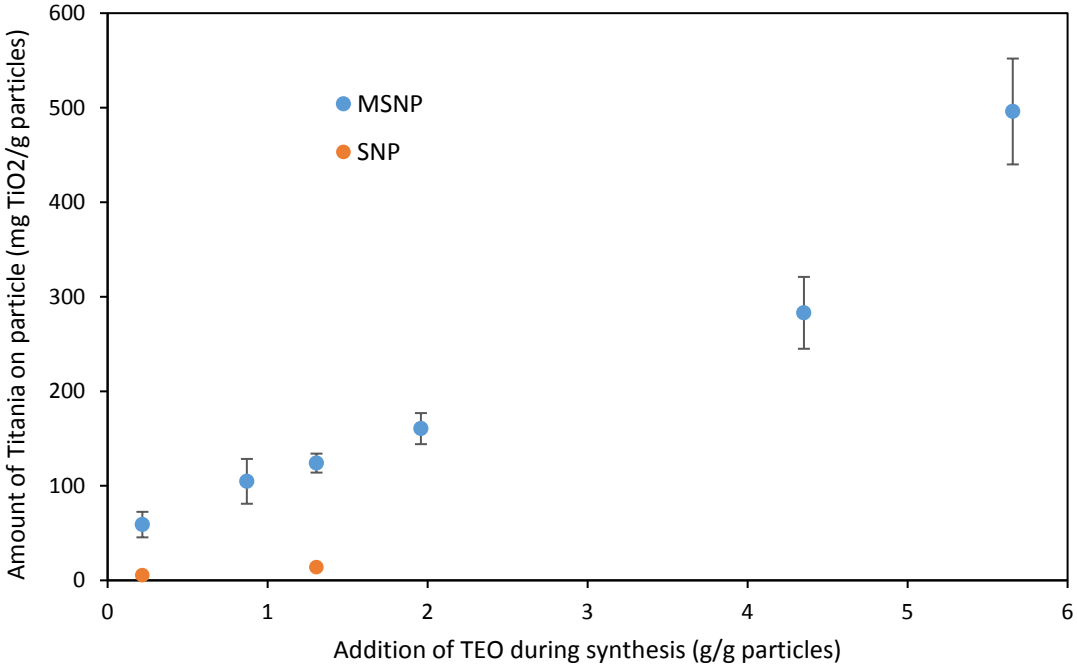

Figure A.5 Comparison of TiO_2 grafting densities on MSNP and nonporous Stöber particles (SNP) with average particle diameter 190 nm.

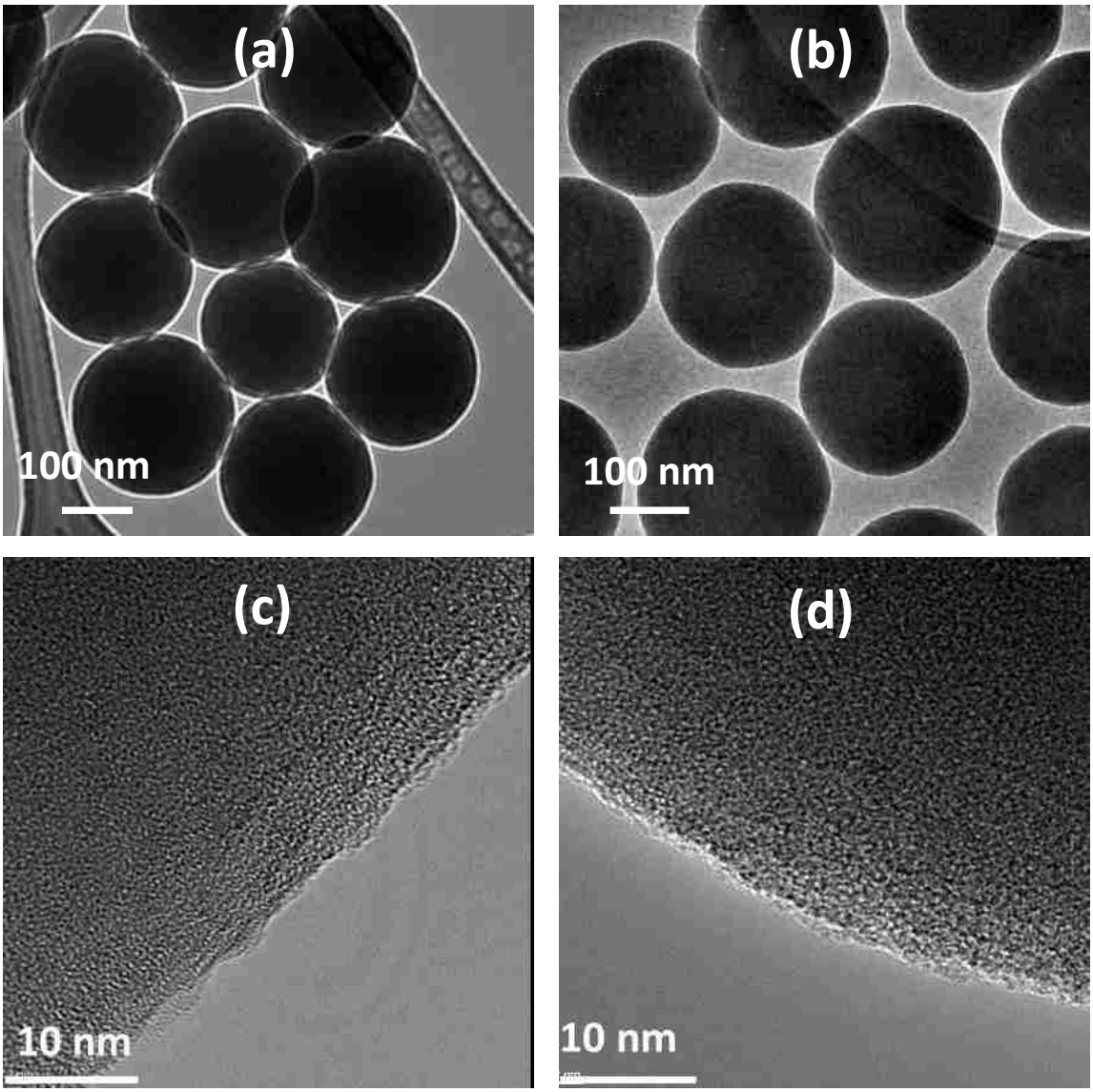

Figure A.6 TEM image of nonporous silica nanoparticles: (a) Low magnification TEM image of non-functionalized SNP and (b) TiO_2 functionalized SNP (SNPT-13.7), and HRTEM images of (c) SNP and (d) SNPT-13.7.

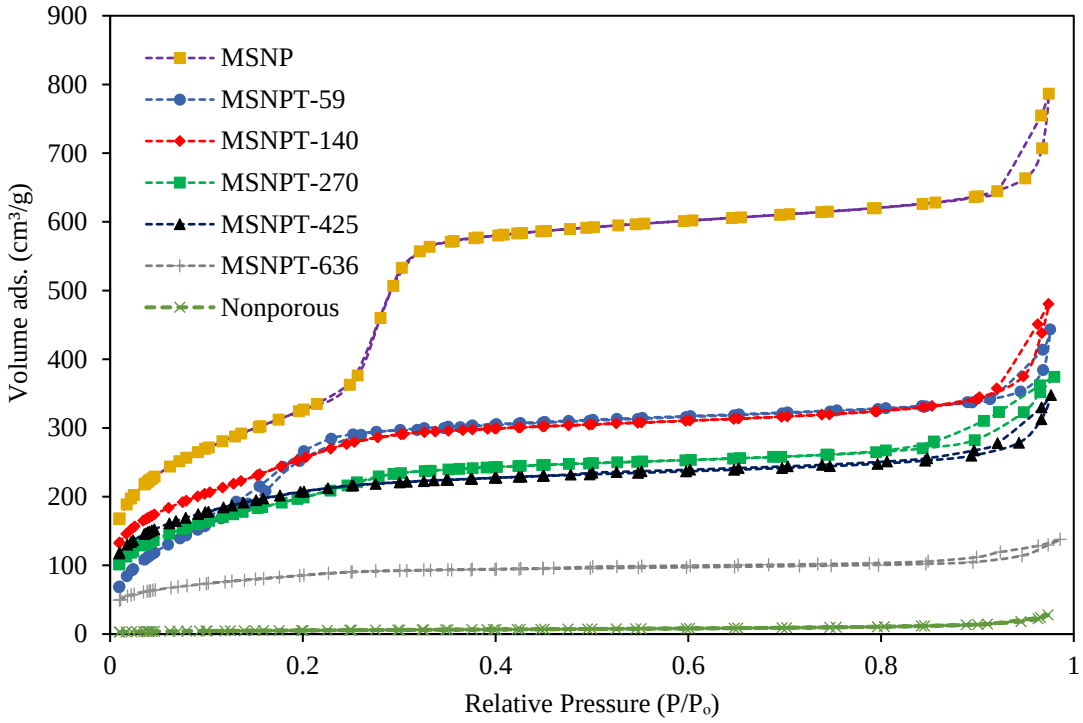

Figure A.7a Nitrogen sorption isotherms on non-functionalized and TiO_2 functionalized MSNP.

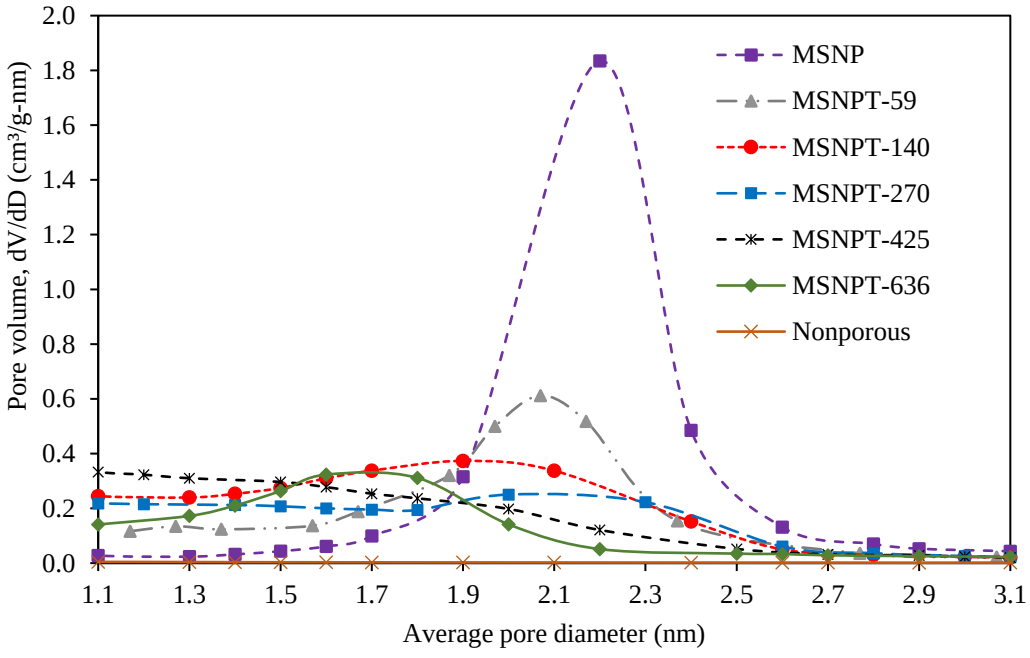

Figure A.7b Pore size distributions of non-functionalized and TiO_2 functionalized MSNP.

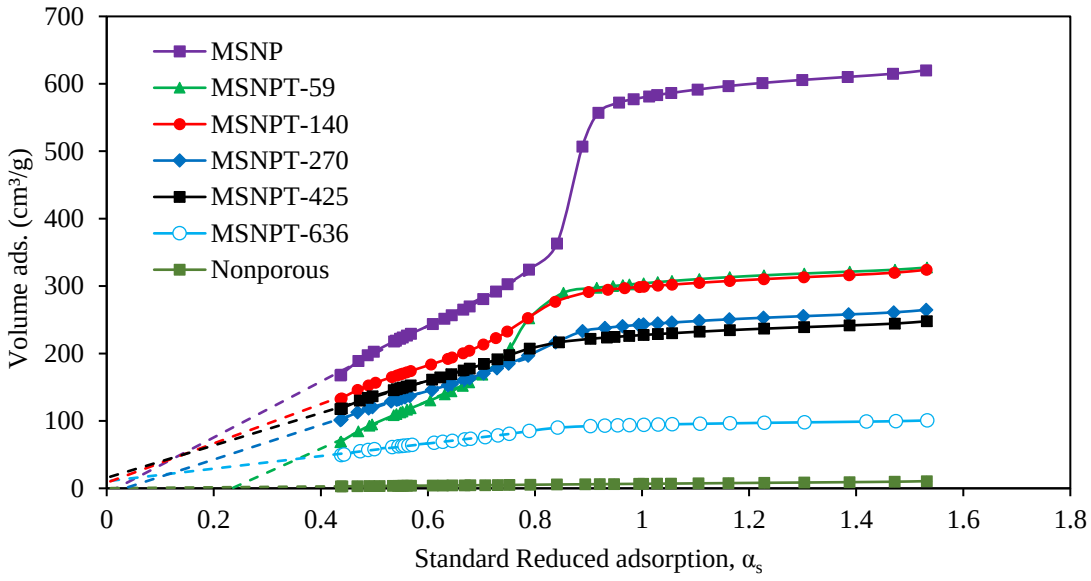

Figure A.7c α_s-plot for nitrogen adsorption isotherms on non-functionalized and TiO_2-functionalized MSNP showing the absence microporosity after functionalization (α-plot determined from the relative pressure vs. standard reduced adsorption table of Jaroniec et al. [269]).

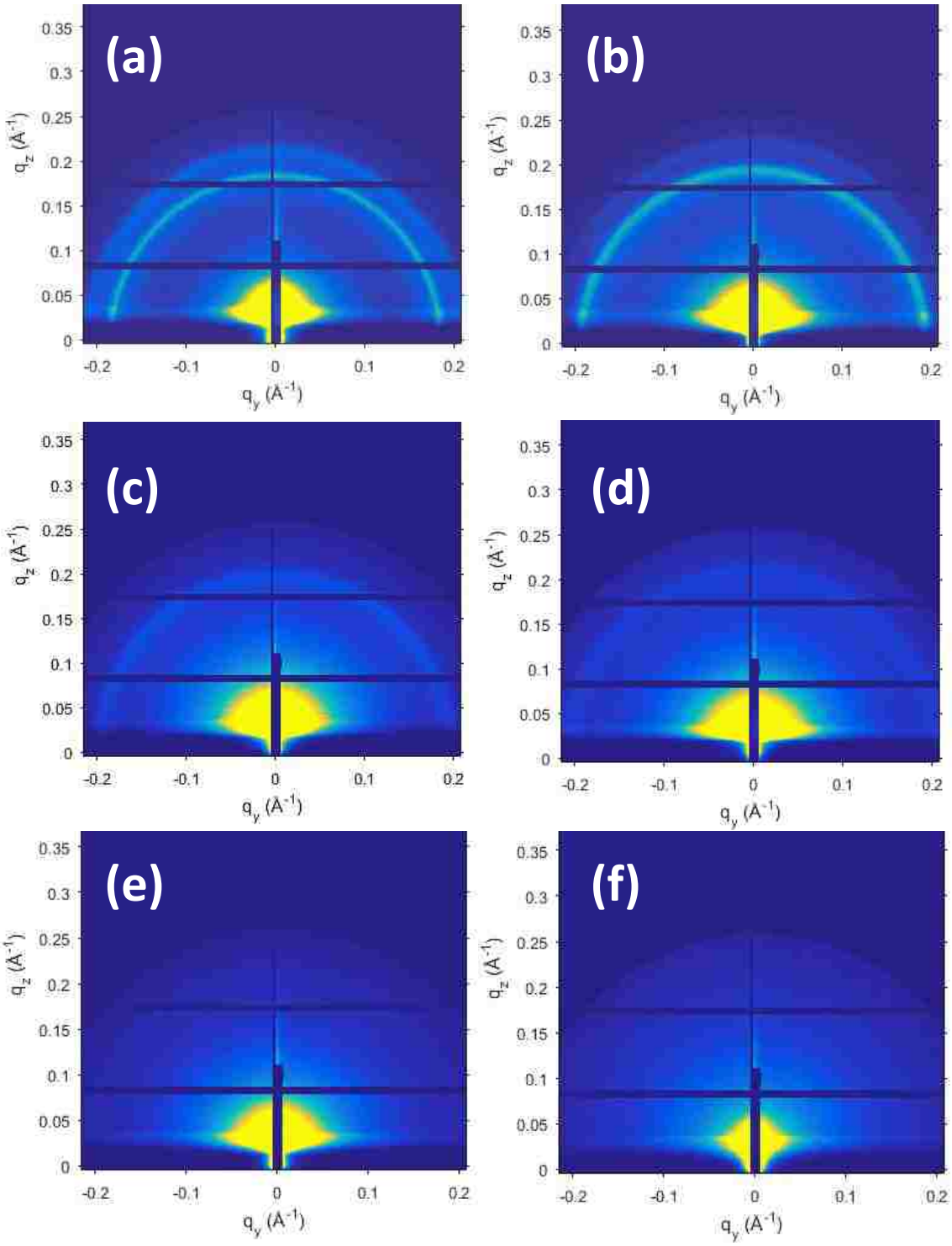

Figure A.8 2D GISAXS patterns (incident angle, α_i = 0.20º) of non-functionalized and TiO_2 functionalized MSNP: (a) bare MSNP, (b) MSNPT-59, (c) MSNPT-110, (d) MSNPT-270, (e) MSNPT-362 and (f) MSNPT-636.

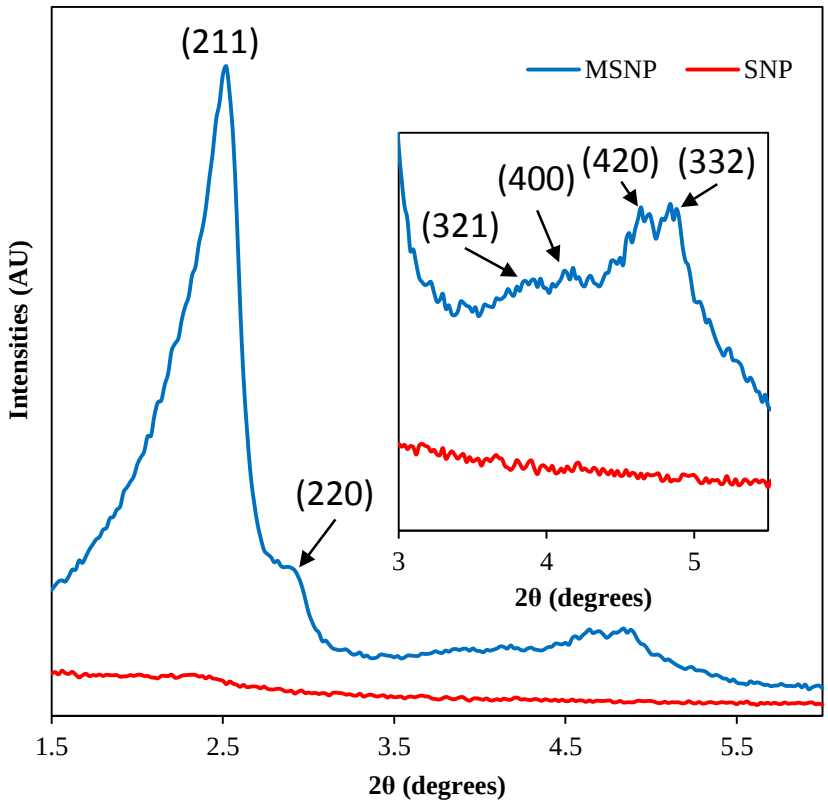

Figure A.9 Low angle XRD pattern of bare MSNPs with Ia$\bar{3}$d cubic mesoporous structure as indexed (211) and (220), and [inset] (321), (400), (420) and (332) compared to SNPs (indices were assigned following Wang et al. [277]).

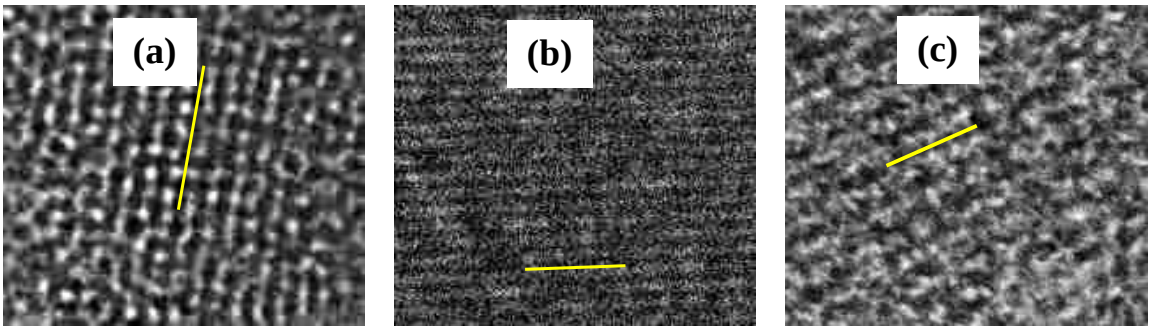

Figure A.10 TEM images of (a) MSNP, (b) MSNPT-59 and (c) MSNPT-110 showing mesopore channels (parallel to the yellow line) along (220) planes. Pore wall thickness determined from these images are 1.47 nm, 1.42 nm and 1.28 nm respectively (each yellow line is 20 nm long).

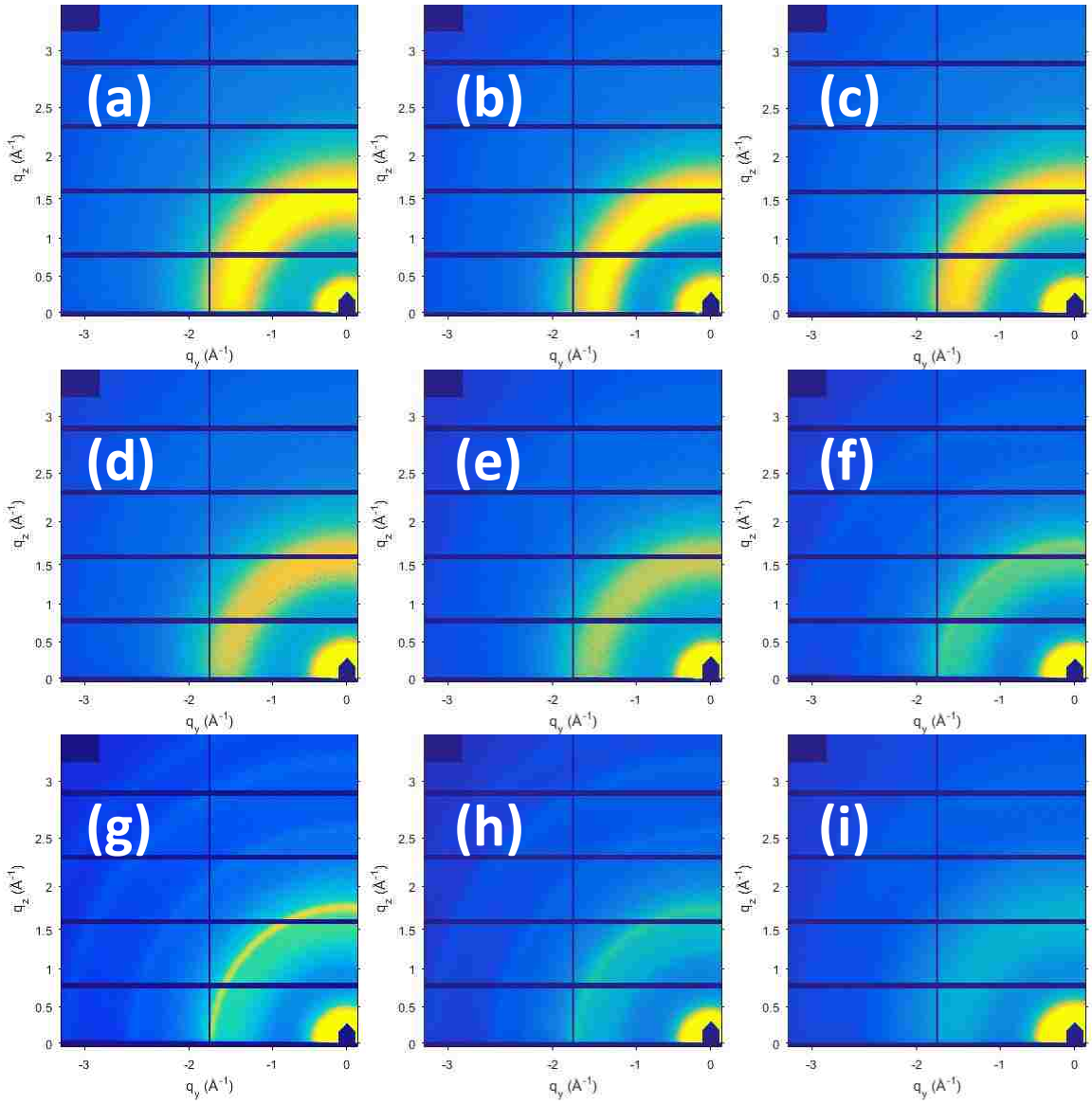

Figure A.11 2D GIWAXS patterns (incident angle, α_i = 0.17º) of non-functionalized and TiO_2 functionalized MSNP: (a) bare MSNP, (b) MSNPT-59, (c) MSNPT-110, (d) MSNPT-134, (e) MSNPT-198, (f) MSNPT-270, (g) MSNPT-362, (h) MSNPT-425 and (i) MSNPT-636.

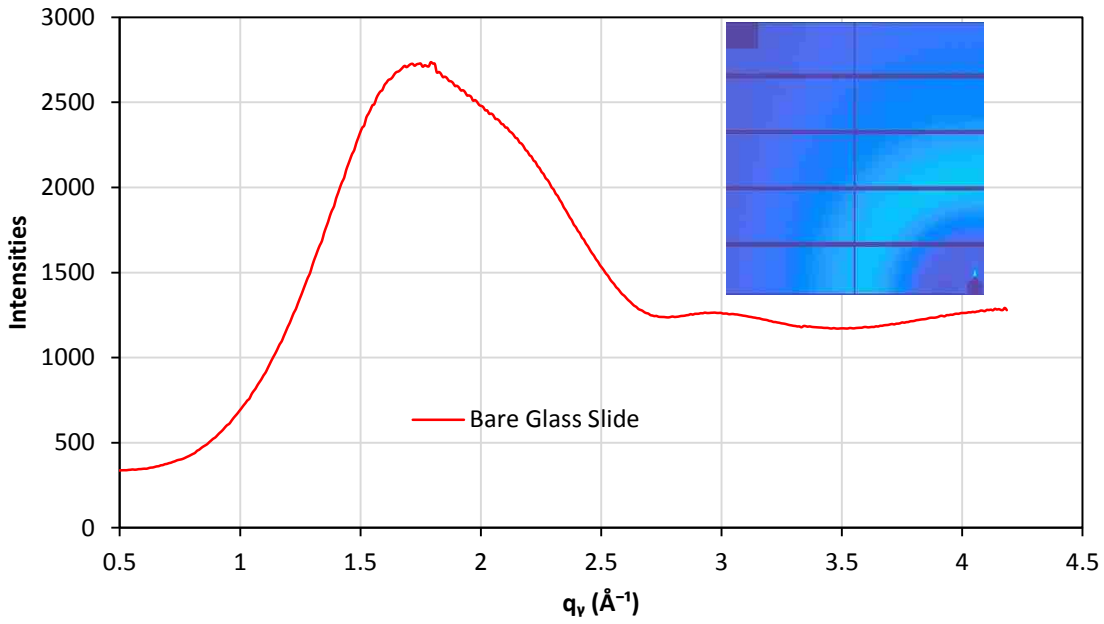

Figure A.12 Integrated data from GIWAXS pattern of bare glass slide for comparison to angular integration results of MSNPT in the text.

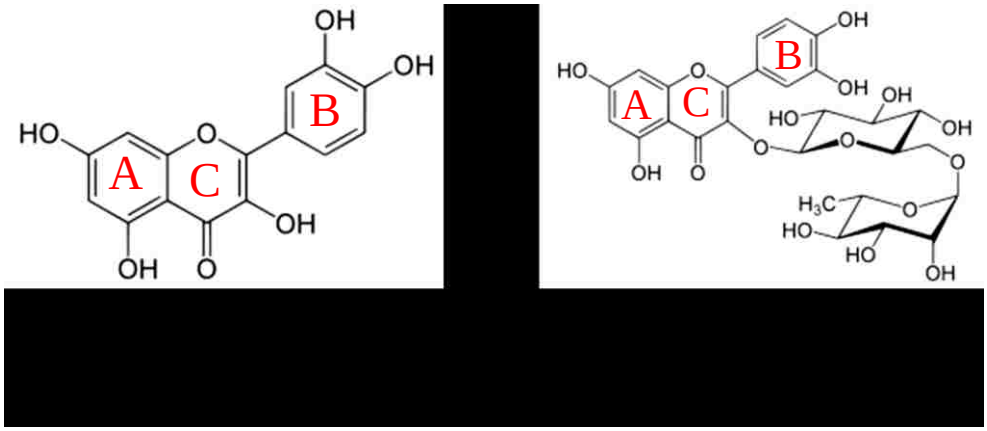

Figure A.13 Chemical structures of flavonoids quercetin and rutin with the three aromatic rings A, B and C highlighted in red.

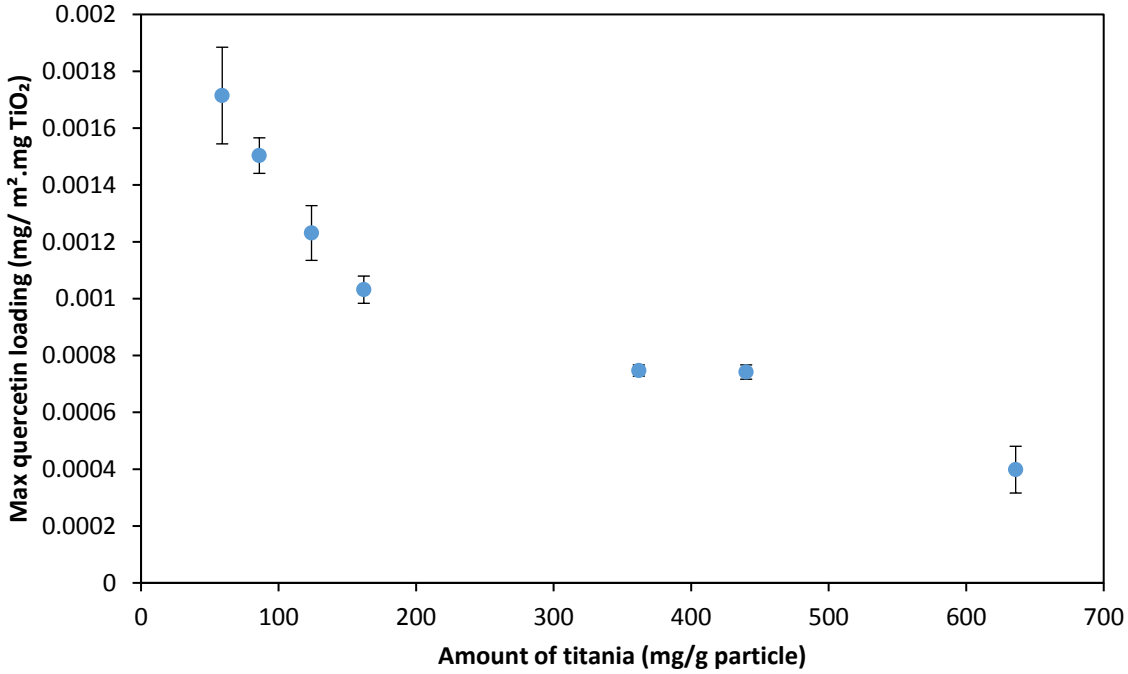

Figure A.14 Maximum quercetin loading on TiO_2 functionalized MSNP normalized by both surface area and amount on TiO_2 on particle surface (mg quercetin/m^2 surface/mg TiO_2).

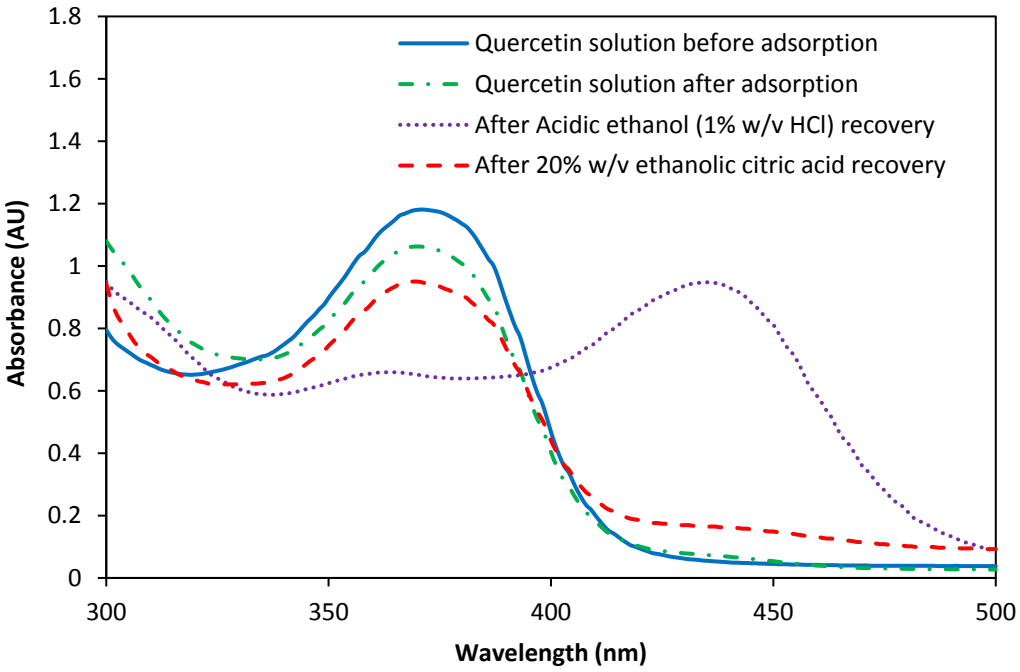

Figure A.15 Quercetin solution UV-visible spectra of supernatant solutions after adsorption. The results show no peak shift after adsorption and after recovery using 20% w/v ethanolic citric acid. However, a significant red shift is observed for recovery using 1% w/v ethanolic HCl, suggesting Ti-leaching into the strong acid solution and complexation with quercetin.

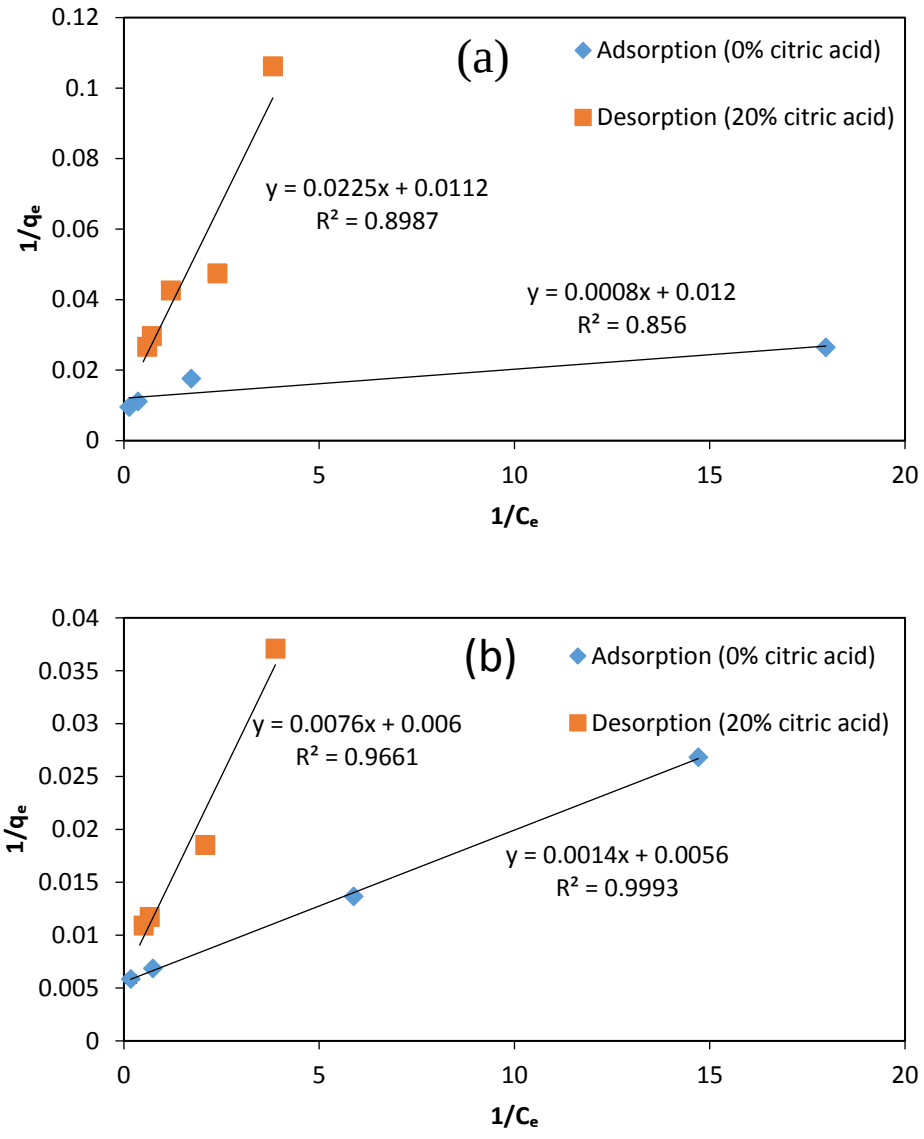

Figure A.16 Linearized Langmuir plots (*1/q_e* vs. *1/C_e*) for adsorption (in ethanol) and desorption (in ethanolic citric acid) of quercetin solution showing competitive adsorption between citric acid and quercetin for (a) MSNPT-86, (b) MSNPT-362.

APPENDIX B. SUPPLEMENTARY MATERIALS OF CHAPTER 4

B.1. Nanoparticle Synthesis, Functionalization and Fluorescent Attachment

B.1.1. Nanoparticle Synthesis

Ordered MSNPs were synthesized by the CTAB-templated modified Stöber method originally reported by Kim et al. [69]. Briefly, 0.5 g of CTAB and 2.05 g of F127 were dissolved in 96 mL of DIUF water, 43 mL of ethanol, and 11.9 mL of concentrated ammonia. 1.9 mL of TEOS was added dropwise to the solution with vigorous mixing and the solution was stirred for one minute at room temperature (RT). The solution was then kept stationary for 24 h (at RT) to facilitate complete silica condensation. Synthesized particles were removed and washed 3 times with water and ethanol by repeated ultrahigh speed centrifugation (Beckman-Coulter) at 17,000 rpm and dried at 84 ºC in air overnight. Finally, template removal from the silica particles was achieved by washing in 200 mL of acidic ethanol (HCl, 1.5 M) for 24 h (acidic ethanol wash) followed by repeated centrifugation and washing with water and ethanol before drying at 84 ºC.

B.1.2. Nanoparticle Functionalization and Fluorescent Group Attachment

B.1.2.1. TiO_2 Functionalization

MSNPs were functionalized by TiO_2 using TEO according to a previously reported method [38]. 2.6 mL of TEO was added to 7.15 mL of ethanol under nitrogen. Separately, 500 mg of MSNPs were sonicated in 100 mL of ethanol for 15 min in a 250 mL round bottom flask. Then 142.5 mL of ethanol was added and the solution was heated with continuous stirring. Once the solution started boiling, the previously prepared TEO

solutions and 1.6 mL of DIUF water were added and the solution was refluxed for 1.5 h under vigorous mixing. Functionalized particles were recovered by centrifugation (17,000 rpm) and washed in ethanol overnight to remove excess unbound TiO2, and finally dried at 84 ºC.

B.1.2.2. Amine Functionalization

Amine functionalized bare MSNPs and amine-TiO_2-functionalized MSNPs (MSNPA and MSNPTA, respectively) were obtained by condensing APTES on the particle surface using modified literature procedures [101, 125, 322, 358]. 200 mg of MSNPs were uniformly dispersed in 25 mL of dry ethanol by sonication for 15 min. 0.5 mL of APTES was added dropwise under constant stirring, and the solution was kept stirring in a closed vessel for 24 h at RT. Particles were centrifuged with repeated ethanol washing, and cured at 84 ºC for 24 h. After curing, particles were stirred in excess ethanol for 24 h to remove any remaining loosely-bound amine species. The functionalized particles were again washed 3 times with dry ethanol and dried at 84 ºC.

B.1.2.3. Fluorescent Tagging

200 mg of amine-functionalized particles were suspended in 25 mL of ethanol and sonicated for 15 min, followed by addition of 3.2 mg of RITC. After 24 h of stirring, the bright red labelled particles were washed and centrifuged in ethanol repeatedly until the supernatant became completely clear, and dried in an oven. The dry particles were then washed in water and ethanol for 24 h each to remove excess dye before drying again in the oven overnight.

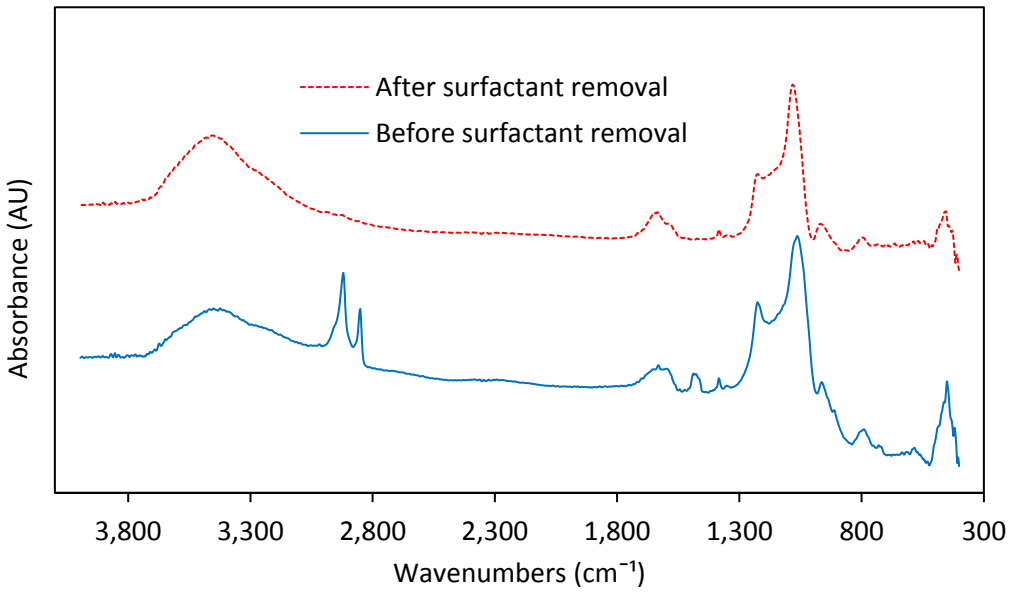

Figure B.1 FTIR analysis for showing organic surfactant CTAB removal (by loss of peaks correspond to C-H stretching vibrations from 2800 to 3000 cm^{-1}) during acidic ethanol washing of synthesized nanoparticles.

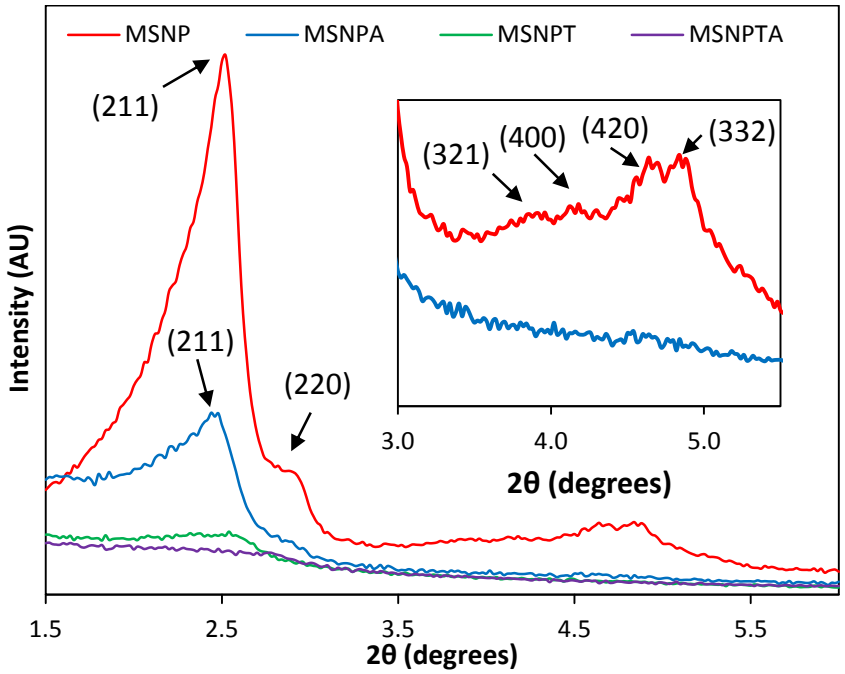

Figure B.2 Low angle XRD profiles of MSNPA, MSNPT and MSNPTA compared to bare MSNPs with the indices for cubic $Ia\bar{3}d$ mesopore structure (peaks were indexed following Wang et al. [277]).

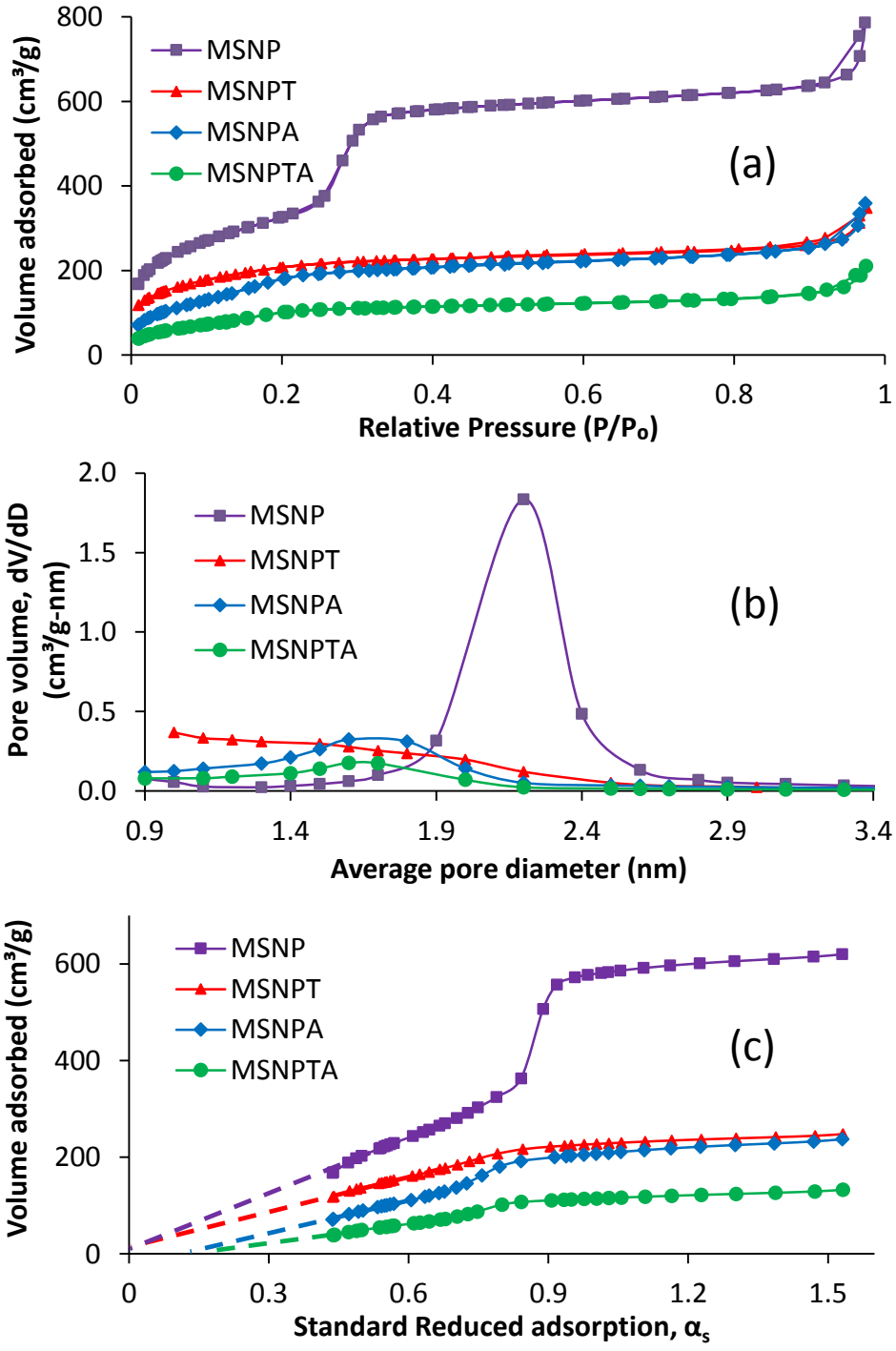

Figure B.3 Surface properties characterization of non-functionalized and functionalized MSNPs: (a) Nitrogen sorption isotherms, (b) Pore size distribution and (c) α_s-plot for nitrogen adsorption determined from the relative pressure vs. standard reduced adsorption table of Jaroniec et al. [269].

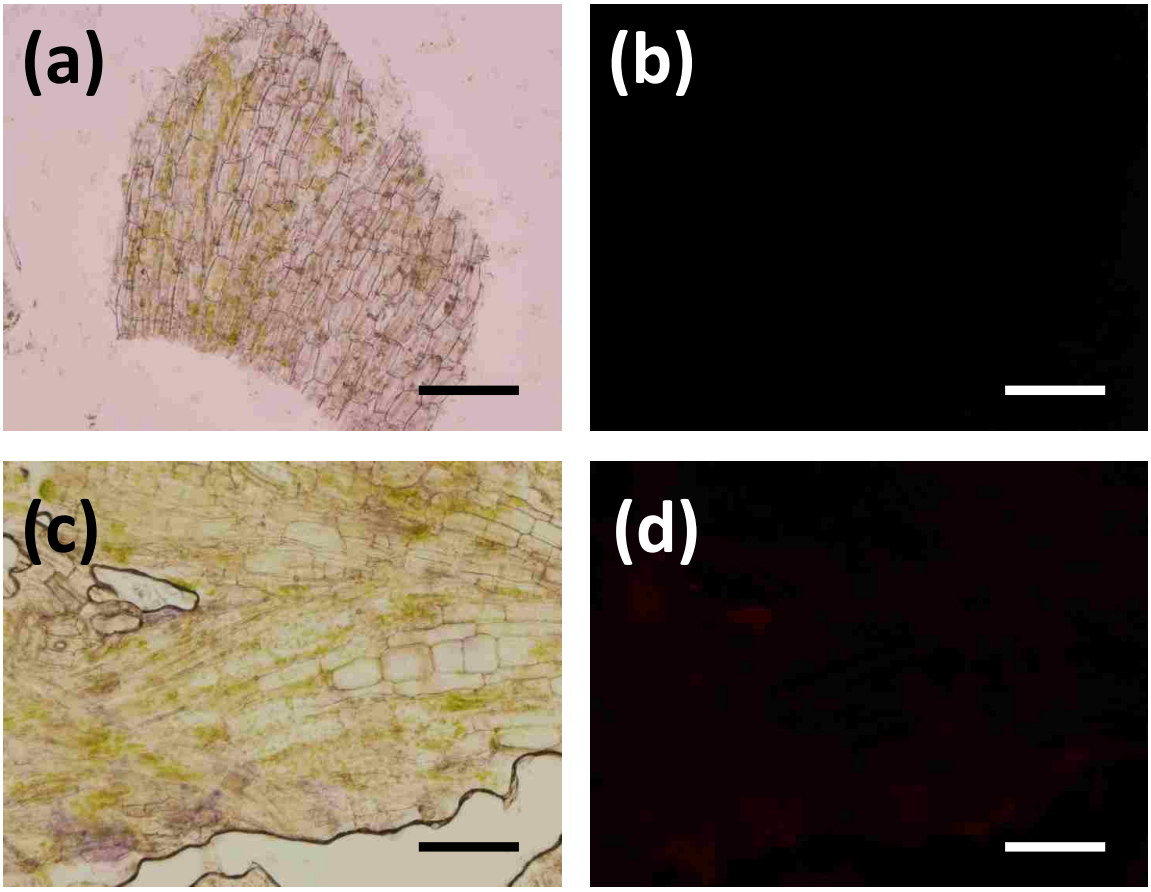

Figure B.4 Bright field (left) and corresponding fluorescence microscopic image (right) of *S. nemoralis* hairy roots without any particle uptake: (a) & (b) without trypan blue addition and (c) & (d) with trypan blue addition (fluorescence imaging exposure time 150 ms). Scale bars are 100 μm for all images.

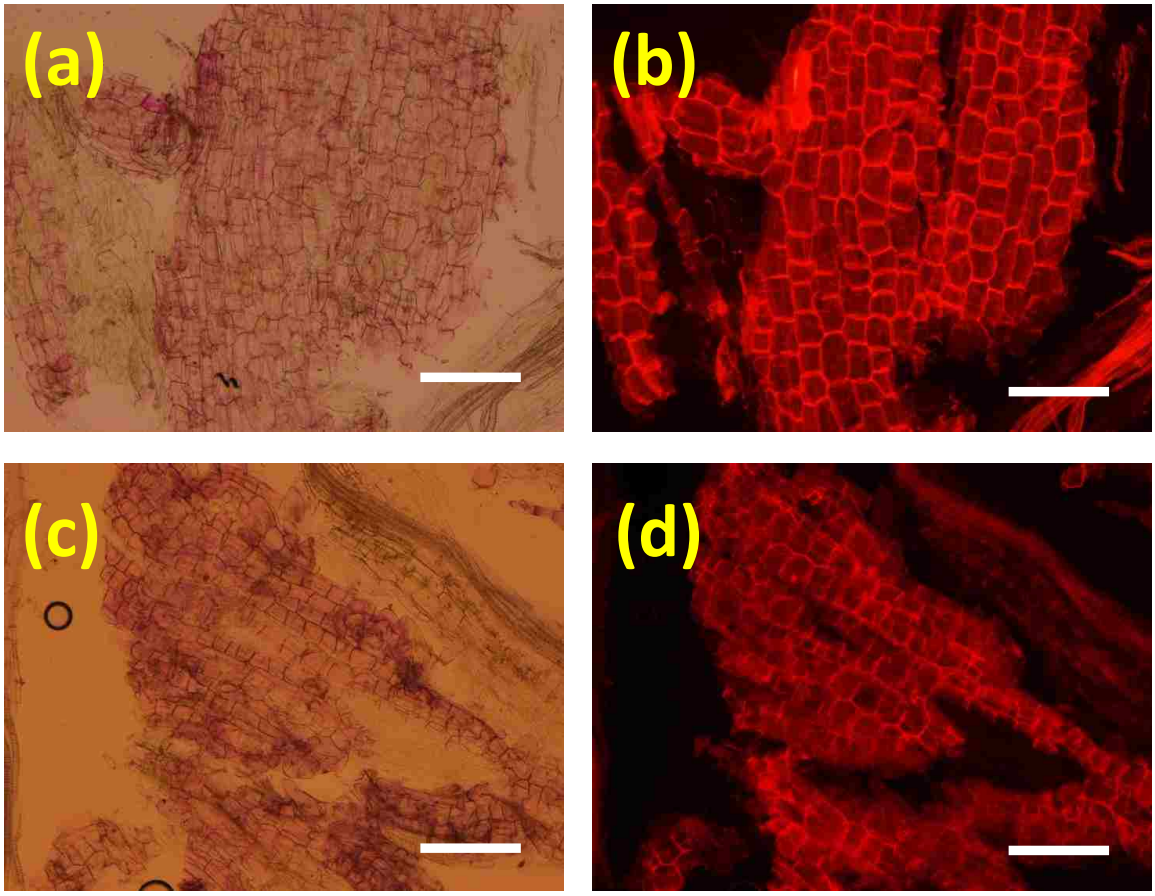

Figure B.5 Bright field (left) and corresponding fluorescence microscopic image (right) of S. nemoralis hairy roots after RITC-tagged functionalized MSNP uptake: (a) & (b) without trypan blue addition and (c) & (d) with trypan blue addition for 1 mg/mL nanoparticle solution (fluorescence imaging exposure time 150 ms). Scale bars are 100 μm for all images.

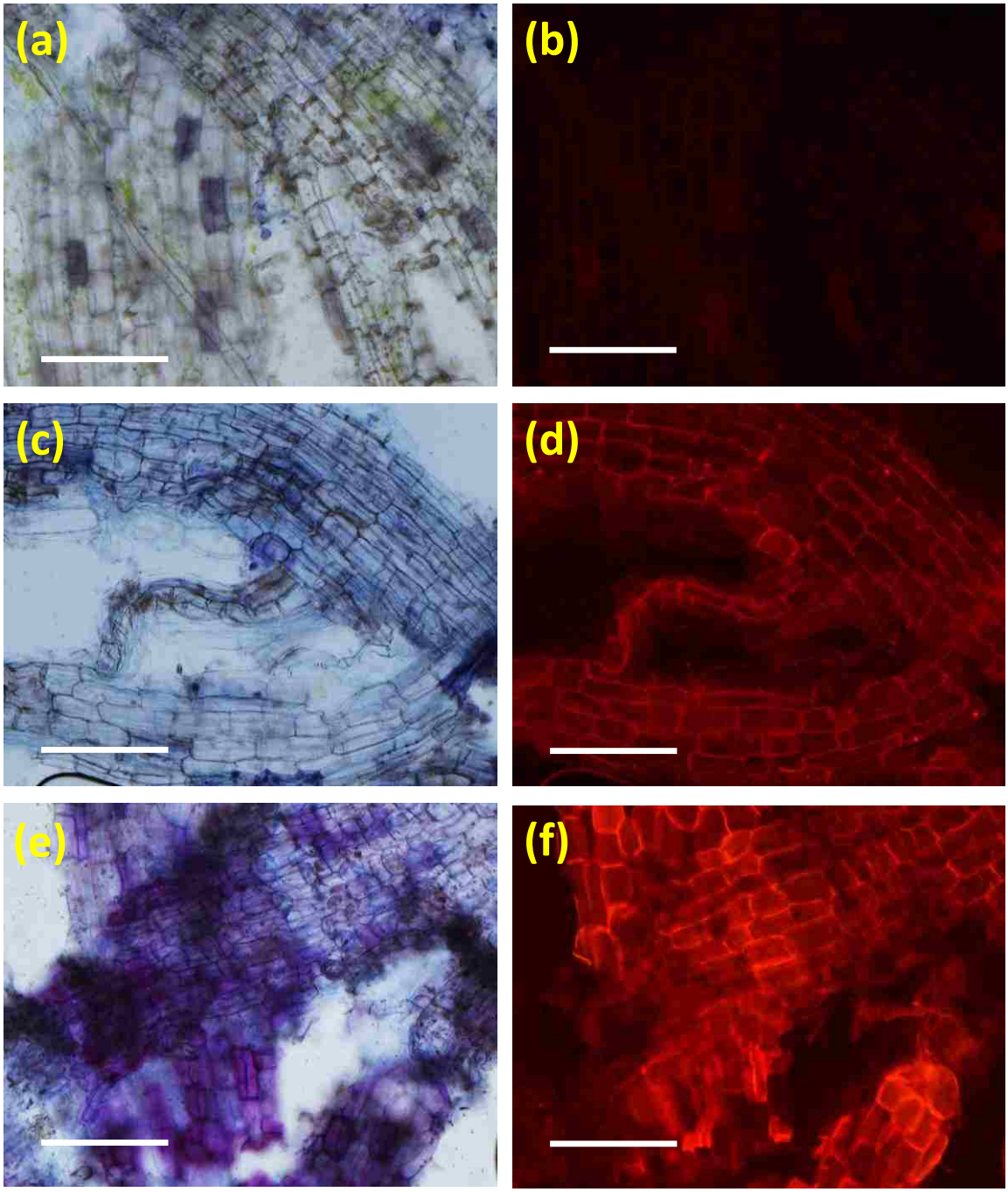

Figure B.6 Bright field (left) and corresponding fluorescence microscopic image (right) of *S. nemoralis* hairy roots after RITC-tagged MSNPTA uptake in trypan blue solution for (a) & (b) 0 (control), (c) & (d) 100 μg/mL and (e) & (f) 1000 μg/mL nanoparticle solution (fluorescence imaging exposure time 150 ms). Scale bars are 100 μm for all images.

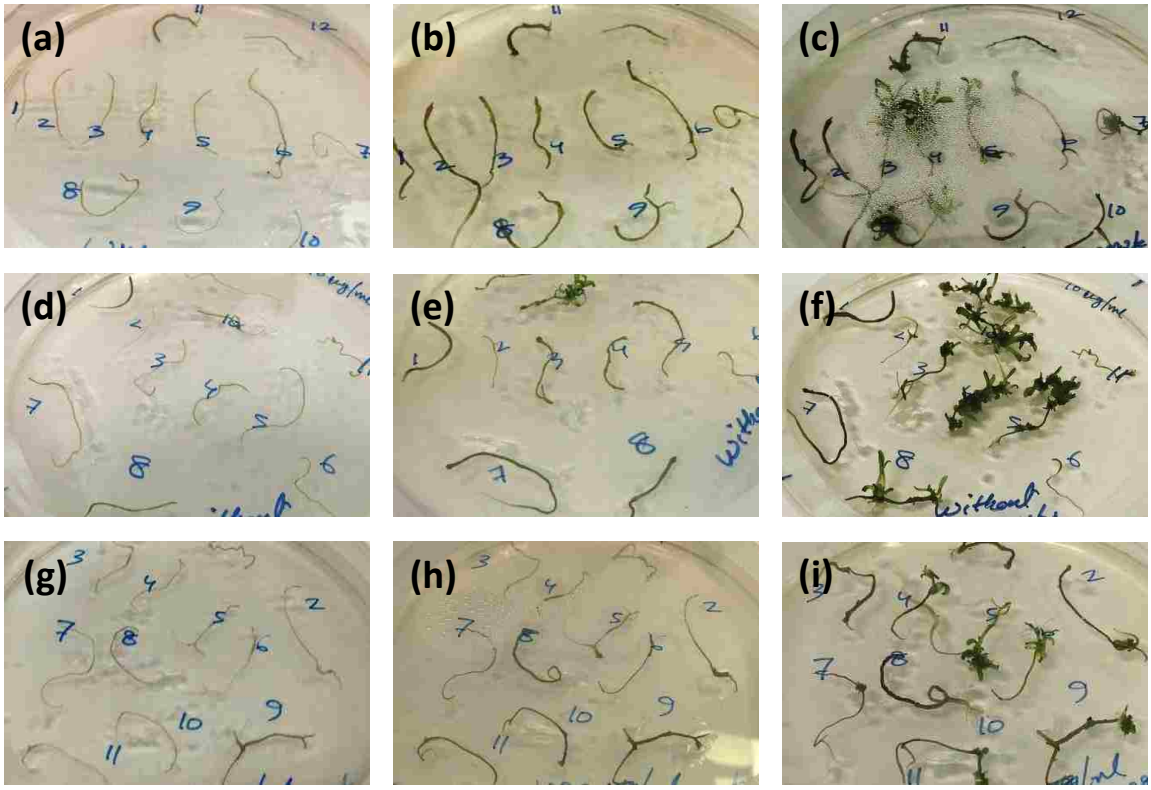

Figure B.7 Viability of *S. nemoralis* hairy roots culture treated with MSNPTAs (0-1000 µg/mL) after reculturing. The top row shows the control (0 µg/mL particles) after (a) 0 weeks, (b) 2 weeks, and (c) 4 weeks. The middle row shows roots with 10 µg/mL MSNPTA after (d) 0 weeks, (e) 2 weeks, and (f) 4 weeks. The bottom row shows roots with 1000 µg/mL MSNPTA after (g) 0 weeks, (h) 2 weeks, and (i) 4 weeks. Viability is indicated by lengthening, thickening, and sprouting new leaves for all roots.

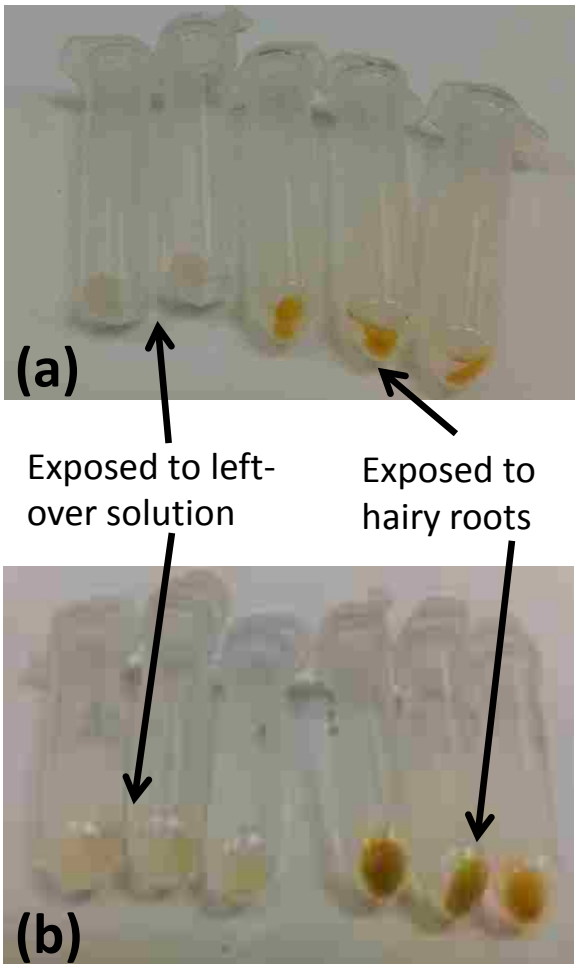

Figure B.8 TiO_2-amine functionalized nanoparticles (MSNPTA) recovered by centrifugation after: 500 μL of (a) 1 mg/mL and (b) 10 mg/mL nanoparticle solutions were exposed to 40 mg of *S. nemoralis* hairy roots compared to nanoparticles exposed to only left-over solution from hairy root cultures.

APPENDIX C. SUPPLEMENTARY MATERIALS OF CHAPTER 5

C.1. Kinetic Analysis for Nanparticle Uptake and Release

An additional kinetic analysis is performed by applying a simple kinetic model to the nanoparticle expulsion data (**Figure 5.3**). In each case, the process of uptake and expulsion is reversible (not all particles are expelled) and the process reaches steady state after certain amount of time. Assuming that uptake is a pseudo-first order process and that expulsion is also first-order, we can analyze the data using the relationship presented in **Equation C.1**.

$$ln\left(1-\frac{[NP]_t}{[NP]_{ss}}\right)=-(k_{in}+k_{out})t \tag{C.1}$$

Where, $[NP]_{ss}$ is the steady state of particles expelled, which is estimated from the plateau at long times (average value > 4 h as presented in **Table 5.2**). $[NP]_t$ is the particle expelled at any time; k_{in} and k_{out} are the first order the rate coefficients for uptake and expulsion, which can be found from the early kinetics.

If $[NP]_{cell,0}$ = the initial concentration of nanoparticles taken up in the cells (also found from **Table 5.2**) and f = the fraction released at steady state, then:

$$f=\frac{[NP]_{cell,0}}{[NP]_{ss}} \tag{C.2}$$

Simple first-order kinetics would suggest that:

$$\frac{k_{in}}{k_{out}}=\frac{1-f}{f} \tag{C.3}$$

Based on this analysis, the average lifetime of a nanoparticle ($\tau_{avg} = (k_{in} + k_{out})^{-1}$) in a cell is obtained, which is the order-of-magnitude estimate of the kinetics of

nanoharvesting. The process of nanoharvesting is obviously more complicated but first-order kinetics can be viewed as a lumped average of all processes going on. Expulsion data is fitted according to the first order kinetics linearized equation in **Figure C.5** and the estimated parameters with average time of nanoharvesting is presented in **Table C.2**.

Table C.1 BET specific surface area, BJH pore volume, average pore diameter and zeta potential of TiO_2 functionalized, amine functionalized, and TiO_2-amine functionalized mesoporous silica nanoparticles (MSNPs) with optimum TiO_2 content compared to non-functionalized MSNPs.

Particle types	Average particle diameter	Amount of TiO_2	Amount of amine	BET surface area	BJH pore volume	Average pore diameter	Zeta potential at pH 4.0
	nm	mg/g particle	mmol/g particle	m^2/g	cm^3/g	nm	mV
MSNP	165 ± 19[a]	-	-	953	1.21	2.76	-2.8
MSNPT	185 ± 29	425 ± 9.2[b]	-	629	0.59	2.21	-9.6
MSNPA	172 ± 26	-	2.00 ± 0.16[b]	400	0.57	2.50	+39.3
MSNPTA	174 ± 32	407 ± 13	0.65 ± 0.07	325	0.33	1.97	+36.7

Standard deviation values resulted from [a]measurement of 20 particles selected randomly (using ImageJ Software) and [b]quadruplicate measurement for chemical analysis.

Table C.2 Estimated kinetic parameters and average time of nanoparticle inside the roots from the first order kinetic fitting of nanoparticle recovery data.

Uptake temperature	4 ºC	23 ºC		
Recovery temperature	4 ºC	4 ºC	23 ºC	
Recovery media	Fresh solution	Fresh solution	Fresh solution	Solution containing 2.5 mg/mL particles
$k_{in} + k_{out}$ (h^{-1})	2.54	3.51	2.35	3.74
τ_{avg} (min)	23.6	17.1	25.5	16.0
k_{in} (h^{-1})	0.11	0.32	0.21	0.46
k_{out} (h^{-1})	2.43	3.19	2.14	3.28

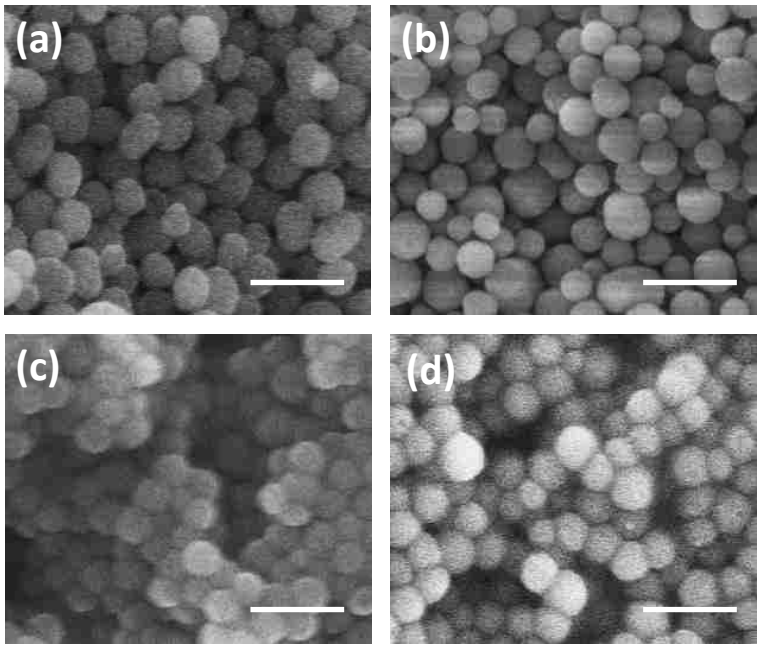

Figure C.1 SEM image of (a) MSNP, (b) MSNPT, (c) MSNPA and (d) MSNPTA (scale bar 500 nm for all images).

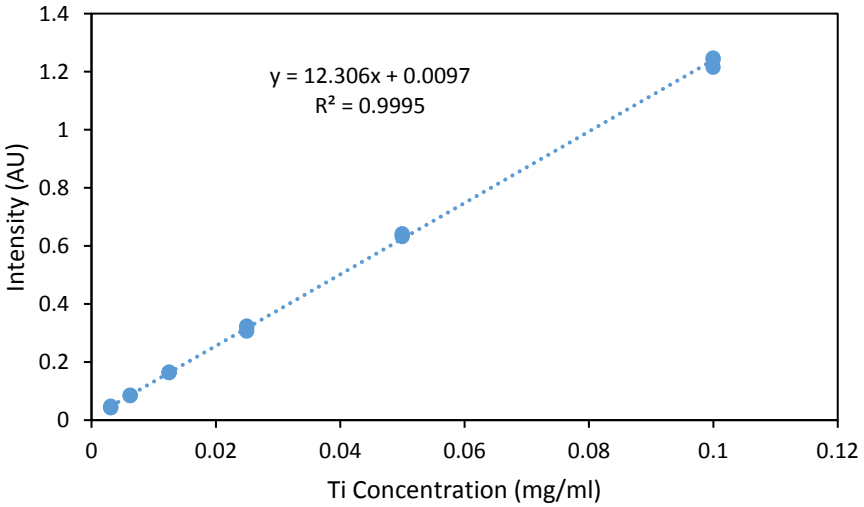

Figure C.2 Calibration curve of UV-vis intensity for the determination of Ti-content and nanoparticle uptake after calcination of roots, constructed in presence of root ash by mixing known quantities of particles with 300 mg of roots and calcining them together.

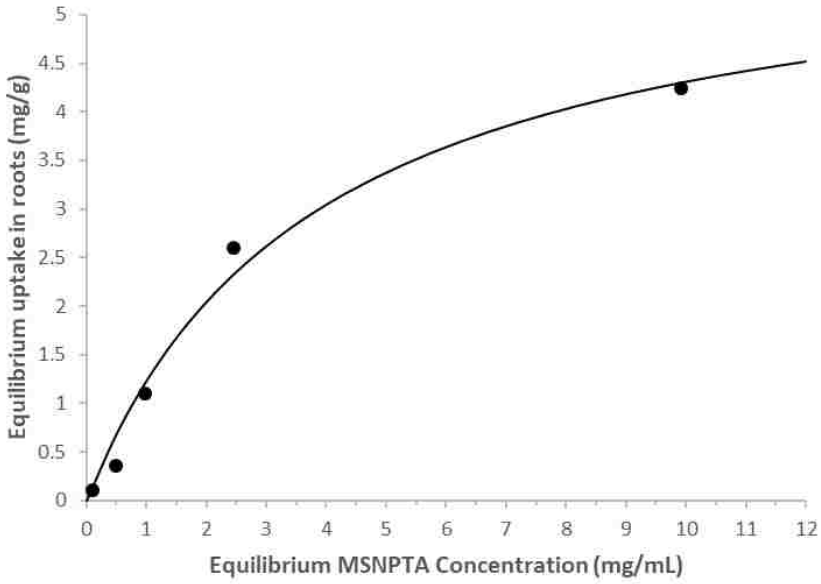

Figure C.3 Uptake of MSNPTA in *Solidago nemoralis* roots after 24 h as a function of the concentration of nanoparticles remaining in solution. The points are data and the curve is a Langmuir model fit to the data by nonlinear regression.

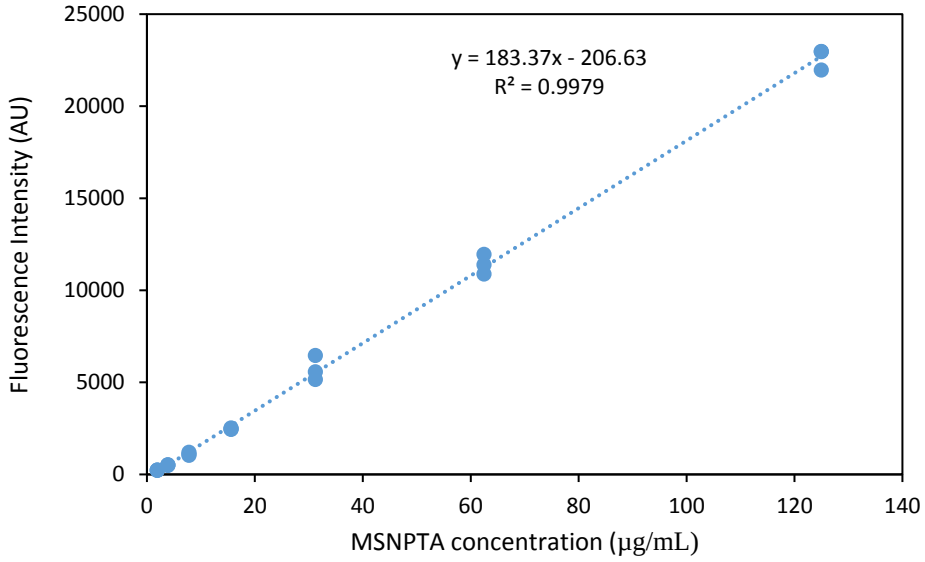

Figure C.4 Calibration curve of fluorescently tagged MSNPTAs in plant media for the determination recovery in solution after uptake in roots.

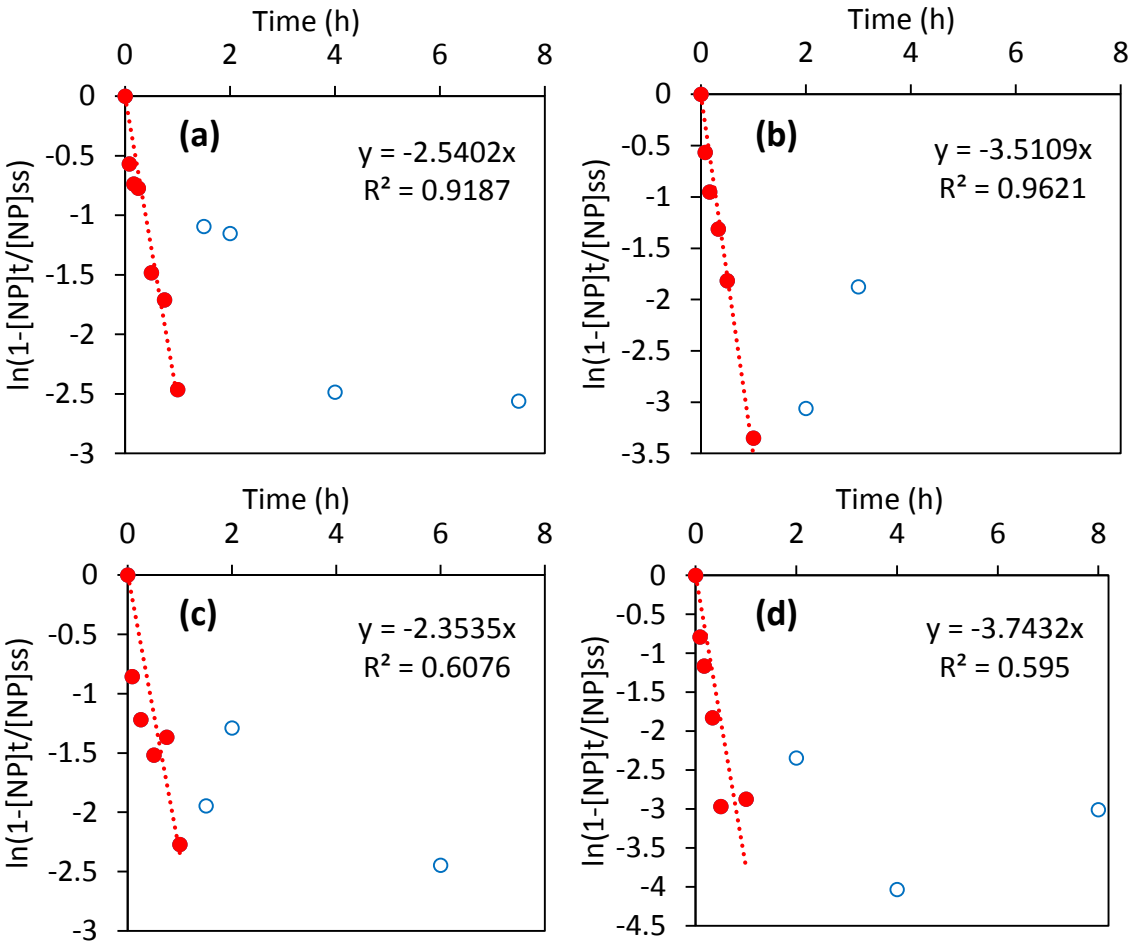

Figure C.5 Kinetic analysis (1st order-linearized) for the time dependent fluorescently tagged MSNPTAs recovery in MS media after 24 h of uptake with initial particle concentration of 2.5 mg/mL: (a) recovery at 4 ºC in fresh solution after uptake at 4 ºC, (b) recovery at 4 ºC in fresh solution at 23 ºC, (c) recovery at 23 ºC in fresh solution after uptake at 23 ºC, and (d) recovery at 23 ºC in non-fluorescent particle solution (2.5 mg/mL) after uptake at 23 ºC.

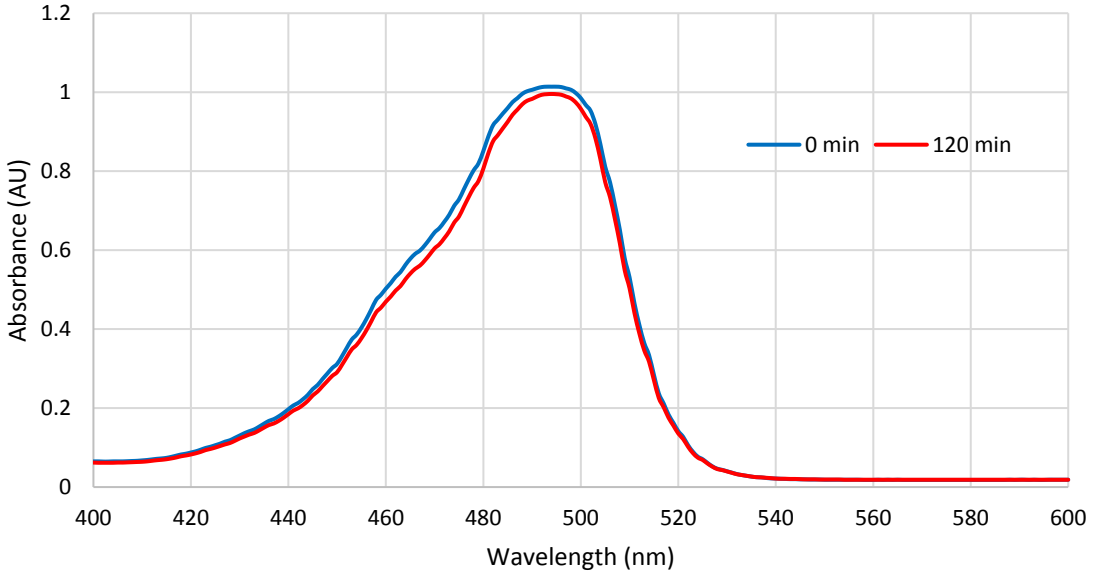

Figure D.1 Absorbance spectra of RSSV-FITC (peak 495 nm) before and after UV exposure for 120 min.

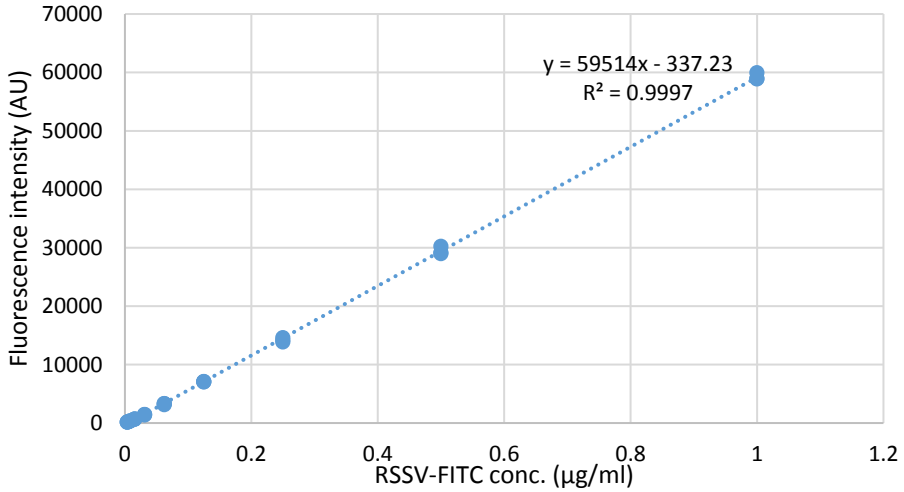

Figure D.2 Calibration curve concentration of RSSV-FITC in solution.

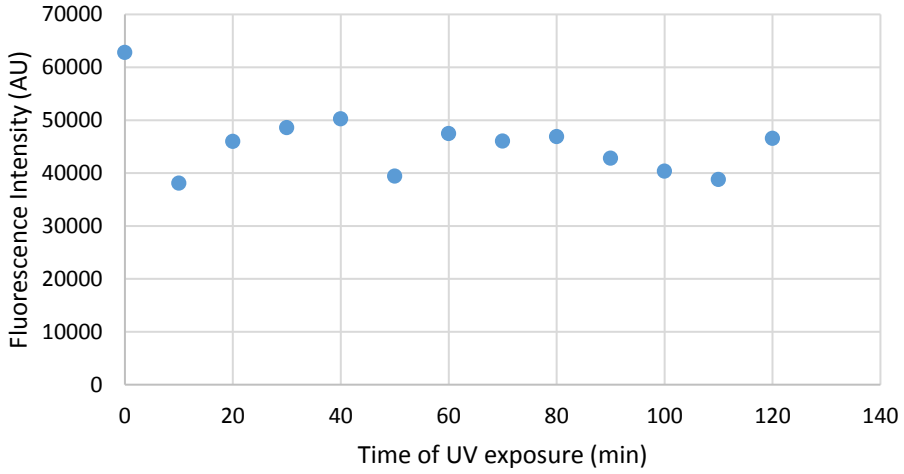

Figure D.3 Fluorescence intensity decrease due to photo-bleaching for RSSV-FITC solution. There are ~25% intensity decrease even after 5 min of UV treatment. After initial drop in intensity, there is no further photo-bleaching.

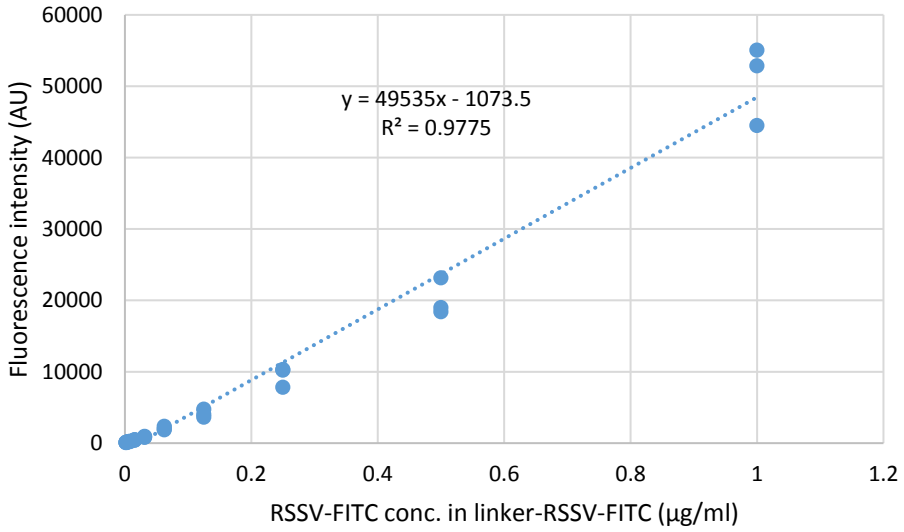

Figure D.4 Calibration curve for SNLD-RSSV-FITC solution fluorescent intensity before UV treatment.

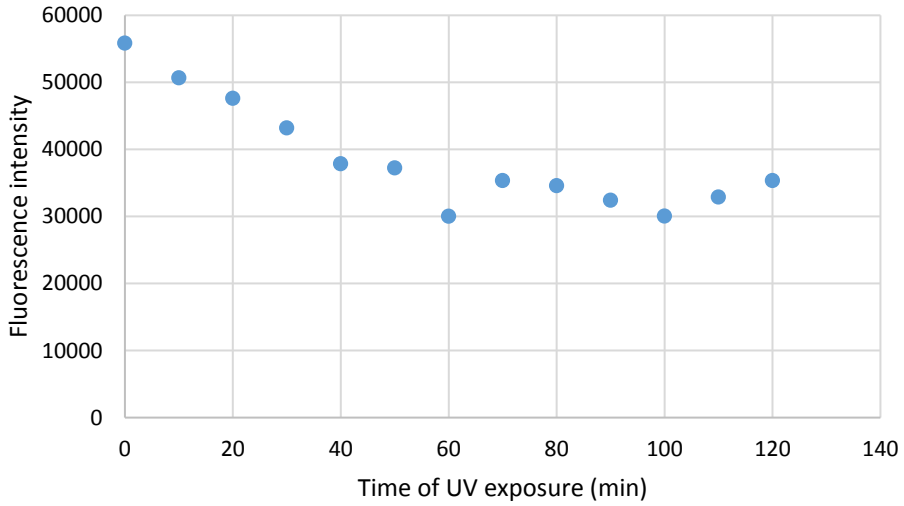

Figure D.5 Fluorescence intensity decrease due to photo-bleaching for SNLD-RSSV-FITC solution. There are ~35% intensity decrease gradually up to 60 min of UV treatment. After that drop in intensity, there is no further photo-bleaching.

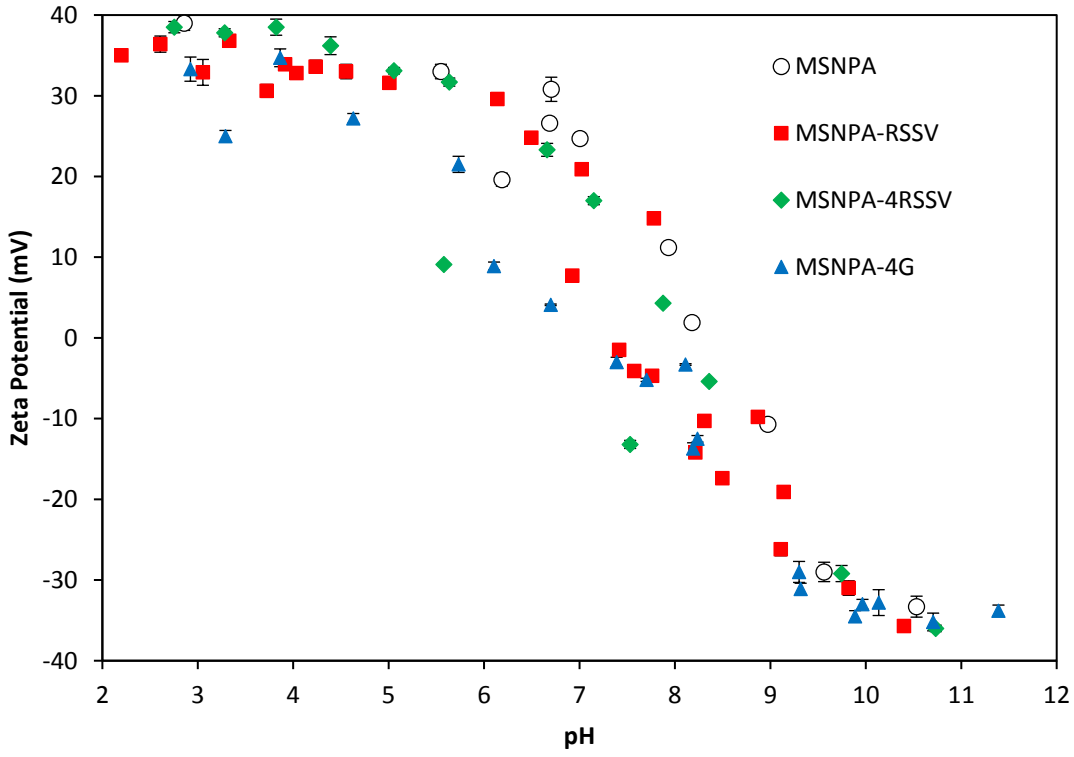

Figure D.6 Comparison of zeta potential of MSNPA-RSSV, MSNPA-4RSSV and MSNPA-4G with bare MSNPAs measured at wide range of pH (2-11).

APPENDIX E. SUPPLEMENTARY MATERIALS OF CHAPTER 7

Table E.1 Particle size, amount of amine grafted and % of monolayer surface coverage by amine group for amine functionalized nonporous and mesoporous nanoparticles.

	SNP	MSNP-2.2	MSNP-4.1	MSNP-7.9
Average particle size (nm)[a]	190 ± 29	165 ± 19	155 ± 32	146 ± 27
mg APTES/g SiO_2	28.6	798.3	466.8	339.1
mmol amine/g SiO_2	0.129	3.61	2.11	1.53
mmol amine/g particles	0.125	2.00	1.44	1.14
mmol amine/m^2 surface	0.00897	0.00378	0.00245	0.00211
% of monolayer coverage	272	114	74	64

[a] Average and standard deviation calculated from SEM images by considering random 20 particles using ImageJ software.

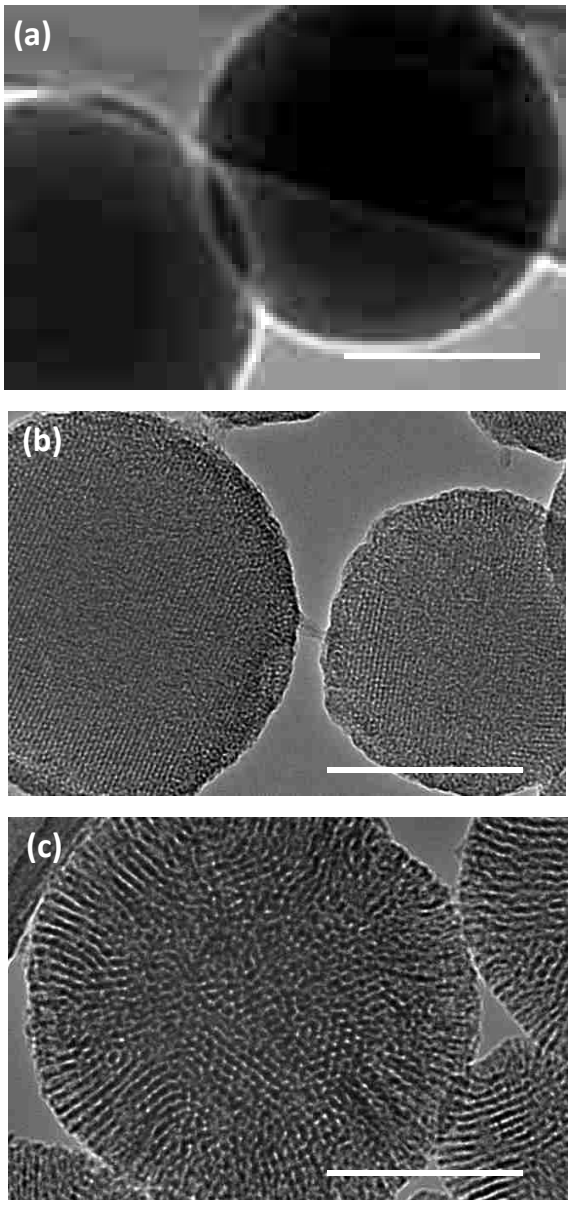

Figure E.1 TEM images nonporous silica nanoparticles (SNPs) along with mesoporous silica nanoparticles (MSNPs) with different pore sizes: (a) SNP, (b) MSNP-2.2 and (c) MSNP-4.1. Scale bar is 100 nm for all images.

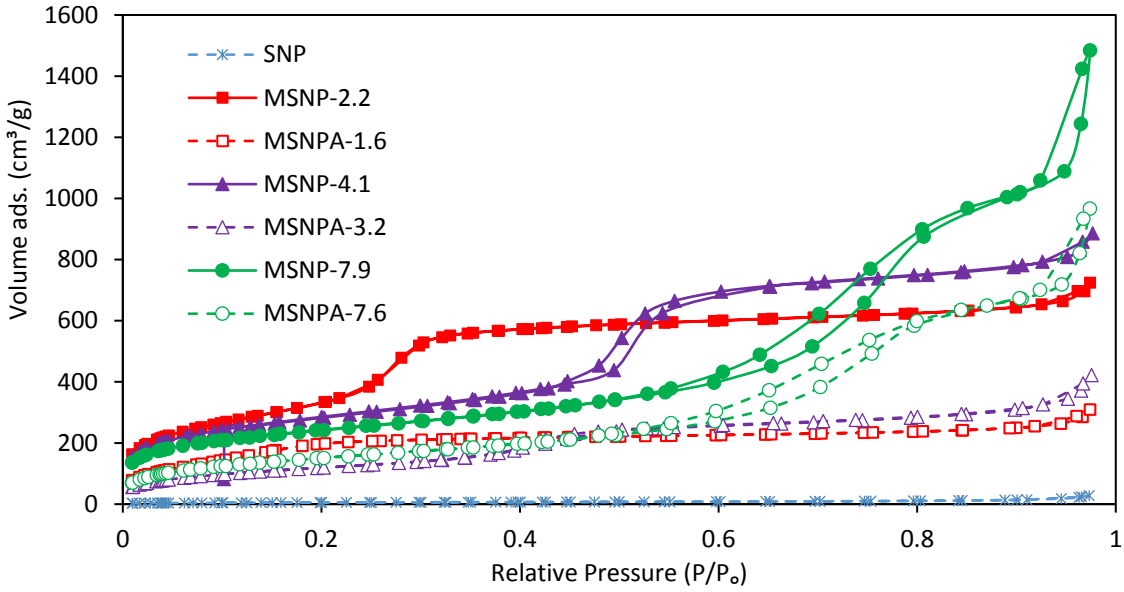

Figure E.2 Nitrogen sorption isotherms of MSNPs before and after amine functionalization compared to that of SNPs.

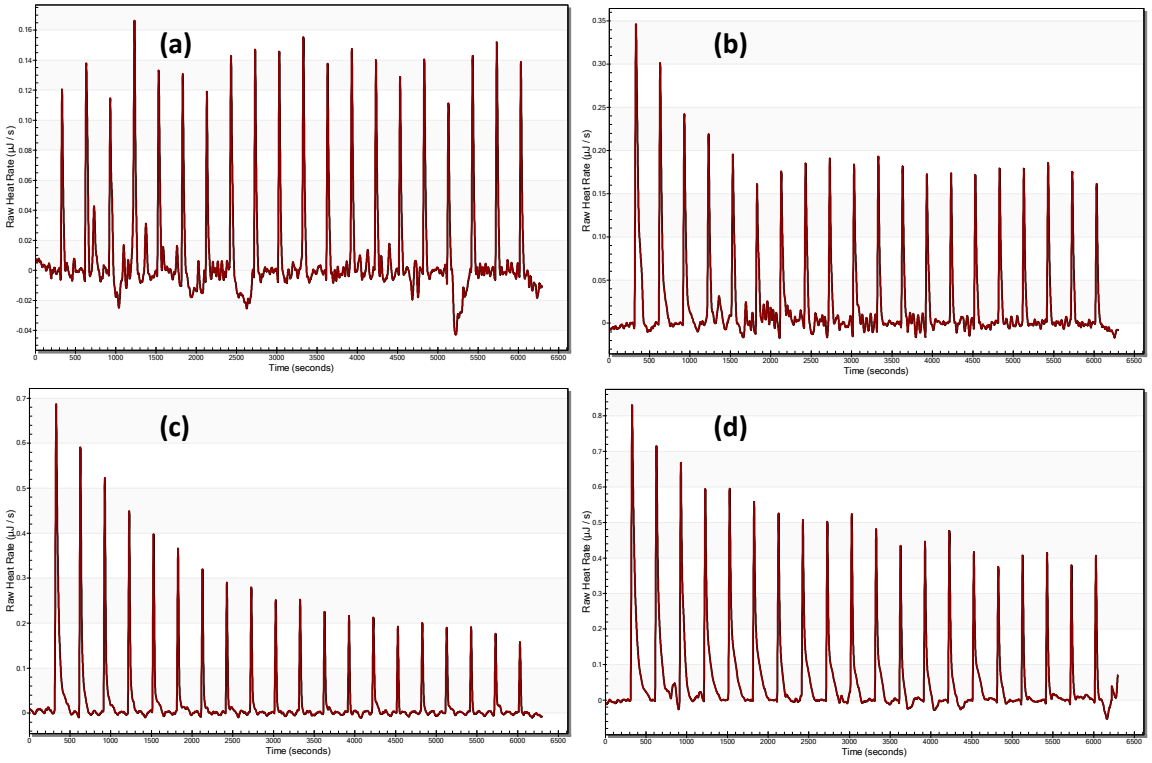

Figure E.3 Heat of dilution of 84 bp RNA for initial RNA concentration of (a) 0.334 mM, (b) 0.835 mM, (c) 1.67 mM and (d) 2.25 mM base pair.

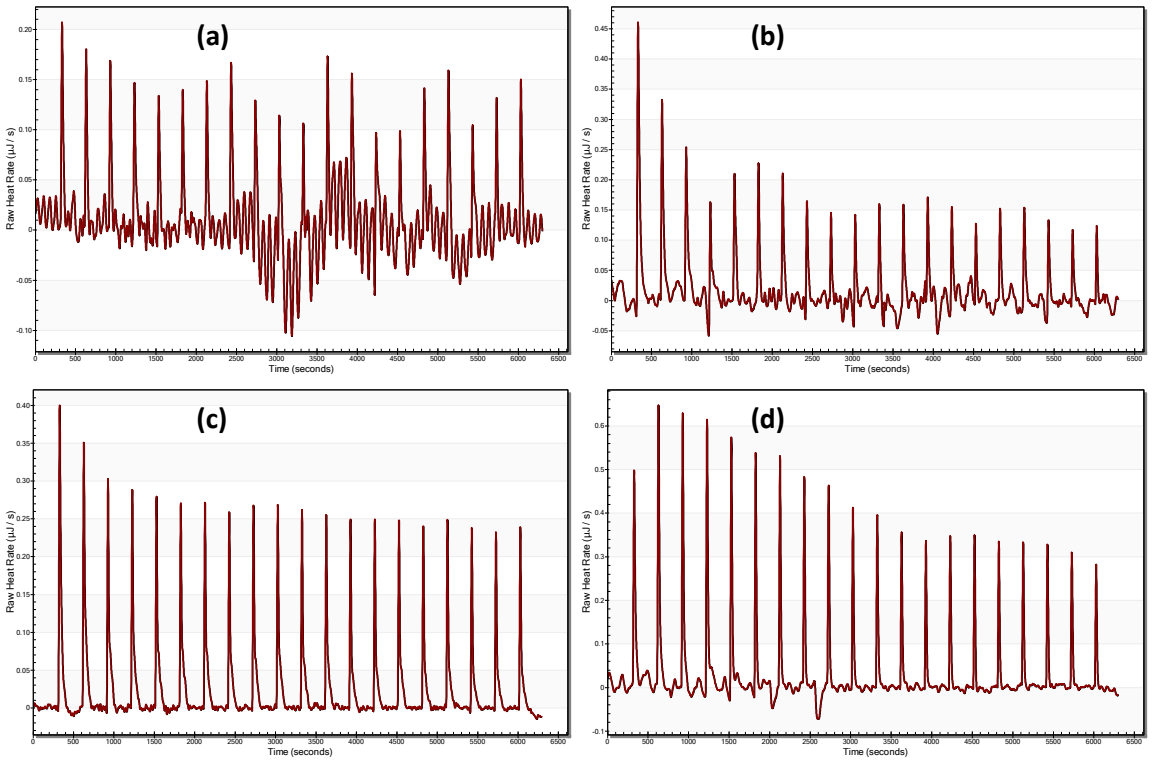

Figure E.4 Heat of dilution of 282 bp RNA for initial RNA concentration of (a) 0.334 mM, (b) 0.835 mM, (c) 1.67 mM and (d) 2.25 mM base pair.

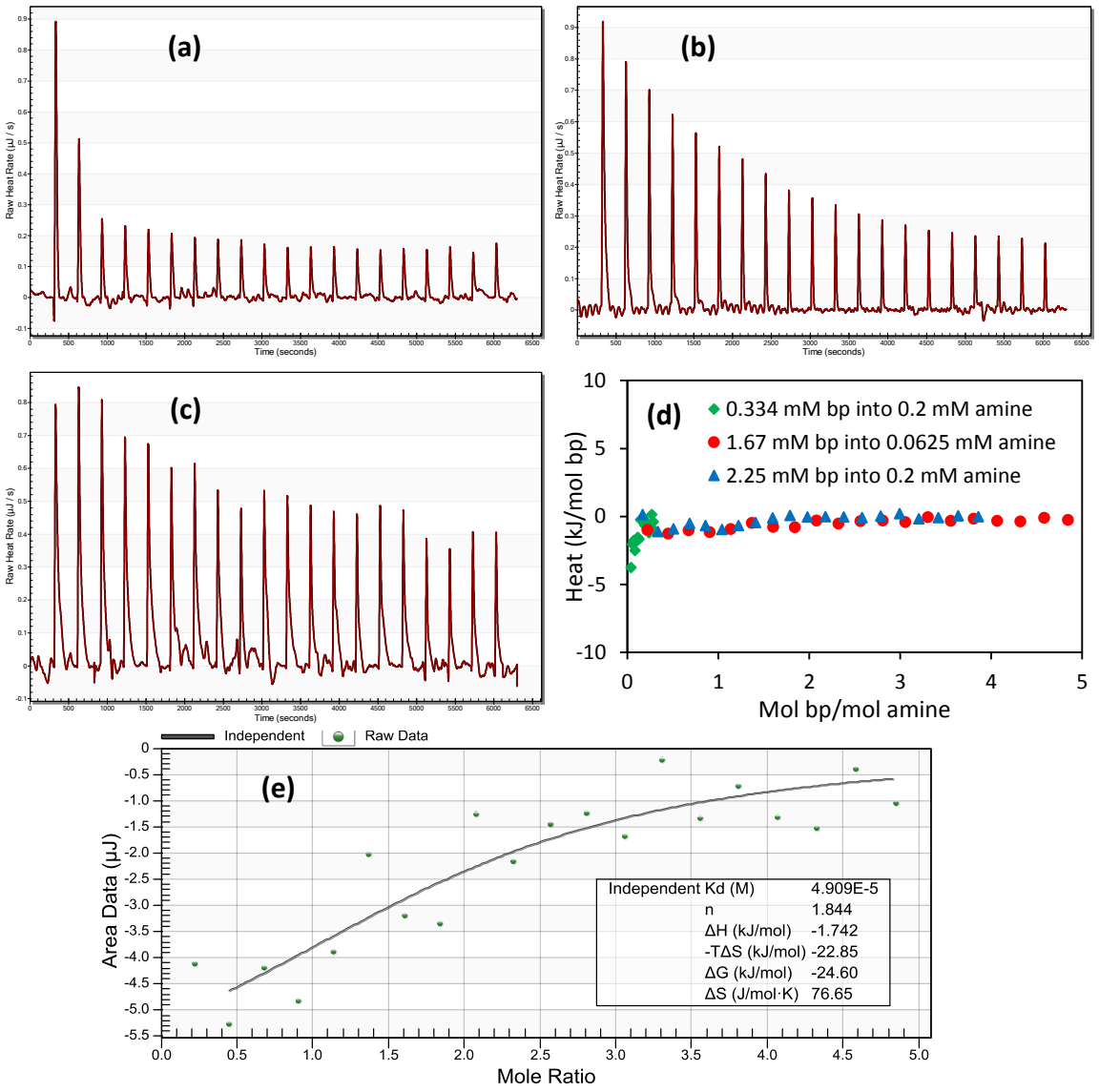

Figure E.5 Raw heat rate with time for 84 bp RNA interaction with SNPA for (a) 0.334 mM bp into 0.2 mM amine, (b) 1.67 mM bp into 0.0625 mM amine, (c) 2.25 mM bp into 0.2 mM amine, (d) integrated heat per mol bp as a function of mol bp/mol amine, and (e) corresponding independent single site binding model fit for 1.67 mM bp into 0.0625 mM amine with estimated thermodynamic parameters.

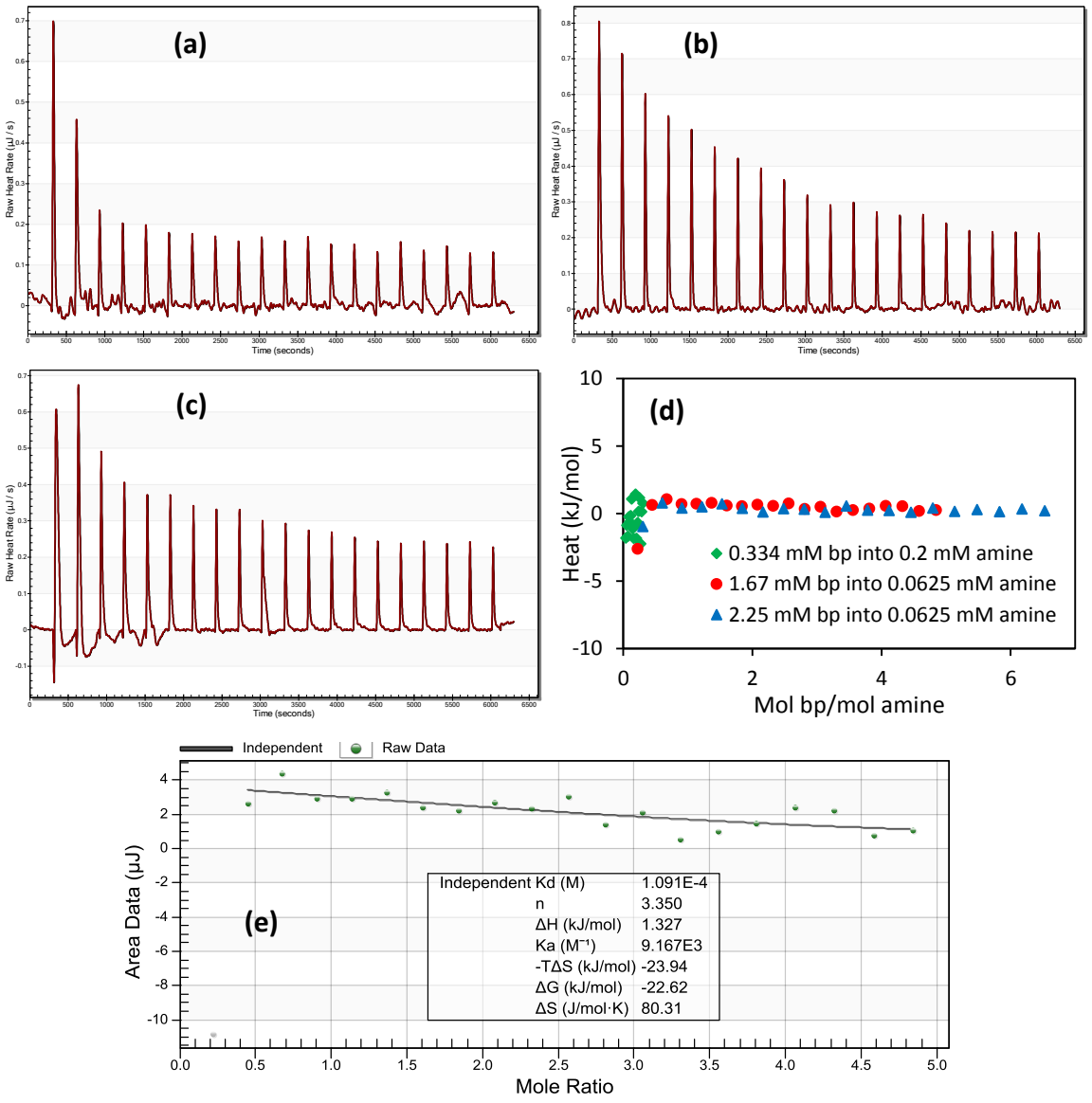

Figure E.6 Raw heat rate with time for 282 bp RNA interaction with SNPA for (a) 0.334 mM bp into 0.2 mM amine, (b) 1.67 mM bp into 0.0625 mM amine, (c) 2.25 mM bp into 0.0625 mM amine, (d) integrated heat per mol bp as a function of mol bp/mol amine, and (e) corresponding independent single site binding model fit for 1.67 mM bp into 0.0625 mM amine with estimated thermodynamic parameters.

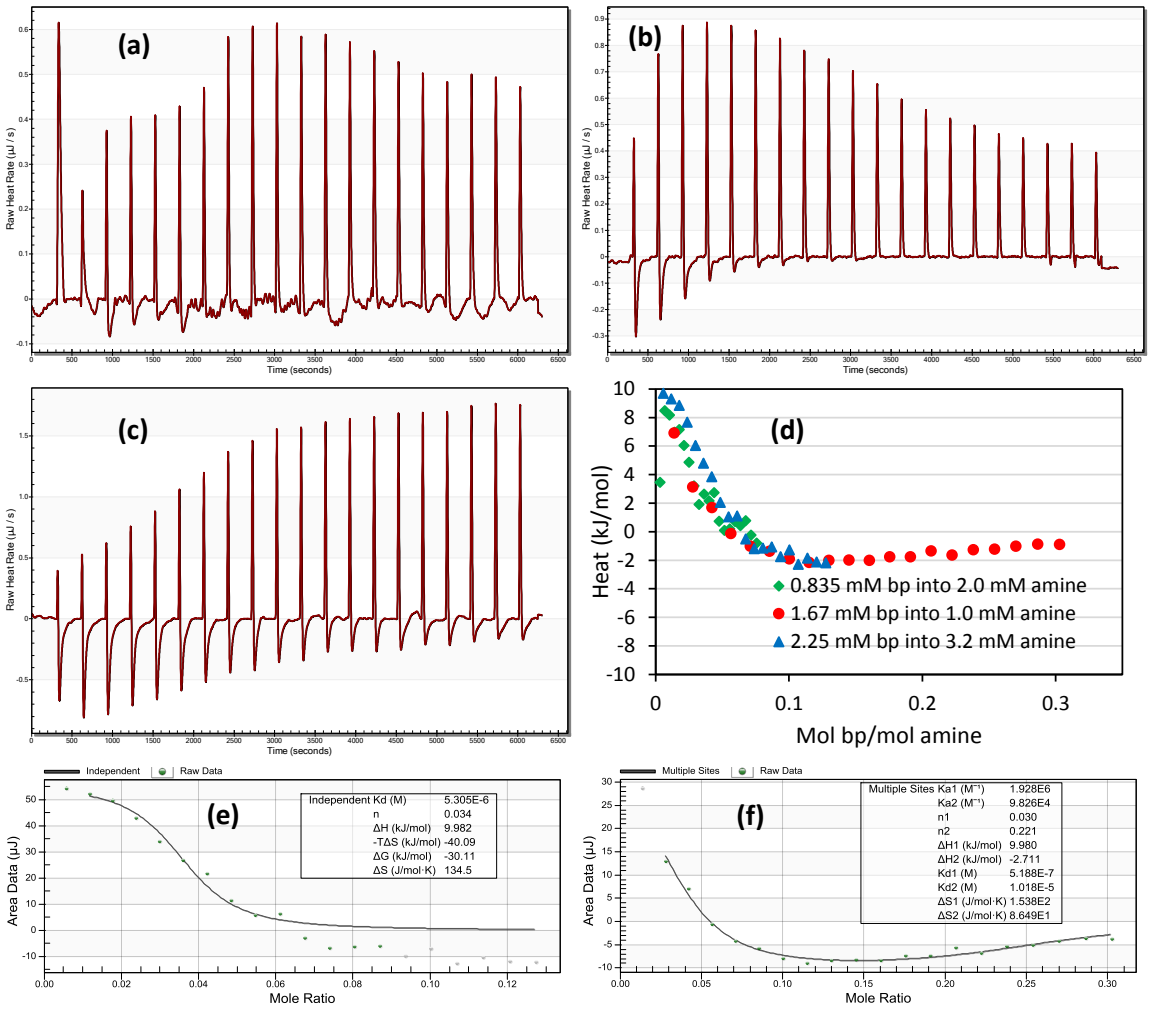

Figure E.7 Raw heat rate with time for 84 bp RNA interaction with MSNPA-1.6 for (a) 0.835 mM bp into 2.0 mM amine, (b) 1.67 mM bp into 1.0 mM amine, (c) 2.25 mM bp into 3.25 mM amine, (d) integrated heat per mol bp as a function of mol bp/mol amine, (e) corresponding independent single site binding model fit for 2.25 mM bp into 3.2 mM amine with estimated thermodynamic parameters, and (f) corresponding two site binding model fit for 1.67 mM bp into 1.0 mM amine with estimated thermodynamic parameters.

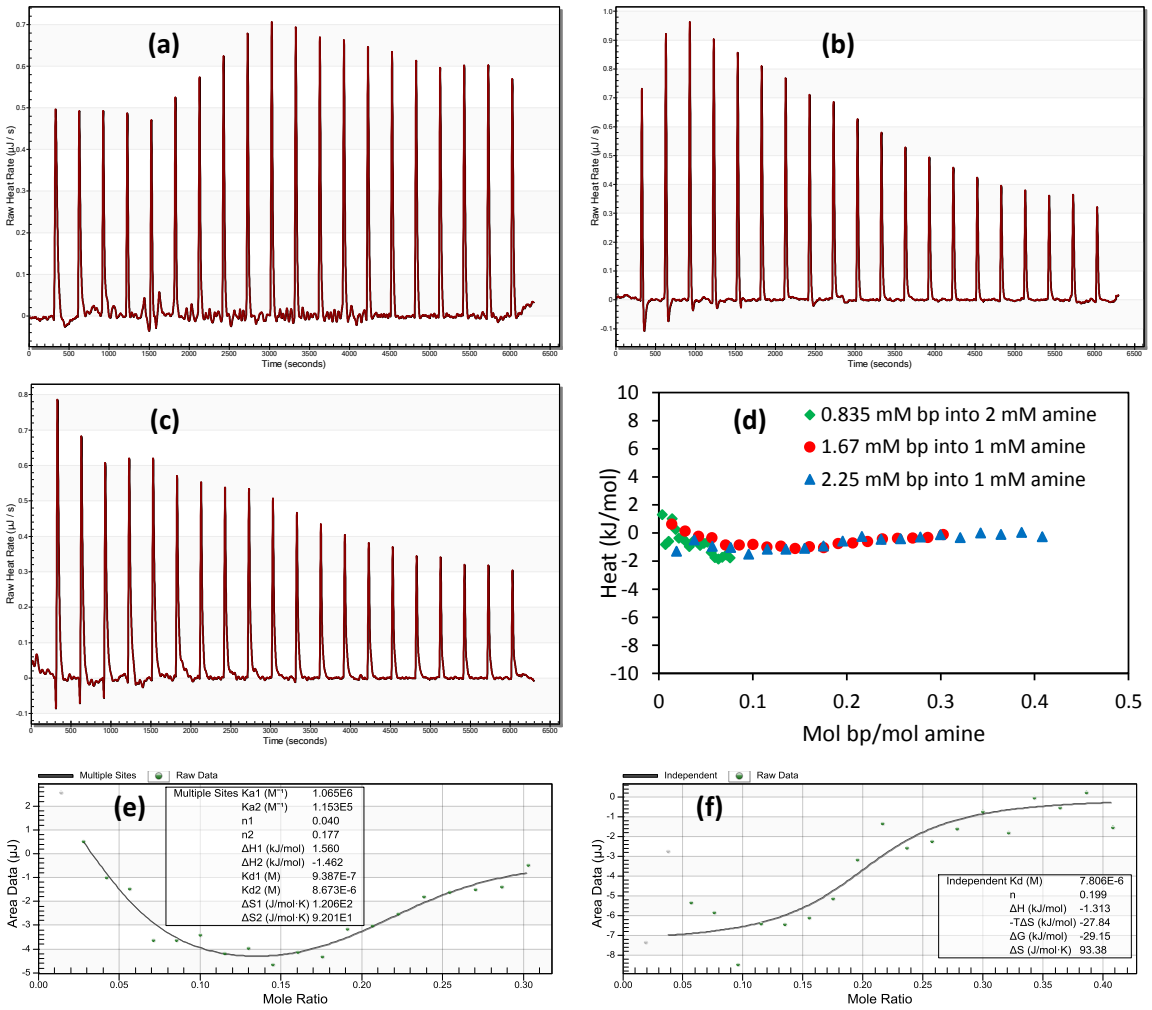

Figure E.8 Raw heat rate with time for 282 bp RNA interaction with MSNPA-1.6 for (a) 0.835 mM bp into 2.0 mM amine, (b) 1.67 mM bp into 1.0 mM amine, (c) 2.25 mM bp into 1.0 mM amine, (d) integrated heat per mol bp as a function of mol bp/mol amine, (e) corresponding two site binding model fit for 1.67 mM bp into 1 mM amine with estimated thermodynamic parameters, and (f) corresponding independent single site binding model fit for 2.25 mM bp into 1.0 mM amine with estimated thermodynamic parameters.

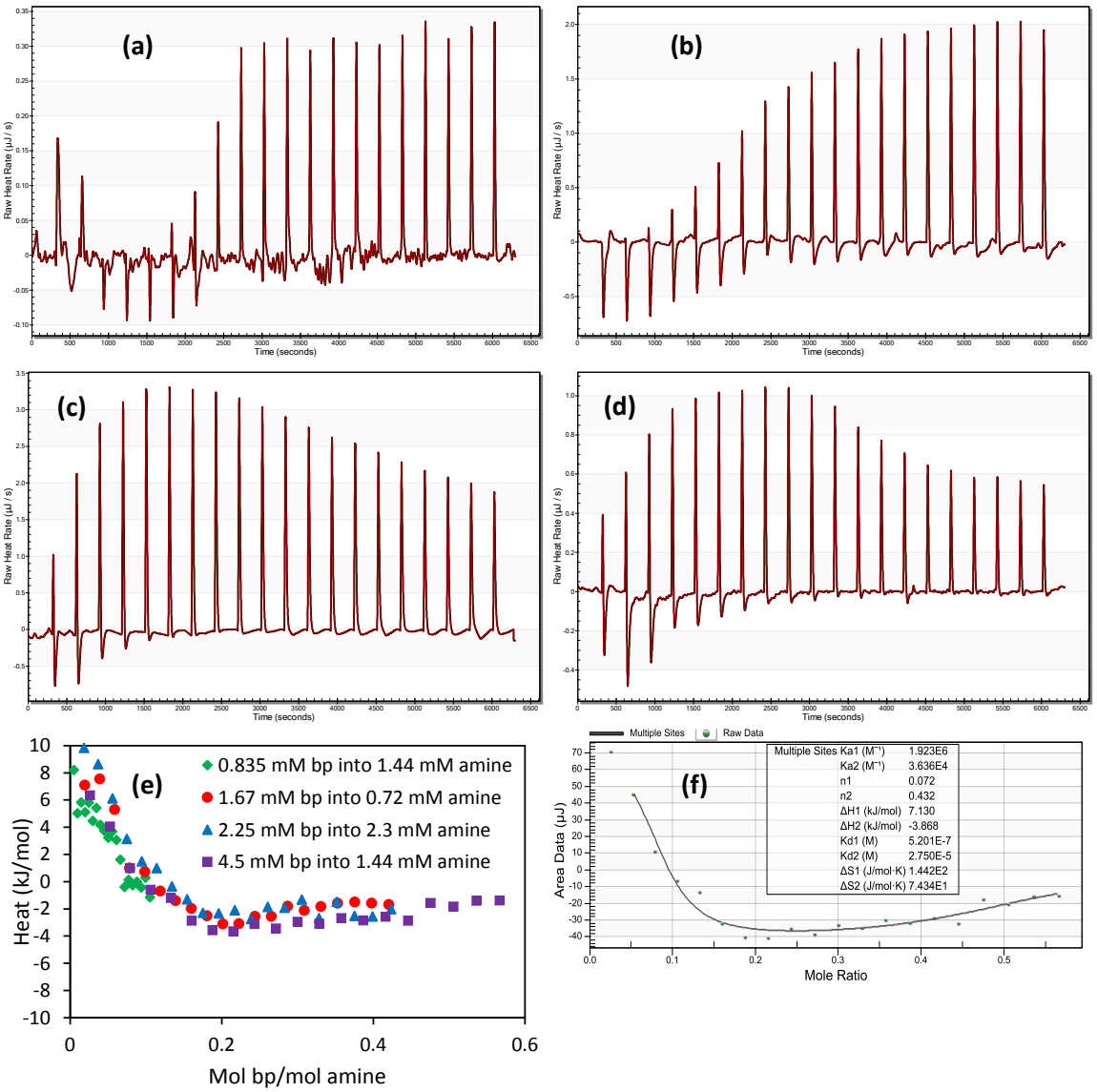

Figure E.9 Raw heat rate with time for 84 bp RNA interaction with MSNPA-3.2 for (a) 0.835 mM bp into 1.44 mM amine, (b) 2.25 mM bp into 2.3 mM amine, (c) 4.5 mM bp into 1.44 mM amine, (d) 1.67 mM bp into 0.72 mM amine, (e) integrated heat per mol bp as a function of mol bp/mol amine, and (f) corresponding two site binding model fit for 1.67 mM bp into 0.72 mM amine with estimated thermodynamic parameters.

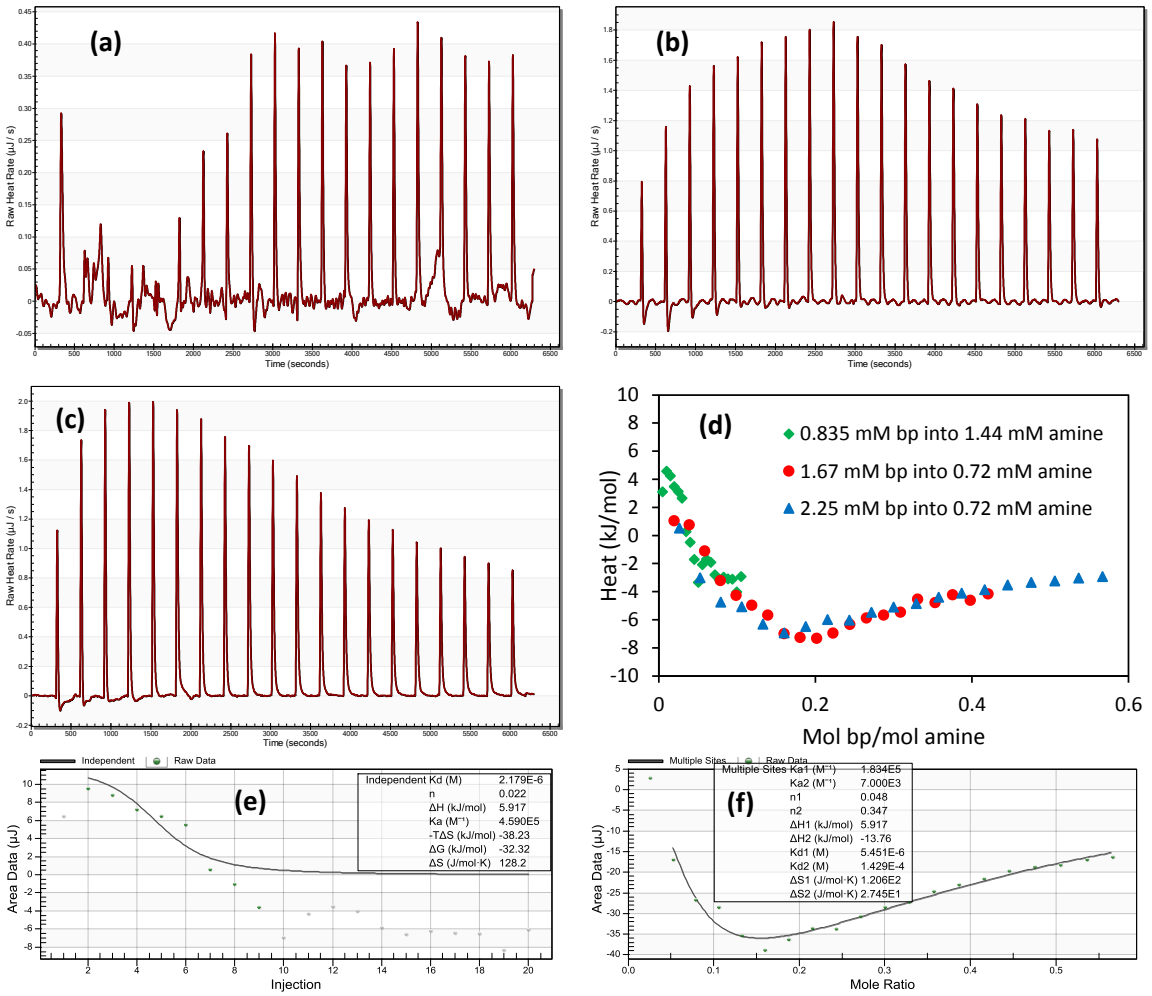

Figure E.10 Raw heat rate with time for 282 bp RNA interaction with MSNPA-3.2 for (a) 0.835 mM bp into 1.44 mM amine, (b) 1.67 mM bp into 0.72 mM amine, (c) 2.25 mM bp into 0.72 mM amine, (d) integrated heat per mol bp as a function of mol bp/mol amine, (e) corresponding independent single binding model fit for 0.835 mM bp into 1.44 mM amine with estimated thermodynamic parameters, and (f) corresponding two site binding model fit for 2.25 mM bp into 0.72 mM amine with estimated thermodynamic parameters.

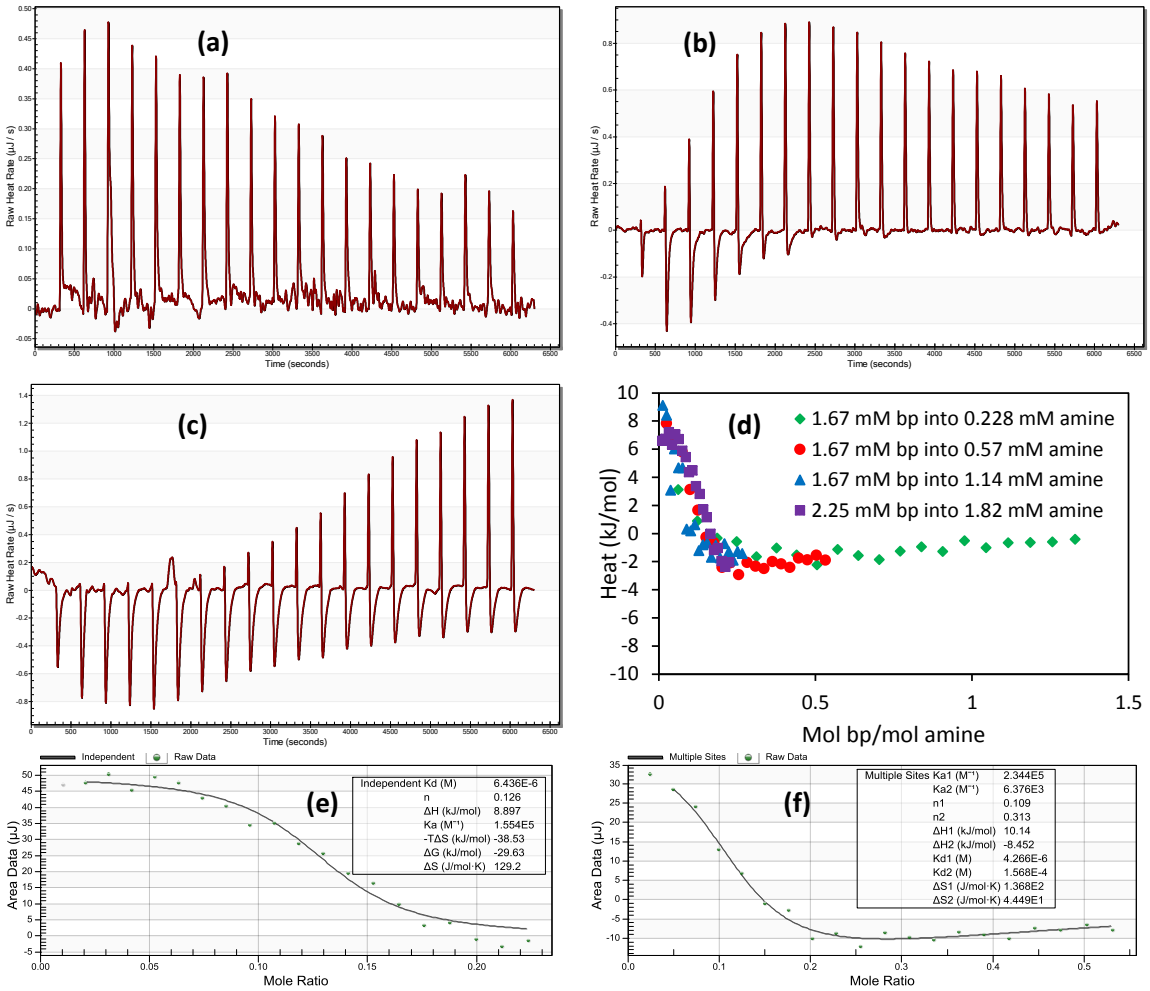

Figure E.11 Raw heat rate with time for 84 bp RNA interaction with MSNPA-7.6 for (a) 0.835 mM bp into 0.228 mM amine, (b) 1.67 mM bp into 0.57 mM amine, (c) 2.25 mM bp into 0.72 mM amine, (d) integrated heat per mol bp as a function of mol bp/mol amine, (e) corresponding independent single binding model fit for 2.25 mM bp into 1.82 mM amine with estimated thermodynamic parameters, and (f) corresponding two site binding model fit for 1.67 mM bp into 0.57 mM amine with estimated thermodynamic parameters.

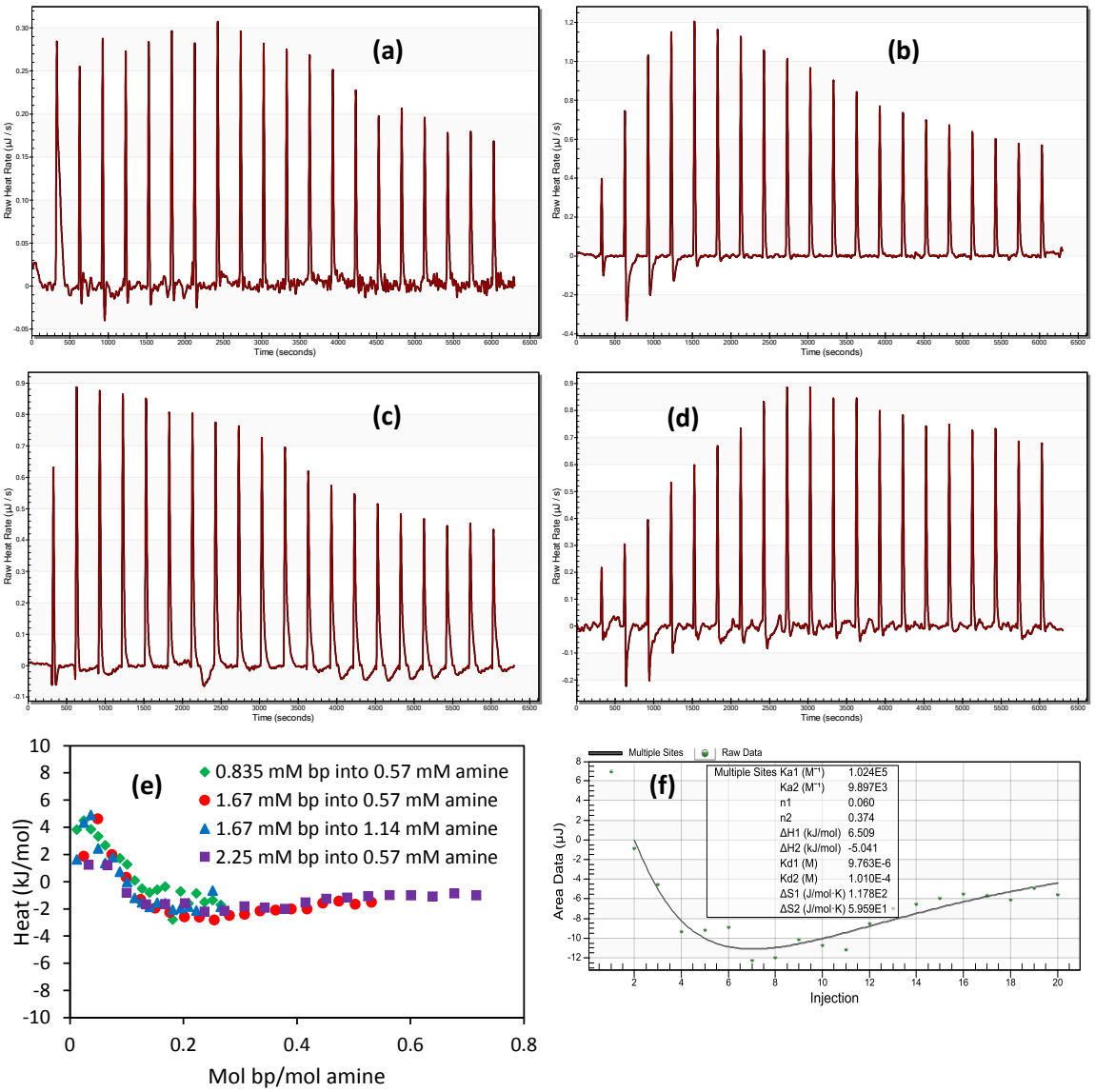

Figure E.12 Raw heat rate with time for 282 bp RNA interaction with MSNPA-7.6 for (a) 0.835 mM bp into 0.57 mM amine, (b) 1.67 mM bp into 0.57 mM amine, (c) 1.67 mM bp into 1.14 mM amine, (d) 2.25 mM bp into 0.57 mM amine, (e) integrated heat per mol bp as a function of mol bp/mol amine, and (f) corresponding two site binding model fit for 2.25 mM bp into 0.57 mM amine with estimated thermodynamic parameters.

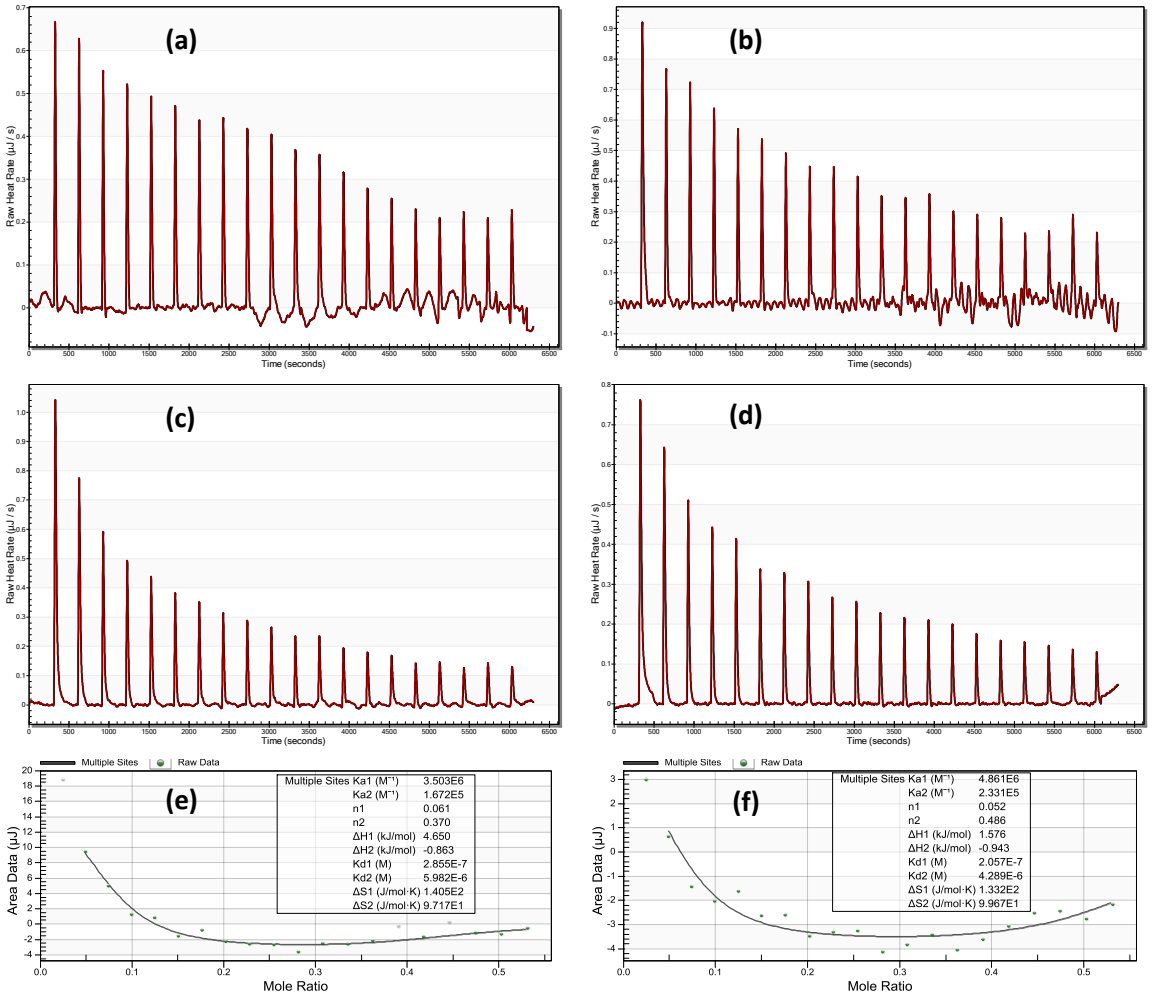

Figure E.13 Raw heat rate with time and two sites model fitting on integrated heat for (left) 84 bp RNA and (right) 282 bp RNA interaction with MSNPA-7.6 in presence of 30 mM NaCl for (a & b) raw heat rate for RNA interaction with particles, (c & d) corresponding heat of dilution in 30 mM NaCl solution and (e & f) integrated heat as a function of mole ratio with corresponding two site binding model fit for 1.67 mM bp into 0.57 mM amine with estimated thermodynamic parameters.

REFERENCES

1. Dias, D.A., S. Urban, and U. Roessner, *A historical overview of natural products in drug discovery.* Metabolites, 2012. **2**(2): p. 303-336.
2. De Luca, V., et al., *Mining the biodiversity of plants: A revolution in the making.* Science, 2012. **336**(6089): p. 1658-1661.
3. Petrovska, B.B., *Historical review of medicinal plants' usage.* Pharmacognosy Reviews, 2012. **6**(11): p. 1-5.
4. Smirnoff, N., *Environment and plant metabolism: Flexibility and acclimation*. 1995: BIOS Scientific publishers.
5. Kabera, J.N., et al., *Plant secondary metabolites: Biosynthesis, classification, function and pharmacological properties.* Journal of Pharmacy and Pharmacology, 2014. **2**: p. 377-392.
6. Kennedy, D.O. and E.L. Wightman, *Herbal extracts and phytochemicals: Plant secondary metabolites and the enhancement of human brain function.* Advances in Nutrition: An International Review Journal, 2011. **2**(1): p. 32-50.
7. Vaishnav, P. and A.L. Demain, *Unexpected applications of secondary metabolites.* Biotechnology Advances, 2011. **29**(2): p. 223-229.
8. Li, J.W.-H. and J.C. Vederas, *Drug discovery and natural products: End of an era or an endless frontier?* Science, 2009. **325**(5937): p. 161-165.
9. Harvey, A.L., *Natural products in drug discovery.* Drug Discovery Today, 2008. **13**(19–20): p. 894-901.
10. Vom Endt, D., J.W. Kijne, and J. Memelink, *Transcription factors controlling plant secondary metabolism: What regulates the regulators?* Phytochemistry, 2002. **61**(2): p. 107-114.
11. Roessner, U., et al., *Metabolic profiling allows comprehensive phenotyping of genetically or environmentally modified plant systems.* Plant Cell, 2001. **13**(1): p. 11-29.
12. Littleton, J., T. Rogers, and D. Falcone, *Novel approaches to plant drug discovery based on high throughput pharmacological screening and genetic manipulation.* Life Sciences, 2005. **78**(5): p. 467-475.
13. Georgiev, M., A. Pavlov, and T. Bley, *Hairy root type plant in vitro systems as sources of bioactive substances.* Applied Microbiology and Biotechnology, 2007. **74**(6): p. 1175-1185.
14. Gunjan, S.K., et al., *Hairy root cultures and plant regeneration in solidago nemoralis transformed with agrobacterium rhizogenes.* American Journal of Plant Sciences, 2013. **4**: p. 1675-1678.
15. Kurepa, J., et al., *Direct isolation of flavonoids from plants using ultra-small anatase TiO_2 nanoparticles.* The Plant Journal: for Cell and Molecular Biology, 2014. **77**(3): p. 443-453.

16. Slowing, I.I., et al., *Exocytosis of mesoporous silica nanoparticles from mammalian cells: From asymmetric cell-to-cell transfer to protein harvesting.* Small, 2011. **7**(11): p. 1526-1532.

17. Bouchoucha, M., et al., *Mesoporous silica nanoparticles: Selective surface functionalization for optimal relaxometric and drug loading performances.* Advanced Functional Materials, 2014. **24**(37): p. 5911-5923.

18. Trewyn, B.G., et al., *Mesoporous silica nanoparticle based controlled release, drug delivery, and biosensor systems.* Chemical Communications, 2007(31): p. 3236-3245.

19. Allen, R.S., et al., *RNAi-mediated replacement of morphine with the nonnarcotic alkaloid reticuline in opium poppy.* Nature Biotechnology, 2004. **22**(12): p. 1559-1566.

20. Nayerossadat, N., T. Maedeh, and P.A. Ali, *Viral and nonviral delivery systems for gene delivery.* Advanced Biomedical Research, 2012. **1**: p. 27.

21. Al-Dosari, M.S. and X. Gao, *Nonviral gene delivery: Principle, limitations, and recent progress.* The AAPS Journal, 2009. **11**(4): p. 671-681.

22. Whitehead, K.A., R. Langer, and D.G. Anderson, *Knocking down barriers: Advances in siRNA delivery.* Nature Reviews Drug Discovery, 2009. **8**(2): p. 129-138.

23. Agrawal, N., et al., *RNA interference: Biology, mechanism, and applications.* Microbiology and Molecular Biology Reviews, 2003. **67**(4): p. 657-685.

24. Sun, R., et al., *Recent advance on mesoporous silica nanoparticles-based controlled release system: Intelligent switches open up new horizon.* Nanomaterials, 2015. **5**(4): p. 2019-2053.

25. Torney, F., et al., *Mesoporous silica nanoparticles deliver DNA and chemicals into plants.* Nature Nanotechnology, 2007. **2**: p. 295-300.

26. Chang, F.-P., et al., *A simple plant gene delivery system using mesoporous silica nanoparticles as carriers.* Journal of Materials Chemistry B, 2013. **1**(39): p. 5279-5287.

27. Wynant, N., D. Santos, and J. Vanden Broeck, *Biological mechanisms determining the success of RNA interference in insects.* International Review of Cell and Molecular Biology, 2014. **312**: p. 139-167.

28. Yu, N., et al., *Delivery of dsRNA for RNAi in insects: An overview and future directions.* Insect science, 2013. **20**(1): p. 4-14.

29. Li, Z., et al., *Mesoporous silica nanoparticles in biomedical applications.* Chemical Society Reviews, 2012. **41**(7): p. 2590-2605.

30. Liu, Z., et al., *The use of multifunctional magnetic mesoporous core/shell heteronanostructures in a biomolecule separation system.* Biomaterials, 2011. **32**(21): p. 4683-4690.

31. Wang, Y., et al., *Mesoporous silica nanoparticles in drug delivery and biomedical applications.* Nanomedicine: Nanotechnology, Biology and Medicine, 2015. **11**(2): p. 313-327.

32. Rahman, I.A. and V. Padavettan, *Synthesis of silica nanoparticles by sol-gel: Size-dependent properties, surface modification, and applications in silica-polymer nanocomposites—a review.* Journal of Nanomaterials, 2012. **2012**: p. 8.

33. Anand, C., et al., *Preparation of mesoporous titanosilicate molecular sieves with a cage type 3D porous structure for cyclohexene epoxidation.* Microporous and Mesoporous Materials, 2012. **160**: p. 159-166.

34. Liberman, A., et al., *Synthesis and surface functionalization of silica nanoparticles for nanomedicine.* Surface Science Reports, 2014. **69**(2–3): p. 132-158.

35. Slowing, I.I., et al., *Mesoporous silica nanoparticles for drug delivery and biosensing applications.* Advanced Functional Materials, 2007. **17**(8): p. 1225-1236.

36. Graf, C., et al., *Surface functionalization of silica nanoparticles supports colloidal stability in physiological media and facilitates internalization in cells.* Langmuir, 2012. **28**(20): p. 7598-7613.

37. Halford, S.E. and J.F. Marko, *How do site-specific DNA-binding proteins find their targets?* Nucleic Acids Research, 2004. **32**(10): p. 3040-3052.

38. Khan, M.A., et al., *Adsorption and recovery of polyphenolic flavonoids using TiO_2-functionalized mesoporous silica nanoparticles.* ACS Applied Materials & Interfaces, 2017. **9**(37): p. 32114-32125.

39. Khan, M.A., et al., *Nanoharvesting of bioactive materials from living plant cultures using engineered silica nanoparticles.* Materials Science and Engineering: C, 2020. **106**: p. 110190.

40. Hench, L.L. and J.K. West, *The sol-gel process.* Chemical Reviews, 1990. **90**(1): p. 33-72.

41. Osterholtz, F.D. and E.R. Pohl, *Kinetics of the hydrolysis and condensation of organofunctional alkoxysilanes: A review.* Journal of Adhesion Science and Technology, 1992. **6**(1): p. 127-149.

42. Alberius, P.C.A., et al., *General predictive syntheses of cubic, hexagonal, and lamellar silica and titania mesostructured thin films.* Chemistry of Materials, 2002. **14**(8): p. 3284-3294.

43. Zhao, D., et al., *Morphological control of highly ordered mesoporous silica SBA-15.* Chemistry of Materials, 2000. **12**(2): p. 275-279.

44. Popat, A., et al., *Mesoporous silica nanoparticles for bioadsorption, enzyme immobilisation, and delivery carriers.* Nanoscale, 2011. **3**(7): p. 2801-2818.

45. Huirache-Acuña, R., et al., *SBA-15 mesoporous silica as catalytic support for hydrodesulfurization catalysts—review.* Materials, 2013. **6**(9): p. 4139-4167.

46. Schlipf, D.M., et al., *Effects of pore size and tethering on the diffusivity of lipids confined in mesoporous silica.* Advanced Materials Interfaces, 2017. **4**(9): p. 1601103.

47. Zhou, S., et al., *Lipid pore-filled silica thin-film membranes for biomimetic recovery of dilute carbohydrates.* Langmuir, 2017. **33**(49): p. 14156-14166.

48. Zou, H., S. Wu, and J. Shen, *Polymer/silica nanocomposites: Preparation, characterization, properties, and applications.* Chemical Reviews, 2008. **108**(9): p. 3893-3957.

49. Tang, L. and J. Cheng, *Nonporous silica nanoparticles for nanomedicine application.* Nano Today, 2013. **8**(3): p. 290-312.

50. Stöber, W., A. Fink, and E. Bohn, *Controlled growth of monodisperse silica spheres in the micron size range.* Journal of Colloid and Interface Science, 1968. **26**(1): p. 62-69.

51. Bogush, G.H., M.A. Tracy, and C.F. Zukoski, *Preparation of monodisperse silica particles: Control of size and mass fraction.* Journal of Non-Crystalline Solids, 1988. **104**(1): p. 95-106.

52. Van Blaaderen, A., J. Van Geest, and A. Vrij, *Monodisperse colloidal silica spheres from tetraalkoxysilanes: Particle formation and growth mechanism.* Journal of Colloid and Interface Science, 1992. **154**(2): p. 481-501.

53. Bogush, G.H. and C.F. Zukoski, *Studies of the kinetics of the precipitation of uniform silica particles through the hydrolysis and condensation of silicon alkoxides.* Journal of Colloid and Interface Science, 1991. **142**(1): p. 1-18.

54. Bogush, G.H. and C.F. Zukoski, *Uniform silica particle precipitation: An aggregative growth model.* Journal of Colloid and Interface Science, 1991. **142**(1): p. 19-34.

55. Green, D.L., et al., *Size, volume fraction, and nucleation of Stober silica nanoparticles.* Journal of Colloid and Interface Science, 2003. **266**(2): p. 346-358.

56. Matsoukas, T. and E. Gulari, *Monomer-addition growth with a slow initiation step: A growth model for silica particles from alkoxides.* Journal of Colloid and Interface Science, 1989. **132**(1): p. 13-21.

57. Lee, K., A.N. Sathyagal, and A.V. McCormick, *A closer look at an aggregation model of the Stöber process.* Colloids and Surfaces A: Physicochemical and Engineering Aspects, 1998. **144**(1-3): p. 115-125.

58. Lei, X., et al., *Synthesis of monodisperse silica microspheres by a modified Stöber method.* Integrated Ferroelectrics, 2014. **154**(1): p. 142-146.

59. Schlipf, D.M., S.E. Rankin, and B.L. Knutson, *Pore-size dependent protein adsorption and protection from proteolytic hydrolysis in tailored mesoporous silica particles.* ACS Applied Materials & Interfaces, 2013. **5**(20): p. 10111-10117.

60. Nakabayashi, H., et al., *Electrolyte-added one-pot synthesis for producing monodisperse, micrometer-sized silica particles up to 7 μm.* Langmuir, 2010. **26**(10): p. 7512-7515.

61. Zhou, S., *Pore-confined carriers and biomolecules in mesoporous silica for biomimetic separation and targeting*. 2017, University of Kentucky: Lexington, Kentucky, United States.

62. Asefa, T. and Z. Tao, *Biocompatibility of mesoporous silica nanoparticles.* Chemical Research in Toxicology, 2012. **25**(11): p. 2265-2284.

63. Lee, J.E., et al., *Multifunctional mesoporous silica nanocomposite nanoparticles for theranostic applications.* Accounts of Chemical Research, 2011. **44**(10): p. 893-902.

64. Chen, N.-T., et al., *Theranostic applications of mesoporous silica nanoparticles and their organic/inorganic hybrids.* Journal of Materials Chemistry B, 2013. **1**(25): p. 3128-3135.

65. Rimola, A., et al., *Silica surface features and their role in the adsorption of biomolecules: Computational modeling and experiments.* Chemical Reviews, 2013. **113**(6): p. 4216-4313.

66. Huo, Q., et al., *Organization of organic molecules with inorganic molecular species into nanocomposite biphase arrays.* Chemistry of Materials, 1994. **6**(8): p. 1176-1191.

67. Huo, Q., D.I. Margolese, and G.D. Stucky, *Surfactant control of phases in the synthesis of mesoporous silica-based materials.* Chemistry of Materials, 1996. **8**(5): p. 1147-1160.

68. Wu, S.-H., C.-Y. Mou, and H.-P. Lin, *Synthesis of mesoporous silica nanoparticles.* Chemical Society Reviews, 2013. **42**(9): p. 3862-3875.

69. Kim, T.-W., P.-W. Chung, and V.S.Y. Lin, *Facile synthesis of monodisperse spherical MCM-48 mesoporous silica nanoparticles with controlled particle size.* Chemistry of Materials, 2010. **22**(17): p. 5093-5104.

70. Qiao, Z.-A., et al., *Synthesis of mesoporous silica nanoparticles via controlled hydrolysis and condensation of silicon alkoxide.* Chemistry of Materials, 2009. **21**(16): p. 3823-3829.

71. Tan, B. and S.E. Rankin, *Interfacial alignment mechanism of forming spherical silica with radially oriented nanopores.* Journal of Physical Chemistry B, 2004. **108**(52): p. 20122-20129.

72. Beck, J.S., et al., *A new family of mesoporous molecular-sieves prepared with liquid-crystal templates.* Journal of the American Chemical Society, 1992. **114**(27): p. 10834-10843.

73. Wan, Y. and D. Zhao, *On the controllable soft-templating approach to mesoporous silicates.* Chemical Reviews, 2007. **107**(7): p. 2821-2860.

74. Yang, P., et al., *Triblock-copolymer-directed syntheses of large-pore mesoporous silica fibers.* Chemistry of Materials, 1998. **10**(8): p. 2033-2036.

75. Kruk, M., *Access to ultralarge-pore ordered mesoporous materials through selection of surfactant/swelling-agent micellar templates.* Accounts of Chemical Research, 2012. **45**(10): p. 1678-1687.

76. Blin, J.L. and B.L. Su, *Tailoring pore size of ordered mesoporous silicas using one or two organic auxiliaries as expanders.* Langmuir, 2002. **18**(13): p. 5303-5308.

77. Corma, A., et al., *Synthesis of MCM-41 with different pore diameters without addition of auxiliary organics.* Chemistry of Materials, 1997. **9**(10): p. 2123-2126.

78. Han, Y. and J.Y. Ying, *Generalized fluorocarbon-surfactant-mediated synthesis of nanoparticles with various mesoporous structures.* Angewandte Chemie International Edition, 2005. **44**(2): p. 288-292.

79. Cao, L., T. Man, and M. Kruk, *Synthesis of ultra-large-pore SBA-15 silica with two-dimensional hexagonal structure using triisopropylbenzene as micelle expander.* Chemistry of Materials, 2009. **21**(6): p. 1144-1153.

80. Suteewong, T., et al., *Highly aminated mesoporous silica nanoparticles with cubic pore structure.* Journal of the American Chemical Society, 2011. **133**(2): p. 172-175.

81. Kao, K.-C. and C.-Y. Mou, *Pore-expanded mesoporous silica nanoparticles with alkanes/ethanol as pore expanding agent.* Microporous and Mesoporous Materials, 2013. **169**: p. 7-15.

82. Kao, K.-C., T.-S. Lin, and C.-Y. Mou, *Enhanced activity and stability of lysozyme by immobilization in the matching nanochannels of mesoporous silica nanoparticles.* Journal of Physical Chemistry C, 2014. **118**(13): p. 6734-6743.

83. Gu, J., et al., *Sub-150 nm mesoporous silica nanoparticles with tunable pore sizes and well-ordered mesostructure for protein encapsulation.* Journal of Colloid and Interface Science, 2013. **407**: p. 236-242.

84. Yamada, H., et al., *A multifunctional role of trialkylbenzenes for the preparation of aqueous colloidal mesostructured/mesoporous silica nanoparticles with controlled pore size, particle diameter, and morphology.* Nanoscale, 2015. **7**(46): p. 19557-19567.

85. Kim, S., et al., *In-depth study on the gene silencing capability of silica nanoparticles with different pore sizes: Degree and duration of RNA interference.* RSC Advances, 2016. **6**(32): p. 27143-27150.

86. Mesa, M., et al., *Preparation of micron-sized spherical particles of mesoporous silica from a triblock copolymer surfactant, usable as a stationary phase for liquid chromatography.* Solid State Sciences, 2003. **5**(9): p. 1303-1308.

87. Wang, Y. and H. Gu, *Core–shell-type magnetic mesoporous silica nanocomposites for bioimaging and therapeutic agent delivery.* Advanced Materials, 2015. **27**(3): p. 576-585.

88. Feng, X., et al., *Functionalized monolayers on ordered mesoporous supports.* Science, 1997. **276**(5314): p. 923-926.

89. Kecht, J., A. Schlossbauer, and T. Bein, *Selective functionalization of the outer and inner surfaces in mesoporous silica nanoparticles.* Chemistry of Materials, 2008. **20**(23): p. 7207-7214.

90. Kim, M.S. and J.Y. Chang, *Preparation of multifunctional mesoporous silica particles: The use of an amphiphilic silica precursor with latent amine functionality in selective functionalization of the inner surface.* Journal of Materials Chemistry, 2011. **21**(24): p. 8766-8771.

91. Cheng, K. and C.C. Landry, *Diffusion-based deprotection in mesoporous materials: A strategy for differential functionalization of porous silica particles.* Journal of the American Chemical Society, 2007. **129**(31): p. 9674-9685.

92. de Juan, F. and E. Ruiz-Hitzky, *Selective functionalization of mesoporous silica.* Advanced Materials, 2000. **12**(6): p. 430-432.

93. Lunn, J.D. and D.F. Shantz, *Novel polypeptide/thiol—SBA-15 hybrid materials synthesized via surface selective grafting.* Chemical Communications, 2010. **46**(17): p. 2926-2928.

94. Gartmann, N. and D. Brühwiler, *Controlling and imaging the functional-group distribution on mesoporous silica.* Angewandte Chemie International Edition, 2009. **48**(34): p. 6354-6356.

95. Serda, R.E., et al., *Logic-embedded vectors for intracellular partitioning, endosomal escape, and exocytosis of nanoparticles.* Small, 2010. **6**(23): p. 2691-2700.

96. Tang, F., L. Li, and D. Chen, *Mesoporous silica nanoparticles: Synthesis, biocompatibility and drug delivery.* Advanced Materials, 2012. **24**(12): p. 1504-1534.

97. Sola-Rabada, A., et al., *Interactions at the silica–peptide interface: Influence of the extent of functionalization on the conformational ensemble.* Langmuir, 2018. **34**(28): p. 8255-8263.

98. Puddu, V. and C.C. Perry, *Interactions at the silica–peptide interface: The influence of particle size and surface functionality.* Langmuir, 2014. **30**(1): p. 227-233.

99. Russo, P.A., et al., *Tailoring the surface chemistry of mesocellular foams for protein adsorption.* Colloids and Surfaces A: Physicochemical and Engineering Aspects, 2011. **386**(1): p. 25-35.

100. Ayad, M.M., et al., *Amine-functionalized mesoporous silica KIT-6 as a controlled release drug delivery carrier.* Microporous and Mesoporous Materials, 2016. **229**: p. 166-177.

101. Ezzeddine, Z., et al., *Divalent heavy metals adsorption onto different types of EDTA-modified mesoporous materials: Effectiveness and complexation rate.* Microporous and Mesoporous Materials, 2015. **212**: p. 125-136.

102. Bauer, F., et al., *Water-based functionalization of mesoporous siliceous materials, part 1: Morphology and stability of grafted 3-aminopropyltriethoxysilane.* Microporous and Mesoporous Materials, 2017. **250**: p. 221-231.

103. Hori, K., et al., *Effect of pore size, aminosilane density and aminosilane molecular length on CO_2 adsorption performance in aminosilane modified mesoporous silica.* Microporous and Mesoporous Materials, 2017. **246**: p. 158-165.

104. Majda, D., et al., *Porosity of SBA-15 after functionalization of the surface with aminosilanes.* Microporous and Mesoporous Materials, 2016. **234**: p. 98-106.

105. Liu, Y., et al., *Kinetics of (3-aminopropyl)triethoxylsilane (APTES) silanization of superparamagnetic iron oxide nanoparticles.* Langmuir, 2013. **29**(49): p. 15275-15282.

106. He, X. and D. Antonelli, *Recent advances in synthesis and applications of transition metal containing mesoporous molecular sieves.* Angewandte Chemie International Edition, 2002. **41**(2): p. 214-229.

107. Reddy, J.S. and R. Kumar, *Synthesis, characterization, and catalytic properties of a titanium silicate, TS-2, with MEL structure.* Journal of Catalysis, 1991. **130**(2): p. 440-446.

108. Taramasso, M., G. Perego, and B. Notari, *Preparation of porous crystalline synthetic material comprised of silicon and titanium oxides.* US Patent 4,410,501, 1983.

109. Alba, M.D., Z. Luan, and J. Klinowski, *Titanosilicate mesoporous molecular sieve MCM-41: Synthesis and characterization.* Journal of Physical Chemistry, 1996. **100**(6): p. 2178-2182.

110. Tanev, P.T., M. Chibwe, and T.J. Pinnavaia, *Titanium-containing mesoporous molecular sieves for catalytic oxidation of aromatic compounds.* Nature, 1994. **368**: p. 321.

111. Araujo, P.Z., P.J. Morando, and M.A. Blesa, *Interaction of catechol and gallic acid with titanium dioxide in aqueous suspensions. 1. Equilibrium studies.* Langmuir, 2005. **21**(8): p. 3470-3474.

112. Brigante, M. and P.C. Schulz, *Adsorption of paraquat on mesoporous silica modified with titania: Effects of pH, ionic strength and temperature.* Journal of Colloid and Interface Science, 2011. **363**(1): p. 355-361.

113. Costa, D., L. Savio, and C.M. Pradier, *Adsorption of amino acids and peptides on metal and oxide surfaces in water environment: A synthetic and prospective review.* Journal of Physical Chemistry B, 2016. **120**(29): p. 7039-7052.

114. Beyers, E., et al., *Combined TiO_2/SiO_2 mesoporous photocatalysts with location and phase controllable TiO_2 nanoparticles.* Applied Catalysis B: Environmental, 2009. **88**(3–4): p. 515-524.

115. Salameh, C., et al., *Dispersion of colloidal TiO_2 nanoparticles on mesoporous materials targeting photocatalysis applications.* Catalysis Today, 2015. **257, Part 1**: p. 35-40.

116. Lafond, V., P.H. Mutin, and A. Vioux, *Control of the texture of titania-silica mixed oxides prepared by nonhydrolytic sol-gel.* Chemistry of Materials, 2004. **16**(25): p. 5380-5386.

117. Rahman, M.S., et al., *Incorporation of isolated Ti sites into mesoporous silica thin films by sugar surfactant complexation.* Microporous and Mesoporous Materials, 2014. **190**(Supplement C): p. 74-83.

118. Blin, J.L., et al., *Direct one-step immobilization of glucose oxidase in well-ordered mesostructured silica using a nonionic fluorinated surfactant.* Chemistry of Materials, 2005. **17**(6): p. 1479-1486.

119. Nakanishi, K., et al., *Specific binding of immunoglobulin-G to protein-A – mesoporous silica composites for affinity column chromatography.* Journal of Materials Chemistry B, 2013. **1**(45): p. 6321-6328.

120. Bae, S.-E., et al., *Intracellular delivery of a native functional protein using cell-penetrating peptide functionalized cubic MSNs with ultra-large mesopores.* Journal of Materials Chemistry B, 2018. **6**(21): p. 3456-3465.

121. Hermanson, G.T., *Bioconjugate techniques*. 2013, London, United Kingdom: Academic press.

122. Gang, A., et al., *A simple two-step silane-based (bio-) receptor molecule immobilization without additional binding site passivation.* RSC Advances, 2015. **5**(45): p. 35631-35634.

123. Kralj, S., et al., *Targeting EGFR-overexpressed A431 cells with EGF-labeled silica-coated magnetic nanoparticles.* Journal of Nanoparticle Research, 2013. **15**(5): p. 1666.

124. Liu, J., et al., *Enzyme responsive mesoporous silica nanoparticles for targeted tumor therapy in vitro and in vivo.* Nanoscale, 2015. **7**(8): p. 3614-3626.

125. Pan, L., et al., *Nuclear-targeted drug delivery of TAT peptide-conjugated monodisperse mesoporous silica nanoparticles.* Journal of the American Chemical Society, 2012. **134**(13): p. 5722-5725.

126. Liu, R., et al., *pH-responsive nanogated ensemble based on gold-capped mesoporous silica through an acid-labile acetal linker.* Journal of the American Chemical Society, 2010. **132**(5): p. 1500-1501.

127. Vivero-Escoto, J.L., et al., *Photoinduced intracellular controlled release drug delivery in human cells by gold-capped mesoporous silica nanosphere.* Journal of the American Chemical Society, 2009. **131**(10): p. 3462-3463.

128. Lim, C.Y., et al., *Succinimidyl ester surface chemistry: Implications of the competition between aminolysis and hydrolysis on covalent protein immobilization.* Langmuir, 2014. **30**(43): p. 12868-12878.

129. Onclin, S., B.J. Ravoo, and D.N. Reinhoudt, *Engineering silicon oxide surfaces using self-assembled monolayers.* Angewandte Chemie International Edition, 2005. **44**(39): p. 6282-6304.

130. Nam, Y., D. Lee, and E.-B. Cho, *Role of phosphate-modified mesoporous silica nanoparticles for altering biomimetic metal-induced aggregation process of Pluronic F127 block copolymer.* Materials Letters, 2013. **110**: p. 176-179.

131. Onbulak, S., et al., *Synthesis and functionalization of thiol-reactive biodegradable polymers.* Macromolecules, 2012. **45**(3): p. 1715-1722.

132. MacBeath, G., A.N. Koehler, and S.L. Schreiber, *Printing small molecules as microarrays and detecting protein−ligand interactions en masse.* Journal of the American Chemical Society, 1999. **121**(34): p. 7967-7968.

133. Modjinou, T., et al., *UV-cured thiol–ene eugenol/zno composite materials with antibacterial properties.* RSC Advances, 2016. **6**(91): p. 88135-88142.

134. Modjinou, T., et al., *Antibacterial and antioxidant bio-based networks derived from eugenol using photo-activated thiol-ene reaction.* Reactive and Functional Polymers, 2016. **101**: p. 47-53.

135. Díaz-García, M.E. and R.B. Laínño, *Molecular imprinting in sol-gel materials: Recent developments and applications.* Microchimica Acta, 2005. **149**(1): p. 19-36.

136. Chen, L., et al., *Molecular imprinting: Perspectives and applications.* Chemical Society Reviews, 2016. **45**(8): p. 2137-2211.

137. Li, J.H., et al. *Preparation and characterization of paclitaxel imprinted silica nanoparticles*. in *Advanced Materials Research*. 2012. Trans Tech Publications.

138. Gao, D., et al., *A surface functional monomer-directing strategy for highly dense imprinting of tnt at surface of silica nanoparticles.* Journal of the American Chemical Society, 2007. **129**(25): p. 7859-7866.

139. Ow, H., et al., *Bright and stable core−shell fluorescent silica nanoparticles.* Nano Letters, 2005. **5**(1): p. 113-117.

140. Chen, L., S. Xu, and J. Li, *Recent advances in molecular imprinting technology: Current status, challenges and highlighted applications.* Chemical Society Reviews, 2011. **40**(5): p. 2922-2942.

141. Tozzi, C., et al., *Chromatographic characterisation of an estrogen-binding affinity column containing tetrapeptides selected by a combinatorial-binding approach.* Journal of Chromatography A, 2002. **966**(1-2): p. 71-79.

142. Verheyen, E., et al., *Challenges for the effective molecular imprinting of proteins.* Biomaterials, 2011. **32**(11): p. 3008-3020.

143. Sulpizi, M., M.-P. Gaigeot, and M. Sprik, *The silica–water interface: How the silanols determine the surface acidity and modulate the water properties.* Journal of Chemical Theory and Computation, 2012. **8**(3): p. 1037-1047.

144. Schrader, A.M., et al., *Surface chemical heterogeneity modulates silica surface hydration.* Proceedings of the National Academy of Sciences, 2018. **115**(12): p. 2890-2895.

145. Dalstein, L., E. Potapova, and E. Tyrode, *The elusive silica/water interface: Isolated silanols under water as revealed by vibrational sum frequency*

spectroscopy. Physical Chemistry Chemical Physics, 2017. **19**(16): p. 10343-10349.

146. Zhou, H.-X., *Loops, linkages, rings, catenanes, cages, and crowders: Entropy-based strategies for stabilizing proteins.* Accounts of Chemical Research, 2004. **37**(2): p. 123-130.

147. De, M., et al., *Biomimetic interactions of proteins with functionalized nanoparticles: A thermodynamic study.* Journal of the American Chemical Society, 2007. **129**(35): p. 10747-10753.

148. Payne, T.E., et al., *Guidelines for thermodynamic sorption modelling in the context of radioactive waste disposal.* Environmental Modelling & Software, 2013. **42**: p. 143-156.

149. Fasting, C., et al., *Multivalency as a chemical organization and action principle.* Angewandte Chemie International Edition, 2012. **51**(42): p. 10472-10498.

150. Leite, F.L., et al., *Theoretical models for surface forces and adhesion and their measurement using atomic force microscopy.* International Journal of Molecular Sciences, 2012. **13**(10): p. 12773-12856.

151. Moore, T.L., et al., *Nanoparticle colloidal stability in cell culture media and impact on cellular interactions.* Chemical Society Reviews, 2015. **44**(17): p. 6287-6305.

152. Exner, J.H. and E.C. Steiner, *Solvation and ion pairing of alkali-metal alkoxides in dimethyl sulfoxide. Conductometric studies.* Journal of the American Chemical Society, 1974. **96**(6): p. 1782-1787.

153. Rahnemaie, R., T. Hiemstra, and W.H. van Riemsdijk, *Inner- and outer-sphere complexation of ions at the goethite–solution interface.* Journal of Colloid and Interface Science, 2006. **297**(2): p. 379-388.

154. Hunter, C.A., et al., *Aromatic interactions.* Journal of the Chemical Society: Perkin Transactions 2, 2001(5): p. 651-669.

155. Vlasova, N.N. and L.P. Golovkova, *The adsorption of amino acids on the surface of highly dispersed silica.* Colloid Journal, 2004. **66**(6): p. 657-662.

156. Wong, M.H., et al., *Lipid exchange envelope penetration (LEEP) of nanoparticles for plant engineering: A universal localization mechanism.* Nano Letters, 2016. **16**(2): p. 1161-1172.

157. Meot-Ner, M., *Update 1 of: Strong ionic hydrogen bonds.* Chemical Reviews, 2012. **112**(10): p. PR22-PR103.

158. Stewart, K.D. and T.A. Gray, *Survey of the DNA binding properties of natural and synthetic polyamino compounds.* Journal of Physical Organic Chemistry, 1992. **5**(8): p. 461-466.

159. Dill, K.A., et al., *Modeling water, the hydrophobic effect, and ion solvation.* Annual Review of Biophysics and Biomolecular Structure, 2005. **34**: p. 173-199.

160. Maibaum, L., A.R. Dinner, and D. Chandler, *Micelle formation and the hydrophobic effect.* Journal of Physical Chemistry B, 2004. **108**(21): p. 6778-6781.

161. Schneider, H.-J., *Binding mechanisms in supramolecular complexes.* Angewandte Chemie International Edition, 2009. **48**(22): p. 3924-3977.

162. Dunitz, J.D., *Win some, lose some: Enthalpy-entropy compensation in weak intermolecular interactions.* Chemistry & Biology, 1995. **2**(11): p. 709-712.

163. Kabiri, M. and L.D. Unsworth, *Application of isothermal titration calorimetry for characterizing thermodynamic parameters of biomolecular interactions: Peptide self-assembly and protein adsorption case studies.* Biomacromolecules, 2014. **15**(10): p. 3463-3473.

164. Jadhav, V.D. and F.P. Schmidtchen, *Surprises in the design of anion receptors: Calorimetry prevents false reasoning.* Organic Letters, 2005. **7**(15): p. 3311-3314.

165. Li, X., J. Zhang, and H. Gu, *Study on the adsorption mechanism of DNA with mesoporous silica nanoparticles in aqueous solution.* Langmuir, 2012. **28**(5): p. 2827-2834.

166. Biedermann, F. and H.-J. Schneider, *Experimental binding energies in supramolecular complexes.* Chemical Reviews, 2016. **116**(9): p. 5216-5300.

167. Huang, R. and B.L. Lau, *Biomolecule–nanoparticle interactions: Elucidation of the thermodynamics by isothermal titration calorimetry.* Biochimica et Biophysica Acta (BBA)-General Subjects, 2016. **1860**(5): p. 945-956.

168. Sokolowsky, K., et al., *Spectroscopic and thermodynamic comparisons of escherichia coli DNA photolyase and vibrio cholerae cryptochrome 1.* Journal of Physical Chemistry B, 2010. **114**(20): p. 7121-7130.

169. Williams, D.H., et al., *Changes in motion vs. Bonding in positively vs. Negatively cooperative interactions.* Chemical Communications, 2002(12): p. 1266-1267.

170. Marcus, Y. and G. Hefter, *Ion pairing.* Chemical Reviews, 2006. **106**(11): p. 4585-4621.

171. Ball, V. and C. Maechling, *Isothermal microcalorimetry to investigate non specific interactions in biophysical chemistry.* International Journal of Molecular Sciences, 2009. **10**(8): p. 3283-3315.

172. Samsonova, O., et al., *The use of isothermal titration calorimetry and molecular dynamics to show variability in DNA transfection performance.* Acta Biomaterialia, 2013. **9**(2): p. 4994-5002.

173. Bloomfield, V.A., *DNA condensation by multivalent cations.* Biopolymers: Original Research on Biomolecules, 1997. **44**(3): p. 269-282.

174. Prevette, L.E., et al., *Deciphering the role of hydrogen bonding in enhancing pDNA−polycation interactions.* Langmuir, 2007. **23**(19): p. 9773-9784.

175. Pellecchia, M., et al., *Perspectives on NMR in drug discovery: A technique comes of age.* Nature Reviews Drug Discovery, 2008. **7**(9): p. 738.

176. Myszka, D.G., *Kinetic analysis of macromolecular interactions using surface plasmon resonance biosensors.* Current Opinion in Biotechnology, 1997. **8**(1): p. 50-57.

177. Lehenkari, P.P., et al., *Adapting atomic force microscopy for cell biology.* Ultramicroscopy, 2000. **82**(1-4): p. 289-295.

178. Freyer, M.W. and E.A. Lewis, *Isothermal titration calorimetry: Experimental design, data analysis, and probing macromolecule/ligand binding and kinetic interactions*, in *Methods in cell biology*. 2008, Academic Press. p. 79-113.

179. TA Instruments, *Nano ITC getting started guide.* TA Instruments-Waters LLC, 2011.

180. Wiseman, T., et al., *Rapid measurement of binding constants and heats of binding using a new titration calorimeter.* Analytical Biochemistry, 1989. **179**(1): p. 131-137.

181. MicroCal, *ITC data analysis in Origin: Tutorial guide.* MicroCal LLC, Northampton, MA, 2004.

182. Brautigam, C.A., *Fitting two- and three-site binding models to isothermal titration calorimetric data.* Methods, 2015. **76**: p. 124-136.

183. Gan, Q., et al., *Effect of size on the cellular endocytosis and controlled release of mesoporous silica nanoparticles for intracellular delivery.* Biomedical Microdevices, 2012. **14**(2): p. 259-270.

184. Mu, Q., et al., *Chemical basis of interactions between engineered nanoparticles and biological systems.* Chemical Reviews, 2014. **114**(15): p. 7740-7781.

185. Lu, F., et al., *Size effect on cell uptake in well-suspended, uniform mesoporous silica nanoparticles.* Small, 2009. **5**(12): p. 1408-1413.

186. Oh, N. and J.-H. Park, *Endocytosis and exocytosis of nanoparticles in mammalian cells.* International Journal of Nanomedicine, 2014. **9**(Suppl. 1): p. 51-63.

187. Slomberg, D.L. and M.H. Schoenfisch, *Silica nanoparticle phytotoxicity to Arabidopsis thaliana.* Environmental Science & Technology, 2012. **46**(18): p. 10247-10254.

188. Navarro, E., et al., *Environmental behavior and ecotoxicity of engineered nanoparticles to algae, plants, and fungi.* Ecotoxicology, 2008. **17**(5): p. 372-386.

189. Miralles, P., T.L. Church, and A.T. Harris, *Toxicity, uptake, and translocation of engineered nanomaterials in vascular plants.* Environmental Science & Technology, 2012. **46**(17): p. 9224-9239.

190. Bajaj, A., et al., *Stability, toxicity and differential cellular uptake of protein passivated-Fe_3O_4 nanoparticles.* Journal of Materials Chemistry, 2009. **19**(35): p. 6328-6331.

191. Zhang, Y., et al., *Influence of silica particle internalization on adhesion and migration of human dermal fibroblasts.* Biomaterials, 2010. **31**(32): p. 8465-8474.

192. Zhao, Y., et al., *Interaction of mesoporous silica nanoparticles with human red blood cell membranes: Size and surface effects.* ACS Nano, 2011. **5**(2): p. 1366-1375.

193. Huang, X., et al., *The effect of the shape of mesoporous silica nanoparticles on cellular uptake and cell function.* Biomaterials, 2010. **31**(3): p. 438-448.

194. Tao, Z., et al., *Mesoporosity and functional group dependent endocytosis and cytotoxicity of silica nanomaterials.* Chemical Research in Toxicology, 2009. **22**(11): p. 1869-1880.

195. Slowing, I., B.G. Trewyn, and V.S.Y. Lin, *Effect of surface functionalization of MCM-41-type mesoporous silica nanoparticles on the endocytosis by human cancer cells.* Journal of the American Chemical Society, 2006. **128**(46): p. 14792-14793.

196. Corbalan, J.J., et al., *Amorphous silica nanoparticles trigger nitric oxide/peroxynitrite imbalance in human endothelial cells: Inflammatory and cytotoxic effects.* International Journal of Nanomedicine, 2011. **6**: p. 2821-2835.

197. Ma, X., et al., *Interactions between engineered nanoparticles (ENPs) and plants: Phytotoxicity, uptake and accumulation.* Science of The Total Environment, 2010. **408**(16): p. 3053-3061.

198. Lin, Y.-S. and C.L. Haynes, *Impacts of mesoporous silica nanoparticle size, pore ordering, and pore integrity on hemolytic activity.* Journal of the American Chemical Society, 2010. **132**(13): p. 4834-4842.

199. Anjum, N.A., et al., *Transport phenomena of nanoparticles in plants and animals/humans.* Environmental Research, 2016. **151**: p. 233-243.

200. Schwab, F., et al., *Barriers, pathways and processes for uptake, translocation and accumulation of nanomaterials in plants–critical review.* Nanotoxicology, 2016. **10**(3): p. 257-278.

201. Sakhtianchi, R., et al., *Exocytosis of nanoparticles from cells: Role in cellular retention and toxicity.* Advances in Colloid and Interface Science, 2013. **201–202**: p. 18-29.

202. Wang, M., et al., *Endosomal escape kinetics of mesoporous silica-based system for efficient siRNA delivery.* International Journal of Pharmaceutics, 2013. **448**(1): p. 51-7.

203. Sauer, A.M., et al., *Role of endosomal escape for disulfide-based drug delivery from colloidal mesoporous silica evaluated by live-cell imaging.* Nano Letters, 2010. **10**(9): p. 3684-3691.

204. Vallhov, H., et al., *Mesoporous silica particles induce size dependent effects on human dendritic cells.* Nano Letters, 2007. **7**(12): p. 3576-3582.

205. Corredor, E., et al., *Nanoparticle penetration and transport in living pumpkin plants: In situ subcellular identification.* BMC Plant Biology, 2009. **9**(1): p. 45.

206. Yanes, R.E., et al., *Involvement of lysosomal exocytosis in the excretion of mesoporous silica nanoparticles and enhancement of the drug delivery effect by exocytosis inhibition.* Small, 2013. **9**(5): p. 697-704.

207. Souris, J.S., et al., *Surface charge-mediated rapid hepatobiliary excretion of mesoporous silica nanoparticles.* Biomaterials, 2010. **31**(21): p. 5564-5574.

208. Ikonen, E., *Roles of lipid rafts in membrane transport.* Current Opinion in Cell Biology, 2001. **13**(4): p. 470-477.

209. Singh, R. and J.W. Lillard, *Nanoparticle-based targeted drug delivery.* Experimental and Molecular Pathology, 2009. **86**(3): p. 215-223.

210. Chen, Y.J., et al., *DNA nanotechnology from the test tube to the cell.* Nature Nanotechnology, 2015. **10**(9): p. 748-760.

211. Xiong, L. and S.Z. Qiao, *A mesoporous organosilica nano-bowl with high DNA loading capacity - a potential gene delivery carrier.* Nanoscale, 2016. **8**(40): p. 17446-17450.

212. Draghici, B. and M.A. Ilies, *Synthetic nucleic acid delivery systems: Present and perspectives.* Journal of Medicinal Chemistry, 2015. **58**(10): p. 4091-4130.

213. Kanasty, R., et al., *Delivery materials for siRNA therapeutics.* Nature Materials, 2013. **12**(11): p. 967-977.

214. Keller, M. and A.D. Miller, *Intracellular delivery of nucleic acids: Differences between transfection and siFection reflect differences between DNA and RNA, and between oligodeoxynucleotides and oligonucleotides*, in *Non-viral gene therapy*. 2005, Springer. p. 441-455.

215. Luo, D. and W.M. Saltzman, *Synthetic DNA delivery systems.* Nature Biotechnology, 2000. **18**(1): p. 33-37.

216. Kesharwani, P., V. Gajbhiye, and N.K. Jain, *A review of nanocarriers for the delivery of small interfering RNA.* Biomaterials, 2012. **33**(29): p. 7138-7150.

217. Ho, W., X.Q. Zhang, and X. Xu, *Biomaterials in siRNA delivery: A comprehensive review.* Advanced Healthcare Materials, 2016. **5**(21): p. 2715-2731.

218. Mastrobattista, E., W.E. Hennink, and R.M. Schiffelers, *Delivery of nucleic acids.* Pharmaceutical Research, 2007. **24**(8): p. 1561.

219. Solberg, S.M. and C.C. Landry, *Adsorption of DNA into mesoporous silica.* The Journal of Physical Chemistry B, 2006. **110**(31): p. 15261-15268.

220. Schlipf, D.M., *Biomolecule localization and surface engineering within size tunable nanoporous silica particles*. 2015, University of Kentucky: Lexington, Kentucky, United States.

221. Yiu, H.H., P.A. Wright, and N.P. Botting, *Enzyme immobilisation using SBA-15 mesoporous molecular sieves with functionalised surfaces.* Journal of Molecular Catalysis B: Enzymatic, 2001. **15**(1-3): p. 81-92.

222. Dordick, J. and A. Freeman, *Biocatalysis as a discovery tool: From nanoscale to high-throughput and beyond.* Current Opinion in Biotechnology, 2006. **17**(6): p. 559-561.

223. Wang, Y. and F. Caruso, *Mesoporous silica spheres as supports for enzyme immobilization and encapsulation.* Chemistry of Materials, 2005. **17**(5): p. 953-961.

224. Brennan, J.D., *Biofriendly sol–gel processing for the entrapment of soluble and membrane-bound proteins: Toward novel solid-phase assays for high-throughput screening.* Accounts of Chemical Research, 2007. **40**(9): p. 827-835.

225. Katiyar, A., et al., *Protein adsorption on the mesoporous molecular sieve silicate SBA-15: Effects of pH and pore size.* Journal of Chromatography A, 2005. **1069**(1): p. 119-126.

226. Sun, Z., et al., *Hierarchically ordered macro-/mesoporous silica monolith: Tuning macropore entrance size for size-selective adsorption of proteins.* Chemistry of Materials, 2011. **23**(8): p. 2176-2184.

227. Katiyar, A. and N.G. Pinto, *Visualization of size-selective protein separations on spherical mesoporous silicates.* Small, 2006. **2**(5): p. 644-648.

228. Ma, Y., et al., *Microspectroscopic analysis of green fluorescent proteins infiltrated into mesoporous silica nanochannels.* Journal of Colloid and Interface Science, 2011. **356**(1): p. 123-130.

229. Luo, Z., et al., *Mesoporous silica nanoparticles end-capped with collagen: Redox-responsive nanoreservoirs for targeted drug delivery.* Angewandte Chemie International Edition, 2011. **50**(3): p. 640-643.

230. Ulbrich, K., et al., *Targeted drug delivery with polymers and magnetic nanoparticles: Covalent and noncovalent approaches, release control, and clinical studies.* Chemical Reviews, 2016. **116**(9): p. 5338-5431.

231. Trewyn, B.G., C.M. Whitman, and V.S.Y. Lin, *Morphological control of room-temperature ionic liquid templated mesoporous silica nanoparticles for controlled release of antibacterial agents.* Nano Letters, 2004. **4**(11): p. 2139-2143.

232. Chen, Z., et al., *Mesoporous silica nanoparticles with manipulated microstructures for drug delivery.* Colloids and Surfaces B: Biointerfaces, 2012. **95**: p. 274-278.

233. Wan, M.M., et al., *Sustained release of heparin on enlarged-pore and functionalized MCM-41.* ACS Applied Materials & Interfaces, 2012. **4**(8): p. 4113-4122.

234. Manzano, M., et al., *Studies on MCM-41 mesoporous silica for drug delivery: Effect of particle morphology and amine functionalization.* Chemical Engineering Journal, 2008. **137**(1): p. 30-37.

235. Thomas, A.G. and K.L. Syres, *Adsorption of organic molecules on rutile TiO_2 and anatase TiO_2 single crystal surfaces.* Chemical Society Reviews, 2012. **41**(11): p. 4207-4217.

236. Wu, H.-P., T.-L. Cheng, and W.-L. Tseng, *Phosphate-modified TiO_2 nanoparticles for selective detection of dopamine, levodopa, adrenaline, and catechol based on fluorescence quenching.* Langmuir, 2007. **23**(14): p. 7880-7885.

237. Belessi, V., et al., *Removal of reactive red 195 from aqueous solutions by adsorption on the surface of TiO_2 nanoparticles.* Journal of Hazardous Materials, 2009. **170**(2–3): p. 836-844.

238. Mudunkotuwa, I.A. and V.H. Grassian, *Histidine adsorption on TiO_2 nanoparticles: An integrated spectroscopic, thermodynamic, and molecular-based approach toward understanding nano–bio interactions.* Langmuir, 2014. **30**(29): p. 8751-8760.

239. Lu, Z., et al., *Self-assembled TiO_2 nanocrystal clusters for selective enrichment of intact phosphorylated proteins.* Angewandte Chemie International Edition, 2010. **49**(10): p. 1862-1866.

240. Wang, Z.-G., et al., *Development of the affinity materials for phosphorylated proteins/peptides enrichment in phosphoproteomics analysis.* ACS Applied Materials & Interfaces, 2015. **7**(16): p. 8377-8392.

241. Liu, H., J. Zhou, and H. Huang, *Amine-functionalized TiO_2 nanoparticles for highly selective enrichment of phosphopeptides.* Talanta, 2015. **143**: p. 431-437.

242. Wijeratne, A.B., et al., *Phosphopeptide separation using radially aligned titania nanotubes on titanium wire.* ACS Applied Materials & Interfaces, 2015. **7**(21): p. 11155-11164.

243. Bian, J., et al., *Solid-phase extraction approach for phospholipids profiling by titania-coated silica microspheres prior to reversed-phase liquid chromatography–evaporative light scattering detection and tandem mass spectrometry analysis.* Talanta, 2014. **123**: p. 233-240.

244. Schlipf, D.M., et al., *Flavonoid adsorption and stability on titania-functionalized silica nanoparticles.* Colloids and Surfaces A, 2015. **478**: p. 15-21.

245. Zdyb, A. and S. Krawczyk, *Adsorption and electronic states of morin on TiO_2 nanoparticles.* Chemical Physics, 2014. **443**: p. 61-66.

246. Murakami, A., H. Ashida, and J. Terao, *Multitargeted cancer prevention by quercetin.* Cancer Letters, 2008. **269**(2): p. 315-325.

247. Hirpara, K.V., et al., *Quercetin and its derivatives: Synthesis, pharmacological uses with special emphasis on anti-tumor properties and prodrug with enhanced bio-availability.* Anti-Cancer Agents in Medicinal Chemistry 2009. **9**(2): p. 138-161.

248. Perez-Vizcaino, F. and J. Duarte, *Flavonols and cardiovascular disease.* Molecular Aspects of Medicine, 2010. **31**(6): p. 478-494.

249. Nijveldt, R.J., et al., *Flavonoids: A review of probable mechanisms of action and potential applications.* The American Journal of Clinical Nutrition, 2001. **74**(4): p. 418-425.

250. Dinesh Kumar, V., P.R.P. Verma, and S.K. Singh, *Development and evaluation of biodegradable polymeric nanoparticles for the effective delivery of quercetin using a quality by design approach.* LWT-Food Science and Technology, 2015. **61**(2): p. 330-338.

251. Gupta, P., et al., *Quercetin conjugated poly(β-amino esters) nanogels for the treatment of cellular oxidative stress.* Acta Biomaterialia, 2015. **27**: p. 194-204.

252. Mukhopadhyay, P. and A.K. Prajapati, *Quercetin in anti-diabetic research and strategies for improved quercetin bioavailability using polymer-based carriers - a review.* RSC Advances, 2015. **5**(118): p. 97547-97562.

253. Xu, L., et al., *Selective separation of flavonoid glycosides in Dalbergia odorifera by matrix solid-phase dispersion using titania.* Journal of Separation Science, 2011. **34**(11): p. 1347-1354.

254. Do, Q.D., et al., *Effect of extraction solvent on total phenol content, total flavonoid content, and antioxidant activity of Limnophila aromatica.* Journal of Food and Drug Analysis, 2014. **22**(3): p. 296-302.

255. Tseng, P.-J., et al., *A facile colorimetric assay for determination of salicylic acid in tobacco leaves using titanium dioxide nanoparticles.* Analytical Methods, 2014. **6**(6): p. 1759-1765.

256. Vivero-Escoto, J.L., et al., *Recent progress in mesoporous titania materials: Adjusting morphology for innovative applications.* Science and Technology of Advanced Materials, 2012. **13**(1): p. 013003.

257. Masolo, E., et al., *Mesoporous titania powders: The role of precursors, ligand addition and calcination rate on their morphology, crystalline structure and photocatalytic activity.* Nanomaterials, 2014. **4**(3): p. 583-598.

258. Signoretto, M., et al., *TiO_2–MCM-41 for the photocatalytic abatement of NOx in gas phase.* Applied Catalysis B: Environmental, 2010. **95**(1–2): p. 130-136.

259. Nayab, S., et al., *Design and fabrication of branched polyamine functionalized mesoporous silica: An efficient absorbent for water remediation.* ACS Applied Materials & Interfaces, 2014. **6**(6): p. 4408-4417.

260. Dahl, M., Y. Liu, and Y. Yin, *Composite titanium dioxide nanomaterials.* Chemical Reviews, 2014. **114**(19): p. 9853-9889.

261. Zaccariello, G., et al., *TiO_2-mesoporous silica nanocomposites: Cooperative effect in the photocatalytic degradation of dyes and drugs.* RSC Advances, 2014. **4**(71): p. 37826-37837.

262. Acosta-Silva, Y.J., et al., *TiO_2/DMS-1 disordered mesoporous silica system: Structural characteristics and methylene blue photodegradation activity.* Microporous and Mesoporous Materials, 2013. **170**: p. 181-188.

263. Tel, H., Y. Altaş, and M.S. Taner, *Adsorption characteristics and separation of Cr(III) and Cr(VI) on hydrous titanium(IV) oxide.* Journal of Hazardous Materials, 2004. **112**(3): p. 225-231.

264. Sriprang, P., S. Wongnawa, and O. Sirichote, *Amorphous titanium dioxide as an adsorbent for dye polluted water and its recyclability.* Journal of Sol-Gel Science and Technology, 2014. **71**(1): p. 86-95.

265. Vradman, L., et al., *Evaluation of metal oxide phase assembling mode inside the nanotubular pores of mesostructured silica.* Microporous and Mesoporous Materials, 2005. **79**(1–3): p. 307-318.

266. Singh, R., et al., *Atomic layer deposited (ALD) TiO_2 on fibrous nano-silica (KCC-1) for photocatalysis: Nanoparticle formation and size quantization effect.* ACS Catalysis, 2016. **6**(5): p. 2770-2784.

267. Liu, C., et al., *Enhanced photocatalytic performance of mesoporous TiO_2 coated SBA-15 nanocomposites fabricated through a novel approach: Supercritical deposition aided by liquid-crystal template.* Materials Research Bulletin, 2016. **75**: p. 25-34.

268. Hanprasopwattana, A., et al., *Titania coatings on monodisperse silica spheres (characterization using 2-propanol dehydration and TEM).* Langmuir, 1996. **12**(13): p. 3173-3179.

269. Jaroniec, M., M. Kruk, and J.P. Olivier, *Standard nitrogen adsorption data for characterization of nanoporous silicas.* Langmuir, 1999. **15**(16): p. 5410-5413.

270. Jiang, Z., et al., *The dedicated high-resolution grazing-incidence X-ray scattering beamline 8-ID-e at the advanced photon source.* Journal of Synchrotron Radiation, 2012. **19**(4): p. 627-636.

271. Jiang, Z., *GIXSGUI: A MATLAB toolbox for grazing-incidence X-ray scattering data visualization and reduction, and indexing of buried three-dimensional periodic nanostructured films.* Journal of Applied Crystallography, 2015. **48**(3): p. 917-926.

272. Busuioc, A.M., et al., *Structural features and photocatalytic behaviour of titania deposited within the pores of SBA-15.* Applied Catalysis A: General, 2006. **312**(0): p. 153-164.

273. Kim, M.-H., et al., *Facile synthesis of monodispersed mesoporous silica nanoparticles with ultralarge pores and their application in gene delivery.* ACS Nano, 2011. **5**(5): p. 3568-3576.

274. Sayari, A., et al., *Characterization of large-pore MCM-41 molecular sieves obtained via hydrothermal restructuring.* Chemistry of Materials, 1997. **9**(11): p. 2499-2506.

275. Šuligoj, A., et al., *TiO_2–SiO_2 films from organic-free colloidal TiO_2 anatase nanoparticles as photocatalyst for removal of volatile organic compounds from indoor air.* Applied Catalysis B: Environmental, 2016. **184**: p. 119-131.

276. Cendrowski, K., et al., *Mesoporous silica nanospheres functionalized by TiO_2 as a photoactive antibacterial agent.* Journal of Nanomedicine & Nanotechnology, 2013. **4**: p. DOI: 10.4172/2157-7439.1000182.

277. Wang, H.J., et al., *A facile way to synthesize mesoporous silica with Ia3d cubic symmetry.* Materials Letters, 2008. **62**(3): p. 422-424.

278. Smilgies, D.-M., *Scherrer grain-size analysis adapted to grazing-incidence scattering with area detectors.* Journal of Applied Crystallography, 2009. **42**(6): p. 1030-1034.

279. Sakurai, K. and M. Mizusawa, *X-ray diffraction imaging of anatase and rutile.* Analytical Chemistry, 2010. **82**(9): p. 3519-3522.

280. Zhang, J., J.S. Brodbelt, and J. Wang, *Threshold dissociation and molecular modeling of transition metal complexes of flavonoids.* Journal of the American Society for Mass Spectrometry, 2005. **16**(2): p. 139-151.

281. Jurasekova, Z., et al., *Adsorption and catalysis of flavonoid quercetin on different plasmonic metal nanoparticles monitored by SERS.* Journal of Raman Spectroscopy, 2012. **43**(12): p. 1913-1919.

282. Arriagada, F., et al., *Morin flavonoid adsorbed on mesoporous silica, a novel antioxidant nanomaterial.* PLoS One, 2016. **11**(11): p. e0164507.

283. Song, X., et al., *Quercetin molecularly imprinted polymers: Preparation, recognition characteristics and properties as sorbent for solid-phase extraction.* Talanta, 2009. **80**(2): p. 694-702.

284. Dai, J. and R.J. Mumper, *Plant phenolics: Extraction, analysis and their antioxidant and anticancer properties.* Molecules, 2010. **15**(10): p. 7313-7352.

285. Khoddami, A., M. Wilkes, and T. Roberts, *Techniques for analysis of plant phenolic compounds.* Molecules, 2013. **18**(2): p. 2328-2375.

286. Zhang, L., et al., *Hydrochloric acid leaching behavior of different treated panxi ilmenite concentrations.* Hydrometallurgy, 2011. **107**(1–2): p. 40-47.

287. Zhao, B.-Y., et al., *Biocompatible deep eutectic solvents based on choline chloride: Characterization and application to the extraction of rutin from Sophora japonica.* ACS Sustainable Chemistry & Engineering, 2015. **3**(11): p. 2746-2755.

288. Mudunkotuwa, I.A. and V.H. Grassian, *Citric acid adsorption on TiO_2 nanoparticles in aqueous suspensions at acidic and circumneutral pH: Surface coverage, surface speciation, and its impact on nanoparticle−nanoparticle interactions.* Journal of the American Chemical Society, 2010. **132**(42): p. 14986-14994.

289. Bishop, L.M., et al., *A citric acid-derived ligand for modular functionalization of metal oxide surfaces via "click" chemistry.* Langmuir, 2012. **28**(2): p. 1322-1329.

290. Wang, X.S., et al., *The removal of basic dyes from aqueous solutions using agricultural by-products.* Journal of Hazardous Materials, 2008. **157**(2–3): p. 374-385.

291. Berlier, G., et al., *Stabilization of quercetin flavonoid in MCM-41 mesoporous silica: Positive effect of surface functionalization.* Journal of Colloid and Interface Science, 2013. **393**: p. 109-118.

292. Lemańska, K., et al., *The influence of pH on antioxidant properties and the mechanism of antioxidant action of hydroxyflavones.* Free Radical Biology and Medicine, 2001. **31**(7): p. 869-881.

293. van Acker, S.A.B.E., et al., *Influence of iron chelation on the antioxidant activity of flavonoids.* Biochemical Pharmacology, 1998. **56**(8): p. 935-943.

294. Isono, R., T. Yoshimura, and K. Esumi, *Preparation of Au/TiO_2 nanocomposites and their catalytic activity for DPPH radical scavenging reaction.* Journal of Colloid and Interface Science, 2005. **288**(1): p. 177-183.

295. Morsella, M., et al., *Improving the sunscreen properties of TiO_2 through an understanding of its catalytic properties.* ACS Omega, 2016. **1**(3): p. 464-469.

296. Kirakosyan, A. and P.B. Kaufman, *Recent advances in plant biotechnology*. 2009, New York, United States: Springer US.

297. Oksman-Caldentey, K.-M. and D. Inzé, *Plant cell factories in the post-genomic era: New ways to produce designer secondary metabolites.* Trends in Plant Science, 2004. **9**(9): p. 433-440.

298. Brown, D.P., et al., *Target-directed discovery and production of pharmaceuticals in transgenic mutant plant cells.* Journal of Biotechnology, 2016. **238**: p. 9-14.

299. Chen, T.-J., et al., *Quercetin inhibition of ROS-dependent and -independent apoptosis in rat glioma C6 cells.* Toxicology, 2006. **223**(1–2): p. 113-126.

300. Del Follo-Martinez, A., et al., *Resveratrol and quercetin in combination have anticancer activity in colon cancer cells and repress oncogenic microRNA-27a.* Nutrition and Cancer, 2013. **65**(3): p. 494-504.

301. Verpoorte, R., *Exploration of nature's chemodiversity: The role of secondary metabolites as leads in drug development.* Drug Discovery Today, 1998. **3**(5): p. 232-238.

302. Littleton, J., *The future of plant drug discovery.* Expert Opinion on Drug Discovery, 2007. **2**(5): p. 673-683.

303. Heilmann, J., *New medical applications of plant secondary metabolites*, in *Annual plant reviews volume 39: Functions and biotechnology of plant secondary metabolites*. 2010, Wiley-Blackwell. p. 348-380.

304. Koehn, F.E. and G.T. Carter, *The evolving role of natural products in drug discovery.* Nature Reviews Drug Discovery, 2005. **4**(3): p. 206-220.

305. Wilson, S.A. and S.C. Roberts, *Recent advances towards development and commercialization of plant cell culture processes for synthesis of biomolecules.* Plant Biotechnology Journal, 2012. **10**(3): p. 249-268.

306. Slowing, I.I., et al., *Mesoporous silica nanoparticles as controlled release drug delivery and gene transfection carriers.* Advanced Drug Delivery Reviews, 2008. **60**(11): p. 1278-1288.

307. Faure, B., et al., *Dispersion and surface functionalization of oxide nanoparticles for transparent photocatalytic and UV-protecting coatings and sunscreens.* Science and Technology of Advanced Materials, 2013. **14**(2): p. 023001.

308. Hartono, S.B., et al., *Functionalized large pore mesoporous silica nanoparticles for gene delivery featuring controlled release and co-delivery.* Journal of Materials Chemistry B, 2014. **2**(6): p. 718-726.

309. Ye, M., et al., *Magnetically recoverable core-shell nanocomposites with enhanced photocatalytic activity.* Chemistry - A European Journal, 2010. **16**(21): p. 6243-6250.

310. Dong, W., et al., *Preparation of secondary mesopores in mesoporous anatase–silica nanocomposites with unprecedented-high photocatalytic degradation performances.* Advanced Functional Materials, 2016. **26**(6): p. 964-976.

311. Martin-Ortigosa, S., et al., *Mesoporous silica nanoparticle-mediated intracellular Cre protein delivery for maize genome editing via loxP site excision.* Plant Physiology, 2014. **164**(2): p. 537-547.

312. Nair, R., et al., *Nanoparticulate material delivery to plants.* Plant Science, 2010. **179**(3): p. 154-163.

313. Klaine, S.J., et al., *Nanomaterials in the environment: Behavior, fate, bioavailability, and effects.* Environmental Toxicology and Chemistry, 2008. **27**(9): p. 1825-1851.

314. Rico, C.M., et al., *Interaction of nanoparticles with edible plants and their possible implications in the food chain.* Journal of Agricultural and Food Chemistry, 2011. **59**(8): p. 3485-3498.

315. Wang, S., J. Kurepa, and J.A. Smalle, *Ultra-small TiO_2 nanoparticles disrupt microtubular networks in Arabidopsis thaliana.* Plant, Cell & Environment, 2011. **34**(5): p. 811-820.

316. Jung, H.-S., D.-S. Moon, and J.-K. Lee, *Quantitative analysis and efficient surface modification of silica nanoparticles.* Journal of Nanomaterials, 2012.

317. Strobel, C., et al., *Fate of cerium dioxide nanoparticles in endothelial cells: Exocytosis.* Journal of Nanoparticle Research, 2015. **17**(5): p. 206.

318. Kurepa, J., et al., *Uptake and distribution of ultrasmall anatase TiO_2 alizarin red S nanoconjugates in Arabidopsis thaliana.* Nano Letters, 2010. **10**(7): p. 2296-2302.

319. Cowen, T., A.J. Haven, and G. Burnstock, *Pontamine sky blue: A counterstain for background autofluorescence in fluorescence and immunofluorescence histochemistry.* Histochemistry, 1985. **82**(3): p. 205-208.

320. Sharma, R.I., J.E. Schwarzbauer, and P.V. Moghe, *Nanomaterials can dynamically steer cell responses to biological ligands.* Small, 2011. **7**(2): p. 242-251.

321. Lutz, J.A., et al., *A nicotinic receptor-mediated anti-inflammatory effect of the flavonoid rhamnetin in BV2 microglia.* Fitoterapia, 2014. **98**: p. 11-21.

322. Lee, J.E., et al., *Uniform mesoporous dye-doped silica nanoparticles decorated with multiple magnetite nanocrystals for simultaneous enhanced magnetic resonance imaging, fluorescence imaging, and drug delivery.* Journal of the American Chemical Society, 2009. **132**(2): p. 552-557.

323. Hu, H., et al., *Biocompatiable hollow silica microspheres as novel ultrasound contrast agents for in vivo imaging.* Journal of Materials Chemistry, 2011. **21**(18): p. 6576-6583.

324. Schlipf, D.M., S.E. Rankin, and B.L. Knutson, *Selective external surface functionalization of large-pore silica materials capable of protein loading.* Microporous and Mesoporous Materials, 2017. **244**: p. 199-207.

325. Ritter, H., et al., *A comparative study of the functionalization of mesoporous silica MCM-41 by deposition of 3-aminopropyltrimethoxysilane from toluene and from the vapor phase.* Microporous and Mesoporous Materials, 2009. **121**(1–3): p. 79-83.

326. Brown, D.P., et al., *Novel multifunctional pharmacology of lobinaline, the major alkaloid from Lobelia cardinalis.* Fitoterapia, 2016. **111**: p. 109-123.

327. Feliczak-Guzik, A., et al., *Synthesis and characterization of SBA-16 type mesoporous materials containing amine groups.* Microporous and Mesoporous Materials, 2016. **220**: p. 231-238.

328. Nordmann, J., et al., *In vivo analysis of the size- and time-dependent uptake of NaYF4:Yb,er upconversion nanocrystals by pumpkin seedlings.* Journal of Materials Chemistry B, 2015. **3**(1): p. 144-150.

329. Servin, A.D., et al., *Synchrotron micro-XRF and micro-XANES confirmation of the uptake and translocation of TiO_2 nanoparticles in cucumber (Cucumis sativus) plants.* Environmental Science & Technology, 2012. **46**(14): p. 7637-7643.

330. Larue, C., et al., *Accumulation, translocation and impact of TiO_2 nanoparticles in wheat (Triticum aestivum spp.): Influence of diameter and crystal phase.* Science of The Total Environment, 2012. **431**: p. 197-208.

331. Mahony, D., et al., *In vivo delivery of bovine viral diahorrea virus, E2 protein using hollow mesoporous silica nanoparticles.* Nanoscale, 2014. **6**(12): p. 6617-6626.

332. Stalmans, P., et al., *Trypan blue not toxic for retinal pigment epithelium in vitro.* American Journal of Ophthalmology, 2003. **135**(2): p. 234-236.

333. Indrasekara, A.S.D.S., et al., *Dimeric gold nanoparticle assemblies as tags for SERS-based cancer detection.* Advanced Healthcare Materials, 2013. **2**(10): p. 1370-1376.

334. Asli, S. and P.M. Neumann, *Colloidal suspensions of clay or titanium dioxide nanoparticles can inhibit leaf growth and transpiration via physical effects on root water transport.* Plant, Cell & Environment, 2009. **32**(5): p. 577-584.

335. Hong, F., et al., *Influences of nano-TiO_2 on the chloroplast aging of spinach under light.* Biological Trace Element Research, 2005. **104**(3): p. 249-260.

336. Saw, C.L.L., et al., *The berry constituents quercetin, kaempferol, and pterostilbene synergistically attenuate reactive oxygen species: Involvement of the Nrf2-ARE signaling pathway.* Food and Chemical Toxicology, 2014. **72**: p. 303-311.

337. Peer, W.A., et al., *Flavonoid accumulation patterns of transparent testa mutants of Arabidopsis.* Plant Physiology, 2001. **126**(2): p. 536-548.

338. Yin, W., et al., *Phytotoxicity, translocation, and biotransformation of $NaYF_4$ upconversion nanoparticles in a soybean plant.* Small, 2015. **11**(36): p. 4774-4784.

339. Serag, M.F., et al., *Trafficking and subcellular localization of multiwalled carbon nanotubes in plant cells.* ACS Nano, 2011. **5**(1): p. 493-499.

340. Low, P.S. and S. Chandra, *Endocytosis in plants.* Annual Review of Plant Biology, 1994. **45**(1): p. 609-631.

341. Hu, L., et al., *Influences of size of silica particles on the cellular endocytosis, exocytosis and cell activity of HepG2 cells.* Journal of Nanoscience Letters, 2011. **1**(1): p. 1-16.

342. Jiang, X., et al., *Endo- and exocytosis of zwitterionic quantum dot nanoparticles by live HeLa cells.* ACS Nano, 2010. **4**(11): p. 6787-6797.

343. Wilson, S.A. and S.C. Roberts, *Recent advances towards development and commercialization of plant cell culture processes for the synthesis of biomolecules.* Plant Biotechnology Journal, 2012. **10**(3): p. 249-268.

344. Cunningham, F.J., et al., *Nanoparticle-mediated delivery towards advancing plant genetic engineering.* Trends in Biotechnology, 2018. **36**(9): p. 882-897.

345. Croissant, J.G., et al., *Mesoporous silica and organosilica nanoparticles: Physical chemistry, biosafety, delivery strategies, and biomedical applications.* Advanced Healthcare Materials, 2018. **7**(4): p. 75.

346. Yang, P.P., S.L. Gai, and J. Lin, *Functionalized mesoporous silica materials for controlled drug delivery.* Chemical Society Reviews, 2012. **41**(9): p. 3679-3698.

347. Zhang, Y., et al., *In situ and timed extraction of cellular peptides from live HeLa cells by photo-switchable mesoporous silica nanocarriers.* Analytical Chemistry, 2016. **88**(17): p. 8380-8384.

348. Ghafariyan, M.H., et al., *Effects of magnetite nanoparticles on soybean chlorophyll.* Environmental Science & Technology, 2013. **47**(18): p. 10645-10652.

349. Naqvi, S., et al., *Calcium phosphate nanoparticle mediated genetic transformation in plants.* Journal of Materials Chemistry, 2012. **22**(8): p. 3500-3507.

350. Xia, B., et al., *Highly efficient uptake of ultrafine mesoporous silica nanoparticles with excellent biocompatibility by Liriodendron hybrid suspension cells.* Science China Life Sciences, 2013. **56**(1): p. 82-89.

351. Liu, Q., et al., *Carbon nanotubes as molecular transporters for walled plant cells.* Nano letters, 2009. **9**(3): p. 1007-1010.

352. Deng, Y.-Q., J.C. White, and B.-S. Xing, *Interactions between engineered nanomaterials and agricultural crops: Implications for food safety.* Journal of Zhejiang University: SCIENCE A, 2014. **15**(8): p. 552-572.

353. Kim, J.-H., et al., *Exposure of iron nanoparticles to Arabidopsis thaliana enhances root elongation by triggering cell wall loosening.* Environmental Science & Technology, 2014. **48**(6): p. 3477-3485.

354. Sun, D., et al., *Uptake and cellular distribution, in four plant species, of fluorescently labeled mesoporous silica nanoparticles.* Plant Cell Reports, 2014. **33**(8): p. 1389-1402.

355. Geisler-Lee, J., et al., *Reproductive toxicity and life history study of silver nanoparticle effect, uptake and transport in Arabidopsis thaliana.* Nanomaterials, 2014. **4**(2): p. 301-318.

356. Wang, W.-N., J.C. Tarafdar, and P. Biswas, *Nanoparticle synthesis and delivery by an aerosol route for watermelon plant foliar uptake.* Journal of Nanoparticle Research, 2013. **15**(1): p. 1417.

357. Deng, Y., et al., *Multiple method analysis of TiO_2 nanoparticle uptake in rice (Oryza sativa L.) plants.* Environmental Science & Technology, 2017. **51**(18): p. 10615-10623.

358. Na, H.-K., et al., *Efficient functional delivery of siRNA using mesoporous silica nanoparticles with ultralarge pores.* Small, 2012. **8**(11): p. 1752-1761.

359. Donahue, N.D., H. Acar, and S. Wilhelm, *Concepts of nanoparticle cellular uptake, intracellular trafficking, and kinetics in nanomedicine.* Advanced Drug Delivery Reviews, 2019.

360. Shomer, I., et al., *Electrical potentials of plant cell walls in response to the ionic environment.* Plant Physiology, 2003. **133**(1): p. 411-422.

361. Kinraide, T.B. and P. Wang, *The surface charge density of plant cell membranes (σ): An attempt to resolve conflicting values for intrinsic σ.* Journal of Experimental Botany, 2010. **61**(9): p. 2507-2518.

362. Xing, X., et al., *Uptake of silica-coated nanoparticles by HeLa cells.* Journal of Nanoscience and Nanotechnology, 2005. **5**(10): p. 1688-1693.

363. Jin, H., D.A. Heller, and M.S. Strano, *Single-particle tracking of endocytosis and exocytosis of single-walled carbon nanotubes in NIH-3T3 cells.* Nano Letters, 2008. **8**(6): p. 1577-1585.

364. Yang, H., et al., *Supramolecular chemistry at interfaces: Host–guest interactions for fabricating multifunctional biointerfaces.* Accounts of Chemical Research, 2014. **47**(7): p. 2106-2115.

365. Houk, K.N., et al., *Binding affinities of host–guest, protein–ligand, and protein–transition-state complexes.* Angewandte Chemie International Edition, 2003. **42**(40): p. 4872-4897.

366. Uhlenheuer, D.A., K. Petkau, and L. Brunsveld, *Combining supramolecular chemistry with biology.* Chemical Society Reviews, 2010. **39**(8): p. 2817-2826.

367. Hage, D.S., *Analysis of biological interactions by affinity chromatography: Clinical and pharmaceutical applications.* Clinical Chemistry, 2017. **63**(6): p. 1083-1093.

368. Frączyk, J., M. Walczak, and Z.J. Kamiński, *Cellulose template assembled synthetic peptides as molecular receptors.* Current Protein and Peptide Science, 2016. **17**(2): p. 117-126.

369. Menegatti, S., *Peptoid affinity ligands.* US Patent, 2018. **10,065,988 B2**.

370. Tozzi, C., L. Anfossi, and G. Giraudi, *Affinity chromatography techniques based on the immobilisation of peptides exhibiting specific binding activity.* Journal of Chromatography B, 2003. **797**(1-2): p. 289-304.

371. Tothill, I.E., *Peptides as molecular receptors*, in *Recognition receptors in biosensors*. 2010, Springer. p. 249-274.

372. Noppe, W., et al., *Immobilised peptide displaying phages as affinity ligands: Purification of lactoferrin from defatted milk.* Journal of Chromatography A, 2006. **1101**(1-2): p. 79-85.

373. Song, N. and Y.-W. Yang, *Molecular and supramolecular switches on mesoporous silica nanoparticles.* Chemical Society Reviews, 2015. **44**(11): p. 3474-3504.

374. Ma, Y., et al., *Large-pore mesoporous silica spheres: Synthesis and application in HPLC.* Colloids and Surfaces A: Physicochemical and Engineering Aspects, 2003. **229**(1-3): p. 1-8.

375. Zhao, J., et al., *Biomolecule separation using large pore mesoporous SBA-15 as a substrate in high performance liquid chromatography.* Chemical Communications, 2002(7): p. 752-753.

376. Thornton, P.D. and A. Heise, *Highly specific dual enzyme-mediated payload release from peptide-coated silica particles.* Journal of the American Chemical Society, 2010. **132**(6): p. 2024-2028.

377. Kinnari, P.J., et al., *Tumour homing peptide-functionalized porous silicon nanovectors for cancer therapy.* Biomaterials, 2013. **34**(36): p. 9134-9141.

378. Farkaš, P. and S. Bystrický, *Chemical conjugation of biomacromolecules: A mini-review.* Chemical Papers, 2010. **64**(6): p. 683-695.

379. Sundoro, B.M., *Bifunctional linker.* US Patent, 1987. **4,680,338**.

380. Thermo Fisher Scientific, *Amine-reactive crosslinker chemistry.* https://www.thermofisher.com. **Accessed 09/02/2019**.

381. Shi, J.-M., et al., *Bis (sulfosuccinimidyl) suberate (BS^3) crosslinking analysis of the behavior of amyloid-β peptide in solution and in phospholipid membranes.* PLoS One, 2017. **12**(3): p. e0173871.

382. Xia, B., et al., *Biofunctionalisation of porous silicon (PS) surfaces by using homobifunctional cross-linkers.* Journal of Materials Chemistry, 2006. **16**(6): p. 570-578.

383. Lee, J.P., et al., *N-terminal specific conjugation of extracellular matrix proteins to 2-pyridinecarboxaldehyde functionalized polyacrylamide hydrogels.* Biomaterials, 2016. **102**: p. 268-276.

384. Kalkhof, S. and A. Sinz, *Chances and pitfalls of chemical cross-linking with amine-reactive n-hydroxysuccinimide esters.* Analytical and Bioanalytical Chemistry, 2008. **392**(1-2): p. 305-312.

385. Karakeçili, A.G., et al., *Enhancement of fibroblastic proliferation on chitosan surfaces by immobilized epidermal growth factor.* Acta Biomaterialia, 2008. **4**(4): p. 989-996.

386. Li, B., J. Chen, and J.H.C. Wang, *Rgd peptide-conjugated poly (dimethylsiloxane) promotes adhesion, proliferation, and collagen secretion of human fibroblasts.* Journal of Biomedical Materials Research Part A, 2006. **79**(4): p. 989-998.

387. Oluwabusola, E., *Development of diazirine-based crosslinking agents for covalently linking protein*. 2015, University of Salford: Manchester, United Kingdom.

388. Shigdel, U.K., J. Zhang, and C. He, *Diazirine-based DNA photo-cross-linking probes for the study of protein–DNA interactions.* Angewandte Chemie International Edition, 2008. **47**(1): p. 90-93.

389. Chim, L.K.-L., *Immobilizing gradients of neurotrophic factors for directed peripheral nervous system cell migration guidance*. 2016, Johns Hopkins University: Baltimore, Maryland, United States.

390. Das, J., *Aliphatic diazirines as photoaffinity probes for proteins: Recent developments.* Chemical Reviews, 2011. **111**(8): p. 4405-4417.

391. Suchanek, M., A. Radzikowska, and C. Thiele, *Photo-leucine and photo-methionine allow identification of protein-protein interactions in living cells.* Nature methods, 2005. **2**(4): p. 261.

392. Tanaka, Y. and J.J. Kohler, *Photoactivatable crosslinking sugars for capturing glycoprotein interactions.* Journal of the American Chemical Society, 2008. **130**(11): p. 3278-3279.

393. Liashkovich, I., et al., *Photopicking: In situ approach for site-specific attachment of single multiprotein nanoparticles to atomic force microscopy tips.* Advanced Functional Materials, 2017. **27**(8): p. 1604506.

394. Moussus, M., et al., *Intracellular stresses in patterned cell assemblies.* Soft Matter, 2014. **10**(14): p. 2414-2423.

395. Lozito, T.P. and R.S. Tuan, *Mesenchymal stem cells inhibit both endogenous and exogenous MMPs via secreted TIMPs.* Journal of Cellular Physiology, 2011. **226**(2): p. 385-396.

396. Berneschi, S., et al., *Fluorescence biosensing in selectively photo–activated microbubble resonators.* Sensors and Actuators B: Chemical, 2017. **242**: p. 1057-1064.

397. Lozito, T.P., et al., *Human mesenchymal stem cells generate a distinct pericellular zone of MMP activities via binding of MMPs and secretion of high levels of TIMPs.* Matrix Biology, 2014. **34**: p. 132-143.

398. Bomgarden, R.D., et al., *New diazirine-based photoreactive crosslinkers: Heterobifunctional crosslinkers for studying extracellular and intracellular protein-protein interactions.* Thermo Fisher Scientific Previews. **12**(2): p. 1-2.

399. Iacobucci, C., et al., *Carboxyl-photo-reactive MS-cleavable cross-linkers: Unveiling a hidden aspect of diazirine-based reagents.* Analytical Chemistry, 2018. **90**(4): p. 2805-2809.

400. Van Itallie, C.M., L.L. Mitic, and J.M. Anderson, *Claudin-2 forms homodimers and is a component of a high molecular weight protein complex.* Journal of Biological Chemistry, 2011. **286**(5): p. 3442-3450.

401. Casanova, D., et al., *Counting the number of proteins coupled to single nanoparticles.* Journal of the American Chemical Society, 2007. **129**(42): p. 12592-12593.

402. Waddell, C., *The development of a rapid fiber-based immunoassay as a point-of-care or In-home diagnostic test*. 2013, Clemson University: Clemson, South Carolina, United States.

403. Ettinger, R., *Infrared spectrum of diazirine.* The Journal of Chemical Physics, 1964. **40**(6): p. 1693-1699.

404. Gambi, A., M. Winnewisser, and J.J. Christiansen, *The infrared spectrum of diazirine: $H_2C<(N=N)$. Rovibrational analysis of the ν_3 fundamental.* Journal of Molecular Spectroscopy, 1983. **98**(2): p. 413-424.

405. Martucci, N.M., et al., *Bioengineered surfaces for real-time label-free detection of cancer cells.* Lab-on-a-Chip Fabrication and Application, 2016: p. 179.

406. Mitchell, R. and J. Merritt, *The infrared spectra of 3, 3-dimethyldiazirine and 3, 3-dimethyl-d6-diazirine.* Journal of Molecular Spectroscopy, 1968. **27**(1-4): p. 197-209.

407. Barth, A., *The infrared absorption of amino acid side chains.* Progress in Biophysics and Molecular Biology, 2000. **74**(3-5): p. 141-173.

408. Kolev, T., M. Spiteller, and B. Koleva, *Spectroscopic and structural elucidation of amino acid derivatives and small peptides: Experimental and theoretical tools.* Amino Acids, 2010. **38**(1): p. 45-50.

409. Zhang, G., et al., *Green synthesis, composition analysis and surface active properties of sodium cocoyl glycinate.* American Journal of Analytical Chemistry, 2013. **4**(09): p. 445.

410. Schwede, T., L. Bordoli, and S. Berneche, *Introduction: Principles of protein structures*. 2007, Swiss Institute of Bioinformatics: Lausanne, Switzerland.

411. Hu, Y., et al., *Layer-by-layer assembly of β-estradiol loaded mesoporous silica nanoparticles on titanium substrates and its implication for bone homeostasis.* Advanced Materials, 2010. **22**(37): p. 4146-4150.

412. Steffi, C., et al., *Estradiol-loaded poly (ε-caprolactone)/silk fibroin electrospun microfibers decrease osteoclast activity and retain osteoblast function.* ACS Applied Materials & Interfaces, 2018. **10**(12): p. 9988-9998.

413. Ejima, D., et al., *Effective elution of antibodies by arginine and arginine derivatives in affinity column chromatography.* Analytical Biochemistry, 2005. **345**(2): p. 250-257.

414. Endo, T., *Fractionation of glycoprotein-derived oligosaccharides by affinity chromatography using immobilized lectin columns.* Journal of Chromatography A, 1996. **720**(1): p. 251-261.

415. Liau, C.Y., et al., *Purification of human plasma haptoglobin by hemoglobin-affinity column chromatography.* Journal of Chromatography B, 2003. **790**(1-2): p. 209-216.

416. Lahcen, A.A., et al., *Synthesis and electrochemical characterization of nanostructured magnetic molecularly imprinted polymers for 17-β-estradiol determination.* Sensors and Actuators B: Chemical, 2017. **241**: p. 698-705.

417. Verma, I.M. and M.D. Weitzman, *Gene therapy: Twenty-first century medicine.* Annual Review of Biochemistry, 2005. **74**: p. 711-38.

418. Wu, G. and H. Lu, *Progress in biomedical applications of functionalized nucleic acid nanodevices (NANDs).* ChemNanoMat, 2016. **2**(5): p. 354-363.

419. Mei, Y., et al., *Recent progress in nanomaterials for nucleic acid delivery in cancer immunotherapy.* Biomaterials Science, 2019. **7**(7): p. 2640-2651.

420. Zakrewsky, M., S. Kumar, and S. Mitragotri, *Nucleic acid delivery into skin for the treatment of skin disease: Proofs-of-concept, potential impact, and remaining challenges.* Journal of Controlled Release, 2015. **219**: p. 445-456.

421. Chen, Z., et al., *DNA translocation through an array of kinked nanopores.* Nature Materials, 2010. **9**(8): p. 667-675.

422. Lam, J.K.W., et al., *siRNA versus miRNA as therapeutics for gene silencing.* Molecular Therapy-Nucleic Acids, 2015. **4**(9): p. e252.

423. Burnett, J.C. and J.J. Rossi, *RNA-based therapeutics: Current progress and future prospects.* Chemistry & Biology, 2012. **19**(1): p. 60-71.

424. Mamta, B. and M.V. Rajam, *RNAi technology: A new platform for crop pest control.* Physiology and Molecular Biology of Plants, 2017. **23**(3): p. 487-501.

425. Kamthan, A., et al., *Small rnas in plants: Recent development and application for crop improvement.* Frontiers in Plant Science, 2015. **6**: p. 17.

426. Edson, J.A. and Y.J. Kwon, *RNAi for silencing drug resistance in microbes toward development of nanoantibiotics.* Journal of Controlled Release, 2014. **189**: p. 150-157.

427. Kim, D.H. and J.J. Rossi, *Strategies for silencing human disease using RNA interference.* Nature Reviews Genetics, 2007. **8**: p. 173.

428. Davidson, B.L. and P.B. McCray, *Current prospects for RNA interference-based therapies.* Nature Reviews Genetics, 2011. **12**(5): p. 329-340.

429. van den Boorn, J.G., et al., *siRNA delivery with exosome nanoparticles.* Nature Biotechnology, 2011. **29**(4): p. 325-326.

430. Li, J.M., S.S. Xue, and Z.W. Mao, *Nanoparticle delivery systems for siRNA-based therapeutics.* Journal of Materials Chemistry B, 2016. **4**(41): p. 6620-6639.

431. Lv, H., et al., *Toxicity of cationic lipids and cationic polymers in gene delivery.* Journal of Controlled Release, 2006. **114**(1): p. 100-109.

432. Tarn, D., et al., *Mesoporous silica nanoparticle nanocarriers: Biofunctionality and biocompatibility.* Accounts of Chemical Research, 2013. **46**(3): p. 792-801.

433. Tao, Z., *Mesoporous silica-based nanodevices for biological applications.* RSC Advances, 2014. **4**(36): p. 18961.

434. Rosenholm, J.M., et al., *Nanoparticles in targeted cancer therapy: Mesoporous silica nanoparticles entering preclinical development stage.* Nanomedicine, 2012. **7**(1): p. 111-120.

435. Hom, C., J. Lu, and F. Tamanoi, *Silica nanoparticles as a delivery system for nucleic acid-based reagents.* Journal of Materials Chemistry, 2009. **19**(35): p. 6308-6316.

436. Lin, D., et al., *Intracellular cleavable poly(2-dimethylaminoethyl methacrylate) functionalized mesoporous silica nanoparticles for efficient siRNA delivery in vitro and in vivo.* Nanoscale, 2013. **5**: p. 4291-4301.

437. Buchman, Y.K., et al., *Silica nanoparticles and polyethyleneimine (PEI)-mediated functionalization: A new method of PEI covalent attachment for siRNA delivery applications.* Bioconjugate Chemistry, 2013. **24**(12): p. 2076-87.

438. Xia, T., et al., *Polyethyleneimine coating enhances the cellular uptake of mesoporous silica nanoparticles and allows safe delivery of siRNA and DNA constructs.* ACS Nano, 2009. **3**(10): p. 3273-3286.

439. Ashley, C.E., et al., *Delivery of small interfering RNA by peptide-targeted mesoporous silica nanoparticle-supported lipid bilayers.* ACS Nano, 2012. **6**(3): p. 2174-2188.

440. Meng, H., et al., *Engineered design of mesoporous silica nanoparticles to deliver doxorubicin and p-glycoprotein siRNA to overcome drug resistance in a cancer cell line.* ACS Nano, 2010. **4**(8): p. 4539-4550.

441. Li, X., et al., *The packaging of siRNA within the mesoporous structure of silica nanoparticles.* Biomaterials, 2011. **32**(35): p. 9546-9556.

442. Vallet-Regí, M., F. Balas, and D. Arcos, *Mesoporous materials for drug delivery.* Angewandte Chemie International Edition, 2007. **46**(40): p. 7548-7558.

443. Zhu, R., et al., *Optical brightener M2R destroys the peritrophic membrane of Spodoptera exigua (Lepidoptera: Noctuidae) larvae.* Pest Management Science, 2007. **63**(3): p. 296-300.

444. Wang, P. and R.R. Granados, *Calcofluor disrupts the midgut defense system in insects.* Insect Biochemistry and Molecular Biology, 2000. **30**: p. 135–143.

445. Castillo, R.R., A. Baeza, and M. Vallet-Regi, *Recent applications of the combination of mesoporous silica nanoparticles with nucleic acids: Development of bioresponsive devices, carriers and sensors.* Biomaterials Science, 2017. **5**(3): p. 353-377.

446. Steinbacher, J.L. and C.C. Landry, *Adsorption and release of siRNA from porous silica.* Langmuir, 2014. **30**(15): p. 4396-4405.

447. Muralidhar, A. and K.D. Dorfman, *Kirkwood diffusivity of long semiflexible chains in nanochannel confinement.* Macromolecules, 2015. **48**(8): p. 2829-2839.

448. de Carvalho, S.J., R. Metzler, and A.G. Cherstvy, *Inverted critical adsorption of polyelectrolytes in confinement.* Soft Matter, 2015. **11**(22): p. 4430-43.

449. Reisner, W., J.N. Pedersen, and R.H. Austin, *DNA confinement in nanochannels: Physics and biological applications.* Reports on Progress in Physics, 2012. **75**(10): p. 106601.

450. Dai, L., C.B. Renner, and P.S. Doyle, *The polymer physics of single DNA confined in nanochannels.* Advances in Colloid and Interface Science, 2016. **232**: p. 80-100.

451. Suryawanshi, H., H. Sabharwal, and S. Maiti, *Thermodynamics of peptide− RNA recognition: The binding of a TAT peptide to TAR RNA.* The Journal of Physical Chemistry B, 2010. **114**(34): p. 11155-11163.

452. Vandiver, M.S., et al., *Effect of ancillary ligands on the DNA interaction of* $[Cr(diimine)_3]^{3+}$ *complexes containing the intercalating dipyridophenazine ligand.* Inorganic Chemistry, 2009. **49**(3): p. 839-848.

453. Alatorre-Meda, M., et al., *DNA− poly (diallyldimethylammonium chloride) complexation and transfection efficiency.* Journal of Physical Chemistry B, 2010. **114**(29): p. 9356-9366.

454. Holzerny, P., et al., *Biophysical properties of chitosan/siRNA polyplexes: Profiling the polymer/siRNA interactions and bioactivity.* Journal of Controlled Release, 2012. **157**(2): p. 297-304.

455. Krivitsky, A., et al., *Molecular weight-dependent activity of aminated poly (α) glutamates as siRNA nanocarriers.* Polymers, 2018. **10**(5): p. 548.

456. Patel, M.M. and T.J. Anchordoquy, *Contribution of hydrophobicity to thermodynamics of ligand-DNA binding and DNA collapse.* Biophysical Journal, 2005. **88**(3): p. 2089-2103.

457. Nadeau, E., *Binding, protection, and RNA delivery properties of porous silica nanoparticles in Spodoptera frugiperda cells*. 2017, University of Kentucky: Lexington, Kentucky, United States.

458. Liu, L.B., Istvan ; Wang, Yan ; Leonard, Joshua N ; Shiloach, Joseph ; Segal, David M ; Davies, David R, *Structural basis of toll-like receptor 3 signaling with double-stranded RNA.* Science, 2008. **320**(5874): p. 379-81.

459. Abels, J.A., et al., *Single-molecule measurements of the persistence length of double-stranded RNA.* Biophysical Journal, 2005. **88**(4): p. 2737-44.

460. Utsuno, K., et al., *Low molecular weight branched PEI binding to linear DNA.* Chemical and Pharmaceutical Bulletin, 2016. **64**(10): p. 1484-1491.

461. Utsuno, K. and H. Uludağ, *Thermodynamics of polyethylenimine-DNA binding and DNA condensation.* Biophysical journal, 2010. **99**(1): p. 201-207.

462. Zheng, M., et al., *Targeting the blind spot of polycationic nanocarrier-based siRNA delivery.* ACS nano, 2012. **6**(11): p. 9447-9454.

463. Giraldo, L. and J.C. Moreno-Piraján, *Calorimetric study of mesoporous SBA-15 modified for controlled valproic acid delivery*. Journal of Chemistry, 2013. **267464**: p. 267464 (1-11).

464. Huang, R., et al., *Effects of surface compositional and structural heterogeneity on nanoparticle–protein interactions: Different protein configurations.* ACS nano, 2014. **8**(6): p. 5402-5412.

465. Prevette, L.E., M.L. Lynch, and T.M. Reineke, *Amide spacing influences pDNA binding of poly(amidoamine)s.* Biomacromolecules, 2010. **11**(2): p. 326-332.

466. Jung, S., T.P. Lodge, and T.M. Reineke, *Structures and protonation states of hydrophilic–cationic diblock copolymers and their binding with plasmid DNA.* Journal of Physical Chemistry B, 2018. **122**(9): p. 2449-2461.

467. Jensen, L.B., et al., *Molecular characterization of the interaction between siRNA and PAMAM G7 dendrimers by SAXS, ITC, and molecular dynamics simulations.* Biomacromolecules, 2010. **11**(12): p. 3571-3577.

468. Shakya, A., et al., *Rapid exchange between free and bound states in RNA–dendrimer polyplexes: Implications on the mechanism of delivery and release.* Biomacromolecules, 2015. **17**(1): p. 154-164.

469. Kim, W., et al., *Thermodynamics of DNA condensation induced by poly (ethylene glycol)-block-polylysine through polyion complex micelle formation.* Biomacromolecules, 2010. **11**(5): p. 1180-1186.

470. Turnbull, W.B. and A.H. Daranas, *On the value of c: Can low affinity systems be studied by isothermal titration calorimetry?* Journal of the American Chemical Society, 2003. **125**(48): p. 14859-14866.

471. Dávila-Ibáñez, A.B., N.J. Buurma, and V. Salgueiriño, *Assessment of DNA complexation onto polyelectrolyte-coated magnetic silica nanoparticles.* Nanoscale, 2013. **5**(11): p. 4797-4807.

472. Fotticchia, I., et al., *Thermodynamic signature of secondary nano-emulsion formation by isothermal titration calorimetry.* Langmuir, 2014. **30**(48): p. 14427-14433.

473. Bharadwaj, S., R. Montazeri, and D.T. Haynie, *Direct determination of the thermodynamics of polyelectrolyte complexation and implications thereof for electrostatic layer-by-layer assembly of multilayer films.* Langmuir, 2006. **22**(14): p. 6093-6101.

474. Gourishankar, A., et al., *Isothermal titration calorimetry studies on the binding of DNA bases and PNA base monomers to gold nanoparticles.* Journal of the American Chemical Society, 2004. **126**(41): p. 13186-13187.

475. Ehtezazi, T., U. Rungsardthong, and S. Stolnik, *Thermodynamic analysis of polycation − DNA interaction applying titration microcalorimetry.* Langmuir, 2003. **19**(22): p. 9387-9394.

476. Matulis, D., I. Rouzina, and V.A. Bloomfield, *Thermodynamics of DNA binding and condensation: Isothermal titration calorimetry and electrostatic mechanism.* Journal of Molecular Biology, 2000. **296**(4): p. 1053-1063.

477. Breiten, B., et al., *Water networks contribute to enthalpy/entropy compensation in protein–ligand binding.* Journal of the American Chemical Society, 2013. **135**(41): p. 15579-15584.

478. Joshi, S., et al., *Interfacial molecular imprinting of Stöber particle surfaces: A simple approach to targeted saccharide adsorption.* Journal of Colloid and Interface Science, 2014. **428**: p. 101-110.

479. Lim, Z.X., et al., *Diet-delivered RNAi in Helicoverpa armigera – progresses and challenges.* Journal of Insect Physiology, 2016. **85**: p. 86-93.

480. Kim, J., et al., *Multifunctional uniform nanoparticles composed of a magnetite nanocrystal core and a mesoporous silica shell for magnetic resonance and fluorescence imaging and for drug delivery.* Angewandte Chemie International Edition, 2008. **47**(44): p. 8438-8441.

481. Lu, A.-H., E.L. Salabas, and F. Schüth, *Magnetic nanoparticles: Synthesis, protection, functionalization, and application.* Angewandte Chemie International Edition, 2007. **46**(8): p. 1222-1244.

482. Knežević, N.Ž., et al., *Magnetic mesoporous silica-based core/shell nanoparticles for biomedical applications.* RSC Advances, 2013. **3**(25): p. 9584-9593.

VITA

Md Arif Khan

Place of Birth: Narsingdi, Dhaka, Bangladesh

EDUCATIONAL INSTITUTIONS AND DEGREES

1. University of Kentucky (UKY), Lexington, KY, USA
   Ph.D. in Chemical Engineering (expected December 2019)
2. North Carolina A&T State University (NCATSU), Greensboro, NC, USA
   M.S. in Chemical Engineering (May 2014)
3. Bangladesh University of Engineering & Technology (BUET), Dhaka, Bangladesh
   B.Sc., Chemical Engineering (January 2008)

PROFESSIONAL POSITIONS HELD

1. Research Assistant, University of Kentucky, United States
   August 2014 - Present
2. Teaching Assistant, University of Kentucky, United States
   August 2014 - May 2015
3. Research Assistant, North Carolina A&T State University, United States
   August 2011 - May 2014
4. Teaching Assistant, North Carolina A&T State University, United States
   August 2011 - May 2014
5. Senior Engineer, Akij Cement Co. Ltd., Narayanganj, Bangladesh
   October 2010 - July 2011
6. (Senior) Production Engineer, Shah Cement In. Ltd., Bangladesh
   March 2008 - September 2010

SCHOLASTIC AND PROFESSIONAL HONORS

1. Outstanding Graduate Student in Chemical Engineering Award, Department of Chemical and Materials Engineering (CME), UKY 2019
2. Nominated for College of Engineering's "Outstanding Doctoral Student" Award, UKY 2019
3. College of Engineering, UKY, Block Grant Travel Award for Argonne National Laboratory visit 2019
4. Department of Chemical and Materials Engineering (CME), UKY, Block Grant Travel Award 2018
5. Department of CME, UKY, Travel Grant Award to attend conferences, 2017 and 2018

6. Certificate for completing training on X-ray scattering techniques (Xeuss 2.0) from Xenocs 2018
7. Invited Graduate Student Presentation, 8th Annual College of Pharmacy Drug Discovery & Development and Natural Product (DDDNP) Symposium, Lexington, KY, 2017
8. University of Kentucky Graduate School Travel Awards, 2016
9. Wadaran Latamore Kennedy Scholarship for outstanding academic achievement at NCATSU 2013
10. Scholarly Accomplishments and Excellence in Academic Performance Certificate, NCATSU, 2011-12
11. Technical Scholarship, Bangladesh University of Engineering & Technology, Bangladesh, 2003-2007

PROFESSIONAL PUBLICATIONS

Journal Publications

Published

1. **M. Arif Khan**, William T. Wallace, Jatinder Sambi, Dennis Trent Rogers, John M. Littleton, Stephen E. Rankin and Barbara L. Knutson, *Nanoharvesting of bioactive materials from living plant cultures using engineered silica nanoparticles*, Materials Science & Engineering C, 2020, 106, 110190.
2. **M. Arif Khan** and Yusuf G. Adewuyi, *Techno-economic modeling and optimization of catalytic reactive distillation for the esterification reactions in bio-oil upgradation*, Chemical Engineering Research and Design, 2019, 148, 86-101.
3. Suraj Nagpure, Qinglin Zhang, **M. Arif Khan**, Syed Z. Islam, Jiagang Xu, Yang-Tse Cheng, Barbara L. Knutson and Stephen E. Rankin, *Layer-by-layer synthesis of thick mesoporous TiO_2 films with vertically oriented accessible nanopores and their application for lithium ion battery negative electrodes*, Advanced Functional Materials, **2018**, 28(37), 1801849.
4. Yusuf G. Adewuyi and **Md Arif Khan**, *Simultaneous NO and SO_2 removal by aqueous persulfate activated by combined heat and Fe^{2+}: Experimental and kinetic mass transfer model studies*, Environmental Science and Pollution Research, **2018**, DOI: 10.1007/s11356-018-2453-9.
5. **M. Arif Khan**, William T. Wallace, Syed Z. Islam, Suraj Nagpure, Joseph Strzalka, John M. Littleton, Stephen E. Rankin and Barbara L. Knutson, A*dsorption and recovery of polyphenolic flavonoids using TiO_2-functionalized mesoporous silica nanoparticles*, ACS Applied Materials & Interfaces, **2017**, 9, 32114-32125.
6. Daniel M. Schlipf, Shanshan Zhou, **M. Arif Khan**, Stephen E. Rankin and Barbara L. Knutson, *Effects of pore size and tethering on the diffusivity of lipids confined in mesoporous silica*, Advanced Materials Interfaces, **2017**, DOI: 10.1002/admi.201601103.

7. Yusuf G. Adewuyi, Nana Y. Sakyi and **M. Arif Khan**, *Simultaneous removal of NO and SO_2 from flue gas by combined heat and Fe^{2+} activated persulfate solutions*, Chemosphere, **2018**, 193, 1216-1225.
8. **M. Arif Khan** and Yusuf G. Adewuyi, *High pressure reactive distillation simulation and optimization for the esterification of pyrolysis bio-oil*, Process Engineering Journal, **2017**, 1, 73-85.
9. Yusuf G. Adewuyi and **M. Arif Khan**, *Nitric oxide removal from flue gas by combined persulfate and ferrous-EDTA solutions: Effects of persulfate and EDTA concentrations, temperature, pH and SO_2*, Chemical Engineering Journal, **2016**, 304, 793-807.
10. Yusuf G. Adewuyi and **Md A. Khan**, *Nitric oxide removal by combined persulfate and ferrous-EDTA reaction systems*, Chemical Engineering Journal, **2015**, 281, 575-587.
11. Yusuf G. Adewuyi, **Md A. Khan** and Nana Y. Sakyi, *Kinetics and modeling of the removal of nitric oxide by aqueous sodium persulfate simultaneously activated by temperature and Fe^{2+}*, Industrial and Engineering Chemistry Research, **2014**, 53, 828-839.

Conference Publications

Conference Proceedings

12. **Md Arif Khan** and Yusuf G. Adewuyi, *Simulation of reactive distillation for the esterification of pyrolysis bio-oil*, Proceedings to 2013 AIChE Annual Meeting, San Francisco, CA, USA.
13. **Md Arif Khan** and Yusuf G. Adewuyi, *Reaction kinetics and mechanistic studies of nitric oxide removal by combined persulfate and ferrous-EDTA systems*, Proceedings to 2013 AIChE Annual Meeting, San Francisco, CA, USA.

Conference Presentations

Invited Speaker

16. **M. Arif Khan**(†), Stephen E. Rankin, John M. Littleton, and Barbara L. Knutson, *Nanoharvesting of therapeutics from hairy roots using engineered mesoporous silica nanoparticles* 2017 Drug Discovery & Development and Natural Product Consortium Symposium, Lexington, KY, USA.
17. **M. Arif Khan**(†), Barbara L. Knutson and Stephen E. Rankin, *Epitaxial formation mechanism of multilayered ordered titania thick films with accessible nanopores*, 2019 Materials and Chemical Engineering (MACE) Symposium, Lexington, KY, USA.

Oral Presentations

18. Mahsa Moradipour(†), Emily Chase, **Arif Khan**, Shadrack Asare, Bert Lynn, Stephen Rankin, Barbara Knutson, *Interaction of eugenol and lignin dimer-functionalized silica nanoparticles with model cell membranes*, 93rd ACS Colloid & Surface Science Symposium, Atlanta, GA, USA.

19. Yuxin He(†), Arif Khan, Folami Ladipo, Barbara Knutson, Stephen E. Rankin, *Molecular transport properties of ionic liquid 1-butyl-3-methylimidazolium hexafluorophosphate under nanopore confinement,* 93rd ACS Colloid & Surface Science Symposium, Atlanta, GA, USA.

20. **M. Arif Khan**(†), Ramy Ghanim, Joshua Garay, Aniruddha Shirodkar, Yuxin He, Mahsa Moradipour, Barbara L. Knutson and Stephen E. Rankin, *Mesostructure thermal transformation kinetics and mechanism for the synthesis of SiO_2-TiO_2 mixed thin films with sub-3 nanometer vertical pore channels,* 2018 AIChE Annual Meeting, Pittsburgh, PA, USA.

21. **M. Arif Khan**(†) and Yusuf G. Adewuyi, *Techno-economic modeling and optimization of catalytic reactive distillation for bio-oil upgradation,* 2018 AIChE Annual Meeting, Pittsburgh, PA, USA.

22. **M. Arif Khan**(†), Syed Z. Islam, Suraj Nagpure, Barbara L. Knutson and Stephen E. Rankin, *Layer-by-layer epitaxial formation mechanism of ordered titania thick films with vertically accessible nanopores,* 2018 North American Membrane Society (NAMS) Annual Meeting, Lexington, KY, USA.

23. Shanshan Zhou, Emily Nadeau, **M. Arif Khan**, Bruce A. Webb, Stephen E. Rankin, and Barbara L. Knutson(†), *Loading and mobility of RNA in porous silica nanoparticles for delivery to insects,* 2017 AIChE Annual Meeting, Minneapolis, MN, USA.

24. **M. Arif Khan**(†), Syed Z. Islam, Suraj Nagpure, Barbara L. Knutson and Stephen E. Rankin, *In situ grazing incidence small angle x-ray scattering (GISAXS) study of the formation of multilayered ordered mesoporous titania films,* 2017 AIChE Annual Meeting, Minneapolis, MN, USA.

25. **M. Arif Khan**(†), Stephen E. Rankin, John M. Littleton, and Barbara L. Knutson, *Nanoharvesting of therapeutics from living plant cultures by engineered mesoporous silica nanoparticles,* 2017 AIChE Annual Meeting, Minneapolis, MN, USA.

26. **M. Arif Khan**(†), Stephen E. Rankin, John M. Littleton, and Barbara L. Knutson, *Nanoharvesting of polyphenolic flavonoids from Solidago nemoralis hairy root cultures using functionalized mesoporous silica nanoparticles,* 2016 AIChE Annual Meeting, San Francisco, CA, USA.

27. **M. Arif Khan**(†), William T. Wallace, Stephen E. Rankin, John M. Littleton, and Barbara L. Knutson, A*dsorption, stabilization and recovery of polyphenolic flavonoids by TiO_2 functionalized mesoporous silica nanoparticles,* 2016 AIChE Annual Meeting, San Francisco, CA, USA.

28. Yusuf G. Adewuyi and **Md Arif Khan**(†), *Simulation of reactive distillation for the esterification of pyrolysis bio-oil,* 2013 AIChE Annual Meeting, San Francisco, CA, USA.

29. Yusuf G. Adewuyi and **Md Arif Khan**(†), *Reaction kinetics and mechanistic studies of nitric oxide removal by combined aqueous persulfate and ferrous-EDTA systems,* 2013 AIChE Annual Meeting, San Francisco, CA, USA.

Poster Presentations

30. **M. Arif Khan**(†), John M. Littleton, Stephen E. Rankin, and Barbara L. Knutson, *Nanoharvesting and nanodelivery of bioactive materials using engineered silica nanoparticles*, 2018 AIChE Annual Meeting, Pittsburgh, PA, USA.
31. **M. Arif Khan**(†), Syed Z. Islam, Suraj Nagpure, Barbara L. Knutson and Stephen E. Rankin, *Epitaxial formation mechanism of multilayered ordered titania thick films with accessible nanopores*, 2018 Materials and Chemical Engineering (MACE) Symposium, Lexington, KY, USA.
32. **M. Arif Khan**(†), Syed Z. Islam, Suraj Nagpure, Barbara L. Knutson and Stephen E. Rankin, *Layer-by-layer epitaxial formation mechanism of multilayered ordered titania thick films with accessible nanopores*, 2018 NSF EPSCoR Super Collider, Lexington, KY, USA.
33. Justin X. Zhong(†), **M. Arif Khan**, Stephen E. Rankin, and Barbara L. Knutson, *Ligand-mediated TiO_2 functionalization of silica nanoparticles for efficient and selective natural product separation*, 2017 AIChE Annual Meeting, Minneapolis, MN, USA.
34. Emily Nadeau(†), **M. Arif Khan**, Shanshan Zhou, Barbara Knutson, Stephen Rankin, and Bruce Webb, *Protection and RNA delivery properties of porous silica nanoparticles in Spodoptera frugiperda cells*, 2017 International Congress of Entomology, Denver, CO, USA
35. **M. Arif Khan**(†), Stephen E. Rankin, John M. Littleton, and Barbara L. Knutson, *Nanoharvesting of therapeutics from plant cultures by engineered mesoporous silica nanoparticles*, 2017 Drug Discovery & Development and Natural Product Consortium Symposium, Lexington, KY, USA.
36. Mahsa Moradipour(†), Audrey Fetsko, **M. Arif Khan**, Barbara L. Knutson, and Stephen E. Rankin, *Interfacial interactions of lignin dimer*, 2017 NSF EPSCoR Annual Conference, Frankfort, KY, USA.
37. Justin X. Zhong(†), **M. Arif Khan**, Stephen E. Rankin, and Barbara L. Knutson, *Engineering of multifunctional silica-based carriers for the selective binding of plant-derived natural products*, 2017 NSF REU Engineered Bioactive Interfaces and Devices, University of Kentucky, Lexington, KY, USA.
38. **M. Arif Khan**(†), Stephen E. Rankin, John M. Littleton, and Barbara L. Knutson, *Nanoharvesting of therapeutics from living plant cultures by functionalized mesoporous silica nanoparticles*, 2017 Materials and Chemical Engineering (MACE) Symposium, Lexington, KY, USA.
39. Emily Nadeau(†), Bruce Webb, Barbara Knutson, Stephen Rankin, and **M. Arif Khan**, *Nanoparticles and nucleic acids: binding, dissociation, and RNAi*, 2016 International Congress of Entomology, Orlando, FL, USA
40. **M. Arif Khan**(†), Stephen E. Rankin, John M. Littleton, and Barbara L. Knutson, *Nanoharvesting of flavonoids using functionalized mesoporous silica nanoparticles*, 2016 University of Kentucky-Natural Products Consortium Symposium, Lexington, KY, USA.

41. **M. Arif Khan**(†), William T. Wallace, Stephen E. Rankin, John M. Littleton, and Barbara L. Knutson, *Adsorption and recovery of polyphenolic flavonoids by TiO_2 functionalized mesoporous silica nanoparticles,* 2016 Materials and Chemical Engineering (MACE) Symposium, Lexington, KY, USA.

42. **M. Arif Khan**(†), Stephen E. Rankin, John M. Littleton, and Barbara L. Knutson, *Flavonoid adsorption on titania functionalized mesoporous silica nanoparticles,* 2015 University of Kentucky-Natural Products Consortium Symposium, Lexington, KY, USA.

43. **Md. Arif Khan**(†), and Yusuf G. Adewuyi, *Reaction mechanisms and kinetics of nitric oxide removal by combined persulfate and Fe^{II}-EDTA system,* 2014 3rd Annual College of Engineering Graduate Student Poster competition, Greensboro, NC, USA.

44. **Md. Arif Khan**(†), and Yusuf G. Adewuyi, *Simulation of reactive distillation for esterification of pyrolysis bio-oil using Aspen PLUS,* 2013 2nd Annual College of Engineering Graduate Student Poster competition, Greensboro, NC, USA.

(†)*Presenting Author*

Md Arif Khan

October 29, 2019